

UNIVERSITY OF NOTTINGHAM  
SIR PETER MANSFIELD IMAGING CENTRE  
SCHOOL OF PHYSICS AND ASTRONOMY

---

**Developing Techniques for Quantitative Renal Magnetic  
Resonance Imaging**

---

*Author:*  
Alexander James Daniel MSci

*Supervisor:*  
Prof. Susan Francis

19<sup>th</sup> July, 2021



Thesis submitted to the University of Nottingham for the degree of Doctor of Philosophy

It's very hard to talk quantum using a language originally designed to tell other monkeys where the ripe fruit is.

---

Terry Pratchett, *Night Watch*

## Abstract

The kidneys are morphologically and functionally complex organs and as such, lend themselves to complex methodologies of study. One such methodology is quantitative Magnetic Resonance Imaging (MRI). Rather than simply taking a structural image of the kidneys, quantitative MRI aims to measure physical properties such as the rate of blood flow, tissue perfusion, oxygen consumption and more fundamental properties of the matter making up the organ such as its proton density or longitudinal relaxation time,  $T_1$  and transverse relaxation time  $T_2$ . This is done without the need for ionising radiation and often without exogenous contrast agents, thus making MRI an ideal tool for both clinical and research use.

Multiple methods have been developed to measure the transverse relaxation time,  $T_2$ , of the kidneys, often leading to inconsistent results between studies. Here, a methodical comparison of four prominent techniques is performed. This comparison makes use of quantitative phantoms before proceeding to assess each technique in-vivo in healthy volunteers. A Gradient Spin Echo (GraSE) sequence is recommended for future renal  $T_2$  mapping.

Techniques to measure the Renal Metabolic Rate of Oxygen (RMRO<sub>2</sub>) would be highly desirable. Susceptibility Based Oximetry (SBO) and  $T_2$  Relaxation Under Spin Tagging (TRUST) are modified for use in the abdomen. SBO is found to be poorly suited to measuring oxygenation in the renal veins, however TRUST is used to successfully measure changes in venous oxygenation in the renal vein during an oxygen challenge.

Manual definition of the kidneys to compute Total Kidney Volume (TKV) is a tedious and labour intensive bottleneck in many renal MRI studies. Here a Convolutional Neural Network (CNN) is developed to generate fully automated masks of the kidneys to compute TKV with better than human precision.

Finally, quantitative renal mapping methods are developed for an ex-vivo renal MRI protocol to enable future correlation with histopathology pipelines. Correlating these two diagnostic methods should aid clinical adoption of renal MRI, increase confidence in diagnostics, improved patient experience, and will have applications in nephrectomy studies and transplantation.

# Contents

<b>Abstract</b>	ii
<b>Contents</b>	iii
<b>Acknowledgments</b>	vii
<b>Abbreviations</b>	viii
<b>1 Introduction</b>	1
1.1 Imaging in the Clinic . . . . .	1
1.2 Clinical Motivation . . . . .	2
1.3 Thesis Overview . . . . .	7
1.4 References . . . . .	9
<b>2 Principles of Nuclear Magnetic Resonance Imaging</b>	12
2.1 Source of the NMR Signal . . . . .	14
2.1.1 Nuclear Spin . . . . .	14
2.1.2 Application of an External Magnetic Field . . . . .	15
2.1.3 Precession . . . . .	17
2.1.4 Resonance . . . . .	18
2.2 Relaxation and Contrast Mechanisms . . . . .	19
2.2.1 Longitudinal Relaxation ( $T_1$ ) . . . . .	20
2.2.2 Transverse Relaxation ( $T_2$ and $T_2^*$ ) . . . . .	22
2.2.3 Dipole-Dipole Interactions . . . . .	27
2.2.4 Diffusion Weighted Imaging . . . . .	30
2.2.5 Optimisation of Tissue Contrast . . . . .	32
2.3 Forming an Image . . . . .	34

2.3.1	Signal Localisation . . . . .	34
2.3.2	Image Acquisition Acceleration . . . . .	44
2.3.3	Image Acquisition Schemes . . . . .	46
2.4	Conclusion . . . . .	54
2.5	References . . . . .	55
<b>3</b>	<b>Assessment of Renal <math>T_2</math> Mapping Methods</b>	<b>57</b>
3.1	Introduction . . . . .	59
3.1.1	Motivation . . . . .	59
3.1.2	Common Sources of Error in $T_2$ Mapping Sequences .	61
3.1.3	$T_2$ Acquisition Schemes . . . . .	64
3.2	Methods . . . . .	70
3.2.1	Phantom Data Acquisition . . . . .	70
3.2.2	In-Vivo Data Acquisition . . . . .	71
3.2.3	$T_2$ Mapping Protocols . . . . .	72
3.2.4	Post Processing . . . . .	73
3.2.5	Assessment of Data . . . . .	75
3.3	Results . . . . .	79
3.3.1	Verification of Phantom Accuracy . . . . .	79
3.3.2	Fitting Methods . . . . .	80
3.3.3	Phantom Verification . . . . .	84
3.3.4	Summary of Evaluation of $T_2$ Mapping Sequences on Phantoms . . . . .	91
3.3.5	In-Vivo . . . . .	91
3.4	Discussion . . . . .	96
3.5	Conclusion and Future Work . . . . .	100
3.6	Acknowledgements . . . . .	101
3.7	References . . . . .	102
<b>4</b>	<b>Quantitative Methods to Measure Renal Oxygenation</b>	<b>109</b>
4.1	Introduction . . . . .	111
4.2	Methods . . . . .	113
4.2.1	Susceptibility-Based Oximetry . . . . .	113

4.2.2	<i>T<sub>2</sub></i> Relaxation Under Spin Tagging . . . . .	115
4.2.3	Inducing Changes in Oxygenation of Blood in the Renal Vein . . . . .	123
4.3	Results and Discussion . . . . .	125
4.3.1	Susceptibility-Based Oximetry . . . . .	125
4.3.2	<i>T<sub>2</sub></i> Relaxation Under Spin Tagging . . . . .	127
4.4	Conclusions and Future Work . . . . .	135
4.5	Acknowledgements . . . . .	137
4.6	References . . . . .	138
<b>5</b>	<b>Automated Segmentation of Kidneys using Machine Learning</b>	<b>144</b>
5.1	Introduction . . . . .	146
5.2	Neural Networks for Image Segmentation . . . . .	149
5.2.1	Artificial Neural Networks . . . . .	149
5.2.2	Convolutional Neural Networks . . . . .	152
5.3	Methods . . . . .	154
5.3.1	MRI Data Acquisition . . . . .	154
5.3.2	Manual Segmentation . . . . .	155
5.3.3	Automated Segmentation Using a CNN Architecture .	156
5.3.4	Statistical Analysis . . . . .	158
5.4	Results . . . . .	160
5.4.1	Characteristics of the Training Cohort . . . . .	160
5.4.2	Reducing Acquisition Time . . . . .	161
5.4.3	Repeatability of Manual Segmentation . . . . .	162
5.4.4	Network Testing . . . . .	165
5.5	Discussion . . . . .	171
5.5.1	Evaluation of Methodology . . . . .	172
5.5.2	Future Directions . . . . .	174
5.6	Conclusion . . . . .	178
5.7	Acknowledgements . . . . .	178
5.8	References . . . . .	179
<b>6</b>	<b>Ex-Vivo Renal MRI</b>	<b>185</b>

6.1	Introduction . . . . .	187
6.1.1	Validation of Multiparametric MRI via a Nephrectomy Model . . . . .	187
6.1.2	Assessment of Allograft Viability . . . . .	191
6.1.3	Ex-Vivo Protocol Aims . . . . .	193
6.2	MRI Protocol Development . . . . .	193
6.2.1	Anatomical Scans . . . . .	196
6.2.2	Longitudinal $T_1$ Mapping . . . . .	197
6.2.3	Transverse $T_2$ Mapping . . . . .	200
6.2.4	Transverse $T_2^*$ Mapping . . . . .	202
6.2.5	Apparent Diffusion Coefficient Mapping . . . . .	205
6.2.6	Diffusion Tensor Imaging . . . . .	209
6.3	Depth Based Analysis of Renal Data . . . . .	216
6.3.1	Motivation . . . . .	216
6.3.2	Method . . . . .	218
6.4	Monitoring Changes in MR Parameters Post Fixation . . . . .	222
6.4.1	Method . . . . .	223
6.5	Correlating MRI Measures with Histology in Porcine Kidneys of Differing Ages . . . . .	226
6.6	Conclusion and Future Work . . . . .	229
6.7	Acknowledgements . . . . .	233
6.8	References . . . . .	234
<b>7</b>	<b>Conclusion</b>	<b>243</b>
<b>A</b>	<b><math>T_2</math> Fitting Methods</b>	<b>248</b>
A.1	NIST Standard $T_2$ Mapping Protocol . . . . .	249
A.2	Renal $T_2$ Mapping Protocols . . . . .	251
A.2.1	Basic Fit . . . . .	251
A.2.2	Noise Fit . . . . .	252
A.2.3	Discard Fit . . . . .	253
A.2.4	Noise and Discard Fit . . . . .	254
<b>B</b>	<b>Tractography Pipeline</b>	<b>255</b>

# Acknowledgements

I would like to take this opportunity to thank those who have supported me through the course of my PhD. First and foremost I would like to express my immense gratitude to the hepatorenal group at the Sir Peter Mansfield Imaging Centre and in particular my supervisor Professor Sue Francis who has guided me through the course of my PhD while also allowing me to shape the project into one that I have such enthusiasm for.

I would also like to show my appreciation for the wider community at work, be that support scanning, synchronised swearing at software, stimulating seminars or simply a willingness to have a nap in the scanner at three in the afternoon (thankfully many of the protocols in this thesis are respiratory triggered so finding volunteers to be scanned has never been difficult).

A PhD is never easy, writing up during a pandemic induced lockdown even less so. The last few years and in particular the closing months of my PhD would not have been the same without my friends at SPMIC, TEC and ONBI, be that in person over a pint or at the other end of a video call.

Last, but by no means least, thanks are due to my family. My parents were called in to meet with a primary school teacher who was disappointed with my performance in science. The teacher explained that I had just drawn squiggles when the class was asked to draw what made us individual. Thankfully, despite my atrocious art skills, my parents recognised the double helices of DNA and saw fit to encourage my enjoyment of science, otherwise my life could have followed a very different path.

# Abbreviations

<b>ADC</b>	Apparent Diffusion Coefficient
<b>ADPKD</b>	Autosomal Dominant Polycystic Kidney Disease
<b>AKI</b>	Acute Kidney Injury
<b>ANN</b>	Artificial Neural Network
<b>ASL</b>	Arterial Spin Labelling
<b>AUC</b>	Area Under Curve
<b>BOLD</b>	Blood Oxygen Level Dependent
<b>CBF</b>	Cerebral Blood Flow
<b>CKD</b>	Chronic Kidney Disease
<b>CMRO<sub>2</sub></b>	Cerebral Metabolic Rate of Oxygen
<b>CNN</b>	Convolutional Neural Network
<b>COST</b>	European Cooperation in Science and Technology
<b>CoV</b>	Coefficient of Variation
<b>CPMG</b>	Carr-Purcell-Meiboom-Gill
<b>CSF</b>	Cerebrospinal Fluid
<b>CT</b>	Computed Tomography
<b>DREAM</b>	Dual Refocusing Echo Acquisition Mode
<b>DTI</b>	Diffusion Tensor Imaging
<b>DWI</b>	Diffusion Weighted Imaging
<b>eGFR</b>	Estimated Glomerular Filtration Rate
<b>EPG</b>	Extended Phase Graph
<b>EPI</b>	Echo Planar Imaging
<b>eTE</b>	Effective Echo Time
<b>ETL</b>	Echo Train Length
<b>EuDX</b>	Euler Delta Crossings
<b>FA</b>	Fractional Anisotropy
<b>FAIR</b>	Flow-sensitive Alternating Inversion Recovery

<b>FFE</b>	Fast Field Echo
<b>FID</b>	Free Induction Decay
<b>FOV</b>	Field Of View
<b>FSE</b>	Fast Spin Echo
<b>FSL</b>	fMRI Software Library
<b>FWHM</b>	Full Width Half Maximum
<b>GE</b>	Gradient Echo
<b>GFR</b>	Glomerular Filtration Rate
<b>GPU</b>	Graphical Processing Unit
<b>GraSE</b>	Gradient Spin Echo
<b>GUI</b>	Graphical User Interface
<b>H and E</b>	Haematoxylin and Eosin
<b>HASTE</b>	Half-Fourier Acquisition Single-shot Turbo spin Echo
<b>HC</b>	Healthy Control
<b>ICC</b>	Intraclass Correlation
<b>ICU</b>	Intensive Care Unit
<b>ISMRM</b>	International Society of Magnetic Resonance in Medicine
<b>IVIM</b>	Intravoxel Incoherent Motion
<b>LSTM</b>	Long Short-Term Memory
<b>MD</b>	Mean Diffusivity
<b>ME-TSE</b>	Multi-Echo Turbo Spin Echo
<b>MPE</b>	Mean Percentage Error
<b>MRI</b>	Magnetic Resonance Imaging
<b>NBF</b>	Neutral Buffered Formalin
<b>NHS</b>	National Health Service
<b>NIST</b>	National Institute of Standards and Technology
<b>NMR</b>	Nuclear Magnetic Resonance
<b>ODF</b>	Orientation Distribution Function
<b>PBS</b>	Phosphate-buffered Saline
<b>PC</b>	Phase Contrast
<b>PET</b>	Positron Emission Tomography
<b>PLD</b>	Post Label Delay
<b>PSD</b>	Pulse Sequence Diagram
<b>PSF</b>	Point Spread Function
<b>PRELUDE</b>	Phase Region Expanding Labeller for Unwrapping Discrete Estimates

<b>QASPER</b>	Quantitative Arterial Spin Labelling Perfusion Reference
<b>QSM</b>	Quantitative Susceptibility Mapping
<b>RARE</b>	Rapid Acquisition with Relaxation Enhancement
<b>RBF</b>	Renal Blood Flow
<b>RNN</b>	Recursive Neural Network
<b>ReLU</b>	Rectified Linear Unit
<b>RF</b>	Radio Frequency
<b>RMRO<sub>2</sub></b>	Renal Metabolic Rate of Oxygen
<b>ROC</b>	Receiver Operating Characteristic
<b>ROI</b>	Region Of Interest
<b>SAR</b>	Specific Absorption Rate
<b>SBO</b>	Susceptibility Based Oximetry
<b>SD</b>	Standard Deviation
<b>SE</b>	Spin Echo
<b>SENSE</b>	Sensitivity Encoding
<b>SNR</b>	Signal to Noise Ratio
<b>SPMIC</b>	Sir Peter Mansfield Imaging Centre
<b>TE</b>	Echo Time
<b>TFE</b>	Turbo Field Echo
<b>TFEPI</b>	Turbo Field Echo Planar Imaging
<b>TI</b>	Inversion Time
<b>TILT</b>	Transfer Insensitive Labelling Technique
<b>TKV</b>	Total Kidney Volume
<b>TLCO</b>	Twelve Layer Concentric Objects
<b>TR</b>	Repetition Time
<b>TRUST</b>	<i>T</i> <sub>2</sub> Relaxation Under Spin Tagging
<b>TSE</b>	Turbo Spin Echo
<b>UKAT</b>	United Kingdom Renal Imaging Network (UKRIN) Kidney Analysis Toolbox
<b>UKKDRI</b>	United Kingdom Kidney Donor Risk Index
<b>UKKW</b>	United Kingdom Kidney Week
<b>UKRIN</b>	United Kingdom Renal Imaging Network
<b>USKDRI</b>	United States Kidney Donor Risk Index
<b>WET</b>	Water suppression Enhanced through <i>T</i> <sub>1</sub> effects

# Chapter 1

## Introduction

### 1.1 Imaging in the Clinic

From April 2019 to March 2020, the United Kingdom's National Health Service (NHS) performed 45 million medical imaging procedures, of these 4 million were Magnetic Resonance Imaging (MRI) [1]. MRI can be used to produce high resolution volumetric images of the body with exquisite soft tissue contrast. Unlike other modalities, such as Computed Tomography (CT) and Positron Emission Tomography (PET), MRI uses non-ionising radiation, making it more suitable for longitudinal analysis of patient progression and research involving healthy volunteers.

The superior soft tissue contrast of MRI compared to CT has meant it has found widespread clinical adoption in the field of neuroimaging. Here MRI has been used for the diagnosis of neurological disorders, monitoring treatment progression and research into cognition. Many of the techniques honed in the brain, can be applied to the abdomen, where similar tissue properties can exploit the same techniques; albeit in a somewhat more challenging environment due to respiratory motion and a more inhomogeneous tissue structure. The kidneys are ideally suited to this translation as they have similar tissue properties to the brain and are highly dynamic organs.

## 1.2. Clinical Motivation

In addition to the acquisition of basic structural images, MRI can be used to collect quantitative information about the tissues being imaged. In this situation the numerical voxel values have physical significance, rather than simply representing signal intensity in arbitrary units [2]. Using quantitative MRI properties such as an organs oxygen consumption [3], perfusion [4], stiffness [5] and temperature [6] can be measured. Although quantitative MRI techniques have been developed for the kidneys, there are still many methods where development, translation from the brain, or standardisation with the wider renal community would be highly desirable.

## **1.2 Clinical Motivation**

The kidneys are two bean shaped organs found in the abdomen, just below the rib cage, symmetrical about the spine, Figure 1.1. They participate in the control of bodily fluids by regulating the balance of electrolytes, excreting waste products of metabolism and excess water from blood into urine [7].

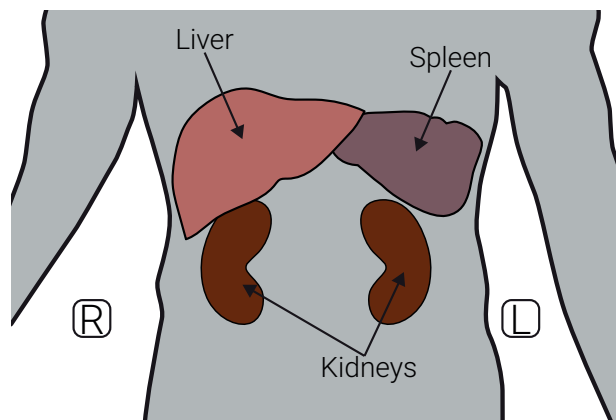


Figure 1.1: Lower abdominal organs.

The kidneys are made up of units called nephrons, Figure 1.2, each of which contains a renal corpuscle and a tubule. The renal corpuscle itself is made up of a glomerulus and a Bowman capsule. The glomerulus is a cluster of capillaries that allow wastes and fluid to pass out of the blood stream into the Bowman capsule, while larger structures such as blood cells and proteins

## 1.2. Clinical Motivation

---

remain in the blood. The substances that pass through the glomerulus are moved to the tubules, each of which has blood vessels running alongside; these vessels reabsorb many of the important components of the blood such as the majority of the water, minerals and nutrients. The remaining fluids and waste in the tubules are collected in the ureter and removed from the body [8].

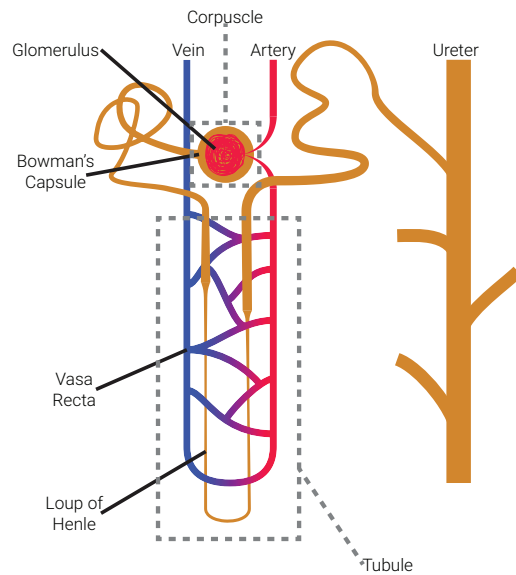


Figure 1.2: A schematic of the anatomy of a nephron.

Tissue in the kidney is separated into the renal cortex, the outer portion of the kidney, and the renal medulla, the inner portion. The cortex contains the corpuscles with the tubules passing from the cortex to the medulla. Medullary tissue is compartmentalised into renal pyramids. Blood is supplied to the kidney via the renal artery, this branches into smaller vessels until it reaches the glomeruli then flows out via the renal vein. An overview of the gross anatomy of the kidney is shown in Figure 1.3.

## 1.2. Clinical Motivation

---

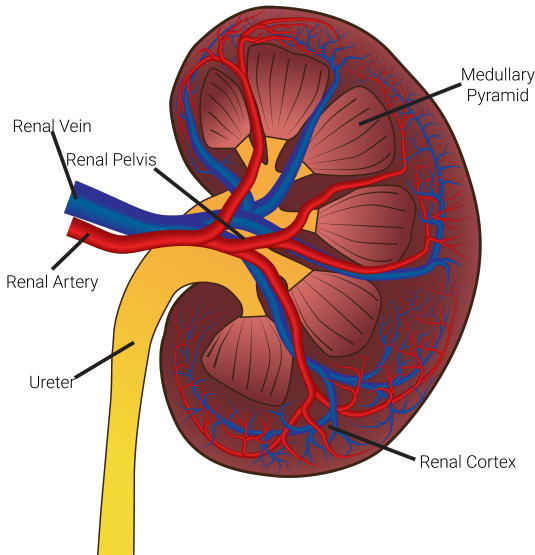


Figure 1.3: The gross anatomy of the kidney.

Due to their vital function in the body and the toxins they encounter as they perform their role, the kidneys are susceptible to problems. Chronic Kidney Disease (CKD) is the progressive destruction of the kidneys and decrease in renal function. Clinically, CKD is assessed by the Glomerular Filtration Rate (GFR), the rate at which fluid is filtered through the kidneys, with a GFR below  $60 \text{ ml/min}/1.73\text{m}^2$  of body surface area being diagnostic or the presence of albumin, the main protein in blood plasma, in the patients urine [9–11]. It is usually more practical to estimate GFR from serum creatinine levels in the subjects blood, taking into account factors such as sex, age, size and race; a measure known as Estimated Glomerular Filtration Rate (eGFR). CKD is stratified into the stages based on eGFR as shown in Table 1.1. Common causes of CKD are high blood pressure and diabetes as these damage the nephrons, with high blood pressure also posing a risk to the blood vessels within the kidney. Since renal tissue is highly vascularised, the risks associated with high blood pressure are especially prevalent. An estimated 5–11 % of the global population suffer from CKD [12–16] making it a significant public health concern. Late referral of renal disorders results in an increase in mortality rate and treatment costs [17–19]. Given that in 2013/2014 renal services cost the NHS £586 million [20] there are

## 1.2. Clinical Motivation

---

clear health and economic advantages to an early diagnosis and improved treatment of CKD. This can either be achieved via directly aiding diagnosis i.e. developing tools to assess patients condition and tailor treatment, or via improving understanding of CKD leading to an earlier, more accurate diagnosis using existing techniques and thus more personalised medicine.

Stage	eGFR ml/min/1.73m <sup>2</sup>	Description
1	> 90	Normal eGFR, but other tests have detected signs of kidney damage
2	60 - 89	Small reduction in kidney function
3a	45 - 59	Mild to moderate reduction in kidney function
3b	30 - 44	Moderate to severely reduced kidney function
4	15 - 29	Severe reduction in kidney function
5	< 15	Very severe reduction in kidney function or end stage renal failure

Table 1.1: CKD stages with corresponding eGFR values.

The current methods available to study CKD are not ideal for a variety of reasons. Histological samples provide the gold standard to study renal tissue, however collecting them is an invasive process and as such they are not suitable for monitoring the progression of a patient's condition on a regular repeated basis. This, coupled with the fact that a small biopsy sample is not representative of the entirety of both kidneys means that this method has large drawbacks. Ultrasound can be used to gather structural information about the kidneys non-invasively, however, it suffers from low spatial resolution and the images can be difficult to interpret [21]. The most common method of diagnosis is to calculate eGFR, however this measure does not allow for the individual assessment of each kidney and is an indirect measure of kidney tissue damage.

MRI is an ideal modality for the study of kidney disease due to its non-ionising, non-invasive and quantitative nature. A current research interest at the Sir Peter Mansfield Imaging Centre (SPMIC) is the use of a multi-parametric quantitative renal MRI protocol to assess and predict CKD [22,

## 1.2. Clinical Motivation

---

23]. This protocol is used to measure multiple quantitative properties of the kidneys with relative increases/decreases between measurements functioning as potential biomarkers and therefore indications of CKD progression, an overview of this protocol is shown in Figure 1.4. The implementation of new quantitative renal imaging methods can improve this protocol, thus increasing its clinical application. In addition to the CKD paradigm, we wish to apply these methods to ex-vivo kidney samples and whole organs, both to allow a more direct comparison of MRI measures with current gold standards, such as histopathology, and to aid with the future assessment of renal allograft viability.

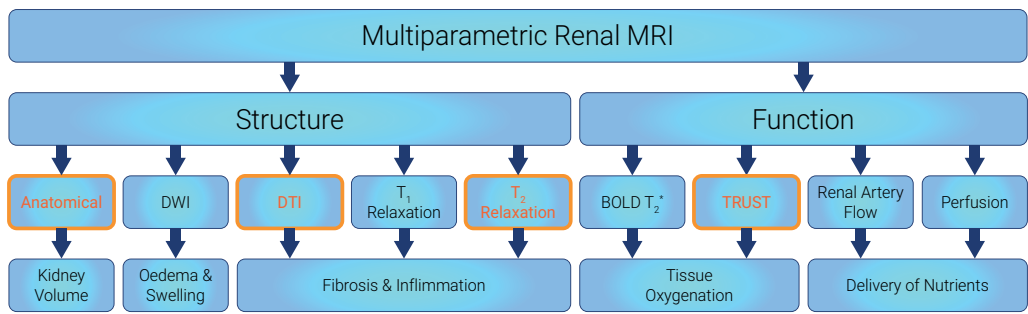


Figure 1.4: An overview of the multiparametric renal MRI protocol. Areas focused on in this thesis are highlighted in orange. This protocol is designed to provide a complete evaluation of renal health using MRI.

## 1.3 Thesis Overview

**Chapter 2** provides the theoretical framework of Nuclear Magnetic Resonance (NMR) and MRI. A detailed description is given of the origin of the measured signal, processes that give rise to contrast between tissues and the methods of image formation.

**Chapter 3** explores  $T_2$  mapping within the kidneys.  $T_2$  mapping has been shown to be a marker of oedema, inflammation and fibrosis, however, there are few studies of renal  $T_2$  mapping and limited consensus as to which method should be used to monitor the kidneys [24], thus leading to inconsistent values quoted between studies [25]. Here different  $T_2$  mapping methods are compared, assessing their quantitative accuracy and image quality in phantoms prior to healthy subjects being scanned to assess these  $T_2$  mapping methods in-vivo.

**Chapter 4** aims to translate methods for measuring blood oxygenation from vessels in the brain to use within the kidneys. Focusing on Susceptibility Based Oximetry (SBO) [26] and  $T_2$  Relaxation Under Spin Tagging (TRUST) [27], this chapter optimises the methods for use in the abdomen, verifying the modifications in the brain, with an oxygen challenge carried out in-vivo to measure changes in oxygen saturation within the renal vein.

**Chapter 5** describes the development of a fully automated method to segment the kidneys from MRI data. Defining renal masks is an important, yet time consuming, aspect of many studies. Renal masks can be used to calculate Total Kidney Volume (TKV) or to inform downstream processing. Here a Convolutional Neural Network (CNN) is developed to segment the kidneys from  $T_2$ -weighted Half-Fourier Acquisition Single-shot Turbo spin Echo (HASTE) images. Software is developed to provide an executable that allows any user to segment the kidneys in a few seconds on a regular desktop computer.

### **1.3. Thesis Overview**

---

**Chapter 6** develops methods for scanning kidneys ex-vivo. The clinical gold standard for diagnosis of renal pathologies is biopsy followed by histological analysis. Comparison between this gold standard and recently developed quantitative MRI techniques is vital for clinical translation. Here a pipeline for multiparametric imaging of the same kidney in-vivo then ex-vivo after nephrectomy followed by histology is developed.

**Chapter 7** concludes the thesis, highlighting key results and their current applications. It provides an overview as to future research directions and how the methods developed in this thesis could be applied to new paradigms.

## 1.4 References

1. *Diagnostic Imaging Dataset Annual Statistical Release 2019/20* <https://www.england.nhs.uk/statistics/statistical-work-areas/ diagnostic-imaging-dataset/diagnostic-imaging-dataset-2019-20-data/> (2021).
2. Tofts, P. *Quantitative MRI of the Brain: Measuring Changes Caused by Disease* 688 pp. Google Books: RbFrAAAAMAAJ (Wiley, 2003).
3. Zhang, J., Liu, T., Gupta, A., Spincemaille, P., Nguyen, T. D. & Wang, Y. Quantitative Mapping of Cerebral Metabolic Rate of Oxygen (CMRO<sub>2</sub>) Using Quantitative Susceptibility Mapping (QSM). *Magnetic Resonance in Medicine* **74**, 945–952 (1st Oct. 2015).
4. Karger, N., Biederer, J., Lüsse, S., Grimm, J., Steffens, J. ...-C., Heller, M. & Glüer, C. ...-C. Quantitation of Renal Perfusion Using Arterial Spin Labeling with FAIR-UFLARE. *Magnetic Resonance Imaging* **18**, 641–647 (1st July 2000).
5. Mariappan, Y. K., Glaser, K. J. & Ehman, R. L. MAGNETIC RESONANCE ELASTOGRAPHY: A REVIEW. *Clinical anatomy (New York, N.Y.)* **23**, 497–511 (July 2010).
6. Yuan, J., Mei, C.-S., Panych, L. P., McDannold, N. J. & Madore, B. Towards Fast and Accurate Temperature Mapping with Proton Resonance Frequency-Based MR Thermometry. *Quantitative Imaging in Medicine and Surgery* **2**, 212–232 (Mar. 2012).
7. Lote, C. J. *Principles of Renal Physiology* 255 pp. Google Books: at6LBQAAQBAJ (Springer Science & Business Media, 6th Dec. 2012).
8. Hall, J. E. *Guyton and Hall Textbook of Medical Physiology* 1171 pp. Google Books: 3sWNCgAAQBAJ (Elsevier Health Sciences, 20th May 2015).
9. Stevens, L. A., Coresh, J., Greene, T. & Levey, A. S. Assessing Kidney Function — Measured and Estimated Glomerular Filtration Rate. *New England Journal of Medicine* **354**, 2473–2483 (8th June 2006).
10. Farrugia, A. Albumin Usage in Clinical Medicine: Tradition or Therapeutic? *Transfusion Medicine Reviews* **24**, 53–63 (1st Jan. 2010).

#### 1.4. References

---

11. Pruijm, M., Milani, B. & Burnier, M. Blood Oxygenation Level-Dependent MRI to Assess Renal Oxygenation in Renal Diseases: Progresses and Challenges. *Frontiers in Physiology* **7**. doi:10 . 3389 / fphys . 2016 . 00667. pmid: 28105019 (5th Jan. 2017).
12. Coresh, J., Astor, B. C., Greene, T., Eknayan, G. & Levey, A. S. Prevalence of Chronic Kidney Disease and Decreased Kidney Function in the Adult US Population: Third National Health and Nutrition Examination Survey. *American Journal of Kidney Diseases: The Official Journal of the National Kidney Foundation* **41**, 1–12 (Jan. 2003).
13. De Lusignan, S. *et al.* Identifying Patients with Chronic Kidney Disease from General Practice Computer Records. *Family Practice* **22**, 234–241 (1st June 2005).
14. Drey, N., Roderick, P., Mullee, M. & Rogerson, M. A Population-Based Study of the Incidence and Outcomes of Diagnosed Chronic Kidney Disease. *American Journal of Kidney Diseases* **42**, 677–684 (1st Oct. 2003).
15. Amato, D. *et al.* Prevalence of Chronic Kidney Disease in an Urban Mexican Population. *Kidney International* **68**, S11–S17 (1st Aug. 2005).
16. Chadban, S. J., Briganti, E. M., Kerr, P. G., Dunstan, D. W., Welborn, T. A., Zimmet, P. Z. & Atkins, R. C. Prevalence of Kidney Damage in Australian Adults: The AusDiab Kidney Study. *Journal of the American Society of Nephrology* **14**, S131–S138 (suppl 2 7th Jan. 2003).
17. Jungers, P., Zingraff, J., Albouze, G., Chauveau, P., Page, B., Hannedouche, T. & Man, N. K. Late Referral to Maintenance Dialysis: Detrimental Consequences. *Nephrology Dialysis Transplantation* **8**, 1089–1093 (1st Jan. 1993).
18. Sesso, R. & Belasco, A. G. Late Diagnosis of Chronic Renal Failure and Mortality on Maintenance Dialysis. *Nephrology Dialysis Transplantation* **11**, 2417–2420 (1st Dec. 1996).
19. Klebe, B. *et al.* The Cost of Implementing UK Guidelines for the Management of Chronic Kidney Disease. *Nephrology Dialysis Transplantation* **22**, 2504–2512 (1st Sept. 2007).

#### 1.4. References

---

20. Precious, K. *NHS England » Programme Budgeting* <https://www.england.nhs.uk/resources/resources-for-ccgs/prog-budgeting/> (2017).
21. Hansen, K. L., Nielsen, M. B. & Ewertsen, C. Ultrasonography of the Kidney: A Pictorial Review. *Diagnostics* **6**, doi:10.3390/diagnostics6010002, pmid: 26838799 (23rd Dec. 2015).
22. Cox, E. F., Buchanan, C. E., Bradley, C. R., Prestwich, B., Mahmoud, H., Taal, M., Selby, N. M. & Francis, S. T. Multiparametric Renal Magnetic Resonance Imaging: Validation, Interventions, and Alterations in Chronic Kidney Disease. *Frontiers in Physiology* **8**, 696 (2017).
23. Buchanan, C. E., Mahmoud, H., Cox, E. F., McCulloch, T., Prestwich, B. L., Taal, M. W., Selby, N. M. & Francis, S. T. Quantitative Assessment of Renal Structural and Functional Changes in Chronic Kidney Disease Using Multi-Parametric Magnetic Resonance Imaging. *Nephrology Dialysis Transplantation* **35**, 955–964 (29th June 2019).
24. Dekkers, I. A. *et al.* Consensus-Based Technical Recommendations for Clinical Translation of Renal T1 and T2 Mapping MRI. *Magnetic Resonance Materials in Physics, Biology and Medicine*. doi:10.1007/s10334-019-00797-5 (22nd Nov. 2019).
25. Wolf, M. *et al.* Magnetic Resonance Imaging T1- and T2-Mapping to Assess Renal Structure and Function: A Systematic Review and Statement Paper. *Nephrology Dialysis Transplantation* **33**, ii41–ii50 (suppl\_2 1st Sept. 2018).
26. Jain, V., Langham, M. C. & Wehrli, F. W. MRI Estimation of Global Brain Oxygen Consumption Rate. *Journal of Cerebral Blood Flow & Metabolism* **30**, 1598–1607 (1st Sept. 2010).
27. Lu, H. & Ge, Y. Quantitative Evaluation of Oxygenation in Venous Vessels Using T2-Relaxation-Under-Spin-Tagging MRI. *Magnetic Resonance in Medicine* **60**, 357–363 (1st Aug. 2008).

## **Chapter 2**

# **Principles of Nuclear Magnetic Resonance Imaging**

---

## Abstract

This chapter outlines the theoretical framework behind Nuclear Magnetic Resonance (NMR) and Magnetic Resonance Imaging (MRI). Beginning with an overview of nuclear spin and resonance, the origin of the signal measured in NMR is explained. The processes responsible for variations within signals such as relaxation mechanisms are then outlined and the techniques used to measure these different signals described. Finally, an overview of the process by which the signals can be used to form images is given, covering concepts such as spacial localisation, image acquisition schemes and acceleration methods.

## 2.1 Source of the NMR Signal

### 2.1.1 Nuclear Spin

The Nuclear Magnetic Resonance (NMR) signal arises from the interaction between the atomic nucleus and an external magnetic field. These atomic nuclei possess intrinsic properties of, mass ( $m$ ), charge ( $q$ ) and spin ( $I$ ). Spin is a quantum mechanical property and as such, can only take values of half integers or integers. Nuclear spin is dictated by the sum of the constituent particles of the nucleus, protons and neutrons, each of which posses their own spin of either  $1/2$  or  $-1/2$  respectively. This means pairs of nucleons with opposite spin can cancel out leaving the nucleus with zero net spin, this happens when the nuclei contains an even number of protons and neutrons. If the nuclei contains an odd number of both protons and neutrons, it will have a positive integer nuclear spin whereas if the nuclei has an odd number of protons or neutrons, it will have a half integer spin.

The spin angular momentum,  $\mathbf{J}$  of a nucleus of spin  $I$  is given by

$$|\mathbf{J}| = \hbar\sqrt{I(I+1)} \quad (2.1)$$

where  $\hbar$  is the reduced Plank's constant,  $h/2\pi$ . As the nucleus is charged and rotating, it gives rise to a current and therefore a magnetic moment  $\mu$ ,

$$\mu = \gamma \mathbf{J} \quad (2.2)$$

where  $\gamma$  is the gyromagnetic ratio for the nucleus, a constant which depends on the charge and mass of the nucleus. Table 2.1 shows the gyromagnetic ratio ( $\gamma$ ) and nuclear spin ( $I$ ) of common NMR sensitive isotopes [1–3]. Due to its high gyromagnetic ratio, compared to other nuclei used for NMR, and relative abundance in the body,  $^1\text{H}$ , a single proton, is most commonly used for Magnetic Resonance Imaging (MRI).

## 2.1. Source of the NMR Signal

---

Isotope	Spin	$\gamma$ (MHzT $^{-1}$ )	Sensitivity Relative to $^1\text{H}$
$^1\text{H}$	$^{1/2}$	42.58	1
$^2\text{H}$	1	6.54	0.0097
$^{13}\text{C}$	$^{1/2}$	10.71	0.016
$^{19}\text{F}$	$^{1/2}$	40.05	0.83
$^{23}\text{Na}$	$^{3/2}$	11.27	0.093
$^{31}\text{P}$	$^{1/2}$	17.25	0.066

Table 2.1: Common NMR isotopes, their nuclear spin, gyromagnetic ratio and sensitivity, relative to  $^1\text{H}$ .

### 2.1.2 Application of an External Magnetic Field

If we consider the hydrogen nuclei in a sample of tissue, the number of possible eigenstates for a nuclear spin  $I$  is  $(2I + 1)$ . This means that for the  $^1\text{H}$  nuclei in our sample, where  $I = ^{1/2}$ , we can observe two possible eigenstates,  $|+^{1/2}\rangle$  and  $|{-}^{1/2}\rangle$  often written as  $|\uparrow\rangle$  and  $|\downarrow\rangle$ . In the absence of an external magnetic field, these states are degenerate as they have the same energy, however, if we move our sample into a static external magnetic field along the  $z$ -axis,  $B_0$ , the energy levels of the states separate.

The  $z$ -component of the magnetic moment is defined by,

$$\mu_z = \gamma \hbar m_I \quad (2.3)$$

where  $m_I$  are the possible spin quantum numbers of the nucleus. For our proton system with spin  $^{1/2}$ ,  $\mu_z$  is given by

$$\mu_z = \pm \frac{1}{2} \gamma \hbar. \quad (2.4)$$

The spins can either be aligned parallel to the external magnetic field in the lower energy of the two eigenstates, also known as spin up, or anti-parallel to the magnetic field in the higher energy eigenstate, spin down. The energy

## 2.1. Source of the NMR Signal

---

difference between these two eigenstates is given by,

$$\Delta E = \gamma \hbar B_0. \quad (2.5)$$

For an ensemble of spins in an external magnetic field, there will be an imbalance between the populations of each state, with more spins occupying the lower of the two energy states. The net magnetisation of the sample is simply the sum of the constituent spins and as such, the application of an external magnetic field leads to the sample gaining a net magnetisation vector,  $\mathbf{M}$ , aligned with  $B_0$ . This effect is very small, the magnitude of the imbalance between eigenstates can be derived from Boltzmann statistics and is given by,

$$\frac{N_\uparrow}{N_\downarrow} = \exp\left(\frac{\Delta E}{k_B T}\right), \quad (2.6)$$

where  $N_\downarrow$  and  $N_\uparrow$  are the number of spins aligned with and against  $B_0$  respectively,  $k_B$  is Boltzmann's constant and  $T$  is the temperature of the system. This means that for a sample of biological tissue at body temperature in a 3T magnetic field, the population difference is approximately three parts per million. Although this measurable proportion is very small, it can be detected due to the high density of protons in the tissue. The signal can be increased by the application of a stronger main magnetic field,  $B_0$ , Figure 2.1.

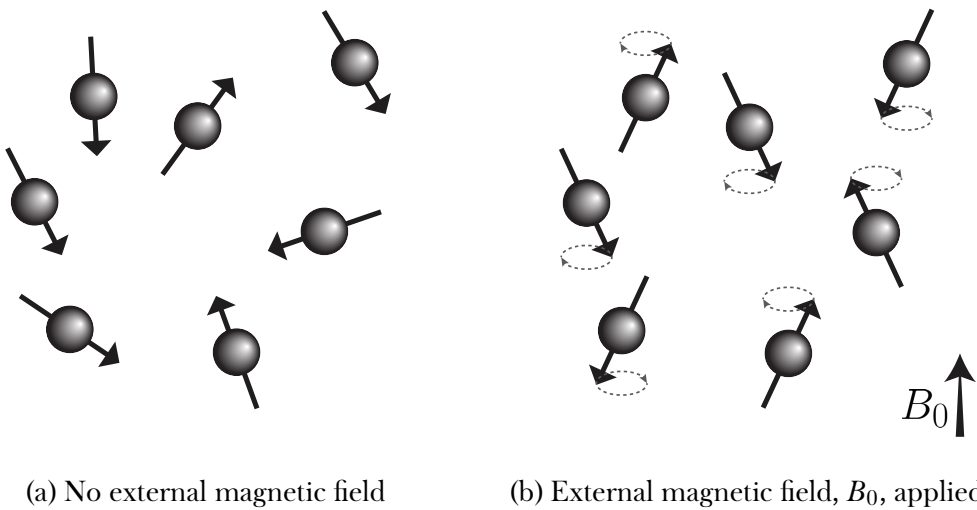


Figure 2.1: Initially the magnetic moments are randomly distributed (a). Upon the application of the external magnetic field,  $B_0$ , the magnetic moments align either parallel or anti-parallel to the external field and precess at the Larmor frequency,  $\omega_0$  (b).

### 2.1.3 Precession

Classically, if a magnetic moment,  $\mu$ , is placed into an external magnetic field,  $\mathbf{B}$ , it will experience a torque,  $\tau$ , proportional to the change in angular momentum and thus induce a rotation.

$$\mu \times \mathbf{B} = \frac{d\mathbf{J}}{dt} = \tau \quad (2.7)$$

From (2.2) the quantum equivalent of (2.7) is the standard form of the Bloch equation [4],

$$\frac{d\mu}{dt} = \gamma \mu \times \mathbf{B} \quad (2.8)$$

This equation states that if the magnetic moment,  $\mu$  is not aligned with the external magnetic field,  $\mathbf{B}$ , it will precess about  $\mathbf{B}$ . The frequency of this precession,  $\omega_0$ , is known as the Larmor frequency and is given by substituting

## 2.1. Source of the NMR Signal

---

Bohr's frequency condition of the Planck relation ( $\Delta E = \hbar\omega$ ) into (2.5),

$$\omega_0 = \gamma B_0, \quad (2.9)$$

Nuclei with a positive gyromagnetic ratio precess clockwise, whereas nuclei (and the electron) with a negative gyromagnetic ratio precess anti-clockwise. For a proton in a 3T magnetic field, the Larmor frequency is 128 MHz.

### 2.1.4 Resonance

Resonance is the process of energy transfer into a system by the application of energy at the natural frequency of the system. In the case of NMR this is the application of a Radio Frequency (RF) pulse, also known as the  $B_1$  field, near the Larmor frequency. Before the RF pulse is applied, the spins are at equilibrium, aligned with  $B_0$ . Upon application of a  $B_1$  field close to the Larmor frequency of the target nucleus and perpendicular to  $B_0$ , the spins aligned with  $B_0$  will be displaced from equilibrium and thus precession is induced. The longer the  $B_1$  field is applied, the more the net magnetisation vector is displaced, or tipped, away from  $B_0$ , this allows arbitrary flip angles,  $\alpha$ , to be achieved, (2.10).

$$\alpha = \int_0^T \gamma B_1(t) dt \quad (2.10)$$

In addition to displacing the spins, the  $B_1$  field also induces phase coherence within the ensemble making up the net magnetisation vector. When considering the effects of RF pulses, it can often be simpler to imagine the system from a reference frame rotating about the  $z$ -axis at the Larmor frequency. This has the effect of making  $B_1$  stationary along the  $x$ -axis. Figure 2.2 shows the evolution of a spin in both the laboratory and rotating frame after the application of a  $90^\circ$  RF pulse. In both figures the spin is tipped into the transverse plane,  $M_{xy}$ .

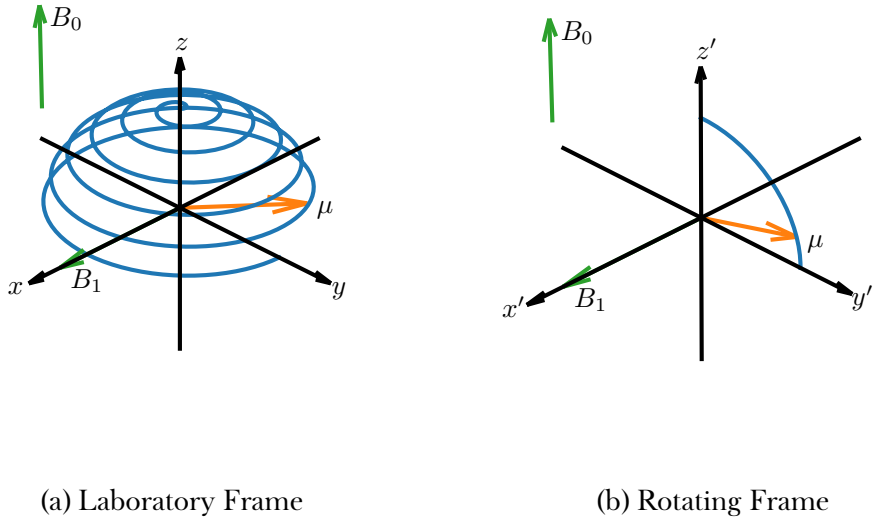


Figure 2.2: The laboratory frame of reference shows the precession of the spin about  $B_0$  while in the rotating frame, the spin simply rotates about the  $x'$ -axis.

## 2.2 Relaxation and Contrast Mechanisms

If disturbed from equilibrium by an RF pulse, the net magnetisation vector will not remain in this new state ad infinitum, instead, once the RF pulse has been turned off the magnetisation will transition back to its equilibrium state in a process known as relaxation. The time constants characterising the relaxation process vary depending on the environment the spins are in and as such, can vary between different biological tissues. These relaxation constants are the principle source of contrast in MRI. Mathematically, this relaxation is described by the full form of the Bloch equation, (2.11),

$$\frac{d\mathbf{M}}{dt} = \gamma (\mathbf{M} \times \mathbf{B}) - \frac{(M_z - M_0)}{T_1} \hat{\mathbf{z}} - \frac{M_x \hat{\mathbf{x}} + M_y \hat{\mathbf{y}}}{T_2}, \quad (2.11)$$

where  $T_1$  is the longitudinal relaxation time and  $T_2$  the transverse relaxation time.

### 2.2.1 Longitudinal Relaxation ( $T_1$ )

Upon excitation, energy is exchanged between the spin system and the surrounding environment. The result of this energy exchange is that the energy of the spin system decreases and the longitudinal magnetisation exponentially decays to its equilibrium position. The time constant of this exponential decay returning to equilibrium,  $M_0$ , is known as the longitudinal relaxation time or  $T_1$  and is dictated by the efficiency of energy transfer between the spin system and the surrounding lattice, hence its historical name, spin-lattice relaxation.

The efficiency of this energy transfer is primarily dictated by the motion of the surrounding lattice. As nearby molecules undergo rotation they cause variations in the local magnetic field. If these fluctuations are at a similar frequency to the Larmor frequency then energy transfer via dipole-dipole interactions will be relatively efficient. The rate of energy transfer can also be increased if the molecules are more closely coupled for example, tissues with a lower molecular mobility tend to have a shorter  $T_1$  than those with a high molecular mobility, this is explored further in Section 2.2.3.

#### Measuring $T_1$

The longitudinal component of the Bloch equation, (2.11), is given by (2.12).

$$\frac{d\mathbf{M}_z}{dt} = -\frac{(M_z - M_0)}{T_1} \quad (2.12)$$

Solving this equation for  $M_z$  gives,

$$M_z = M_0 \left[ 1 - \exp \left( -\frac{t}{T_1} \right) \right] + M_z(0) \exp \left( -\frac{t}{T_1} \right), \quad (2.13)$$

where  $M_z(0)$  is the magnetisation at time  $t = 0$ .

## 2.2. Relaxation and Contrast Mechanisms

---

The gold standard method for quantification of  $T_1$  is the inversion recovery pulse sequence, Figure 2.3, in which a  $180^\circ$  pulse is used to fully invert the magnetisation, such that  $M_z(0) = -M_0$  and as such (2.13) reduces to,

$$M_z = M_0 \left[ 1 - 2 \exp \left( -\frac{t}{T_1} \right) \right]. \quad (2.14)$$

Typically a hyperbolic secant pulse is used for inversion. This pulse is adiabatic and as such a complete inversion is performed provided a minimum  $B_1$  amplitude threshold is met. This decouples the inversion angle from  $B_1$ , thus increasing inversion homogeneity within the sample.

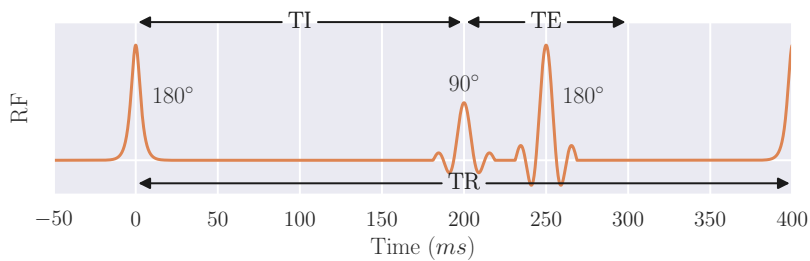


Figure 2.3: The RF pulse train used in an inversion recovery spin echo scheme. Here the inversion time (TI) shown is 200 ms, this can be adjusted to modulate the  $T_1$  weighting.

To measure  $T_1$ , the most standard method is to repeat an inversion recovery sequence multiple times, with measurements of  $M_z$  taken at different times after the  $180^\circ$  inversion pulse, the Inversion Time (TI). The magnetisation must have fully recovered to  $M_0$  between each inversion pulse, as such the minimum time between inversions, termed the Repetition Time (TR), is five times  $T_1$ . Curve fitting can then be used to estimate  $M_0$  and  $T_1$ , Figure 2.4. This method is expanded upon when it is used in Chapter 6.

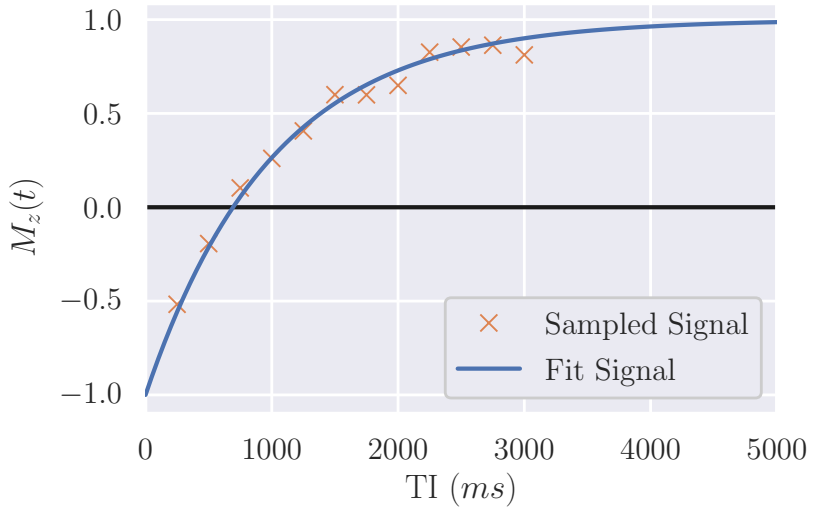


Figure 2.4: The longitudinal magnetisation for a sample of  $T_1 = 1000$  ms in an inversion recovery experiment. The experiment was repeated with inversion times from 250 ms to 3000 ms in 250 ms steps.

### 2.2.2 Transverse Relaxation ( $T_2$ and $T_2^*$ )

Upon the application of a  $90^\circ x'$  RF pulse, the net magnetisation vector is tipped in the  $y'$  direction resulting in phase coherence and creating transverse magnetisation,  $M_{x'y'}$ . The spins then precess about the  $z$ -axis at their Larmor frequency, dictated by the magnetic field they are in. This magnetic field is not perfectly homogeneous over the whole ensemble though, random dipole-dipole interaction with neighbouring spins produce short-lived fluctuations in the local magnetic field and thus the Larmor frequency of each spin varies. As the spins precess at different frequencies, they de-phase, resulting in the transverse magnetisation decaying to zero as phase coherence is lost. This mechanism is driven by energy transfer between the spins within the system and is termed, the spin-spin relaxation. The rate at which this loss of phase coherence due to spin-spin interactions occurs is characterised by the time constant  $T_2$ .

## 2.2. Relaxation and Contrast Mechanisms

---

The local magnetic field is not just influenced by spin-spin interactions. Local inhomogeneities in the static  $B_0$  field can be caused by susceptibility differences within the sample and hardware imperfections. These  $B_0$  inhomogeneities result in additional perturbation to the local magnetic field and therefore additional de-phasing of the system. The rate at which this de-phasing due to static  $B_0$  inhomogeneities occurs is characterised by the time constant  $T'_2$ . The net measured decay in transverse magnetisation is therefore dictated by  $T_2^*$ , which is related to  $T_2$  and  $T'_2$  by

$$\frac{1}{T_2^*} = \frac{1}{T_2} + \frac{1}{T'_2}. \quad (2.15)$$

### Measuring $T_2$ and $T_2^*$

The transverse component of the Bloch equation, (2.11), is given by (2.16).

$$\frac{dM_{xy}}{dt} = -\frac{M_{xy}}{T_2} \quad (2.16)$$

Solving the differential equation for  $M_{xy}$  with respect to  $t$  gives,

$$M_{xy}(t) = M_{xy}(0) \exp\left(-\frac{t}{T_2}\right), \quad (2.17)$$

It should be noted that (2.17) is an idealised equation and thus does not include static field inhomogeneities that contribute to  $T'_2$  and thus the magnetisation of a real signal will decay with  $T_2^*$ .

After a  $90^\circ$  RF pulse the envelope of the signal will decay with  $T_2^*$ , known as a Free Induction Decay (FID). As such, by measuring the amplitude of the signal at different time points,  $t$ , the decay can be sampled and fit to estimate  $T_2^*$ .

## Spin Echoes

To measure  $T_2$ , rather than  $T_2^*$ , the effects of static  $B_0$  inhomogeneities that lead to  $T_2'$  must be negated. Because the processes driving the de-phasing that leads to  $T_2'$  are constant over time, the refocussing effects of a Spin Echo (SE) sequence, outlined in Figure 2.5, can be utilised to reform this de-phasing component. In a SE sequence, an initial  $90^\circ$  excitation pulse shifts  $M$  into the transverse plane and induces phase coherence, Figure 2.6a.  $T_2^*$  effects will then cause some spins to precess quickly and others more slowly and thus de-phase with  $T_2^*$ , Figure 2.6b. At time, Echo Time (TE)/2, later a  $180^\circ$  pulse is used to flip the spin ensemble, reversing the phase shift meaning those spins that have accrued the largest positive phase shift will now have the largest negative phase shift and vice versa, Figure 2.6c. Because the  $B_0$  inhomogeneities that lead to  $T_2'$  are static, they will still be acting to the same degree on each spin. This leads to an echo forming at  $t = \text{TE}$  as those spins with the highest Larmor frequency, and largest negative phase shift, refocus or “catch up” with those spins with a lower Larmor frequency, Figure 2.6d. The processes leading to  $T_2$  are not constant over time and as such are not refocussed by the  $180^\circ$  pulse, hence the echo in Figure 2.6d is not perfectly refocussed and the signal will be attenuated at a rate dictated by  $T_2$ .

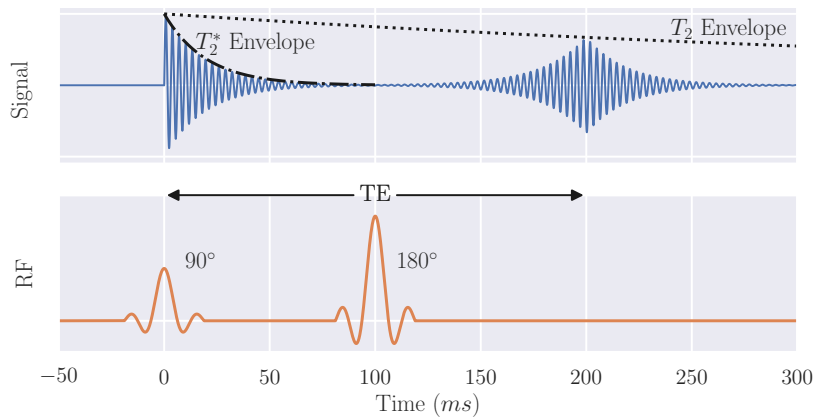


Figure 2.5: The signal produced in a spin-echo sequence used to measure  $T_2$ . This sequence has a TE of 200 ms.

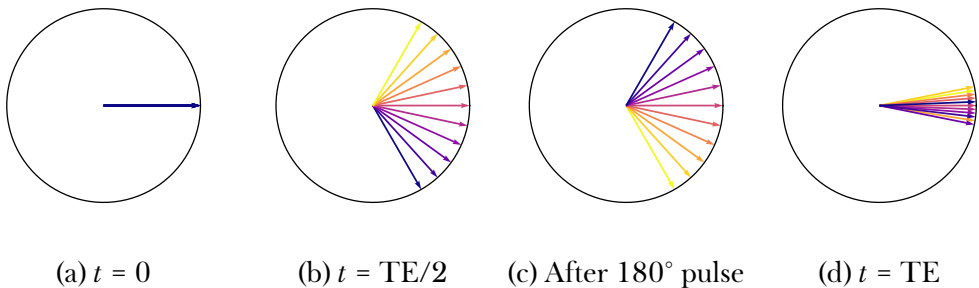


Figure 2.6: Spins evolving in a spin echo sequence showing the de-phasing, (b), refocusing pulse, (c), and subsequent refocusing, (d).

By repeating this sequence over a range of echo times the  $T_2$  curve can be sampled and fit to (2.17) to estimate  $T_2$  and  $M_{xy0}$ . The SE sequence is the most basic form of  $T_2$  mapping, more methods are explored and compared in Chapter 3 of this thesis.

### Gradient Echoes

Echoes can be generated via another mechanism, the Gradient Echo (GE). In addition to the homogeneous  $B_0$  field and RF fields encountered thus far, MRI scanners can produce additional fields known as gradients. These switchable fields can induce linearly varying spatially dependent magnetic fields to perturb  $B_0$ . They are used for image formation, explained in Section 2.3, but can also be used to form an echo. The GE pulse sequence uses a single  $90^\circ$  RF excitation pulse to tip the net magnetisation vector into the transverse plane. A gradient is then applied to the sample causing areas of higher field to de-phase quickly whereas areas with a relatively lower field will de-phase slower. At time  $TE/2$  the polarity of the gradient is reversed thus causing the spins to refocus and an echo to be formed at time  $TE$ . An overview of the sequence is shown in Figure 2.7.

## 2.2. Relaxation and Contrast Mechanisms

---

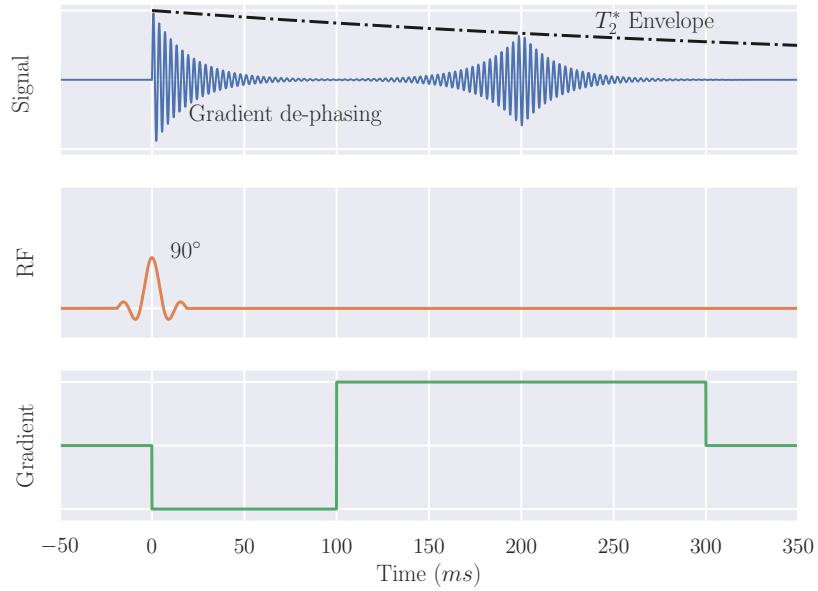


Figure 2.7: A schematic of a basic Gradient Echo (GE) sequence with TE 200 ms.

In reality, the gradients cannot switch polarity instantaneously due to the inductance of the gradient coils and characteristics of the amplifiers used to generate the gradients. This phenomenon leads to the gradient waveform being trapezoidal, however, to aid clarity in schematics within this chapter, an idealised gradient waveform has been shown. This characteristic of a gradient is known as the slew rate and is defined as the peak gradient amplitude upon the rise time, Figure 2.8, and for modern MRI scanners is of the order of 200 T/m/s.

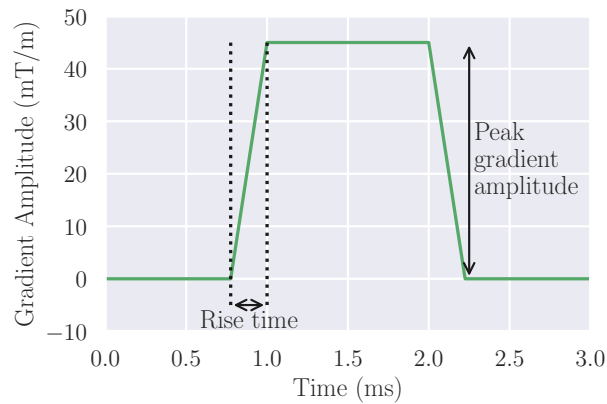


Figure 2.8: A gradient waveform with typical peak gradient amplitude, rise time and slew rate.

### 2.2.3 Dipole-Dipole Interactions

As outlined in 2.2.1 and 2.2.2, dipole-dipole interactions are a primary contributing factor to  $T_1$  and  $T_2$  times. The factors that dictate the strength of these interactions are the types of spin involved, the distance between them, the angle between the line joining them and the  $B_0$  field and their motion. The strength of the interaction depends on the gyromagnetic ratio of the spins involved. The magnitude of an electrons gyromagnetic ratio is much greater than that of a proton ( $-28025 \text{ MHz T}^{-1}$  and  $43 \text{ MHz T}^{-1}$  respectively [5]) and as such proton-electron interactions are much stronger than proton-proton interactions. The strength of the interaction is inversely proportional to the sixth power of distance (seen in Equations (2.19) and (2.20)) and thus means that dipole-dipole interactions are only effective over a very short range. As such, the majority of interactions are intramolecular rather than intermolecular.

The  $z$  component of a magnetic field produced by a dipole,  $\mu$ , is given by Equation 2.18,

$$B_{\mu z} \propto \frac{\mu}{r^3} (3 \cos^2 \theta - 1) \quad (2.18)$$

producing the field shown in Figure 2.9. Here it can be seen that at a certain angle, the magnetic field is zero, this occurs when  $(3 \cos^2 \theta - 1) = 0$  and equates to an angle of approximately  $54.7^\circ$ . This angle is known as the magic angle. If the dipoles are orientated at approximately the magic angle to the  $B_0$  field, their  $T_2$  will be increased.

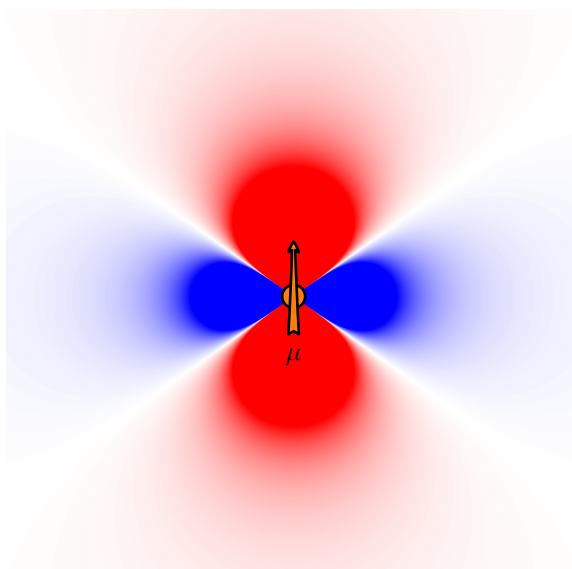


Figure 2.9: The  $z$  component of the magnetic field produced by dipole,  $\mu$ .

Molecules can move in three different ways, translation, vibration and rotation. Translation has little effect on NMR signals as it is usually omnidirectional. Vibrational oscillations are at a much higher frequency than NMR phenomenon and as such do not affect the MRI signal. Rotations can be at similar frequencies to MRI and as such, influence  $T_1$  and  $T_2$  due to dipole-dipole interactions.

Each molecule in a sample will have a characteristic correlation time,  $\tau_c$ , the time it takes the molecule to rotate by one radian. The correlation time is affected by how tightly bound the molecules are and their mass, light freely bound molecules like water in liquid form will have a short correlation time while heavy tightly bound molecules such as those found in bone, will have a longer correlation time. If a molecule is tumbling at a rate similar to the Larmor frequency, it will cause energy transfer to be more efficient, thus reducing  $T_1$ . As the tumbling rate slows, the properties of the dipole become more similar to those of a static field, this means that nearby dipoles will experience magnetic fields perturbed about  $B_0$  and as such  $T_2$  will decrease.

## 2.2. Relaxation and Contrast Mechanisms

---

The mathematical framework of this phenomenon is given by the Solomon-Bloembergen equations [6] (Equations (2.19) and (2.20)). These equations predict  $T_1$  and  $T_2$  dependence on correlation time, Figure 2.10, where it can be observed that  $T_1$  is lowest when the frequency of the molecular tumbling is similar to the Larmor frequency (labelled as  $\tau_0$  where  $\tau_0 = 1/\omega_0$ ) and that  $T_2$  decreases as correlation time increases. Tissues with a range of tumbling rates are highlighted in Figure 2.10; the molecules in Cerebrospinal Fluid (CSF) are weakly bound as they are in the liquid phase, whereas solid tissues such as bone are tightly bound. Renal tissue is expected to have a similar tumbling rate to muscle and cysts a similar tumbling rate to CSF.

$$\frac{1}{T_1} = \frac{6}{20} \frac{\hbar^2 \gamma^4}{r^6} \left[ \frac{\tau_c}{1 + \omega^2 \tau_c^2} + \frac{4\tau_c}{1 + 4\omega^2 \tau_c^2} \right] \quad (2.19)$$

$$\frac{1}{T_2} = \frac{3}{20} \frac{\hbar^2 \gamma^4}{r^6} \left[ 3\tau_c + \frac{5\tau_c}{1 + \omega^2 \tau_c^2} + \frac{2\tau_c}{1 + 4\omega^2 \tau_c^2} \right] \quad (2.20)$$

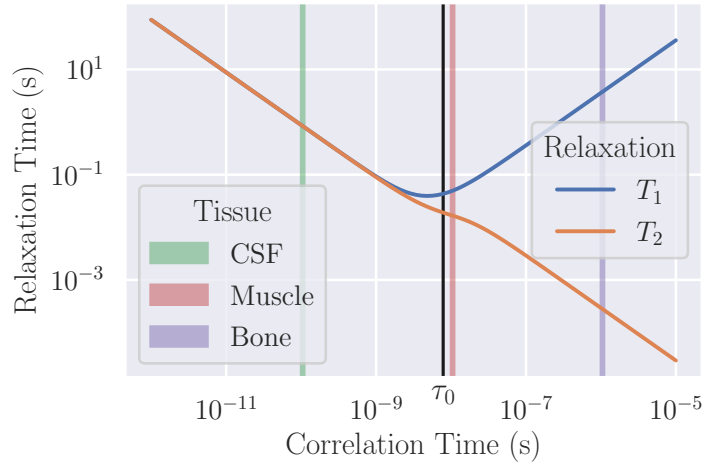


Figure 2.10:  $T_1$  and  $T_2$  dependence on molecular correlation time as predicted by the Solomon-Bloembergen equations. Tissues with a range of correlation times are highlighted.

### 2.2.4 Diffusion Weighted Imaging

In biological tissues molecules have thermal energy, this energy leads to random motion known as Brownian motion. This process can be statistically modelled as a random walk where the distance of each step is drawn from a normal distribution. The movement of molecules due to Brownian motion is known as diffusion and can be characterised by the diffusion coefficient,  $D$  which is proportional to the flux of particles travelling through an area over a period of time and is normally expressed in  $\text{mm}^2/\text{sec}$ . The MRI signal from a sample can be made sensitive to the degree of diffusion taking place by using diffusion gradients applied between the excitation and echo.

Figure 2.11 shows a Diffusion Weighted Imaging (DWI) pulse sequence and the phase evolution of two spins, one stationary and the other diffusing along the direction in which the diffusion gradient is applied. The stationary spin accrues a positive phase shift relative to  $\omega_0$  while the first diffusion gradient pulse is applied. The  $180^\circ$  RF pulse then flips the spin system so the positive phase shift reverses to a negative phase shift of equal magnitude. The spin then evolves under the same field strength in the second diffusion gradient pulse and as such, the diffusion pulses result in no net phase shift. In contrast, for the diffusing spin, the strength of the magnetic field experienced is dependent on time, in this example, increasing in strength as time passes. This means that the rate at which phase shifts are accrued increases over time and therefore the refocussing effects of the second diffusion pulse are reduced. This sensitivity of the diffusion sequence to water motion is dependent on the strength of the diffusion gradients, the time the diffusion gradients are applied for and the time between the two diffusion pulses. This is termed the diffusion weighting factor,  $b$ , and for a monopolar Stejskal-Tanner sequence is given by (2.21) where  $b$  has units of  $\text{s}/\text{mm}^2$ ,  $G$  is the amplitude of the gradient,  $\delta$  is the duration of the gradient and  $\Delta$  is the time interval [7]. To increase the  $b$ -value, either the gradient amplitude, duration or time interval can be increased, however it is often preferable to adjust  $b$ -values purely by altering the gradient amplitude to keep the diffusion time constant.

$$b = \gamma^2 G^2 \delta^2 (\Delta - \delta/3) \quad (2.21)$$

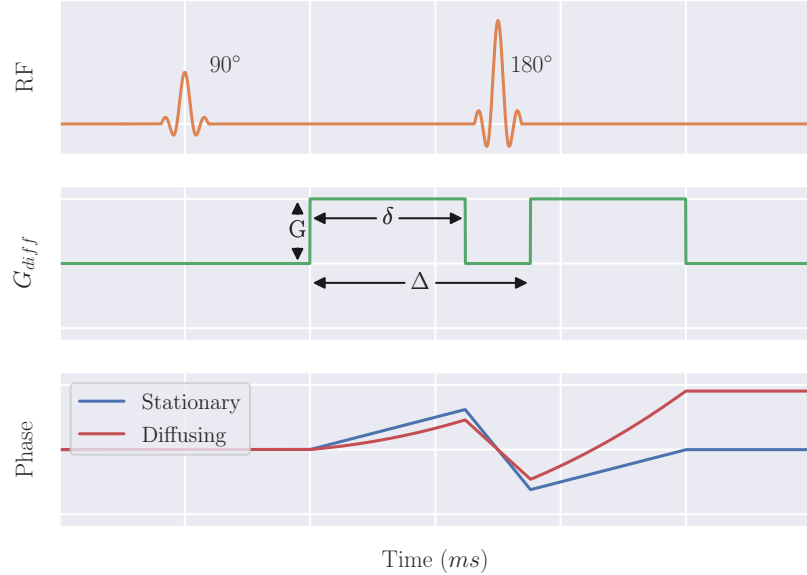


Figure 2.11: Phase evolution of two spins under the influence of monopolar diffusion encoding gradients.

The interplay between diffusion gradients and measured signal can be mathematically modelled by Equation (2.22),

$$S(b) = S_0 \cdot e^{-b \cdot ADC}, \quad (2.22)$$

where  $b$  is the b-value, and ADC is the Apparent Diffusion Coefficient of the tissue and reflects the degree with which spins can diffuse through a tissue, given in  $\text{mm}^2/\text{sec}$ . By repeating the acquisition with different b-values, the signal from each voxel at each b-value can be used to estimate ADC (and  $S_0$ ) by fitting the data to Equation (2.22).

For large b-values, typically greater than  $250 \text{ s/mm}^2$ , diffusion is the primary contributing factor to signal attenuation. For b-values less than  $250 \text{ s/mm}^2$  an additional mechanism in the form of perfusion, micro-circulation of blood in capillaries, leads to additional signal attenuation. This additional factor can be modelled by the Intravoxel Incoherent Motion

## 2.2. Relaxation and Contrast Mechanisms

---

(IVIM) model, (2.23), where  $f$  is the perfusion fraction, the proportion of a voxels volume occupied by capillaries,  $D$  is the tissues diffusion coefficient and  $D^*$  is the pseudodiffusion coefficient, reflecting the additional de-phasing due to perfusion within capillaries in a voxel [8, 9].

$$S(b) = S_0 \left[ f \cdot e^{-b(D+D^*)} + (1-f) \cdot e^{-b \cdot D} \right] \quad (2.23)$$

By acquiring data at a range of b-values, ensuring that low b-values are well sampled, a voxel-by-voxel fit can be performed to estimate  $f$ ,  $D$  and  $D^*$ .

Not all diffusion is isotropic (occurs to the same degree in all directions), often the motion of the spins is restricted e.g. within tissue fibres. The amount of restriction is known as the Fractional Anisotropy (FA) where 0 represents isotropic diffusion e.g. a large vial of water, and 1 represents diffusion being constrained to a single dimension. By applying the diffusion gradients in different directions (and strengths) the preferred direction of diffusion and fractional anisotropy can be calculated. These techniques are used in Chapter 6 to study Diffusion Tensor Imaging (DTI) in ex-vivo tissue samples.

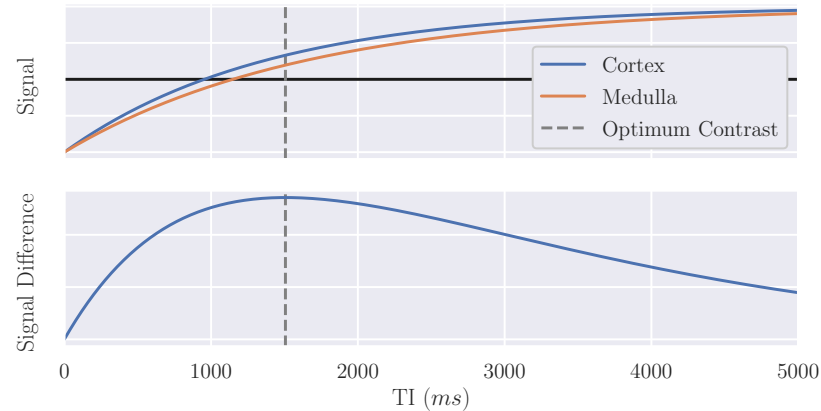
### 2.2.5 Optimisation of Tissue Contrast

Quantitative mapping of  $T_1$ ,  $T_2$  and  $T_2^*$  can often be a slow process due to the number of acquisitions required at different time points to sample relaxation curves. Often it is more desirable to acquire a volume at a single inversion/echo time with the intensity difference between tissues of interest maximised. Although the voxel intensities do not directly represent any quantitative underlying physical properties of the tissue, the contrast between tissues is sufficient for diagnosis or further analysis. For example, in Chapter 5 optimised contrast between organs is used for segmentation of the kidneys. Figure 2.12 shows how the acquisition parameters of a  $T_1$ -weighted and  $T_2$ -

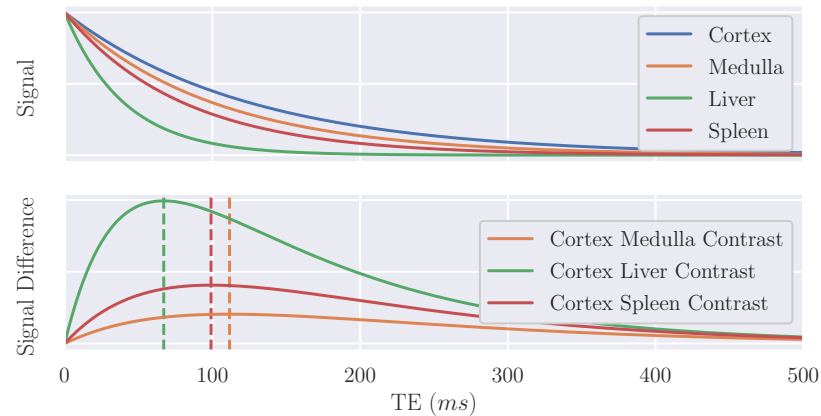
## 2.2. Relaxation and Contrast Mechanisms

---

weighted scheme can be optimised to produce the maximum signal difference, or contrast, between tissues.



(a)



(b)

Figure 2.12: (a) The signal generated from renal cortical and medullary tissues [10] following an inversion recovery and difference between signals. This shows that the contrast between the two tissues is optimal if the Inversion Time (TI) is 1500 ms. (b) The signal generated from the kidneys, liver and spleen following a spin echo sequence and the difference between the signals.

## 2.3 Forming an Image

### 2.3.1 Signal Localisation

So far, NMR has been applied to measure signals from the entire sample, gaining no information about the spatial variation within it. MRI applies the techniques of NMR to spatially resolve the location of the signal.

The key concepts of MRI were developed by multiple groups in the 1970s. Lauterbur used magnetic field gradients and a back-projection reconstruction technique to generate 2D images in 1973 [11]. Simultaneously Mansfield was working on “NMR diffraction” introducing the mathematical framework of reciprocal  $k$ -space [12] and later slice selective excitation [13]. The final key insight was provided by Ernst who published the first Fourier imaging method [14], this used non-selective excitations and linear gradients to generate 2D Fourier encoded images. These techniques are still the basis of MRI today.

The concepts of signal localisation will be introduced through the example of an axial acquisition, Figure 2.13. Throughout this chapter, the brain is used for examples of image formation as this anatomy highlights some of the concepts discussed more clearly. A typical series of equivalent renal scans is shown in Figure 2.14.

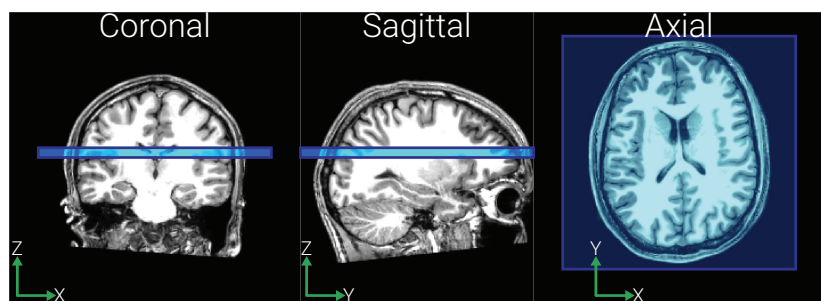


Figure 2.13: Planning used in the signal localisation example.

## 2.3. Forming an Image

---

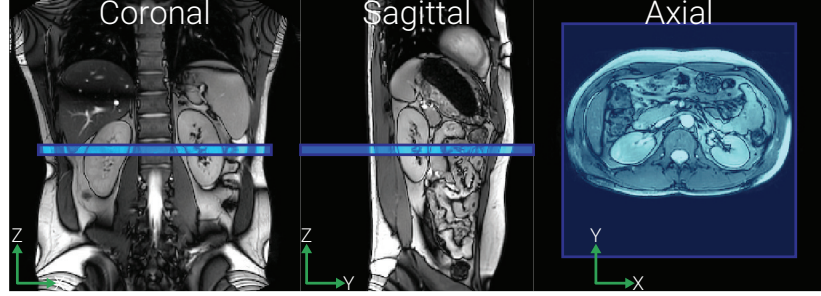


Figure 2.14: Typical localisers used to plan further renal scans.

### Gradient Fields

Signal localisation makes use of gradient fields. These produce small linear perturbations in  $B_0$  and are applied in a combination of the  $x$ ,  $y$  and  $z$  direction to enable arbitrary gradient directions and result in  $B_0$  varying with spatial position,  $\mathbf{r}$ ,

$$B_z(r) = (B_0 + \mathbf{G} \cdot \mathbf{r}) \hat{k}. \quad (2.24)$$

As such, the resonant frequency of the spins can also be described as a function of position and, because the gradients are not static, also in time;

$$\omega(x, y, z, t) = \gamma(B_0 + G_x(t)x + G_y(t)y + G_z(t)z). \quad (2.25)$$

### Slice Selection

The initial step in localisation is to measure the signal from a single, spatially defined, slice. If a gradient is applied along the  $z$  direction,  $G_z$ , the magnetic field experienced by the spins at position  $z$  will be

$$B(z) = B_0 + G_z z. \quad (2.26)$$

As such, from the simplification of (2.25), the Larmor frequency becomes

$$\omega(z) = \gamma(B_0 + G_z z). \quad (2.27)$$

### 2.3. Forming an Image

---

If a frequency selective RF pulse is applied to the sample, it will only excite spins within the corresponding bandwidth and thus only a slice of desired thickness. This slice-selective thickness,  $\Delta z$ , can be changed by either adjusting the amplitude of  $G_z$  or the bandwidth of the excitation RF pulse,  $\Delta\omega$ .

$$\Delta z = \frac{\Delta\omega}{\gamma G_z} \quad (2.28)$$

The excitation profile achieved by a slice selective pulse can be approximated by a Fourier transform. Generally, a rectangular slice profile is wanted and as such, the RF pulse takes the form of a sinc function. To achieve a perfect rectangular pulse, the sinc would have to be infinite in length. Given the lack of infinite time available during an MRI examination, a truncated sinc pulse is used, generally including three or five lobes and a Gaussian filter.

The gradient applied will result in de-phasing of the spins as in a GE sequence, therefore a gradient of the opposite polarity and half the magnitude is applied after the RF pulse to re-phase the spins, Figure 2.15a.

### 2.3. Forming an Image

---

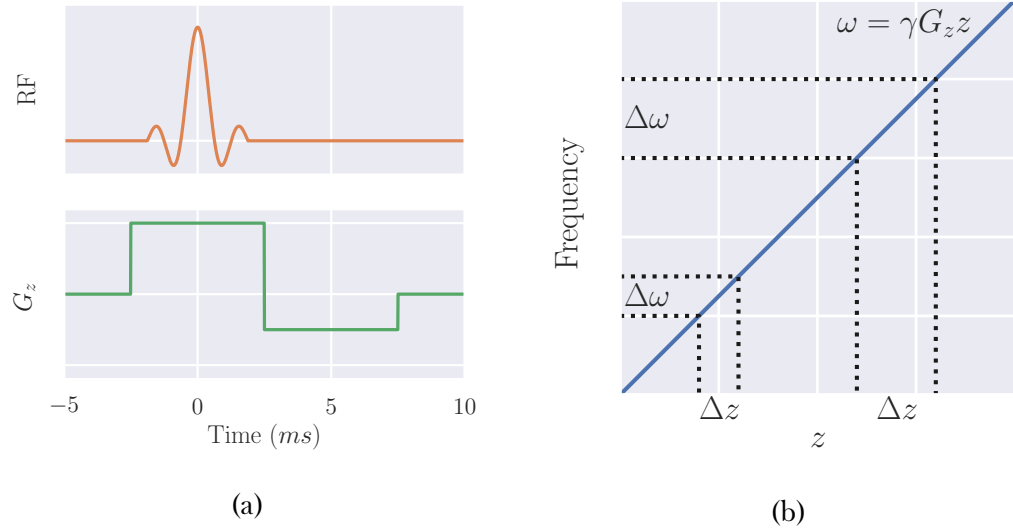


Figure 2.15: (a) A truncated sinc pulse of bandwidth  $\Delta\omega$  is applied at the same time as a slice selective gradient, this is followed by the negative re-phasing gradient lobe. Note that the area under the re-phasing gradient is half that of the slice selective gradient. (b) Example slices of thickness  $\Delta z$  being excited by RF pulses of bandwidth  $\Delta\omega$ , showing that excitation pulses with larger bandwidth result in thicker slice profiles.

### Phase Encoding

So far, the signal has been localised from a full 3D volume to a defined 2D volumetric slice. To localise the signal in the next dimension, phase encoding is used. This technique uses a gradient in the  $y$  direction applied for time  $T$ . For the duration of  $G_y$  the spins precess with a frequency according to their position in the  $y$  direction

$$\omega(y) = \gamma(B_0 + G_y y), \quad (2.29)$$

and as such accrue a phase shift,  $\phi(y)$ , relative to the situation if no gradient was applied. This is given by

$$\phi(y) = \gamma y \int_0^T G_y(t) dt. \quad (2.30)$$

### 2.3. Forming an Image

---

Acquisitions must be repeated with different amplitudes/durations of  $G_y$  to fully sample the  $y$  direction.

An artefact that manifests itself in the phase encode direction is phase wrap-around. This is a specific type of aliasing artefact. Aliasing occurs when the sampling frequency of a signal is not sufficient to accurately represent the underlying signal. The Nyquist criterion states that for a digitally sampled signal to be free from aliasing, the sampling rate must be at least twice that of the highest frequency component of the signal.

Phase aliasing occurs because the whole sample produces signal, whether it is in the Field Of View (FOV) or not. As there is a finite range of phase values (0 to  $2\pi$ ) tissue outside the FOV can have the same value as tissue within the FOV, this results in the two signals becoming indistinguishable and therefore combined in a process known as wrapping. This artefact is illustrated in Figure 2.16 using the brain because its simple oval shape lends itself to a clearer diagram. This artefact is just as, if not more, prevalent in the body where there is a much larger variance in subject size and thus, in the interest of consistent protocols, larger FOVs are acquired, slowing the acquisition.

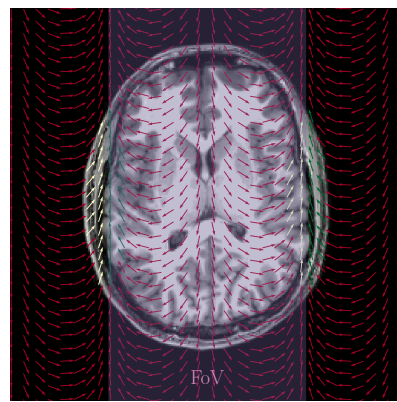


Figure 2.16: Spins outside the FOV have the same phase value as those within the FOV and thus wrapping occurs.

### Frequency Encoding

Finally, the signal needs to be localised in the  $x$  direction. This is achieved using frequency encoding. Here the gradient,  $G_x$  is applied during the acquisition component of the sequence i.e. when the signal is being sampled. As the gradient is applied during readout, those spins in the centre of the gradient (at field  $B_0$ ) will precess at the Larmor frequency while those in a stronger or weaker field will precess faster or slower respectively. By sampling the signal generated and applying a Fourier transform to separate components of the signal at each frequency, the signal is spatially resolved in all three dimensions. An overview of a basic signal localisation scheme is shown in Figure 2.17.

Aliasing is rarely seen in the frequency encode direction as, in modern scanners, the sampling frequency is more than twice the maximum frequency expected in the frequency encode direction i.e. the Nyquist criterion is satisfied. Additionally, low-pass filtering can be applied on acquisition to remove components of the signal that would not be accurately characterised by the sampling frequency.

### 2.3. Forming an Image

---

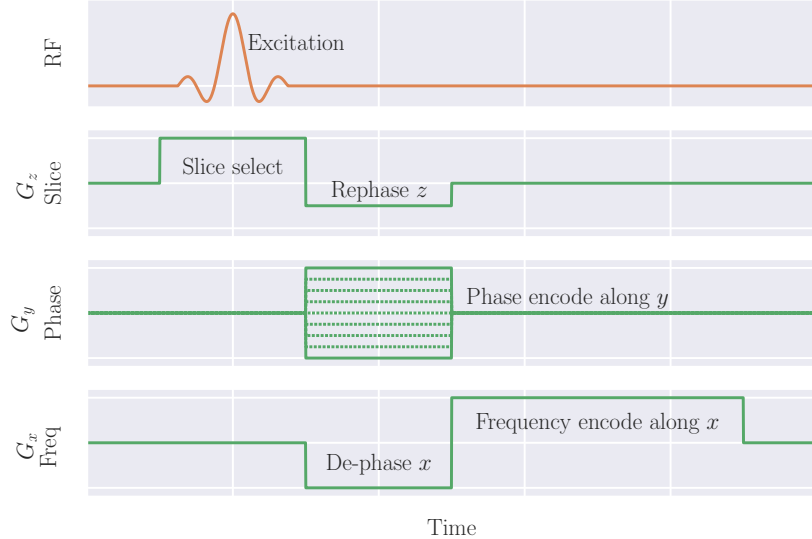


Figure 2.17: A basic spacial localisation pulse sequence showing how gradients applied along the  $z$ ,  $y$  and  $x$  directions can be used to localise the signal in the corresponding dimensions. The repetitions with different phase encoding gradient amplitudes are represented by the dotted lines in  $G_y$ .

### $k$ -space

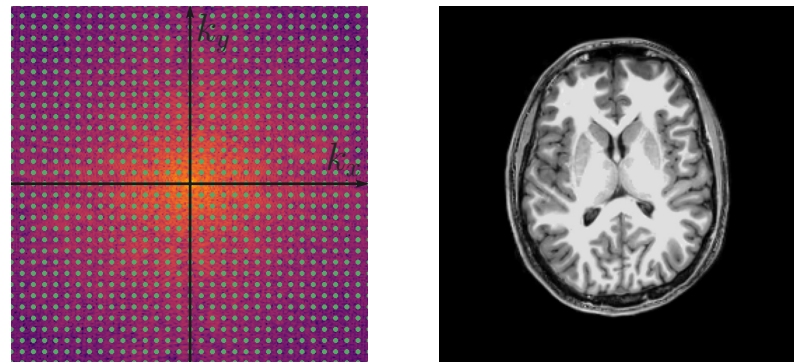
$k$ -space, sometimes known as Fourier space, is a useful concept for interpreting MRI pulse sequences and represents the spatial frequencies of the image. Immediately after an excitation pulse and rewind gradient, the signal being sampled is at the origin of  $k$ -space, corresponding to low spatial frequencies, or the low resolution aspects of the image e.g. which voxels are inside or outside the body. As gradients are applied to the sample, sampling moves out from the centre of  $k$ -space to higher spatial frequencies corresponding to finer detail within the image. For a 2D acquisition, as above, the location in  $k$ -space is defined by (2.31) and (2.32) where  $G_x$  and  $G_y$  are the gradients in the frequency encode and phase encode directions respectively and  $t_x$  and  $t_y$  are the duration the gradient is applied for.

$$k_x = \gamma G_x t_x \quad (2.31)$$

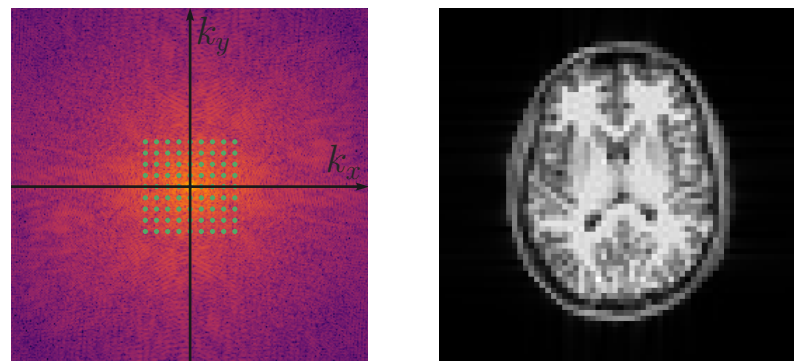
$$k_y = \gamma G_y t_y \quad (2.32)$$

### 2.3. Forming an Image

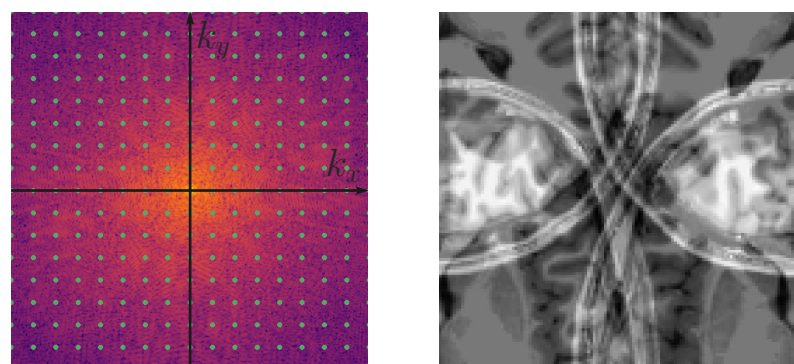
When recording MRI data, the continuous signal must be discretised. The higher the sampling frequency i.e. the closer together in  $k$ -space the samples are,  $\Delta k$ , the wider the FOV and the further out from the origin of  $k$ -space is sampled, the higher resolution the image will be. Examples of  $k$ -space sampling patterns and their corresponding image are shown in Figure 2.18.



(a)



(b)



(c)

Figure 2.18: (a) Fully sampled  $k$ -space and the corresponding image. (b) Centre sampling of  $k$ -space produces a lower resolution image. (c) Sampling with a larger  $\Delta k$  resulting in a decreased FOV and aliasing.

### 2.3. Forming an Image

---

#### From $k$ -space to Image Space

The raw data sampled in  $k$ -space can be reconstructed to an image via a Fourier transform. When the quadrature data undergoes a 2D Fourier transform, it produces a complex image composed of a real and imaginary part. These constituent parts of the image can be converted into magnitude and phase images with the magnitude representing the spin density, example magnitude and phase images are shown in Figure 2.19.

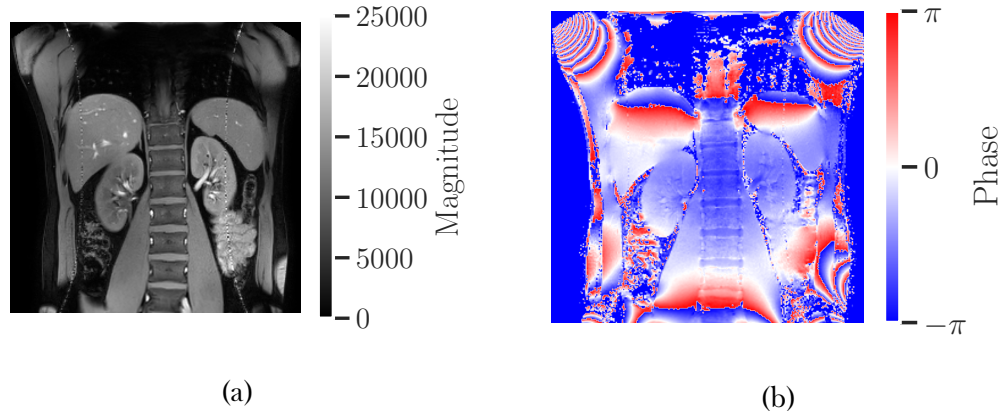


Figure 2.19: Example magnitude (a) and phase (b) images. Note that phase data is limited to values between  $-\pi$  and  $\pi$  and as such, phase wrapping can be observed.

#### Coordinate Systems

The above example was chosen so that only one gradient is used at once however if the planning of the acquisition is more complicated, the nomenclature can become more confusing, as such, for clarity multiple coordinate systems are often used.

**Scanner Space:** This coordinate system has its origin at isocentre of the scanner and is defined in terms of  $x$ ,  $y$  and  $z$ .

### 2.3. Forming an Image

---

**Imaging Space:** The coordinates of this system are defined by the directions used in signal localisation,  $M$  for the frequency encode direction (also called magnitude),  $P$  for the phase encode direction and  $S$  for the slice select direction.

**Anatomical Space:** Defined in terms of the subjects orientation in the scanner, this coordinate system has the axis, Right-Left (R-L), Anterior-Posterior (A-P) and Superior-Inferior (S-I).

#### 2.3.2 Image Acquisition Acceleration

One of the recurring limiting factors in MRI is the acquisition time. For neuroimaging applications, the relatively slow acquisition of MRI limits subject throughput or the number of different measures that can be performed. In abdominal imaging, acquisition times can be even more of a hindrance given many scans are performed while the subject is holding their breath on expiration as typically used in this thesis. As such, image acquisition acceleration techniques have been developed. These techniques sacrifice a small amount of Signal to Noise Ratio (SNR) for a decrease in acquisition time.

##### Partial Fourier

Fully sampled  $k$ -space contains inherent redundancy as it contains its own complex conjugate; the real components of the signal are symmetric while the imaginary components are anti-symmetric. This means that theoretically no contrast information is lost if a reduced area of  $k$ -space is sampled e.g. only 66 % of  $k$ -space is sampled. However, this technique does impact phase information and so should not be used in acquisitions where downstream processing requires accurate phase. Known as partial Fourier or halfscan, this technique results in a decreased SNR and can introduce image artefacts as the

### 2.3. Forming an Image

---

partial Fourier factor approaches 50 %, however, the acquisition time reduces by approximately the percentage of  $k$ -space sampled e.g. an acquisition that would take three minutes fully sampled will take two minutes if a partial Fourier factor of 66 % is used. An example of reconstructions of 100 %, 75 % and 51 % of  $k$ -space are shown in Figure 2.20.

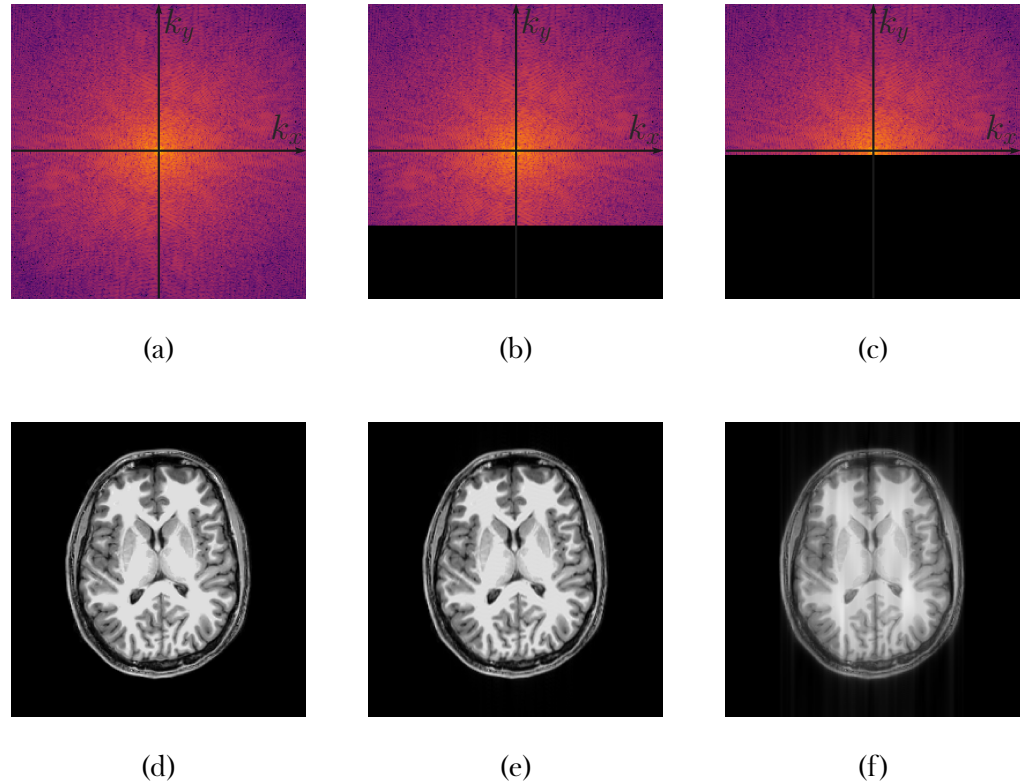


Figure 2.20: Full, (a), 75 %, (b), and 51 %, (c),  $k$ -space sampling and their corresponding reconstructions in image space, (d), (e) and (f) respectively.

### Sensitivity Encoding (SENSE)

Most modern scanners use different coils for RF transmission, and signal reception. The transmission coil is usually built into the bore of the magnet while the receive coil is placed as close to the source of the signal as possible. These receive coils are usually composed of multiple smaller coils to make an array, each with its own signal sampling hardware. This system architecture can be utilised to reduce acquisition times through the use of parallel imaging techniques. This family of techniques exploit the limited area signal is

### 2.3. Forming an Image

---

received from by each coil in the receive array to aid the spatial localisation of the signal; Sensitivity Encoding (SENSE) is one such technique. Before the main image is acquired, a SENSE reference scan is acquired, this scan ascertains the spatial sensitivity profile of each element in the array i.e. the location in which the signal recorded by a particular channel is likely to be coming from. While acquiring the desired image, for each coil in the array, fewer lines of  $k$ -space are recorded in the phase encoded direction thus decreasing acquisition time, however this leads to wrapping as seen in Figure 2.18c, albeit only in the phase encode direction. The wrapped images from each coil can then be unwrapped and combined using the SENSE reference scan as a prior to accurately unwrap the image [15].

The SENSE factor is the degree to which  $k$ -space is under-sampled and is limited to the number of elements in the receive array. Applying higher SENSE factors increases acquisition speeds, however, reduces SNR. This is the method implemented on Philips scanners as used in this thesis, different vendors have slightly different methodologies to accelerate imaging by utilising the limited range of elements within an RF coil array.

#### 2.3.3 Image Acquisition Schemes

Many different acquisition schemes have been developed for sampling  $k$ -space. Outlined below are some of the key sequences that form the basis of MRI and that are employed in this thesis.

##### Spin Warp Imaging

The simplest uniformly sampled  $k$ -space trajectory is spin warp imaging. This technique is based on the GE scheme and samples one line of  $k$ -space per excitation, or shot, a schematic is shown in Figure 2.21. Each shot applies a different phase encode gradient to move a different amount in the  $k_y$  direction. The signal is then sampled while a gradient is applied in the

### 2.3. Forming an Image

---

frequency direction, also known as the readout gradient. The acquisition time for this sequence is long because it only collects one line of  $k$ -space per shot and as such this technique is sensitive to subject motion.

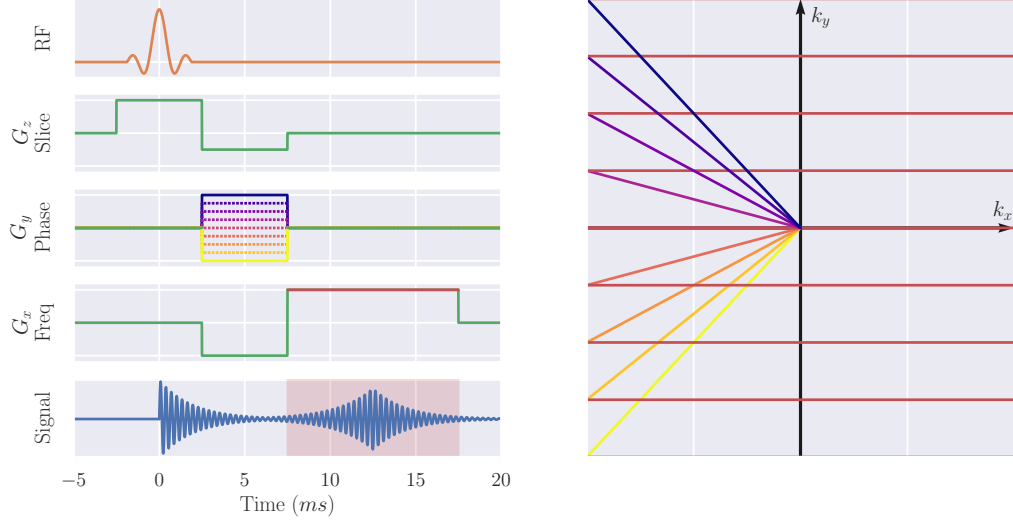


Figure 2.21: A schematic of the spin warp image sequence. The Pulse Sequence Diagram (PSD) shows the different phase encoding gradients,  $G_y$ , in colours from yellow to purple and the readout gradient,  $G_x$ , in red. These colours correlate with the colours in the  $k$ -space trajectory. The signal recorded is highlighted in red.

### Turbo Spin Echo (TSE)

The Turbo Spin Echo (TSE) sequence, also known as Fast Spin Echo (FSE) or Rapid Acquisition with Relaxation Enhancement (RARE), is an expansion on the conventional SE sequence applying evenly spaced  $180^\circ$  RF refocusing pulses to generate multiple echoes from a single excitation, these echoes are used to record multiple lines of  $k$ -space. The number of echoes is known as the Echo Train Length (ETL), or ‘turbo factor’ and is the factor by which the scan time is reduced compared to a conventional spin echo sequence, and this is anywhere between 2 and 30 per TR; the time between echoes is known as the echo spacing and is typically of 15 - 25 ms. A schematic of the TSE sequence is shown in Figure 2.22.

### 2.3. Forming an Image

---

Each line of  $k$ -space is acquired at a different time after excitation, as such the lines will have different  $T_2$  weightings, it is therefore important to ensure the centre of  $k$ -space is acquired at the desired TE as this echo will dominate the image contrast. The time between excitation and the centre of  $k$ -space is known as the Effective Echo Time (eTE).

The decrease in acquisition time comes at the expense of RF exposure, the large number of  $180^\circ$  pulses leads to more energy in the form of heat being deposited in the tissue being imaged, this is known as Specific Absorption Rate (SAR). SAR limits are imposed when scanning to avoid damaging any tissue and as such TSE with its high RF power can easily exceed these limits. Modern TSE sequences can reduce the angle of the refocusing pulse, however this can come at the expense of quantitative accuracy. This sequence is discussed further in Chapter 3.

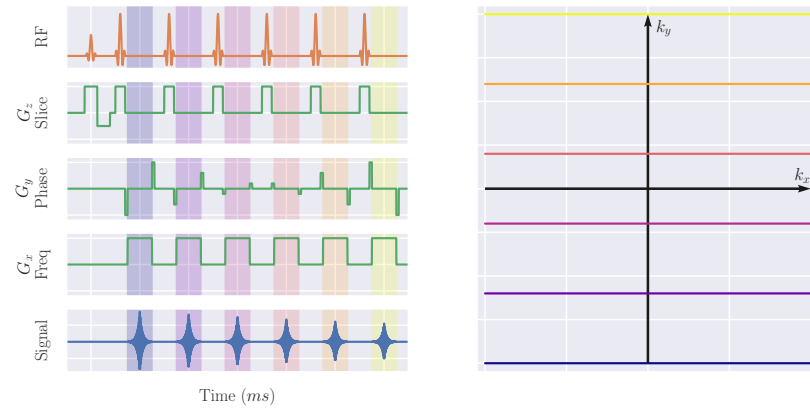


Figure 2.22: A schematic of the TSE pulse sequence and  $k$ -space trajectory. The coloured bands on the Pulse Sequence Diagram (PSD) correspond to the colours of the  $k$ -space trajectories. Note this diagram is not to scale.

### Half-Fourier Acquisition Single-shot Turbo spin Echo (HASTE)

The Half-Fourier Acquisition Single-shot Turbo spin Echo (HASTE) sequence uses a combination of the techniques above and can be seen as an extension of the TSE sequence. A single excitation is followed by a very long echo train with short echo spacing. This allows a large proportion of  $k$ -

### 2.3. Forming an Image

---

space to be sampled within a single TR and thus a whole slice is acquired. To minimise the number of lines of  $k$ -space acquired and thus the ETL, partial Fourier techniques as outlined in Section 2.3.2 can be utilised. The relatively long TE required for a HASTE sequence means images are normally  $T_2$ -weighted. An example PSD and  $k$ -space trajectory for the HASTE sequence is shown in Figure 2.23.

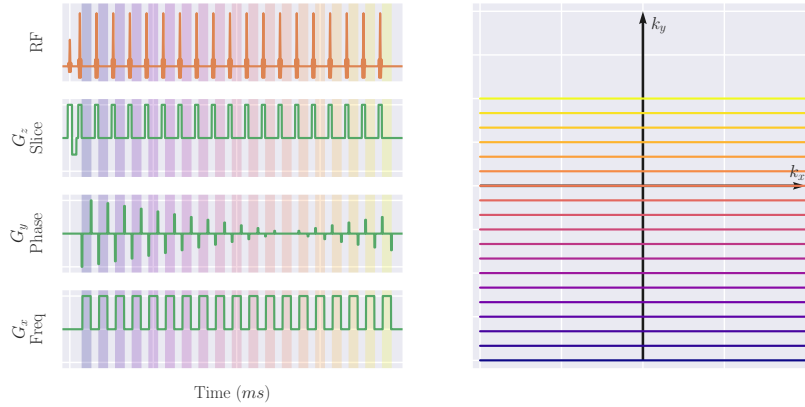


Figure 2.23: A schematic of the HASTE pulse sequence and  $k$ -space trajectory.

The advantage of HASTE is its rapid acquisition. It can be used to minimise the effects of motion when scanning uncooperative patients, fetuses or structures the subject has no control over such as the bowel. Alternatively it can be used to capture a large FOV in a single breath hold, thus minimising the effects of inconsistent expiration level, as in Chapter 5. However the very long ETL can cause significant blurring of the image. An example abdominal HASTE image is shown in Figure 2.24.



Figure 2.24: An example abdominal image acquired using the HASTE readout scheme.

#### Turbo Field Echo (TFE)

Turbo Field Echo (TFE), also known as ultrafast gradient echo, is designed to speed up the acquisition of gradient echo images by reducing the TR between excitations. Typical basic gradient echo sequences have relatively long TR to allow the recovery of longitudinal magnetisation. The flip angle used in the TFE sequence is much smaller than the examples explored so far, usually approximately  $10^\circ$  thus leaving a large component of the magnetisation in the longitudinal direction while tipping enough magnetisation into the transverse plane to record a signal at an acceptable SNR. Between each excitation, the transverse magnetisation is spoiled to ensure the images are only  $T_1$ -weighted.

After a train of equally spaced RF pulses of flip angle,  $\alpha$ , and period, TR, the longitudinal magnetisation reaches a steady state,  $S_{TFE}$ , after a sufficient number of pulses. This steady state signal depends on the  $T_1$  of the tissue and the FA and TR of the sequence. Assuming perfect transverse magnetisation spoiling between each RF pulse, this equilibrium signal is given by,

### 2.3. Forming an Image

---

$$S_{TFE} = M_0 \frac{\sin(\alpha) [1 - \exp(-TR/T_1)]}{1 - \cos(\alpha) \exp(-TR/T_1)} \exp\left(-\frac{TE}{T_2^*}\right). \quad (2.33)$$

The angle that produces the maximum signal, known as the Ernst angle,  $\alpha_E$ , is given by,

$$\alpha_E = \arccos\left[\exp\left(-\frac{TR}{T_1}\right)\right]. \quad (2.34)$$

Figure 2.25 shows the ratio of the steady state signal to the fully recovered,  $90^\circ$  excitation signal of renal cortex ( $T_1$  of 1376 ms) for a range of flip angles and TR. Additionally the Ernst angle is shown.

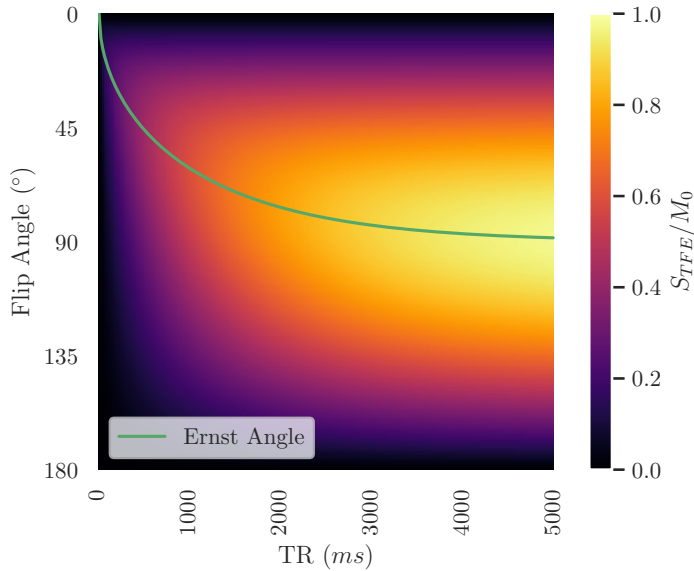


Figure 2.25: The expected steady state signal of a TFE pulse sequence and Ernst angle when imaging renal cortex.

An example TFE pulse sequence is shown in Figure 2.26. This schematic includes three startup echoes while the longitudinal magnetisation reaches a steady state then sixteen further pulses and gradient echoes where the signal is sampled to form an image. TFE sequences are often used when  $T_1$  contrast is desirable, hence Figure 2.26 shows an inversion recovery TFE sequence, beginning with a  $180^\circ$  inversion pulse.

### 2.3. Forming an Image

---

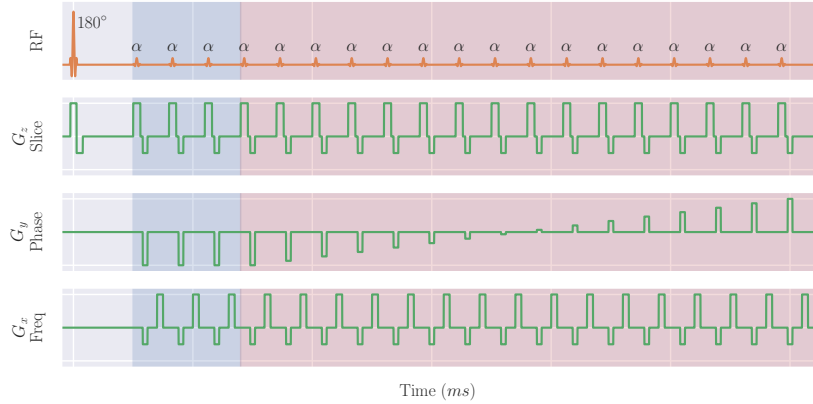


Figure 2.26: A schematic of the TFE pulse sequence. Startup echoes are highlighted in blue, echoes used in image acquisition are highlighted in red. This example begins with a  $180^\circ$  inversion pulse to enhance  $T_1$  contrast.

An image generated using a TFE sequence is shown in Figure 2.27.



Figure 2.27: An example of an abdominal image acquired using the TFE scheme. This  $T_1$ -weighted image is used to segment the renal cortex and medulla.

### Echo Planar Imaging (EPI)

A much faster imaging technique is Echo Planar Imaging (EPI) [12]. This technique samples all lines of  $k$ -space in a single excitation shot with an acquisition time typically less than 100 ms. The PSD and  $k$ -space trajectory

### 2.3. Forming an Image

---

for this sequence are shown in Figure 2.28. The sequence begins with a slice selective excitation and an acquisition of the bottom line of  $k$ -space, however, instead of a spoiler followed by another excitation as in spin warp imaging, in EPI a small positive phase encode gradient ‘blip’ is applied to move up a line in  $k$ -space, followed by an inversion of the readout gradient polarity. This blip followed by reversed readout is repeated, zig-zagging up  $k$ -space until the desired  $k$ -space is sampled.

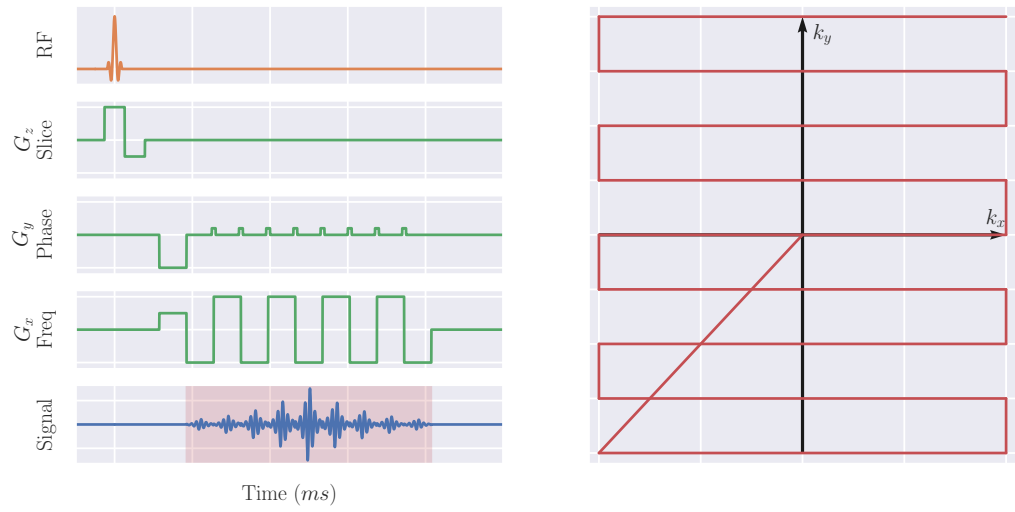


Figure 2.28: A schematic of the GE-EPI pulse sequence and  $k$ -space trajectory. This diagram is not to scale.

While this sequence has a very short acquisition time, it does have drawbacks. Imperfections in gradient coils and eddy currents can cause small differences in lines collected in the positive and negative direction, leading to a Nyquist ghost artefact. Additionally geometric distortions are induced in the image due to inhomogeneities in the  $B_0$  field and a poor bandwidth in the phase encode direction [16], these distortions are seen in Figures 2.29a and 2.29b. Common sources of  $B_0$  imperfections include differences in tissue susceptibility, poor shimming and eddy currents induced by diffusion sensitising gradients. Multiple post-processing techniques have been developed with the aim of correcting these distortions by either using quantitative  $B_0$  maps or collecting data with phase encode blips in both directions i.e. collect images sampling  $k$ -space from both bottom to top and

## 2.4. Conclusion

---

top to bottom. The latter of these techniques is used to correct the image in Figure 2.29c and is outlined further in Chapter 6.

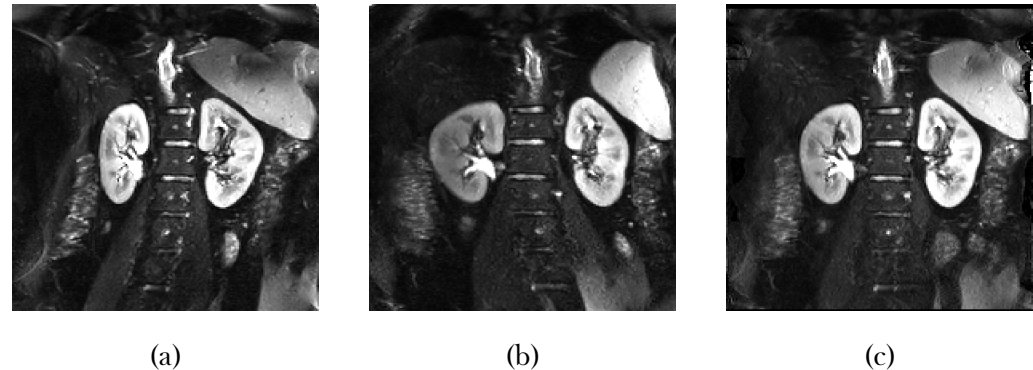


Figure 2.29: Geometric distortions in a SE-EPI when phase encode blips are (a) positive, (b) negative and (c) corrected via post processing.

## 2.4 Conclusion

This chapter has introduced the basic concepts of NMR and MRI required for interpreting this thesis. These techniques are built upon in the experimental chapters for quantification of renal properties, both in-vivo and ex-vivo.

## 2.5 References

1. Harris, R. K. N.m.r. and the Periodic Table. *Chemical Society Reviews* **5**, 1–22 (1st Jan. 1976).
2. Bernstein, M. A., King, K. F. & Zhou, X. J. *Handbook of MRI Pulse Sequences* 1041 pp. Google Books: d6PLHcyejEIC (Elsevier, 21st Sept. 2004).
3. Westbrook, C. *MRI at a Glance* 138 pp. Google Books: WeRbCwAAQBAJ (John Wiley & Sons, 18th Nov. 2015).
4. Bloch, F. Nuclear Induction. *Physical Review* **70**, 460–474 (1st Oct. 1946).
5. Mohr, P. J., Newell, D. B. & Taylor, B. N. CODATA Recommended Values of the Fundamental Physical Constants: 2014. *Reviews of Modern Physics* **88**, 035009 (26th Sept. 2016).
6. Solomon, I. Relaxation Processes in a System of Two Spins. *Physical Review* **99**, 559–565 (15th July 1955).
7. Stejskal, E. O. & Tanner, J. E. Spin Diffusion Measurements: Spin Echoes in the Presence of a Time-Dependent Field Gradient. *The Journal of Chemical Physics* **42**, 288–292 (1st Jan. 1965).
8. Le Bihan, D., Breton, E., Lallemand, D., Grenier, P., Cabanis, E. & Laval-Jeantet, M. MR Imaging of Intravoxel Incoherent Motions: Application to Diffusion and Perfusion in Neurologic Disorders. *Radiology* **161**, 401–407 (1st Nov. 1986).
9. Le Bihan, D., Breton, E., Lallemand, D., Aubin, M. L., Vignaud, J. & Laval-Jeantet, M. Separation of Diffusion and Perfusion in Intravoxel Incoherent Motion MR Imaging. *Radiology* **168**, 497–505 (1st Aug. 1988).
10. Cox, E. F., Buchanan, C. E., Bradley, C. R., Prestwich, B., Mahmoud, H., Taal, M., Selby, N. M. & Francis, S. T. Multiparametric Renal Magnetic Resonance Imaging: Validation, Interventions, and Alterations in Chronic Kidney Disease. *Frontiers in Physiology* **8**, 696 (2017).

## 2.5. References

---

11. Lauterbur, P. C. Image Formation by Induced Local Interactions: Examples Employing Nuclear Magnetic Resonance. *Nature* **242**, 190–191 (5394 Mar. 1973).
12. Mansfield, P. & Grannell, P. K. NMR "Diffraction" in Solids? *Journal of Physics C: Solid State Physics* **6**, L422–L426 (Nov. 1973).
13. Garroway, A. N., Grannell, P. K. & Mansfield, P. Image Formation in NMR by a Selective Irradiative Process. *Journal of Physics C: Solid State Physics* **7**, L457–L462 (Dec. 1974).
14. Kumar, A., Welti, D. & Ernst, R. R. NMR Fourier Zeugmatography. *Journal of Magnetic Resonance (1969)* **18**, 69–83 (1st Apr. 1975).
15. Pruessmann, K. P., Weiger, M., Scheidegger, M. B. & Boesiger, P. SENSE: Sensitivity Encoding for Fast MRI. *Magnetic Resonance in Medicine* **42**, 952–962 (1999).
16. Andersson, J. L. R., Skare, S. & Ashburner, J. How to Correct Susceptibility Distortions in Spin-Echo Echo-Planar Images: Application to Diffusion Tensor Imaging. *NeuroImage* **20**, 870–888 (1st Oct. 2003).

# **Chapter 3**

## **Assessment of Renal $T_2$ Mapping Methods**

---

## Abstract

Renal  $T_2$  mapping shows promising early results for the evaluation of multiple pathologies, however, of the few studies there is very little consistency due to the differing methodologies being employed across research groups. Here the four most common  $T_2$  mapping sequences for use in the kidneys, basic Spin Echo (SE)-Echo Planar Imaging (EPI), Multi-Echo Turbo Spin Echo (ME-TSE), Gradient Spin Echo (GraSE) and Carr-Purcell-Meiboom-Gill (CPMG)  $T_2$  preparation methods, are evaluated.

Each of the four sequences was used to image a phantom designed by the National Institute of Standards and Technology (NIST) with an array of spheres of known  $T_2$  to evaluate quantitative accuracy across the range of  $T_2$  values reported in the kidneys. The sensitivity of each sequence to flow was evaluated using a Quantitative Arterial Spin Labelling Perfusion Reference (QASPER) phantom over a range of flow rates. Additionally, the image quality of each sequence was assessed by estimating the point spread function. All sequences were then used to acquire  $T_2$  maps of five healthy volunteers.

In the NIST phantom, the basic spin echo sequence delivered the most accurate quantitative results over the range of  $T_2$  reported in the kidneys (40 ms - 200 ms), however its sensitivity to flow and wide point spread function limit its use in-vivo. Instead, a gradient spin echo sequence is recommended, with a mean relative error of  $15 \pm 4\%$  over the range of  $T_2$  reported within the kidneys (40 ms – 200 ms), superior readability due to its smaller point spread function and insensitivity to flow.

*This work was presented as an oral presentation at the International Society of Magnetic Resonance in Medicine (ISMRM) 28th Annual Meeting (2020) [1].*

## 3.1 Introduction

### 3.1.1 Motivation

Quantitative Magnetic Resonance Imaging (MRI) is the process of taking measurements where the voxel values have numerical significance rather than simply representing signal intensity in arbitrary units [2]. These numerically significant values can take the form of macroscale properties such as rate of oxygen consumption and blood vessel flow rates or microscale properties such as tissue  $T_1$ ,  $T_2$ , diffusion and susceptibility. When interpreted, these values may provide useful biomarkers for improved diagnosis and treatment of patients.

The kidneys are structurally and functionally complex organs and as such lend themselves to the wide variety of MRI protocols designed to probe different aspects of the tissue and processes carried out within, termed multiparametric MRI. While high resolution images of the kidneys morphology and basic measures such as Total Kidney Volume (TKV) can be very useful in diagnosing and monitoring disease progression [3–5], these do not fully leverage the quantitative nature of MRI. Measurements of  $T_1$  have been shown to correlate well with fibrosis in the myocardium [6, 7], liver [8, 9] and kidneys [10] and an increase in  $T_1$  has been associated with Chronic Kidney Disease (CKD) [3, 11, 12]. Arterial Spin Labelling (ASL) techniques can be used to quantify renal perfusion in physiological units ( $\text{m}\ell/100\text{g}/\text{min}$ ) and have been shown to correlate with allograft function post renal transplant in addition to cold ischemia time and the recipients Estimated Glomerular Filtration Rate (eGFR) [13–16]. ASL has been used to demonstrate a decrease in perfusion in CKD subjects [11, 17, 18]. These techniques have proved useful when used in isolation however they can be combined and used in the same scanning session to greater effect within a multiparametric protocol [3, 12, 19–21].

### 3.1. Introduction

---

$T_2$  mapping has found wide use in cardiac MRI for the assessment of myocardial oedema [22–24] and iron overload [25, 26].  $T_2$  mapping has also effectively been used in the brain to study multiple sclerosis [27], epilepsy [28], dementia [29] and Parkinson’s disease [30]. Despite these developments elsewhere in the body,  $T_2$  mapping has had limited uptake in the renal community.

Renal  $T_2$  mapping has seen most research focusing on repeatability measures [31–34] with clinical uses in the field of assessment of allograft function in mice [21] and humans [35, 36], and has shown potential for early diagnosis of Autosomal Dominant Polycystic Kidney Disease (ADPKD) [37] and assessment of clear cell renal cell carcinoma [38].

In the existing literature, there is a substantial variation in quoted  $T_2$  values within the kidneys of healthy volunteers, Table 3.1, this is thought to be, in part, due to the differences in  $T_2$  mapping methodologies. There are currently four main  $T_2$  mapping methods that have been published in the kidneys: basic Spin Echo (SE)-Echo Planar Imaging (EPI), Multi-Echo Turbo Spin Echo (ME-TSE), Gradient Spin Echo (GraSE) and Carr-Purcell-Meiboom-Gill (CPMG)  $T_2$  preparation.

Author	Year	Sample Size	Sequence	Cortex $T_2$ (ms)	Medulla $T_2$ (ms)
<b>3T</b>					
de Bazelaire <i>et al</i> [31]	2004	6	SE $T_2$ prep	$76 \pm 7$	$81 \pm 8$
Li <i>et al</i> [33]	2015	5	CPMG $T_2$ prep	$121 \pm 5$	$138 \pm 7$
Franke <i>et al</i> [37]	2017	3	GraSE	$132 \pm 6$	
Adams <i>et al</i> [36]	2020	16	GE $T_2$ prep	$78 \pm 4$	$59 \pm 2$
<b>1.5T</b>					
de Bazelaire <i>et al</i> [31]	2004	4	SE $T_2$ prep	$87 \pm 4$	$85 \pm 11$
Zhang <i>et al</i> [32]	2011	4	2D ME-TSE	$112 \pm 8$	$137 \pm 13$
Mathys <i>et al</i> [35]	2011	6	ME-SE	$125 \pm 7$	
Siedek <i>et al</i> [39]	2020	10	GraSE	$130 \pm 6$	

Table 3.1: Studies documenting renal  $T_2$  in healthy volunteers at 3T and 1.5T. This is an updated table from Wolf *et al* [40].

### 3.1. Introduction

---

Here each of these four methods are compared in the context of renal  $T_2$  mapping to ascertain which is most suitable. This is achieved by evaluating each methods quantitative accuracy, image quality, sensitivity to flow in phantoms and suitability for use in-vivo in final evaluation across five healthy subjects.

#### 3.1.2 Common Sources of Error in $T_2$ Mapping Sequences

The basic principles of  $T_2$  mapping are outlined in Section 2.2.2, these principles can be achieved using multiple methods, described in Section 3.1.3, however many of these methods have common sources of error leading to inaccuracies in measured  $T_2$ .

##### Diffusion

$T_2$  mapping sequences negate  $T_2'$  effects cause by static  $B_0$  inhomogeneities by refocusing this mechanism of signal attenuation. This is possible because, if spins are in an area of slightly higher magnetic field than  $B_0$  they will dephase quicker than spins in an area at  $B_0$ . Upon the application of a 180° Radio Frequency (RF) pulse the spins being to re-phase, with those in areas of slightly higher magnetic field precessing quicker and ultimately causing an echo with the effects of static field inhomogeneities negated. This technique relies upon the environment each spin is in remaining constant before and after the 180° pulse to achieve purely  $T_2$  weighted echoes. The movement of molecules via diffusion violates this requirement as spins can move into an area of slightly different magnetic field and thus precess at different rates before and after the 180° refocusing pulse, causing an attenuation in transverse magnetisation above that of  $T_2$  [41].

#### Outflow

Multi-slice imaging uses slice selective RF pulses to image one slice while the longitudinal magnetisation of other slices is returning to equilibrium. This allows excitation to occur at a rate quicker than five times  $T_1$  as slices can be acquired without affecting the preceding or next slice to be acquired. The use of slice selective RF pulses leads to potential outflow artefacts. These occur when the spin in an imaging plane flows out of the plane and is replaced by another spin and as such the full pulse sequence isn't delivered to the same spin. As the slice thickness of these schemes is typically in the order of 5 mm, a significant proportion of the excited spins within a voxel can be replaced in the tens to hundreds of milliseconds between excitation and acquisition. This results in artificially reduced signal with the effect becoming more prominent as echo time increases thus leading to underestimations of  $T_2$ .

#### RF Pulse Imperfections

Some  $T_2$  mapping schemes involve long trains of successive RF pulses. These pulses need to be very accurate to ensure that the spin ensemble is evolving as expected however this is not possible for multiple reasons, including but not limited to, pulse profile imperfections [42],  $B_0$  inhomogeneities [43] and slice profile imperfections [44].

Upon the application of an imperfect 180° refocusing pulse, an ensemble of spins can be decomposed into three components, a transverse component that rephrases i.e. the desired behaviour, a transverse component that continues to de-phase and a longitudinal component with the proportion of the initial magnetisation in each component being dependent on the accuracy of the refocusing pulse. This splitting of magnetisation results in a reduced intensity echo.

### 3.1. Introduction

---

As subsequent refocusing pulses are applied, each of the split components can further split into three components resulting in large numbers of potential phase evolutions. Some of the possible phase evolutions will not form an echo between every refocusing pulse and as such the point at which the additional signal due to alternative paths will contribute to an echo in the train is difficult to predict.

The many potential paths a spin ensemble can take can be represented using Extended Phase Graphs (EPGs), an example of which is shown for four refocusing pulses in Figure 3.1. If all refocusing pulses were perfect, the magnetisation would remain on the red path forming an echo every time the path crosses the  $x$ -axis (blue circles). If imperfect refocusing pulses are applied, the magnetisation splits at the first refocusing pulse where a component follows the initial red path, another component continues to dephase in the transverse plane (green path) and another component is shifted to the longitudinal plane (blue path) and undergoes  $T_1$  relaxation. The example alternative path shown in blue does not contribute to the first echo but does contribute to the intensity of the second echo, the green path contributes to the intensity of the third echo.

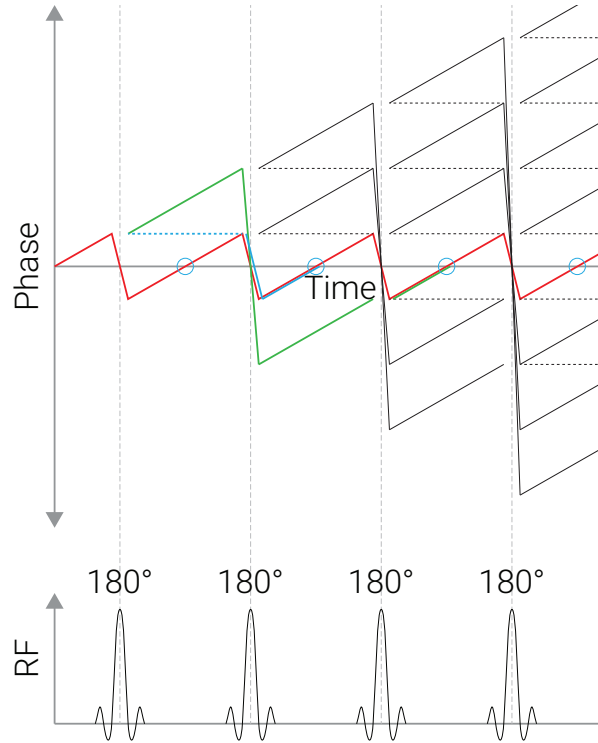


Figure 3.1: The EPG produced from four successive imperfect refocussing pulses. The simple path shown in red produces an echo every time it crosses the  $x$ -axis while the more complex paths shown in blue and green only contribute to the intensity of the second and third echoes respectively.

#### 3.1.3 $T_2$ Acquisition Schemes

Below the four methods to be compared in the context of renal imaging are outlined.

##### Spin Echo-Echo Planar Imaging

The Spin Echo (SE)-Echo Planar Imaging (EPI) technique is the simplest of the four methods, and so achievable on any MRI scanner, and consists of a  $90^\circ$  excitation pulse, followed by a  $180^\circ$  RF pulse Echo Time (TE)/2 ms later, leading to an echo at TE. The  $180^\circ$  pulse corrects for components of the signal lost due to static field inhomogeneities,  $T_2'$  effects, however does

### 3.1. Introduction

---

not correct for  $T_2$  effects. By repeating the sequence multiple times with a different TE, the  $T_2$  decay can be sampled. An EPI readout is used to sample the signal during the echo. The relatively long Repetition Time (TR) of this scheme means multiple slices can be sampled within a single TR. In this case, the acquisition of each echo time is divided into two packages with odd numbered slices being sampled in the first TR and even numbered slices being sampled in the second TR to avoid contamination across slices due to the width of the slice selected by the  $180^\circ$  refocussing pulse. An overview of the sequence is shown in Figure 3.2.

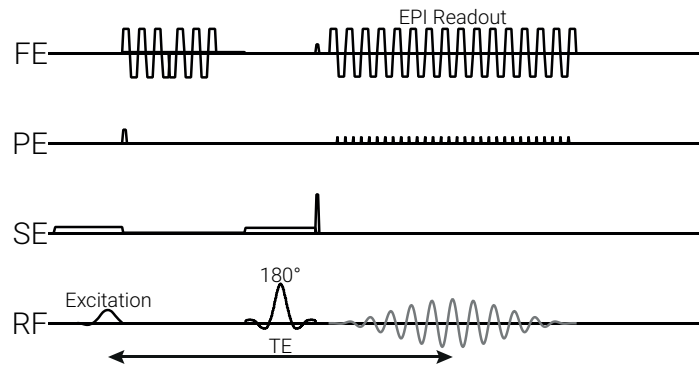


Figure 3.2: A pulse sequence diagram of the SE-EPI scheme. Data is collected by repeating the acquisition across repetitions with different echo times.

### Multi-Echo Turbo Spin Echo

The Multi-Echo Turbo Spin Echo (ME-TSE) sequence comprises a series of  $180^\circ$  pulses with an echo forming between each. Unlike in Section 2.3.3, where every echo was collecting a different line of  $k$ -space, here the same line of  $k$ -space is collected at a different TE. This allows the whole  $T_2$  decay to be sampled in a single echo train. Different echo times are sampled by varying the number and spacing of the  $180^\circ$  pulses, the number of echoes is limited by the Turbo Spin Echo (TSE) factor. If a TSE factor of twice the number of echoes is used, two lines of  $k$ -space can be collected per excitation, however this results in much longer echo trains and as such reduced Signal to Noise Ratio (SNR) and quantitative accuracy. By using a multi-slice acquisition, many slices can be acquired per TR, meaning that for the small number of slices usually imaged in the body and if TSE factor is equal to the number of echoes, the number of TRs required is simply the number of lines of  $k$ -space sampled. A schematic of the Pulse Sequence Diagram (PSD) can be seen in Figure 3.3.

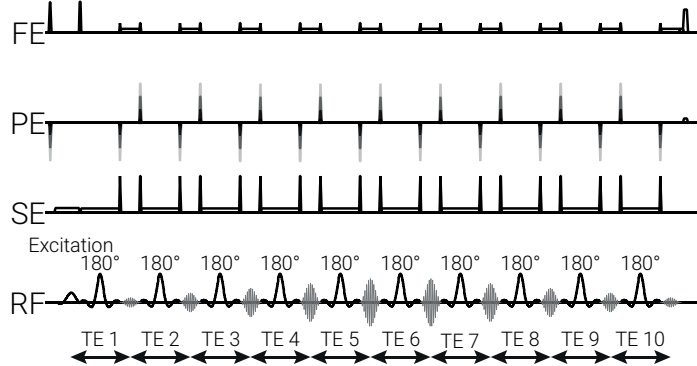


Figure 3.3: A pulse sequence diagram of the ME-TSE scheme for a given TR. If multiple lines of  $k$ -space are sampled per excitation, phase encode ‘blips’ will not be consistent over the echo train.

### 3.1. Introduction

---

#### Gradient Spin Echo

To achieve further acceleration over the Multi-Echo Turbo Spin Echo (ME-TSE) sequence, a GraSE sequence can be used. Here two gradient echoes are collected for every spin echo; the spin echo and gradient echo are used for the acquisition of the centre and periphery of  $k$ -space respectively. GraSE sequences tend to use shorted RF pulses and as such this enables a decrease in the echo spacing of the GraSE sequence compared to the ME-TSE sequence. The first echo of the train has an artificially high signal, however the short echo spacing of this technique means a startup echo can be sacrificed i.e. in this work the first echo is sampled at 11.2 ms (twice the echo spacing) rather than 5.6 ms. This leads to a more accurate fit, while also retaining accuracy when measuring short  $T_2$  signals that will quickly decay. The PSD for the GraSE acquisition is shown in Figure 3.4.

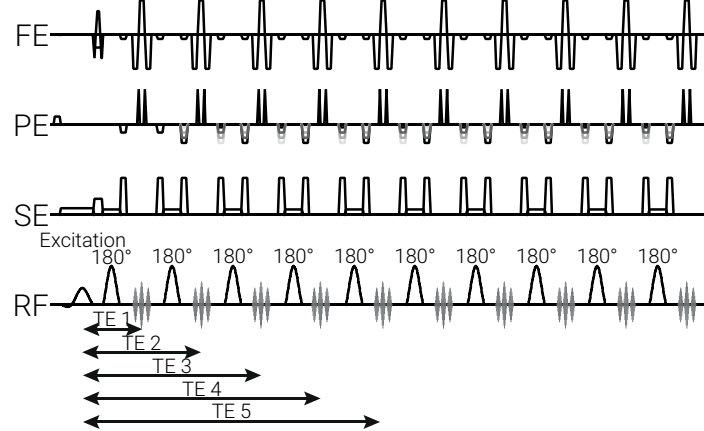


Figure 3.4: A pulse sequence diagram of the GraSE scheme.

### 3.1. Introduction

---

#### CPMG $T_2$ Preparation

As in the other sequences, the CPMG sequence begins with a  $90^\circ$  excitation pulse to transfer the magnetisation into the transverse plane. Carr and Purcell showed that a series of  $180^\circ$  pulses of alternating phase could be used to reduce the effects of molecular diffusion [41]. This technique relies on very accurate  $180^\circ$  pulses as small imperfections could result in large cumulative errors over the length of the pulse train. Later Meiboom and Gill showed that by delivering the  $180^\circ$  pulses  $90^\circ$  out of phase to the initial excitation pulse e.g. excite about  $x'$  and refocus about  $y'$ , the undesirable effects of imperfect  $180^\circ$  pulses and  $B_1$  inhomogeneity could be greatly reduced [45]. The resulting sequence, known as a Carr-Purcell-Meiboom-Gill (CPMG) sequence, can be used to generate robust measurements of  $T_2$ ; by varying the number and temporal spacing,  $\tau_{\text{CPMG}}$ , of the  $180^\circ$  pulses the degree of  $T_2$  weighting can be modulated to achieve different Effective Echo Time (eTE). This sequence is not widely available and as such has been coded for the Philips platform specifically for this work. Here an EPI readout scheme is then used to sample the signal. An overview of this sequence is shown in Figure 3.5.

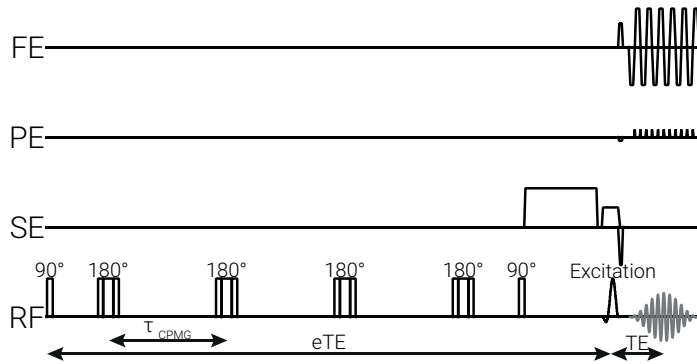


Figure 3.5: A pulse sequence diagram of the CPMG  $T_2$  preparation scheme. This example is shown for four CPMG refocusing pulses, to achieve a longer eTE the number of refocusing pulses is increased.

### 3.1. Introduction

---

#### Multi-Echo Spin-Echo

In addition to the four techniques above which can be applied in the required time frame for in-vivo measurements, a Multi-Echo Spin-Echo scheme was used to evaluate the quantitative accuracy of the phantom. This scheme is recommended by National Institute of Standards and Technology (NIST) for use with their phantom to validate scanner hardware. It is however, impractical to implement in-vivo due to its very long acquisition time (16 minutes for a single slice). The sequence is similar to the ME-TSE sequence, however, no fast imaging techniques are employed to achieve maximum SNR, additionally, this sequence can only ever collect one line of  $k$ -space per excitation. A PSD for this scheme is shown in Figure 3.6.

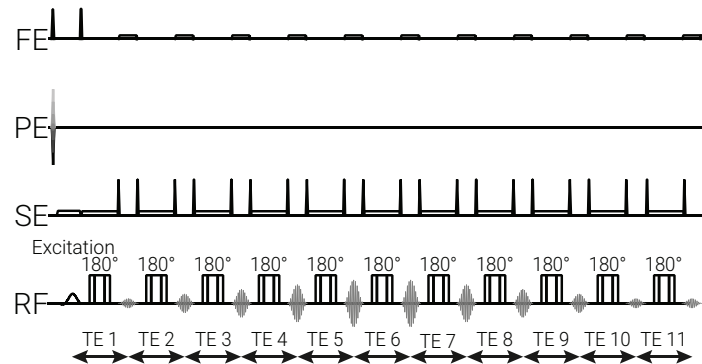


Figure 3.6: A pulse sequence diagram of the Multi-Echo Spin-Echo scheme.

## 3.2 Methods

### 3.2.1 Phantom Data Acquisition

All data was acquired on a 3T Philips Ingenia system (Philips Medical Systems, Best, The Netherlands). The 14 element  $T_2$  array of a QalibreMD System Standard Model 130 contains spheres doped with varying concentrations of  $MnCl_2$  to modulate  $T_2$  between 5 ms and 650 ms, Figure 3.7a. This array was used to compare the accuracy of  $T_2$  measurements to a known ground truth. Additionally, a square grid etched into the plastic of the phantom was used to assess the degree of image blurring.

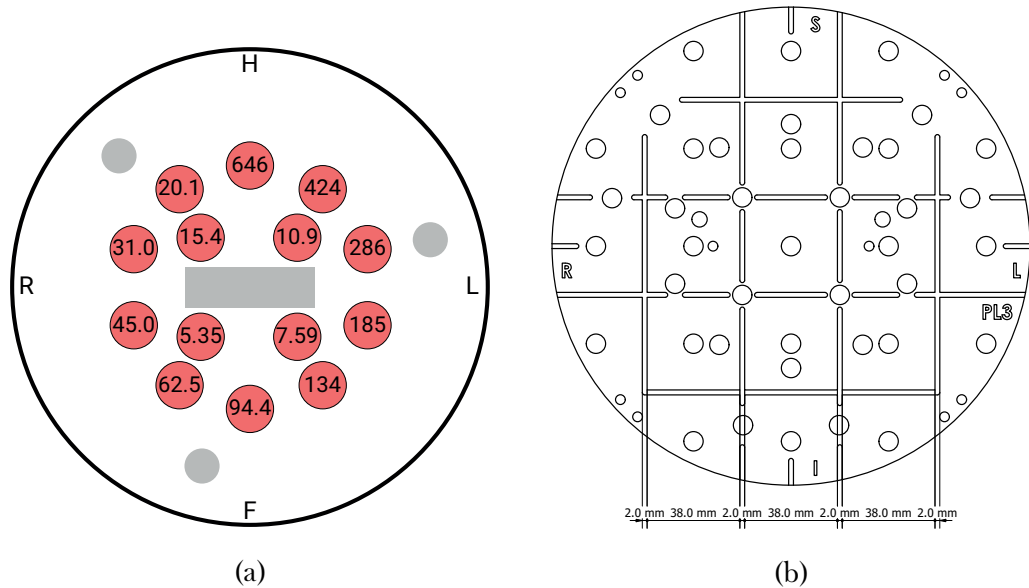


Figure 3.7: (a) A schematic of the  $T_2$  spheres in the QalibreMD phantom showing the 14 element  $T_2$  array and each of the  $T_2$  values (in ms). (b) A scale drawing of plate three of the QalibreMD system phantom. The grid etched into this plate was used to assess the blurring of each  $T_2$  mapping sequence.

The kidneys are highly perfused organs, as such, the effects of fluid flow through the area being imaged should be evaluated. This was achieved using a Gold Standard Phantoms Quantitative Arterial Spin Labelling Perfusion Reference (QASPER) phantom. This phantom comprises of a

### 3.2. Methods

---

MRI compatible pump with adjustable, continuous, flow rates from 0  $\text{mL}/\text{min}$  to 350  $\text{mL}/\text{min}$ . The perfusate exits the pump into a series of simulated arterioles before entering a cylinder of porous media designed to simulate a capillary bed. Having travelled through the porous media, the perfusate exits at the centre of the cylinder and is returned to the pump, Figure 3.8.

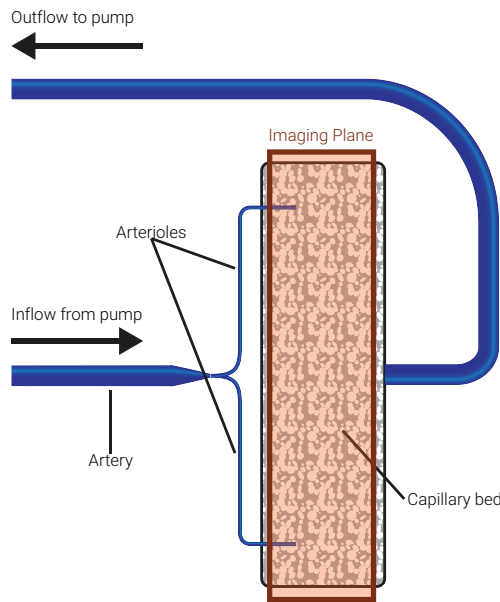


Figure 3.8: A schematic of the QASPER phantom used to quantify the effects of flow upon the  $T_2$  measurements.

Both the QalibreMD and QASPER phantoms were scanned using a 32-channel head coil.

#### 3.2.2 In-Vivo Data Acquisition

All data acquired on human subjects was with approval of the local ethics committee and the study was conducted in accordance with the Helsinki Declaration. The subjects gave written, informed consent. Humans were scanned using a 16-channel anterior coil array and 16-channel posterior coil array. The final in-vivo comparison dataset consisted of 5 healthy participants (2 female, 3 male, mean age  $31 \pm 8$  years).

### **3.2. Methods**

---

The final protocol comprised a survey, localisers, dual-echo gradient echo  $B_0$  map and Dual Refocusing Echo Acquisition Mode (DREAM)  $B_1$  map [46], and each of the optimised  $T_2$  mapping sequences. Subjects also had  $T_2$ -weighted and  $T_1$ -weighted structural scans collected to enable segmentation of the whole kidneys, and cortex/medulla respectively [47, 48], see Chapter 5. These Region Of Interest (ROI) were then used to calculate the mean  $T_2$  of each tissue type.

#### **3.2.3 $T_2$ Mapping Protocols**

A summary of the acquisition parameters of each  $T_2$  mapping sequence is shown in Table 3.2. In-vivo respiratory motion was counteracted via use of respiratory triggering. Each protocol was designed to be approximately 2-3 minutes (although this will increase when respiratory triggering is used for in-vivo acquisitions) and have matched key parameters such as voxel size and Field Of View (FOV). More accurate or higher resolution  $T_2$  mapping may be possible with longer acquisition times, however as the aim is for this sequence to be used as part of a multiparametric renal protocol, the time constraints of the whole protocol must be considered.

### 3.2. Methods

	Spin Echo - Echo Planar Imaging	Multi-Echo Turbo Spin Echo	Gradient Spin Echo	CPMG $T_2$ Pre- paration - Echo Planar Imaging
Abbreviation	SE-EPI	ME-TSE	GraSE	CPMG $T_2$ Prep
TE (min:step:max) (ms)	20:10:70	13:13:130	11.2:5.6:173.3	0:20:160
Number of echoes	6	10	30	9
Startup echoes	N/A	0	1	N/A
TR (ms)	5000	3000	3000	3000
Acquisition Voxel Size (mm <sup>3</sup> )	$3 \times 3 \times 5$	$3 \times 3 \times 5$	$3 \times 3 \times 5$	$3 \times 5.65 \times 5$
Reconstruction Voxel Size (mm <sup>3</sup> )	$3 \times 3 \times 5$	$3 \times 3 \times 5$	$3 \times 3 \times 5$	$3 \times 3 \times 5$
FoV (mm <sup>3</sup> )	$288 \times 288 \times 25$	$288 \times 288 \times 25$	$288 \times 288 \times 25$	$288 \times 288 \times 25$
Signal Averages	2	1	1	1
Packages	1	1	2	1
Acquisition Mode	Multi Slice	Multi Slice	Multi Slice	Multiple 2D
Fast Imaging Mode	EPI	TSE	GraSE	TFEPI
Flip Angle	90°	90°	90°	90°
Bandwidth (Hz)	40 (Phase), 1787 (Freq)	180	405 (Phase), 2268 (Freq)	113 (Phase), 2845 (Freq)
SENSE	2.55	2.55	2.55	3
Halfscan	0.838	No	No	0.706
TSE Factor	N/A	10	30	N/A
EPI Factor	37	N/A	3	17
Respiratory Compensation	Triggered	Triggered	Triggered	Triggered
Acquisition Time (before respiratory compensation)	1 min 45 sec	1 min 57 sec	2 min 6 sec	2 min 23 sec

Table 3.2: A summary of the acquisition parameters of each of the  $T_2$  mapping methods compared. SE-EPI, ME-TSE and GraSE are standard vendor sequences, whilst the CPMG  $T_2$  prep sequence has been coded specially.

#### 3.2.4 Post Processing

All post processing was performed using Python 3.7 making use of the United Kingdom Renal Imaging Network (UKRIN) Kidney Analysis Toolbox (UKAT) [49, 50]. This open source software is specially designed for quantitative renal MRI. All curve fitting uses a least squares trust region

### 3.2. Methods

---

reflective method to estimate unknown parameters.

#### **$T_2$ Fitting Methods**

The data were fit using a mono-exponential model. Since there are multiple models for fitting noisy data, each of these was evaluated and is illustrated in Figure 3.9.

The “basic fit” simply takes the signal from each voxel at each TE and fits to a monoexponential decay

$$S(t) = S_0 \cdot e^{-t/T_2}. \quad (3.1)$$

If no noise was present in the data and the sample was a single pure substance i.e. does not exhibit partial voluming effects, this would be the optimum method however, the decreased SNR of later TEs often leads to inaccurate fits. To combat this, the data can be fit to

$$S(t) = S_0 \cdot e^{-t/T_2} + \epsilon, \quad (3.2)$$

where  $\epsilon$  represents thermal noise and a baseline in the signal due to long  $T_2$  compartments; this fitting method is referred to as “noise fit”. This method is implemented in the software written by NIST and distributed with the QalibreMD phantom. Another common method of negating the effects of the low SNR of later TE is to discard data below a threshold, illustrated in Figure 3.9 at 0.2 AU and referred to as “discard fit”. Finally, a combination of both noise estimation and discarding can be performed (“discard and noise fit”). All four of these fitting methods will be compared.

### 3.2. Methods

---

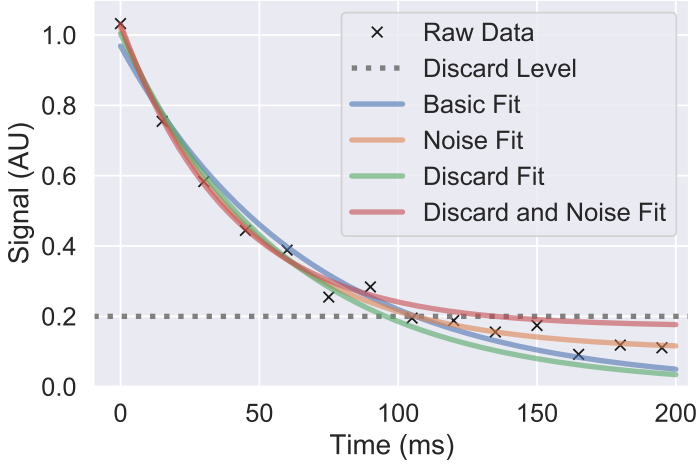


Figure 3.9: The four fitting methods used to estimate  $T_2$  of simulated data shown here with  $T_2 = 50$  ms and mean SNR=23. Simulated data is used here only for illustration, all evaluations of fitting methods were performed on true data collected from the QalibreMD phantom.

These fitting methods can either be applied on a voxel-by-voxel basis to generate spatial maps or, the signal from all voxels in an ROI with a single  $T_2$  can be averaged at each TE with parameters being fit to the subsequent mean signal.

#### 3.2.5 Assessment of Data

##### Quantifying Accuracy

Using the QalibreMD phantom, the quantitative accuracy of each of the sequences was assessed. A voxel-by-voxel  $T_2$  map was calculated for each sequence, ROIs were then defined for each of the spheres in the  $T_2$  array, Figure 3.10, and the mean  $T_2$  within each sphere calculated. The estimated values of  $T_2$  were compared to the ground truth literature values and their discrepancy assessed over both the full range of  $T_2$  values in the array (5 ms – 650 ms) and the range of  $T_2$  reported in the kidneys (40 ms – 200 ms) [40]. Accuracy was summarised over these ranges using Mean Percentage

### 3.2. Methods

---

Error (MPE) defined as

$$\text{MPE} = \frac{1}{N} \sum_n^{i=1} \left| \frac{t_{2i}^{\text{ground truth}} - t_{2i}^{\text{estimate}}}{t_{2i}^{\text{ground truth}}} \right| \cdot 100. \quad (3.3)$$

In addition to the four protocols that can be applied in-vivo, the NIST recommended ME-SE scheme was also used to validate that the  $T_2$  values of the phantom used in this study were in agreement with the literature values.

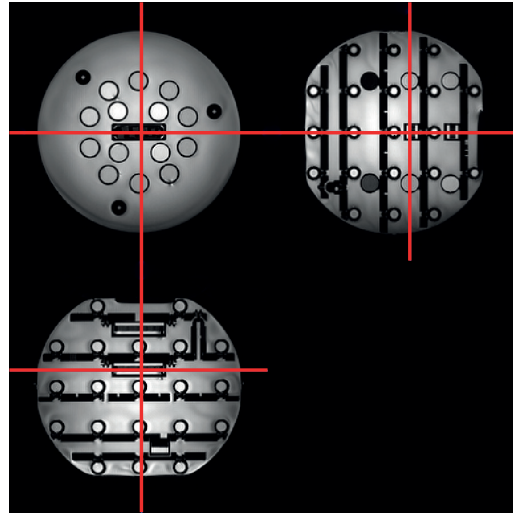


Figure 3.10: The  $T_2$  spheres inside the QalibreMD phantom.

### Effects of Flow

To investigate the effects of flow upon  $T_2$  measurements, the QASPER phantom was used. The porous media was imaged using each sequence over the full range of flow rates the phantoms pump can deliver.  $T_2$  maps are calculated and the mean  $T_2$  calculated to evaluate the robustness of each sequence to variations in perfusion.

### Blurring

The amount of blurring of an image is different for each sequence and can dramatically effect the readability of an image and ultimately its clinical utility. In MRI the amount and characteristics of the blur is usually spatially invariant, that is to say, if a voxel in the centre of an image is blurred over its five neighbouring voxels in the phase encode direction, a voxel at the edge of the image would also be blurred over its five neighbouring voxels. The degree of blurring produced by each of the sequences outlined in Section 3.2.3 was quantified.

The observed image,  $h$ , can be modelled as an ideal, unblurred signal,  $f$  distorted by a filter,  $g$ , Figure 3.11. This distorting filter is known as the Point Spread Function (PSF) and is the theoretical signal produced when imaging an infinitely small point source object or, in practice, the blurring observed in the imaging system when an object much smaller than the systems resolving power is imaged. In a spatially invariant system, such as MRI, the recorded signal is simply a convolution of the true signal and the PSF i.e.  $f * g = h$ . By fitting a Gaussian to the PSF the degree of blurring in the image can be quantified [51, 52].

$$f * g = h$$

Figure 3.11: The convolution of the ideal signal,  $f$ , and the PSF,  $g$ , produces the measured signal,  $h$ .

A 3 mm deep, 2 mm thick, grid etched into one of the plastic plates of the QalibreMD phantom, Figure 3.7b, was imaged using each of the  $T_2$  mapping methods with an echo time of 20 ms. A  $0.5 \text{ mm}^3$  isotropic structural scan was also collected. The thickness of the grid is smaller than the imaging resolution of the  $T_2$  mapping sequences and the resolution of the structural scan is much

### 3.2. Methods

---

greater than the resolution of the  $T_2$  mapping scans, therefore the structural scan can be seen as an approximation of the ideal image produced by each  $T_2$  mapping method. As shown in Figure 3.12, this allows a deconvolution of the PSF from the  $T_2$  mapping scans and, by fitting a Gaussian to the line profiles through the centre of the PSF in each direction (indicated by the blue and orange dashed lines on the estimated PSF), an estimate of the Full Width Half Maximum (FWHM) of the PSF. Quoted values are the maximum PSF of each of the in-plane directions as this is the limiting factor in the readability of an image, for the example in Figure 3.12, the quoted PSF would be  $9.5 \pm 0.2$  mm.

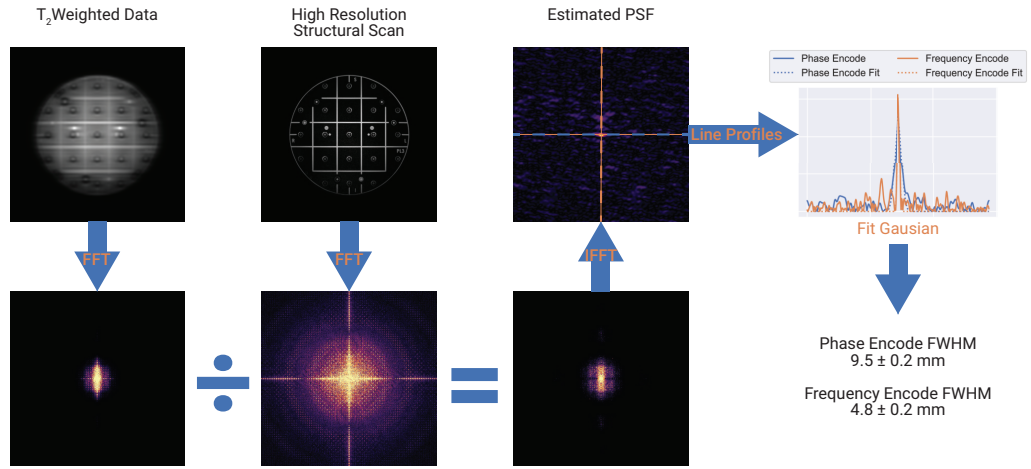


Figure 3.12: An overview of the estimation of the PSF. For this illustration the  $T_2$ -weighted data has had additional blur added to make the effect of each processing step clearer.

### In-Vivo

Using the  $T_1$ -weighted structural scans ROI were defined for both the renal cortex and medulla of each subject. These ROI were then used to calculate the mean and standard deviation  $T_2$  for each tissue type of each subject. Histogram analysis was also performed to interrogate the distribution of  $T_2$  within each tissue.  $T_2$  maps were qualitatively assessed for their readability.

## 3.3 Results

### 3.3.1 Verification of Phantom Accuracy

To ascertain the accuracy of the scanner and QalibreMD phantom, the NIST recommended ME-SE protocol was first performed. This verifies that the phantom has been manufactured correctly, that the scanner produces acceptable results when running a standardised protocol and provides context to the accuracies of the in-vivo sequences i.e. understanding how much accuracy has been sacrificed to make the protocol practical for renal imaging. Fitting is shown using the basic fit as this resulted in the closest fit to literature values, however all fitting methods were evaluated, with results included in Appendix A.1. The only noteworthy variances between fitting methods was observed for the spheres of very short  $T_2$ .

When comparing the  $T_2$  calculated to the literature values supplied with the phantom, Figure 3.13, the MPE over the full range of spheres was  $-5 \pm 7\%$ , and over the range of  $T_2$  expected in the kidneys was  $-6 \pm 3\%$  where values are expressed as mean percentage error over the range of spheres  $\pm$  the standard deviation in percentage error over the range of spheres.

### 3.3. Results

---

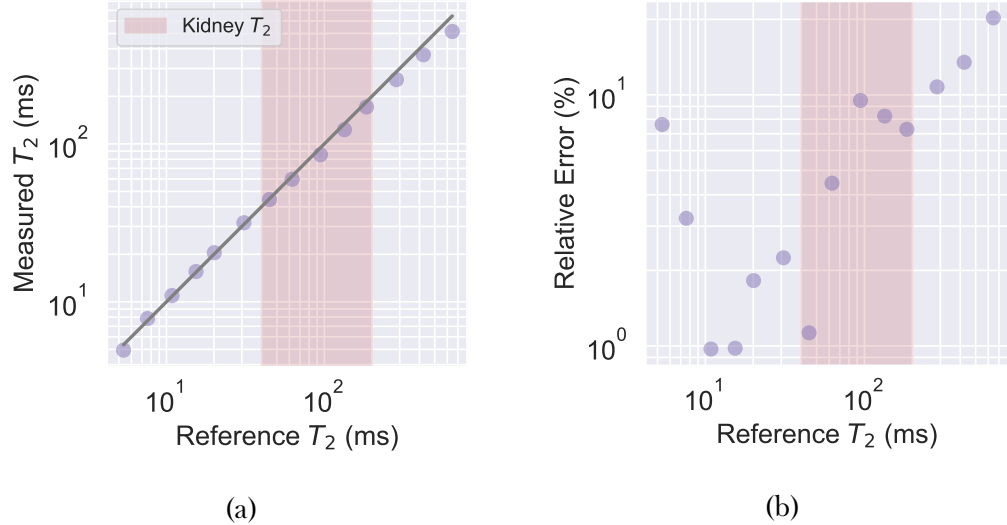


Figure 3.13:  $T_2$  measured using the standardised NIST protocol compared to the reference  $T_2$  from the manufacturer. (a) shows the correlation and (b) shows the relative error between these values.

#### 3.3.2 Fitting Methods

Each fitting method was tested using data acquired on the QalibreMD phantom and in-vivo. A full breakdown of the accuracy of each fitting method, applied to each sequence, over different ranges of  $T_2$  can be seen in Table 3.3 and Figure 3.14. Figures showing the accuracy and MPE of each sequence and fitting method are included in Appendix A.2. The QalibreMD analysis software for the phantom calculates the mean signal from each sphere then fits this to a  $T_2$  decay, resulting in a quicker and more accurate measurement of the homogeneous  $T_2$  of each sphere [53]. Due to the heterogeneity within the kidneys, this method could not be applied in-vivo and as such, the accuracy of the sequences and fitting methods was evaluated by performing a voxel-by-voxel fit, then calculating the mean  $T_2$  from an ROI of each sphere in the resulting map.

### 3.3. Results

$T_2$ Range	MPE (5 ms – 650 ms) (%)				MPE (40 ms – 200 ms) (%)			
	Basic	Noise	Discard	Discard and Noise	Basic	Noise	Discard	Discard and Noise
SE-EPI	36 ± 34	202 ± 437	33 ± 34	238 ± 463	8 ± 5	32 ± 42	22 ± 8	31 ± 42
ME-TSE	38 ± 31	13 ± 16	41 ± 35	35 ± 36	23 ± 13	14 ± 3	15 ± 13	13 ± 4
GraSE	32 ± 29	23 ± 27	26 ± 28	33 ± 37	15 ± 4	11 ± 5	13 ± 4	9 ± 7
CPMG $T_2$ Prep	18 ± 15	30 ± 53	20 ± 18	28 ± 28	11 ± 1	8 ± 5	11 ± 1	6 ± 5
Mean over sequences	31 ± 8	67 ± 90	30 ± 9	83 ± 103	14 ± 7	16 ± 11	14 ± 36	15 ± 11

Table 3.3: MPE when measuring  $T_2$  of the QalibreMD phantom over different ranges using each sequence and fitting method. 5 ms – 650 ms is the full range of  $T_2$  available in the phantom and 40 ms – 200 ms is the range of  $T_2$  reported in the kidneys. Values are expressed as mean percentage error of the spheres within the specified range of  $T_2$  ± the standard deviation of percentage error over the spheres within the specified range of  $T_2$ .

### 3.3. Results

---

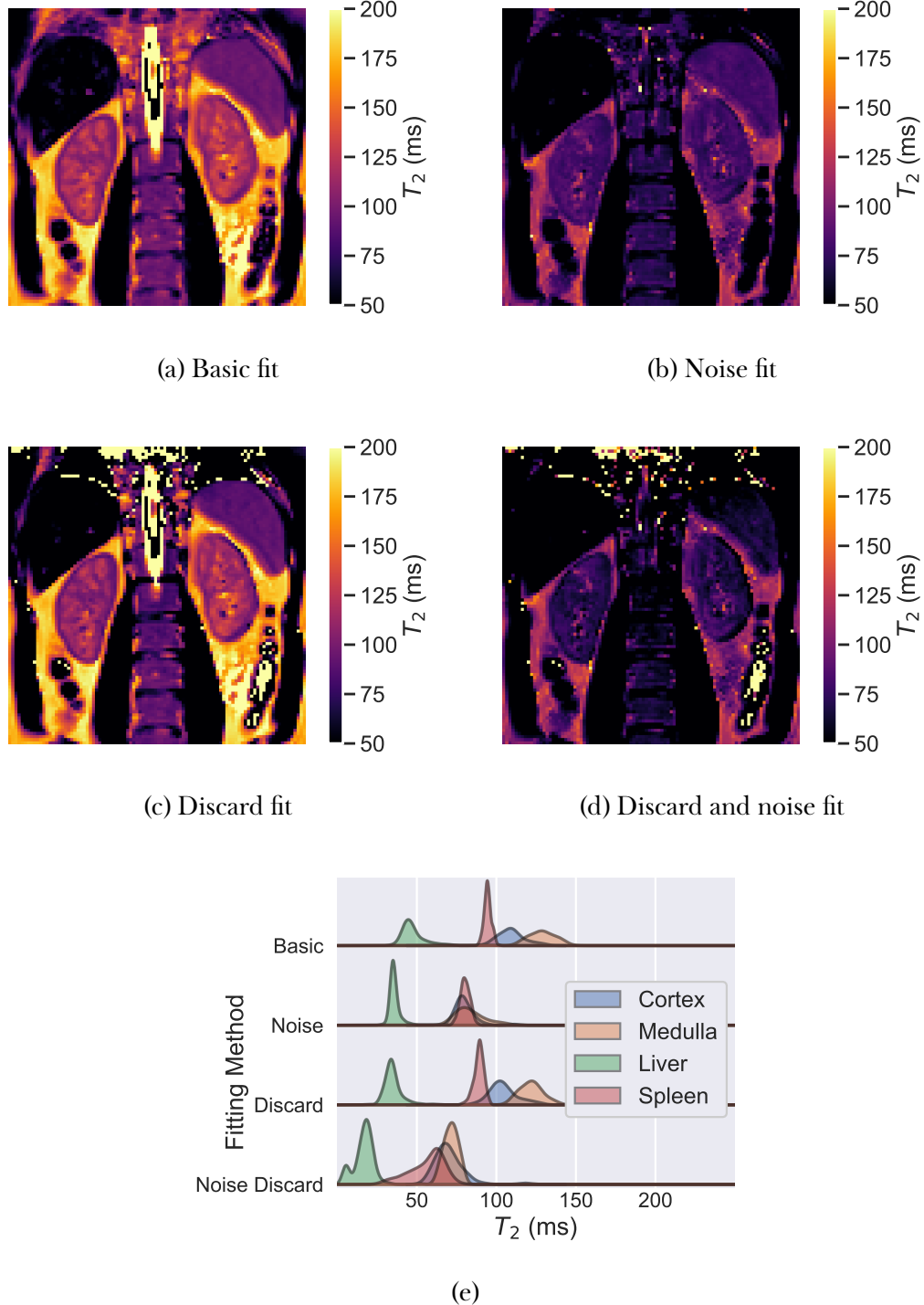


Figure 3.14: (a-d)  $T_2$  maps generated using each of the fitting methods for the GraSE sequence and (e) histograms of  $T_2$  values within the renal cortex, renal medulla, liver and spleen. The reduction in longer  $T_2$  values when fit with a noise term observed in the phantom can be seen here in the large decrease in  $T_2$  of the kidneys, while the spleen and liver only decrease a small amount. Discarding has relatively little effect on the kidneys but does slightly increase the variance in  $T_2$  within each ROI.

### 3.3. Results

---

The noise fit results in an increase in accuracy compared to the basic fit when measuring the  $T_2$  of the shortest  $T_2$  spheres, especially for sequences with a short echo spacing where the majority of echoes in the signal are after the sphere has fully relaxed back to its baseline noise level. This increase in accuracy for short  $T_2$  is at the expense of the accuracy of the long  $T_2$  spheres. The combination of decreased dynamic range and an extra parameter to optimise resulted in an inaccurate characterisation of these spheres, especially of the SE-EPI sequence due to the short final echo time and thus lower dynamic range. This can be observed in Figure 3.14e where the variance in  $T_2$  within the liver is decreased when using the noise fit compared to the basic fit, however the variance of the longer  $T_2$  values in the kidneys has increased. In the range of  $T_2$  reported in the kidney, the noise fit increased the average error over the four sequences.

The discard fit requires an empirical threshold to be chosen. If chosen correctly, this results in a slightly improved accuracy however, if the threshold was not correctly chosen the accuracy of  $T_2$  was compromised. While optimising the threshold is trivial when the known reference values are available, this is more difficult in-vivo and therefore, given the increase in accuracy was marginal and only effected spheres of short  $T_2$ , consistent results were deemed preferable. The combination of discard and noise fit resulted in a decreased accuracy from the basic fit. Spheres that benefited from the additional noise term relax to their baseline noise quickly, however by discarding these echoes, the estimate of noise becomes inaccurate and thus so does the estimate of  $T_2$ . It was therefore concluded that a basic fit should be used for all subsequent renal data.

#### 3.3.3 Phantom Verification

##### Accuracy

Each sequence was used to image the  $T_2$  array in the QalibreMD phantom. Figure 3.15 shows the measured  $T_2$  plot against the reference  $T_2$  for each method. All methods struggle to accurately measure the very short  $T_2$  spheres in the array, with the CPMG  $T_2$  prep method performing best. The SE-EPI method overestimates short  $T_2$  spheres due to the first TE being sampled at 20 ms but is also underestimating long  $T_2$  because of its small range in TE. When considering only the spheres with physiologically similar  $T_2$  to the kidneys, the SE-EPI method is the most accurate with the GraSE and CPMG  $T_2$  prep delivering similar results. This is mirrored by the MPE shown in Table 3.4. Example  $T_2$  maps of the phantoms  $T_2$  array imaged with each sequence are shown in Figure 3.16.

### 3.3. Results

---

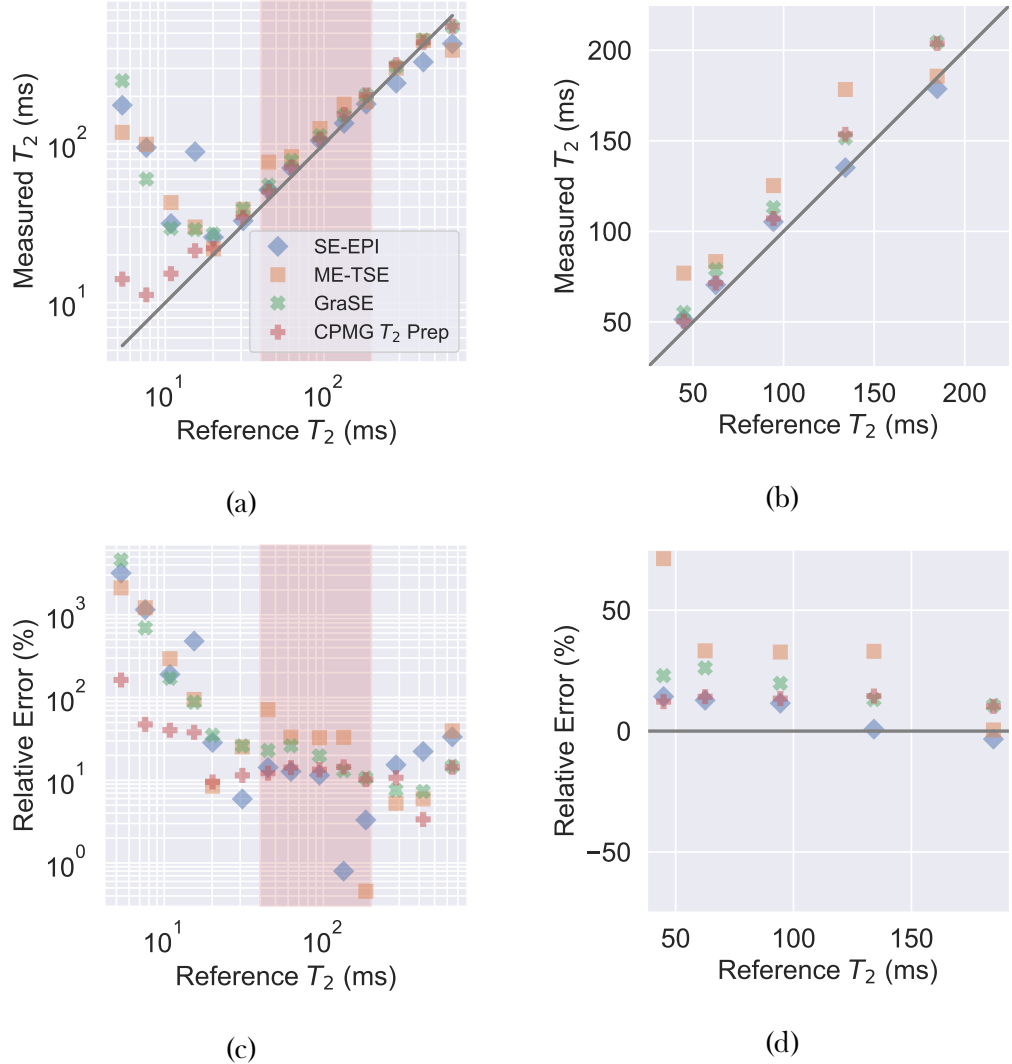


Figure 3.15:  $T_2$  measured using each acquisition method compared to the reference  $T_2$  from literature. (a) The full range of  $T_2$  spheres is shown on logarithmic axis with the range of  $T_2$  reported in the kidneys shaded in red (b) The spheres with  $T_2$  in the range of the kidneys are shown on linear axis. (c) and (d) show the relative error of each sphere for the full and renal range of spheres respectively.

### 3.3. Results

---

Acquisition Method	MPE (5 ms – 650 ms) (%)	MPE (40 ms – 200 ms) (%)
SE-EPI	$36 \pm 34$	$8 \pm 5$
ME-TSE	$38 \pm 31$	$23 \pm 13$
GraSE	$32 \pm 29$	$15 \pm 4$
CPMG $T_2$ Prep	$18 \pm 15$	$11 \pm 1$

Table 3.4: MPE when measuring  $T_2$  of the QalibreMD phantom over different ranges using each sequence. 5 ms – 650 ms is the full range of  $T_2$  available in the phantom and 40 ms – 200 ms is the range of  $T_2$  expected in the kidneys. Values are expressed as mean percentage error of the spheres within the specified range of  $T_2 \pm$  the standard deviation of percentage error over the spheres within the specified range of  $T_2$ .

### 3.3. Results

---

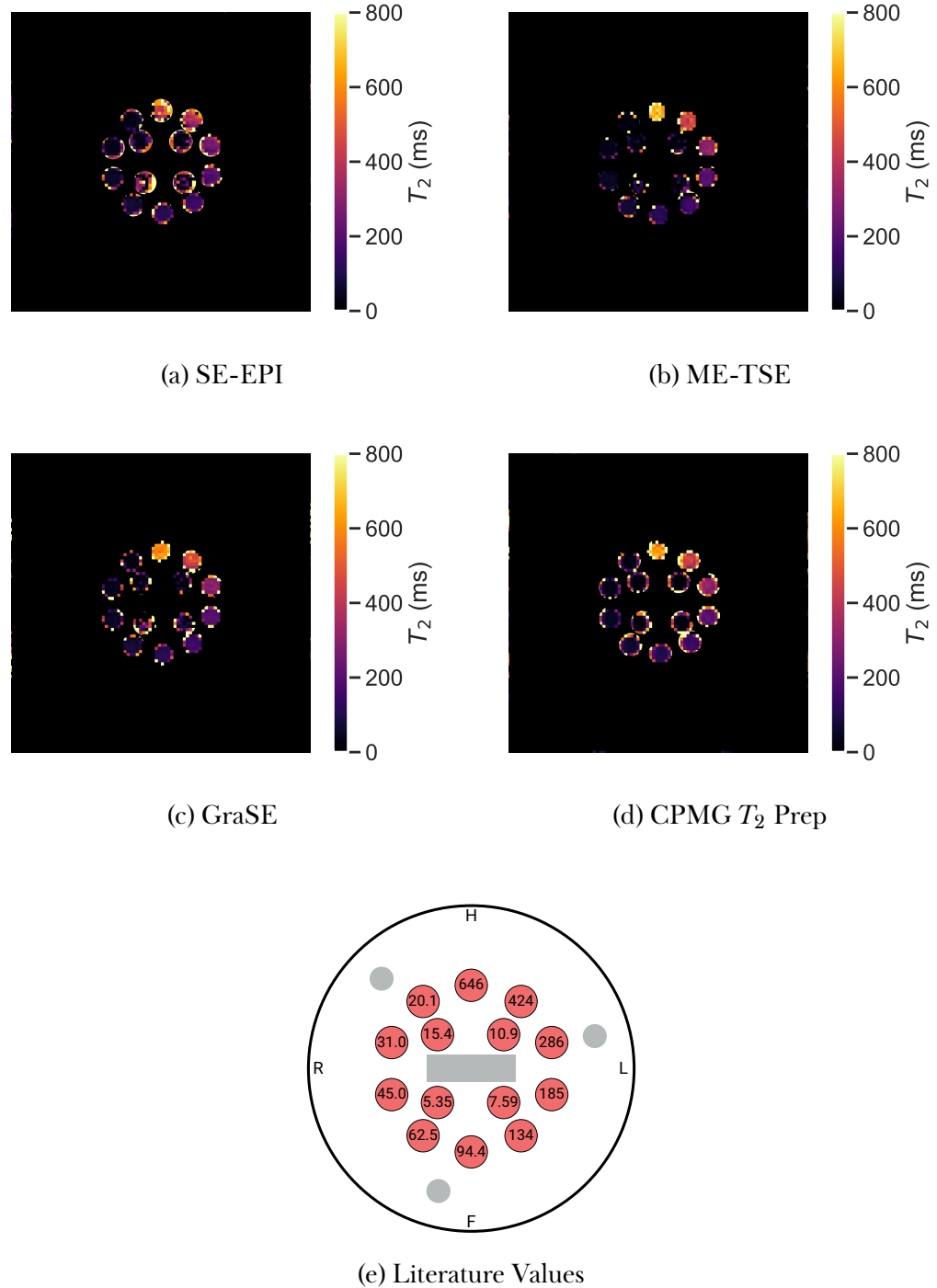


Figure 3.16:  $T_2$  maps of the QaliberMD system phantom  $T_2$  array generated using each sequence.

### 3.3. Results

---

#### Sensitivity to Flow

To assess the sensitivity of each of the  $T_2$  mapping schemes to flow, the simulated capillary bed of the flow phantom was imaged with the perfusate pumped at rates from 0 to 350 ml/min. The absolute change in measured  $T_2$  is shown in Figure 3.17a and the change in  $T_2$  as a percentage of  $T_2$  measured when the pump was turned off is shown in Figure 3.17b. The  $T_2$  of the perfusate is relatively long and as such the inaccuracies measuring long  $T_2$  observed in the static phantom (Figure 3.15a and Figure 3.15c) manifest themselves here. This causes a large range in  $T_2$  even when the pump is turned off. In Figure 3.17b the SE-EPI sequence can be seen to be most sensitive to perfusion due to its largest deviation as flow rate increased, the GraSE sequence produced the minimum proportional change in  $T_2$  as the rate perfusate was pumped through the capillary bed was increased.

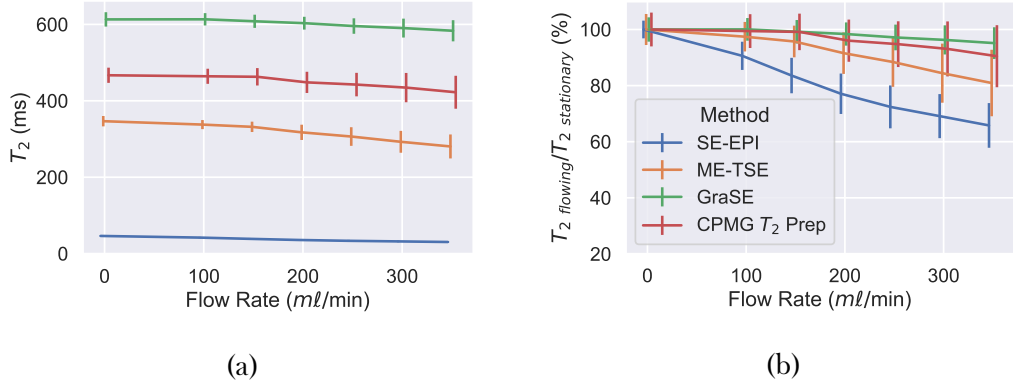


Figure 3.17: The effects of flow on measurements of  $T_2$  using each method. Points have been slightly staggered on the  $x$ -axis to aide the visibility of error bars. (a) Absolute measured  $T_2$ . (b) Change in  $T_2$  as a percentage of  $T_2$  measured at rest for each sequence. Error bars are derived from the standard deviation within the ROI.

The flow rate is measured at the pump, therefore the perfusate will not be travelling at the reported rate through the capillary bed. To quantify the movement of the perfusate using techniques widely available in the kidneys, Apparent Diffusion Coefficient (ADC) maps of the capillary bed were

### 3.3. Results

---

calculated at each flow rate. More information on ADC mapping is given in Sections 2.2.4 and 6.2.5. The protocol used here was a monopolar SE-EPI scheme with fixed diffusion time i.e. different b-values were achieved solely by modulating the gradient strength. b-values acquired were 0, 5, 15, 30, 45, 60, 75, 400 and 600 s/mm<sup>2</sup>. Using this scheme, ADC in the capillary bed with different perfusate flow rates was calculated, Figure 3.18.

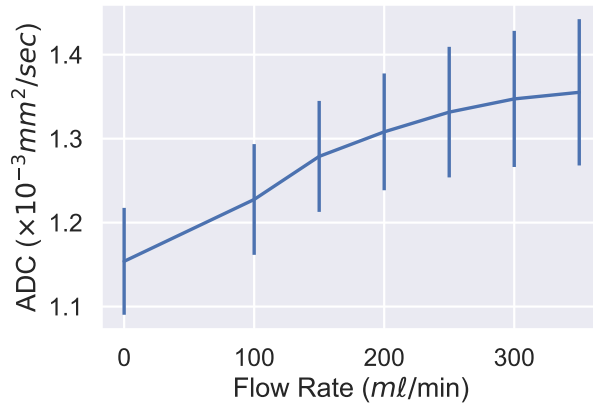


Figure 3.18: Changes in ADC as the rate at which perfusate is pumped through the simulated capillary bed is increased. Error bars are derived from the standard deviation within the ROI.

### Image Blurring

Each sequence was slightly modified to contain an acquisition with a TE of 20 ms to ensure a constant  $T_2$  weighting across techniques and this was used to image the orthogonal grid in the QalibreMD phantom, Figure 3.7b. A high-resolution structural scan was then used to deconvolve an estimate of the PSF from each of the  $T_2$ -weighted images allowing the FWHM to be estimated, Table 3.5. Examples of the central slice of the grid imaged with each method are shown in Figure 3.19.

### 3.3. Results

---

Acquisition Method	PSF FWHM (mm)
SE-EPI	$4.80 \pm 0.18$
ME-TSE	$4.20 \pm 0.14$
GraSE	$4.26 \pm 0.12$
CPMG $T_2$ Prep	$6.48 \pm 0.33$

Table 3.5: The FWHM of the estimated PSF for each acquisition method. Uncertainty is calculated from the confidence in the Gaussian fit.

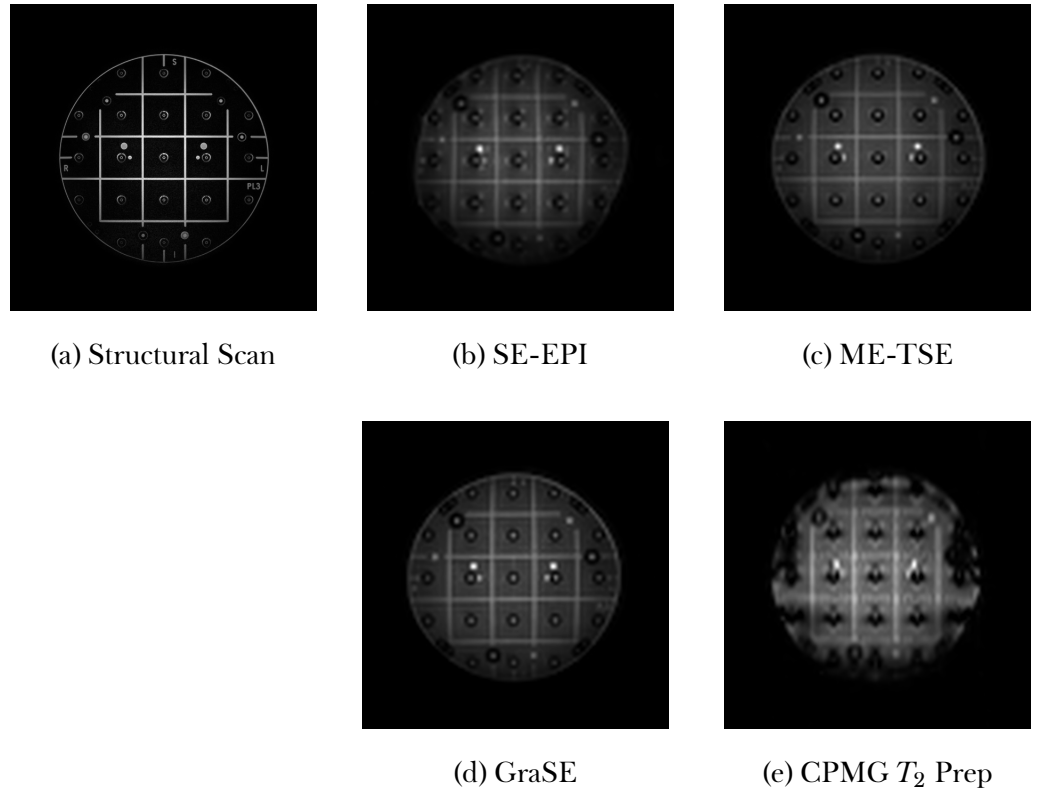


Figure 3.19: Examples of the orthogonal grid imaged with a TE of 20 ms using each  $T_2$  mapping sequence and the high-resolution structural scan used as the gold standard to deconvolve from each  $T_2$ -weighted scan.

Both the SE-EPI and CPMG  $T_2$  prep EPI sequences suffer from significant image distortions due to their EPI readout with the ME-TSE and GraSE both producing similar image quality and a comparable width of PSF.

### 3.3. Results

#### 3.3.4 Summary of Evaluation of $T_2$ Mapping Sequences on Phantoms

The phantom evaluation of each sequence is summarised in Figure 3.20. This figure combines the quantitative accuracy of  $T_2$  within the range of the kidneys, the sensitivity to fluid motion and blurring characteristics of each sequence. The GraSE and CPMG  $T_2$  prep sequences produce the most accurate results, however the GraSE has a much smaller PSF.

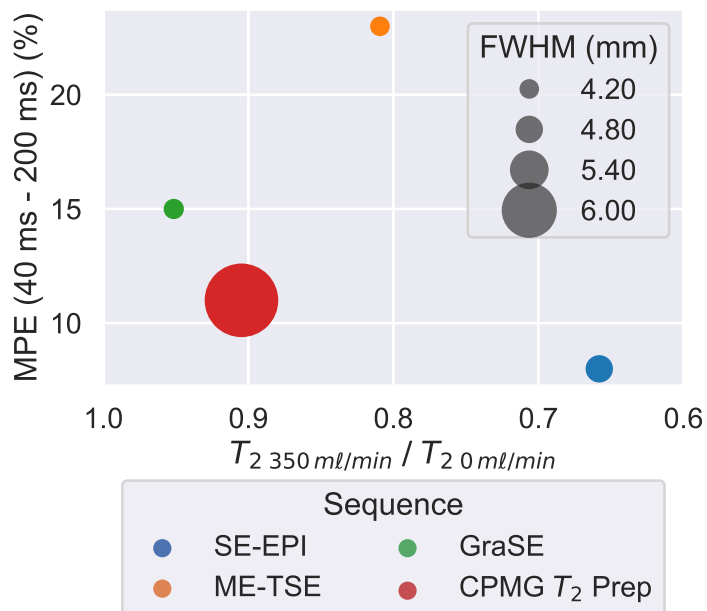


Figure 3.20: A summary of the quantitative accuracy, sensitivity to flow and degree of blurring observed for each  $T_2$  mapping sequence when evaluated on phantoms.

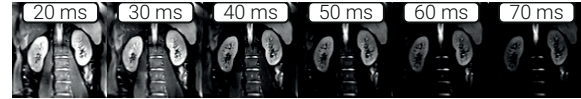
#### 3.3.5 In-Vivo

Having assessed each of the sequences, five healthy volunteers were then imaged using all four methods. Example in-vivo multi echo data and resulting  $T_2$  maps are shown in Figures 3.21 and 3.22 respectively. The measured  $T_2$  using the SE-EPI method is much lower than that measured using the other three methods. The GraSE scheme shows the largest contrast between cortex

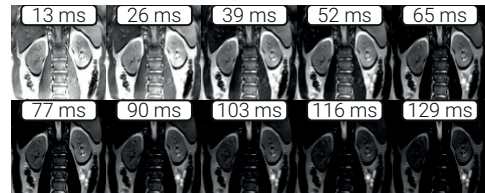
### 3.3. Results

---

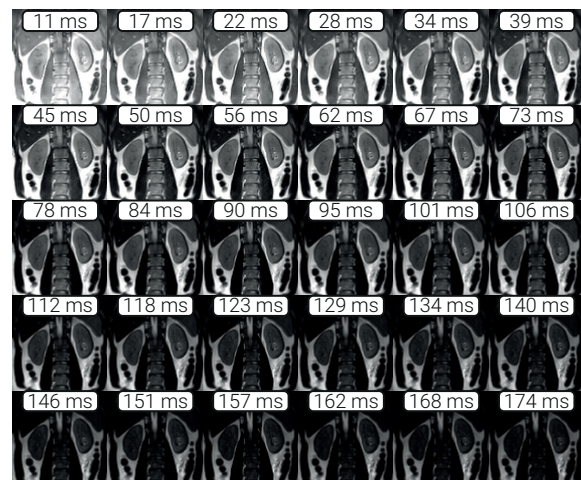
and medulla while the CPMG  $T_2$  prep suffers from image artefacts with the largest amount of blurring as measured on the phantom.



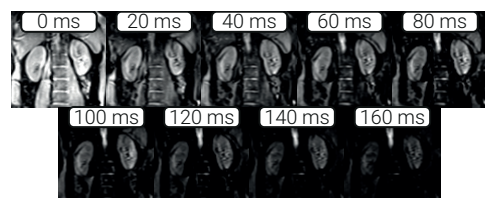
(a) SE-EPI



(b) ME-TSE



(c) GraSE



(d) CPMG  $T_2$  Prep

Figure 3.21: Example in-vivo multi echo data using each of the  $T_2$  mapping sequences.

### 3.3. Results

---

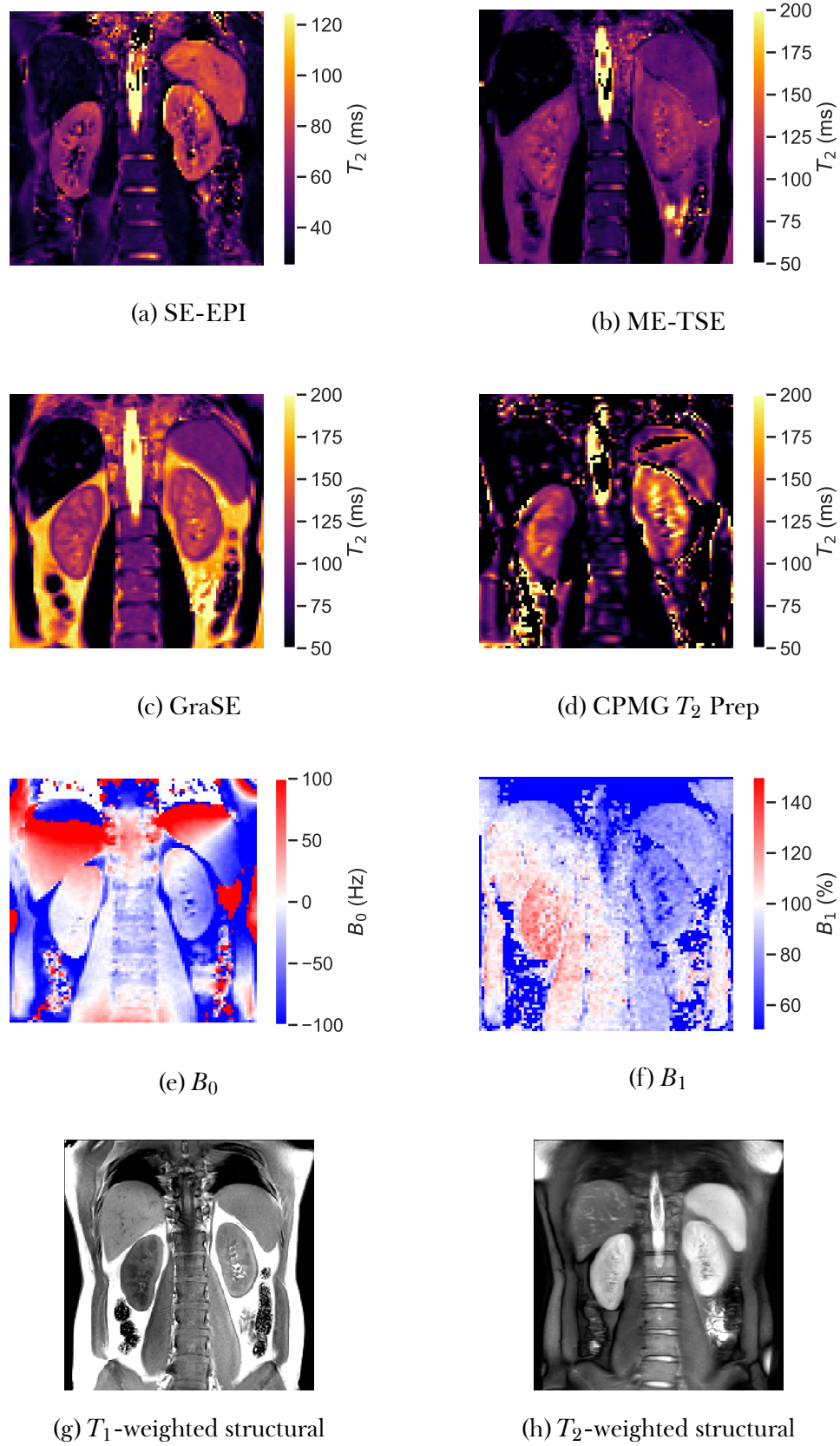


Figure 3.22: Example in-vivo maps generated using each of the sequences and the associated  $B_0$  and  $B_1$  maps used for quality control and structural scans used for segmentation.

### 3.3. Results

---

ROI for the cortex and medulla were defined from the  $T_1$ -weighted structural scan (Figure 3.22g) and these ROI used to calculate the mean  $T_2$  for the renal cortex and medulla using each mapping method. The mean across the five subjects is shown in Figure 3.23a. Additionally the Coefficient of Variation (CoV), defined as standard deviation upon the mean, between subjects was calculated to assess the repeatability of each measure, Figure 3.23b.

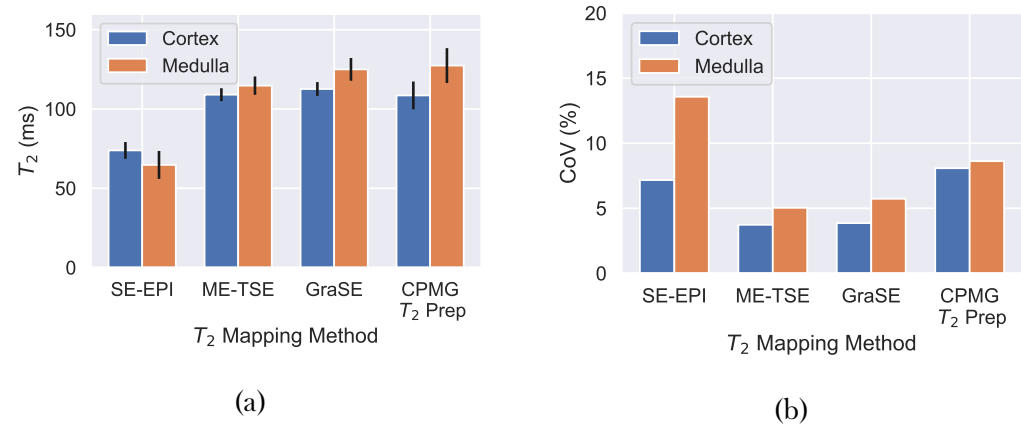


Figure 3.23: (a) Mean cortical and medullary  $T_2$  values across five subjects measured using each sequence. Error bars are the standard deviation across subjects. (b) The CoV between subjects for each sequence.

To better explore the variation between subjects, histograms of the  $T_2$  values of each tissue type were generated for each subject, Figure 3.24. A Gaussian was fit to each histogram to calculate the peak and FWHM  $T_2$  for each sequence and tissue type across subjects, Table 3.6.

### 3.3. Results

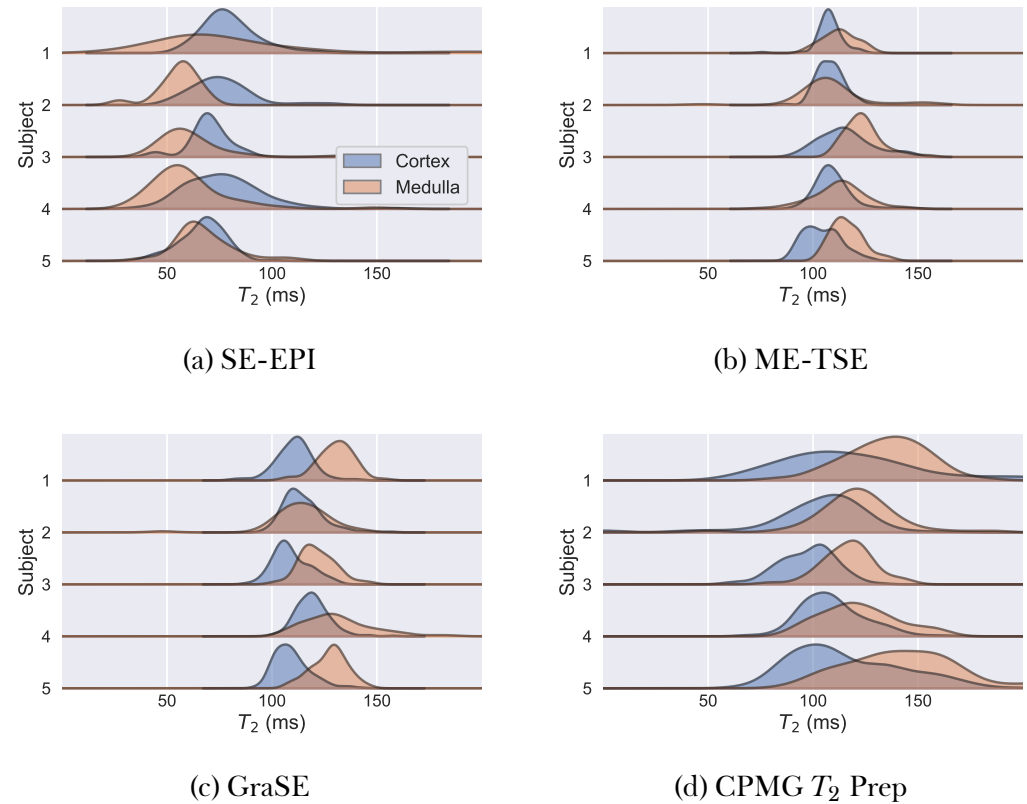


Figure 3.24: Histograms of the  $T_2$  of cortex and medulla for all subjects and mapping methods.

Sequence	Tissue	Peak (ms)	FWHM (ms)
SE-EPI	Cortex	$74 \pm 4$	$25 \pm 9$
	Medulla	$61 \pm 4$	$18 \pm 8$
ME-TSE	Cortex	$109 \pm 4$	$18 \pm 8$
	Medulla	$115 \pm 5$	$19 \pm 4$
GraSE	Cortex	$112 \pm 5$	$17 \pm 1$
	Medulla	$126 \pm 6$	$22 \pm 8$
CPMG $T_2$ Prep	Cortex	$109 \pm 5$	$44 \pm 17$
	Medulla	$130 \pm 11$	$41 \pm 13$

Table 3.6: Peak and FWHM of a Gaussian fit to the histogram of each tissue type. Values are expressed as mean and standard deviation across the five subjects.

## 3.4 Discussion

In this chapter, four of the most common  $T_2$  mapping methods have been evaluated for use in the kidneys; SE-EPI, ME-TSE, GraSE and CPMG  $T_2$  prep. These sequences were validated for quantitative accuracy, image quality and sensitivity to flow using phantoms before being used to image five healthy volunteers. Additionally, four different methods of fitting  $T_2$  maps from the subsequent multi-echo imaging data were compared.

Of the fitting methods explored, the basic fit was deemed the most appropriate over the range of  $T_2$  within the kidneys. Fitting for a baseline noise term reduced the calculated  $T_2$  of longer  $T_2$  tissues because they had not fully recovered before the final TE and as such the noise term was overestimated. This method would be more appropriate for use in tissues with a shorter  $T_2$  such as the liver or sequences with a very wide range of TE. Discarding TE with signal below an empirically derived threshold can result in an increased accuracy for short  $T_2$  tissues but does not improve the accuracy within the range of the kidneys. The discard threshold can be manually defined; however, this leads to potentially inaccurate results if a sub-optimum threshold is chosen, these inaccurate results can be difficult to identify in-vivo with no gold standard to compare against. An alternative to manually setting a threshold is to define a ROI over the liver, the signal from the final TE is then used to inform the estimation of the discard threshold as, in most cases due to its very short  $T_2$ , the liver will have fully recovered by the final TE. While this method does eliminate the manual aspect of threshold definition between subjects, it requires the additional manual processing step of delineating an additional ROI for no increase in accuracy within the kidneys. Discarding low intensity echoes and fitting for noise also produced inferior results to the basic fit. By discarding the late echo times that the fitting method uses to estimate noise, the  $\epsilon$  term becomes less accurate and as such, so does  $T_2$ . It was therefore concluded that the basic fit should be used for renal studies, however, the noise fit should be considered for liver  $T_2$  measurements.

### 3.4. Discussion

---

The only sequence that was able to accurately estimate the  $T_2$  of the shortest  $T_2$  spheres of the QalibreMD phantom was the CPMG  $T_2$  prep, Figure 3.15 and Table 3.4. This is able to achieve an effective echo time of 0 ms and thus sample the signal before it has decayed; for other sequences the first echo time can be multiple times the  $T_2$  of these short spheres and as such the signal has already decayed by a large proportion of its initial signal. Additionally, the CPMG sequence is self-correcting for imperfect 180° pulses, and thus the longer TE are more accurate. It is the very large relative error of the shortest  $T_2$  spheres (spheres of  $T_2 < 20$  ms) that leads to the unacceptably large MPE in the other sequences over the full range of  $T_2$  within the phantom, Figure 3.15c. Both the ME-TSE and GraSE yield similar accuracies over the range of  $T_2$  seen in the kidneys due to their rapid acquisition, initial TE much shorter than the  $T_2$  of the kidneys and, in the case of GraSE, the short echo spacing and thus more TE to fit each voxel to. The SE-EPI sequence suffers due to being relatively slow and therefore a limited number of echo times can be acquired. This is because the standard “unpatched” thick slice profile of the 180° pulse means that each TE needs to be collected in two packets with slices interleaved. As such only a limited number of TE could be acquired within the time limits prescribed and, without any of the more advance elements of the CPMG sequence its accuracy is compromised for  $T_2$  outside the central range of the kidneys.

From Figure 3.17b it can be observed that the SE-EPI sequence is most sensitive to flow due to its largest proportional change in measured  $T_2$  as the rate of flow is increased. The sequences with the lowest absolute  $T_2$  with the pump off i.e. the sequences with the lowest  $T_2$  in the left most point of Figure 3.17a, are also the sequences that are affected most when the pump is turned on i.e. have the largest deviation from 100 % as flow rate increases in Figure 3.17b. The effects of diffusion remain even with the pump turned off and as such the  $T_2$  is still reduced, even when the flow rate is 0 ml/min. The ADC increases from  $1.15 \times 10^{-3} \pm 0.06 \times 10^{-3}$  mm<sup>2</sup>/s to  $1.36 \times 10^{-3} \pm 0.09 \times 10^{-3}$  mm<sup>2</sup>/s over the full range of flow rates the pump can produce, Figure 3.18, corresponding to an increase of 17 % therefore

### 3.4. Discussion

---

it is expected that there will still be considerable confounding influences of diffusion on the  $T_2$  mapping sequences when the pump is turned off. This is also a contributing factor in the large range in  $T_2$  observed when the pump was turned off in Figure 3.17a. The GraSE sequence is least sensitive to flow with only a 5 % decrease in  $T_2$ . This is due to the GraSE sequence's short echo spacing and the fact multiple TEs are collected within the same TR, as such, the effects of diffusion are not proportional to TE and therefore have minimal influence upon  $T_2$ .

The large amount of blurring of the CPMG  $T_2$  prep sequence limits its readability in-vivo. This is due to the Turbo Field Echo Planar Imaging (TFEPI) scheme leading to an increased acquisition voxel size. The degree of blurring measured in the ME-TSE and GraSE sequences was comparable, with the SE-EPI having a slightly broader PSF.

Comparing the in-vivo data in Figure 3.22 and Figure 3.23 it can be seen that the relative strengths and weaknesses of each sequence observed in the phantoms are mirrored in-vivo. The SE-EPI sequence is estimating much shorter  $T_2$  than the other three sequences. Additionally, this sequence results in a shorter  $T_2$  in the medulla than the cortex, this effect was also observed by de Bazelaire et al [31]. In Figure 3.17 it was observed that measured  $T_2$  decreases as flow increases, the renal cortex is more highly perfused than the medulla [8, 54] however, fluid flowing through renal tubules will also lead to a decrease in  $T_2$  and renal tubular density is higher in the medullary pyramids. Another contributing factor to this effect could be the difference in the direction of flow between the phantom and the medulla. In the flow phantom the perfusate flows radially in from the circumference of the porous media towards the outlet at the centre. This results in a predominantly in-plain flow, whereas in the kidney, the renal vein quickly ascends to the inferior vena cava and is thus out-of-plain. This out-of-plain flow means that for longer TE, some protons have travelled out of the profile of the 180° refocusing pulse and as such do not contribute to the signal. This effect manifests itself more at longer TE and thus the measured  $T_2$  decreases. The

### 3.4. Discussion

---

SE-EPI sequence also appears to be the most sensitive to  $B_1$  inhomogeneity. A relatively large difference in  $T_2$  is observed between the left and right kidneys, this matches the pattern of  $B_1$  seen in Figure 3.22f. These factors combine and lead to the SE-EPI sequence having the largest CoV between subjects of the sequences tested.

The ME-TSE sequence produces good quality images and broadly similar mean  $T_2$  to the GraSE and CPMG  $T_2$  prep for the cortex, however the mean  $T_2$  measured in the medulla is lower resulting in little contrast between the cortex and medulla. The image quality and CoV produced by the GraSE sequence is similar to that of the ME-TSE as expected given the comparable PSF and similar sequence architecture. The GraSE measures higher medullary  $T_2$  than the ME-TSE resulting in greater corticomedullary contrast; this increased contrast can be observed across subjects, Figure 3.24c. The GraSE sequence has the highest Specific Absorption Rate (SAR) and is the acoustically loudest of the four sequences. The SAR is well below safety limits, however these factors may be a consideration when scanning nervous subjects as heating can be felt. The effects of the wide PSF can be seen in the image produced by CPMG  $T_2$  prep with a large amount of blurring decreasing the readability of the image. The mean  $T_2$  of the cortex and medulla are similar to that measured using the GraSE sequence, however due to the inferior image quality, the variance within the ROI is much higher, Figure 3.24d.

Table 3.7 compares the quantitative accuracy, image quality and acquisition time of the four  $T_2$  mapping sequences on phantoms and in-vivo for use in the kidneys, it is concluded that overall the GraSE sequence provides the optimum protocol for renal  $T_2$  mapping. In phantoms, the accuracy was shown to be comparable with the ME-TSE sequence and its superior in-vivo image quality and insensitivity to flow lead us to recommend this sequence for further renal studies.

### 3.5. Conclusion and Future Work

Sequence	Acquisition Time (before respiratory compensation)	MPE (5 ms - 650 ms) (%)	MPE (40 ms - 200 ms) (%)	FWHM (mm)	Sensitivity to Flow	In-Vivo CoV (cortex/medulla) (%)	In-Vivo Comments
SE-EPI	1 min 45 sec	36 ± 34	8 ± 5	4.80 ± 0.18	0.65 ± 0.08	7.17/13.57	Inaccurate Sensitive to $B_1$ and diffusion
ME-TSE	1 min 57 sec	38 ± 31	23 ± 13	4.20 ± 0.14	0.81 ± 0.12	3.73/5.04	Reduced corticomedullary contrast
GraSE	2 min 6 sec	32 ± 29	15 ± 4	4.26 ± 0.12	0.95 ± 0.06	3.86/5.73	High SAR
CPMG $T_2$ Prep	2 min 23 sec	18 ± 15	11 ± 1	6.48 ± 0.33	0.90 ± 0.11	8.08/8.62	Large degree of image artefacts

Table 3.7: A summary of the results both in phantoms and in-vivo.

## 3.5 Conclusion and Future Work

A SE-EPI, ME-TSE, GraSE and CPMG  $T_2$  prep sequence were assessed using phantoms to assess their accuracy when quantifying  $T_2$ , sensitivity to flow and image quality by estimating the PSF. These sequences were then used to acquire  $T_2$  maps of the kidneys in five healthy volunteers. The GraSE sequence is recommended for future renal studies due to its superior image quality and accuracy within the time constraints.

This chapter assesses the accuracy of the  $T_2$  mapping sequences however the precision of the sequences should be explored in future. A more detailed analysis of variance within each sphere of the QalibreMD phantom should be performed. Additionally, both the phantoms and humans should be scanned over multiple sessions. The data presented in this chapter shows promising results for the ME-TSE and GraSE sequences, both of which show a small CoV between subjects. By scanning the same subject in multiple sessions, inter-subject physiological variability is eliminated thus gaining a better understanding of each sequences precision.

All acquisitions presented here were carried out on a Philips system. In future these methods should be evaluated on other vendors (GE and Siemens) to enable a comparison of sequences available between sites prior

### **3.6. Acknowledgements**

---

to performing multisite studies of renal  $T_2$  mapping in healthy controls and patients.

## **3.6 Acknowledgements**

I am grateful for access to the University of Nottingham's Augusta high performance computing service.

### 3.7 References

1. Daniel, A. J., Cox, E., Buchanan, C. & Francis, S. *A Comparison of T2 Mapping Methods in the Kidneys* in *Proc. Intl. Soc. Mag. Reson. Med.* 28 International Society of Magnetic Resonance in Medicine Annual Meeting (Online, Aug. 2020).
2. Tofts, P. *Quantitative MRI of the Brain: Measuring Changes Caused by Disease* 688 pp. Google Books: RbFrAAAAMAAJ (Wiley, 2003).
3. Buchanan, C. E., Mahmoud, H., Cox, E. F., McCulloch, T., Prestwich, B. L., Taal, M. W., Selby, N. M. & Francis, S. T. Quantitative Assessment of Renal Structural and Functional Changes in Chronic Kidney Disease Using Multi-Parametric Magnetic Resonance Imaging. *Nephrology Dialysis Transplantation* **35**, 955–964 (29th June 2019).
4. Chapman, A. B. *et al.* Kidney Volume and Functional Outcomes in Autosomal Dominant Polycystic Kidney Disease. *Clinical Journal of the American Society of Nephrology* **7**, 479–486 (1st Mar. 2012).
5. Gong, I. H., Hwang, J., Choi, D. K., Lee, S. R., Hong, Y. K., Hong, J. Y., Park, D. S. & Jeon, H. G. Relationship Among Total Kidney Volume, Renal Function and Age. *The Journal of Urology* **187**, 344–349 (Jan. 2012).
6. Bull, S. *et al.* Human Non-Contrast T1 Values and Correlation with Histology in Diffuse Fibrosis. *Heart* **99**, 932–937 (1st July 2013).
7. Ferreira, V. M. *et al.* T1 Mapping for the Diagnosis of Acute Myocarditis Using CMR: Comparison to T2-Weighted and Late Gadolinium Enhanced Imaging. *JACC: Cardiovascular Imaging* **6**, 1048–1058 (1st Oct. 2013).
8. Hoad, C. L. *et al.* A Study of T1 Relaxation Time as a Measure of Liver Fibrosis and the Influence of Confounding Histological Factors. *NMR in Biomedicine* **28**, 706–714 (2015).
9. Luetkens, J. A. *et al.* Quantification of Liver Fibrosis at T1 and T2 Mapping with Extracellular Volume Fraction MRI: Preclinical Results. *Radiology* **288**, 748–754 (26th June 2018).

### 3.7. References

---

10. Friedli, I. *et al.* New Magnetic Resonance Imaging Index for Renal Fibrosis Assessment: A Comparison between Diffusion-Weighted Imaging and T1 Mapping with Histological Validation. *Scientific Reports* **6**. doi:10.1038/srep30088. pmid: 27439482 (21st July 2016).
11. Gillis, K. A. *et al.* Non-Contrast Renal Magnetic Resonance Imaging to Assess Perfusion and Corticomedullary Differentiation in Health and Chronic Kidney Disease. *Nephron* **133**, 183–192 (2016).
12. Cox, E. F., Buchanan, C. E., Bradley, C. R., Prestwich, B., Mahmoud, H., Taal, M., Selby, N. M. & Francis, S. T. Multiparametric Renal Magnetic Resonance Imaging: Validation, Interventions, and Alterations in Chronic Kidney Disease. *Frontiers in Physiology* **8**, 696 (2017).
13. Hueper, K. *et al.* Functional MRI Detects Perfusion Impairment in Renal Allografts with Delayed Graft Function. *American Journal of Physiology-Renal Physiology* **308**, F1444–F1451 (29th Apr. 2015).
14. Artz, N. S., Sadowski, E. A., Wentland, A. L., Grist, T. M., Seo, S., Djamali, A. & Fain, S. B. Arterial Spin Labeling MRI for Assessment of Perfusion in Native and Transplanted Kidneys. *Magnetic Resonance Imaging* **29**, 74–82 (1st Jan. 2011).
15. Ren, T. *et al.* Evaluation of Renal Allografts Function Early after Transplantation Using Intravoxel Incoherent Motion and Arterial Spin Labeling MRI. *Magnetic Resonance Imaging* **34**, 908–914 (1st Sept. 2016).
16. Niles, D. J., Artz, N. S., Djamali, A., Sadowski, E. A., Grist, T. M. & Fain, S. B. Longitudinal Assessment of Renal Perfusion and Oxygenation in Transplant Donor-Recipient Pairs Using ASL and BOLD MRI. *Investigative radiology* **51**, 113–120 (Feb. 2016).
17. Rossi, C., Artunc, F., Martirosian, P., Schlemmer, H.-P., Schick, F. & Boss, A. Histogram Analysis of Renal Arterial Spin Labeling Perfusion Data Reveals Differences Between Volunteers and Patients With Mild Chronic Kidney Disease. *Investigative Radiology* **47**, 490–496 (Aug. 2012).

### 3.7. References

---

18. Tan, H., Koktzoglou, I. & Prasad, P. V. Renal Perfusion Imaging with Two-Dimensional Navigator Gated Arterial Spin Labeling. *Magnetic Resonance in Medicine* **71**, 570–579 (2014).
19. Eckerbom, P., Hansell, P., Cox, E., Buchanan, C., Weis, J., Palm, F., Francis, S. & Liss, P. Multiparametric Assessment of Renal Physiology in Healthy Volunteers Using Noninvasive Magnetic Resonance Imaging. *American Journal of Physiology-Renal Physiology* **316**, F693–F702 (16th Jan. 2019).
20. Schley, G., Jordan, J., Ellmann, S., Rosen, S., Eckardt, K.-U., Uder, M., Willam, C. & Bäuerle, T. Multiparametric Magnetic Resonance Imaging of Experimental Chronic Kidney Disease: A Quantitative Correlation Study with Histology. *PLOS ONE* **13**, e0200259 (16th July 2018).
21. Hueper, K. *et al.* Kidney Transplantation: Multiparametric Functional Magnetic Resonance Imaging for Assessment of Renal Allograft Pathophysiology in Mice. *Investigative Radiology* **51**, 58–65 (Jan. 2016).
22. Gouya, H., Vignaux, O., Le Roux, P., Chanson, P., Bertherat, J., Bertagna, X. & Legmann, P. Rapidly Reversible Myocardial Edema in Patients with Acromegaly: Assessment with Ultrafast T2 Mapping in a Single-Breath-Hold MRI Sequence. *American Journal of Roentgenology* **190**, 1576–1582 (1st June 2008).
23. Giri, S., Chung, Y.-C., Merchant, A., Mihai, G., Rajagopalan, S., Raman, S. V. & Simonetti, O. P. T2 Quantification for Improved Detection of Myocardial Edema. *Journal of Cardiovascular Magnetic Resonance* **11**, 56 (30th Dec. 2009).
24. Naßenstein, K., Nensa, F., Schlosser, T., Bruder, O., Umutlu, L., Lauenstein, T., Maderwald, S. & Ladd, M. E. Cardiac MRI: T2-Mapping Versus T2-Weighted Dark-Blood TSE Imaging for Myocardial Edema Visualization in Acute Myocardial Infarction. *RöFo - Fortschritte auf dem Gebiet der Röntgenstrahlen und der bildgebenden Verfahren* **186**, 166–172 (Feb. 2014).

### 3.7. References

---

25. Guo, H. *et al.* Myocardial T2 Quantitation in Patients with Iron Overload at 3 Tesla. *Journal of Magnetic Resonance Imaging* **30**, 394–400 (2009).
26. Krittayaphong, R., Zhang, S., Saiviroonporn, P., Viprakasit, V., Tanapibunpon, P., Komoltri, C. & Wangworatrakul, W. Detection of Cardiac Iron Overload with Native Magnetic Resonance T1 and T2 Mapping in Patients with Thalassemia. *International Journal of Cardiology* **248**, 421–426 (1st Dec. 2017).
27. Neema, M., Stankiewicz, J., Arora, A., Dandamudi, V. S. R., Batt, C. E., Guss, Z. D., Al-Sabbagh, A. & Bakshi, R. T1- and T2-Based MRI Measures of Diffuse Gray Matter and White Matter Damage in Patients with Multiple Sclerosis. *Journal of Neuroimaging* **17**, 16S–21S (2007).
28. Rugg-Gunn, F. J., Boulby, P. A., Symms, M. R., Barker, G. J. & Duncan, J. S. Whole-Brain T2 Mapping Demonstrates Occult Abnormalities in Focal Epilepsy. *Neurology* **64**, 318–325 (25th Jan. 2005).
29. Knight, M. J., McCann, B., Tsivos, D., Dillon, S., Coulthard, E. & Kauppinen, R. A. Quantitative T2 Mapping of White Matter: Applications for Ageing and Cognitive Decline. *Physics in Medicine and Biology* **61**, 5587–5605 (July 2016).
30. Vymazal, J., Righini, A., Brooks, R. A., Canesi, M., Mariani, C., Leonardi, M. & Pezzoli, G. T1 and T2 in the Brain of Healthy Subjects, Patients with Parkinson Disease, and Patients with Multiple System Atrophy: Relation to Iron Content. *Radiology* **211**, 489–495 (1st May 1999).
31. De Bazelaire, C. M. J., Duhamel, G. D., Rofsky, N. M. & Alsop, D. C. MR Imaging Relaxation Times of Abdominal and Pelvic Tissues Measured in Vivo at 3.0 T: Preliminary Results. *Radiology* **230**, 652–659 (1st Mar. 2004).
32. Zhang, J. L. *et al.* Reproducibility of R2\* and R2 Measurements in Human Kidneys in Proc. Intl. Soc. Mag. Reson. Med. 19 ISMRM. **19** (2011), 2954.
33. Li, X., Bolan, P. J., Ugurbil, K. & Metzger, G. J. Measuring Renal Tissue Relaxation Times at 7 T. *NMR in Biomedicine* **28**, 63–69 (2015).

### 3.7. References

---

34. De Boer, A. *et al.* Multiparametric Renal MRI: An Intrasubject Test–Retest Repeatability Study. *Journal of Magnetic Resonance Imaging* **n/a**. doi:10.1002/jmri.27167 (16th Apr. 2020).
35. Mathys, C., Blondin, D., Wittsack, H.-J., Miese, F. R., Rybacki, K., Walther, C., Holstein, A. & Lanzman, R. S. T2' Imaging of Native Kidneys and Renal Allografts – a Feasibility Study. *RöFo - Fortschritte auf dem Gebiet der Röntgenstrahlen und der bildgebenden Verfahren* **183**, 112–119 (Feb. 2011).
36. Adams, L. C. *et al.* Multiparametric Assessment of Changes in Renal Tissue after Kidney Transplantation with Quantitative MR Relaxometry and Diffusion-Tensor Imaging at 3 T. *Journal of Clinical Medicine* **9**, 1551 (5 May 2020).
37. Franke, M. *et al.* Magnetic Resonance T2 Mapping and Diffusion-Weighted Imaging for Early Detection of Cystogenesis and Response to Therapy in a Mouse Model of Polycystic Kidney Disease. *Kidney International* **92**, 1544–1554 (1st Dec. 2017).
38. Adams, L. C. *et al.* Use of Quantitative T2 Mapping for the Assessment of Renal Cell Carcinomas: First Results. *Cancer Imaging* **19**, 35 (7th June 2019).
39. Siedek, F. *et al.* Magnetic Resonance Kidney Parenchyma-T2 as a Novel Imaging Biomarker for Autosomal Dominant Polycystic Kidney Disease. *Investigative Radiology* **55**, 217–225 (Apr. 2020).
40. Wolf, M. *et al.* Magnetic Resonance Imaging T1- and T2-Mapping to Assess Renal Structure and Function: A Systematic Review and Statement Paper. *Nephrology Dialysis Transplantation* **33**, ii41–ii50 (suppl\_2 1st Sept. 2018).
41. Carr, H. Y. & Purcell, E. M. Effects of Diffusion on Free Precession in Nuclear Magnetic Resonance Experiments. *Physical Review* **94**, 630–638 (1st May 1954).
42. Majumdar, S., Orphanoudakis, S. C., Gmitro, A., O'Donnell, M. & Gore, J. C. Errors in the Measurements of T2 Using Multiple-Echo

### 3.7. References

---

- MRI Techniques. I. Effects of Radiofrequency Pulse Imperfections. *Magnetic Resonance in Medicine* **3**, 397–417 (1st June 1986).
43. Majumdar, S., Orphanoudakis, S. C., Gmitro, A., O'Donnell, M. & Gore, J. C. Errors in the Measurements of T2 Using Multiple-Echo MRI Techniques. II. Effects of Static Field Inhomogeneity. *Magnetic Resonance in Medicine* **3**, 562–574 (1986).
44. Crawley, A. P. & Henkelman, R. M. Errors in T2 Estimation Using Multislice Multiple-Echo Imaging. *Magnetic Resonance in Medicine* **4**, 34–47 (1987).
45. Meiboom, S. & Gill, D. Modified Spin-Echo Method for Measuring Nuclear Relaxation Times. *Review of Scientific Instruments* **29**, 688–691 (1st Aug. 1958).
46. Nehrke, K. & Börnert, P. DREAM—a Novel Approach for Robust, Ultrafast, Multislice B1 Mapping. *Magnetic Resonance in Medicine* **68**, 1517–1526 (2012).
47. Petzold, K. *et al.* Building a Network of ADPKD Reference Centres across Europe: The EuroCYST Initiative. *Nephrology Dialysis Transplantation* **29**, iv26–iv32 (suppl\_4 1st Sept. 2014).
48. Will, S., Martirosian, P., Würslin, C. & Schick, F. Automated Segmentation and Volumetric Analysis of Renal Cortex, Medulla, and Pelvis Based on Non-Contrast-Enhanced T1- and T2-Weighted MR Images. *Magnetic Resonance Materials in Physics, Biology and Medicine* **27**, 445–454 (1st Oct. 2014).
49. Daniel, A. J. *et al.* UKRIN Kidney Analysis Toolbox (UKAT): A Framework for Harmonized Quantitative Renal MRI Analysis in Proc. Intl. Soc. Mag. Reson. Med. 29 International Society of Magnetic Resonance in Medicine Annual Meeting. **29** (Online, May 2021), 2379.
50. Nery, F., Daniel, A. J., Sousa, J. & Buchanan, C. UKRIN Kidney Analysis Toolbox version v0.1.0. UK Renal Imaging Network, Dec. 2020.
51. Chaimow, D. & Shmuel, A. A More Accurate Account of the Effect of K-Space Sampling and Signal Decay on the Effective Spatial Resolution in Functional MRI. *bioRxiv*, 097154 (17th Sept. 2017).

### 3.7. References

---

52. Chaimow, D. & Shmuel, A. *A More Accurate Account of the Effect of K-Space Sampling and Signal Decay on the Effective Spatial Resolution in Functional MRI* in *Proc. Intl. Soc. Mag. Reson. Med.* 25 International Society of Magnetic Resonance in Medicine Annual Meeting. **25** (Honolulu, Hawai'i, USA, Apr. 2017), 5240.
53. MRIStandards. *MRIStandards/PhantomViewer* 20th Dec. 2020.
54. Nery, F. *et al.* Consensus-Based Technical Recommendations for Clinical Translation of Renal ASL MRI. *Magnetic Resonance Materials in Physics, Biology and Medicine* **33**, 141–161 (1st Feb. 2020).

## **Chapter 4**

# **Quantitative Methods to Measure Renal Oxygenation**

---

## Abstract

Measurements of oxygenation of blood entering and leaving the kidneys would be a highly desirable quantitative biomarker allowing the calculation of renal metabolic rate of oxygen. Two methods of measuring blood oxygen saturation using MRI are used in the brain, Susceptibility Based Oximetry (SBO) and  $T_2$  Relaxation Under Spin Tagging (TRUST).

Here both methods are tailored for use in the abdomen, these modified sequences are compared to their unmodified counterparts in the controlled environment of the brain, verifying that the modifications do not alter the quantitative accuracy. The methods are then applied to measure oxygenation in the renal vein. The geometry of the renal vessels leads to a high degree of uncertainty when applying SBO, however TRUST produced results concordant with literature.

To verify the TRUST was able to measure a change in renal oxygenation, a hyperoxia challenge was undertaken. Measurements of oxygen saturation in the renal vein were collected using TRUST and BOLD  $T_2^*$  maps, the current standard for assessing renal oxygenation, were collected while the subject was breathing room air, then pure oxygen. A  $16 \pm 3\%$  increase in oxygenation was measured using TRUST whereas no significant difference in  $T_2^*$  could be detected.

*This work was presented as an oral presentation at the International Society of Magnetic Resonance in Medicine (ISMRM) 26th Annual Meeting (2018) [1].*

## 4.1 Introduction

As part of a multiparametric quantitative Magnetic Resonance Imaging (MRI) protocol, Section 1.2, properties such as haemodynamics, oxygenation, and microstructure are assessed in a single 45 minute scanning session [2, 3]. Currently renal oxygenation is typically assessed by using Blood Oxygen Level Dependent (BOLD)  $T_2^*/R_2^*$  maps to infer oxygenation of different tissues within the kidney, predominately the separation in mean  $T_2^*$  between the renal cortex and medulla, an example of which is shown in Figure 4.1. These BOLD  $T_2^*$  maps are, however, affected by other factors such as susceptibility effects, shimming and baseline blood flow and thus may be limited in their ability to draw quantitative conclusions despite their widespread use [4]. For a detailed review of these confounding factors see Niendorf *et al* [5]. More recently it has been suggested that the gradient in the  $T_2^*/R_2^*$  across the corticomedullary interface may provide a better biomarker of renal oxygenation [4, 6].

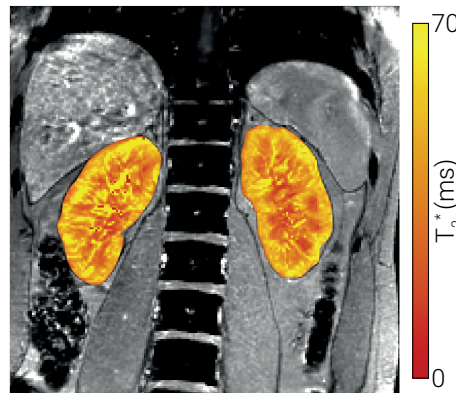


Figure 4.1: An example  $T_2^*$  map. A clear difference can be seen between the renal medulla and cortex.

A welcome addition to this multiparametric model would be the assessment of Renal Metabolic Rate of Oxygen (RMRO<sub>2</sub>); a measure analogous to the Cerebral Metabolic Rate of Oxygen (CMRO<sub>2</sub>) [7]. This measure can be

#### 4.1. Introduction

---

calculated via Equation (4.1),

$$\text{RMRO}_2 = (Y_a - Y_v) \times \text{RBF} \times [\text{Hct}] \quad (4.1)$$

where  $Y_a$  and  $Y_v$  are arterial and venous oxygen saturation respectively, RBF is renal blood flow (in  $\text{mL}/\text{min}$ ) and Hct is the ratio of the volume of erythrocytes to the volume of the rest of the blood, known as haematocrit. RBF can be measured relatively easily using Phase Contrast (PC)-MRI [8] and Hct is usually of the order of 0.41 for healthy adults but can be measured from a simple blood test [9, 10] or established using the correlation between the  $T_1$  of blood and its haematocrit [11]. This means that only a measurement of blood oxygen saturation in the renal vein via a non-invasive protocol is required to generate a quantitative value of  $\text{RMRO}_2$ .

Blood oxygen saturation can be measured precisely via the insertion of catheters into the subject, however this is clearly an invasive process which is not viable in humans [12]. There are currently two well established methods of measuring blood oxygenation via MRI, however thus far these techniques have only been used to measure oxygen saturation in the sagittal sinus, a prominent vein in the brain. These methods are  $T_2$  Relaxation Under Spin Tagging (TRUST) [13–16] and Susceptibility Based Oximetry (SBO) [17–20]. TRUST builds on the idea of Arterial Spin Labelling (ASL) in the fact that by subtracting control images from label images an image of only blood is generated. However, instead of labelling a slab of tissue in the neck and imaging a superior slice in the brain, when implementing TRUST the imaging plane is inferior to the label slab allowing a difference image of the blood in the sagittal sinus to be generated. By collecting a series of pairs of label and control images with different  $T_2$  weightings it is possible to fit the data from the sagittal sinus to a  $T_2$  relaxation, and using a calibration curve to convert the value of  $T_2$  in the sagittal sinus to venous oxygenation [21]. SBO is based on the differences in magnetic susceptibility between the blood and the surrounding tissue. Using a phase map it is possible to model this difference in susceptibility and using the known difference in susceptibility between fully

## **4.2. Methods**

---

oxygenated blood and fully deoxygenated blood, venous oxygenation can be calculated.

Here both of the above techniques were applied to study oxygenation in the renal vein in young healthy individuals to assess the technicalities of transferring these protocols from the brain to the body. Given that these techniques have already been used in the brain with a number of studies in the literature, the sequences were first implemented on the brain to assess oxygenation in the superior sagittal sinus, then adapted to work within the more challenging environment of the abdomen. These adapted sequences were compared to the results gained using the standard implementation in the brain before testing on the renal vein. Finally an oxygen challenge was carried out to verify that changes in oxygenation can be measured in the renal vein.

## **4.2 Methods**

Imaging was performed on a whole body 3 Tesla MRI scanner (Ingenia, Philips Medical Systems, The Netherlands) using a 32 channel head or body coil. Studies were carried out according to the principles of the Declaration of Helsinki and approved by either the Local Ethics Committee or the East Midlands Research Ethics Committee. Written informed consent was obtained from all subjects.

### **4.2.1 Susceptibility-Based Oximetry**

#### **MRI Protocol**

The principle behind SBO is based on the fact that there is a difference in magnetic susceptibility between the blood within a vessel and the tissue surrounding it [22]. As outlined by Jain *et al* [17], if a blood vessel is modelled as a long paramagnetic cylinder, it is possible to calculate the oxygenation of

## 4.2. Methods

---

the blood by knowing the phase difference between the blood in the vessel and the surrounding tissue, the angle ( $\theta$ ) of the vessel to the static field,  $B_0$ , the echo time of the scan and the subject's haematocrit, Hct. This relationship is given by,

$$Y_v = \left[ 1 - \frac{2|\Delta\phi|}{\gamma TE \Delta \chi_{do} B_0 (\cos^2 \theta - 1/3) Hct} \right] \times 100, \quad (4.2)$$

where  $\Delta\phi$  is the average phase difference between the blood in the vessel and the surrounding tissue,  $\gamma$  is the gyromagnetic ratio of a proton,  $\Delta \chi_{do}$  is the susceptibility difference between fully deoxygenated and fully oxygenated blood ( $4\pi \times 0.27$ p.p.m) [23, 24]. Given the haematocrit can be assumed or measured with a blood test or by measuring the  $T_1$  of the blood [25], this means that from a simple phase map it is possible to calculate  $Y_v$ . The optimum phase map for this purpose was produced using a 2D  $T_1$ -weighted Fast Field Echo (FFE) sequence with a flip angle of  $25^\circ$ , flow compensation, coil homogeneity correction and flyback. The Field Of View (FOV) was  $230 \times 184 \times 29$  mm, matrix size of  $400 \times 300$ , Repetition Time (TR) of 12 ms, Echo Time (TE) of 7.5 ms and three signal averages. This led to a total acquisition time of 9 seconds and as such could be completed in a single breath hold if required when moved to a body imaging protocol.

## Analysis

A Region Of Interest (ROI) containing the superior sagittal sinus was defined on the phase map. This mask was then dilated with concentric shells to generate the two ROI shown in Figure 4.2, note that the outer ROI has been constrained to within the brain during its dilation. There were no occurrences of phase wrapping in or immediately surrounding the superior sagittal sinus observed due to its small size and the high field homogeneity within the head and of the 3T scanner used. Any occurrences of phase wrapping could easily be corrected using Phase Region Expanding Labeller for Unwrapping Discrete Estimates (PRELUDE), a tool within

## 4.2. Methods

---

fMRIB Software Library (FSL) (fMRIB, The University of Oxford) [26]. The average values of phase within these two ROIs along with the angle of the vessel to the  $B_0$  field,  $\theta$ , as calculated from the localisation scans can be used together with Equation (4.2) to calculate  $Y_v$ .

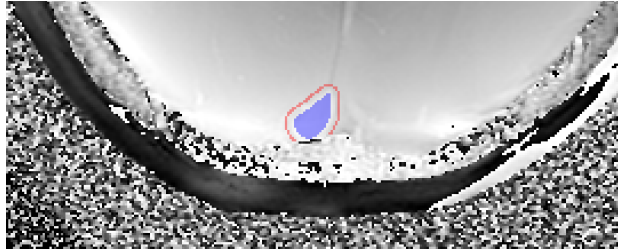


Figure 4.2: The region of interest averaged to find the intra-vascular phase (blue) and the region of interest used to find the phase of the surrounding tissue (red).

### 4.2.2 $T_2$ Relaxation Under Spin Tagging

#### MRI Protocol

The protocol for the TRUST MRI sequence in the brain involved the acquisition of a series of paired images using the pulse sequence shown in Figure 4.3a. A series of four presaturation pulses using the Water suppression Enhanced through  $T_1$  effects (WET) scheme ( $\theta_1 = 88.9^\circ$ ,  $\theta_2 = 98.7^\circ$ ,  $\theta_3 = 82.5^\circ$ ,  $\theta_4 = 159^\circ$ ) were applied to the imaging slice, shown in Figure 4.3b, to reduce the signal from static tissue and reduce contamination of the magnetisation in the imaging slice by an imperfect labelling slab profile [27]. This choice of flip angles for the WET scheme has been shown to be very efficient at providing saturation over a wide range of  $T_1$  values [28]. In the first of each image pair, a label scheme was applied consisting of two successive slice-selective  $90^\circ$  Radio Frequency (RF) pulses to generate a  $180^\circ$  label. The next image in the sequence followed a control scheme instead of the labelling scheme; for this the second of the  $90^\circ$  pulses was applied  $180^\circ$  out of phase to result in zero net effect. As such any effects of magnetisation transfer related

## 4.2. Methods

---

signal in the stationary tissue are cancelled out because the net RF effect on the macromolecular spin magnetization is identical for both the labelling pulse and control pulse. This method of labelling is known as Transfer Insensitive Labelling Technique (TILT) and is widely used in literature for TRUST in the brain [29]. A series of non-selective  $T_2$  preparation pulses were then applied to minimise the blood outflow effect and modulate the  $T_2$  weighting of the image as in the Carr-Purcell-Meiboom-Gill (CPMG) sequence described in Chapter 3, the time between the application of the labelling pulse and the  $T_2$  preparation is known as the Post Label Delay (PLD). Finally a slice-selective  $90^\circ$  excitation pulse was applied followed by a standard Echo Planar Imaging (EPI) readout at time TE later [14]. Both the  $90^\circ$  pulses at the end of the  $T_2$  preparation block and the  $90^\circ$  excitation pulse are required because the  $T_2$  preparation block is non-slice-selective. By subtracting the control image from the label image, only the venous blood that flowed from the label slab to the imaging slab is visible, as shown in Figure 4.4.

## 4.2. Methods

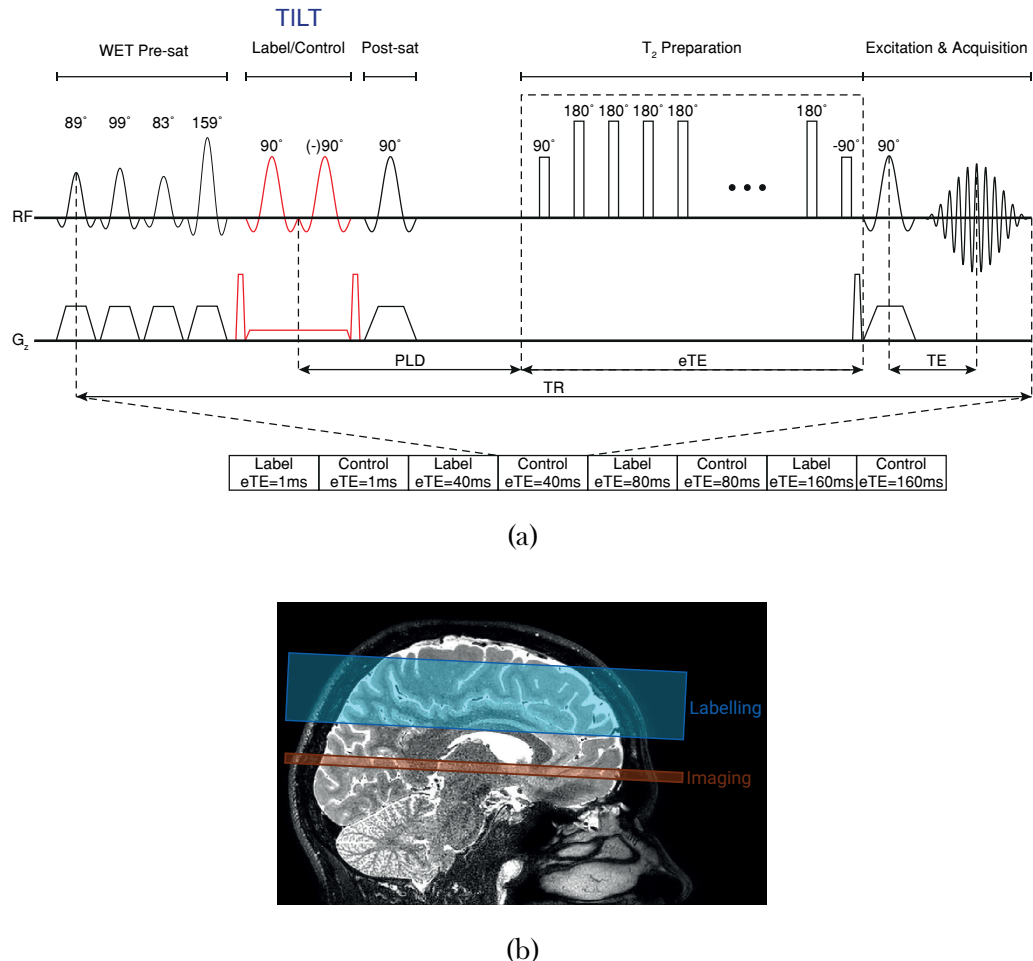


Figure 4.3: (a) The pulse sequence for TRUST MRI which was implemented using the standard TILT labelling scheme. (b) The labelling and imaging volumes used for TILT within the brain, note that the labelling was applied above the sagittal sinus.

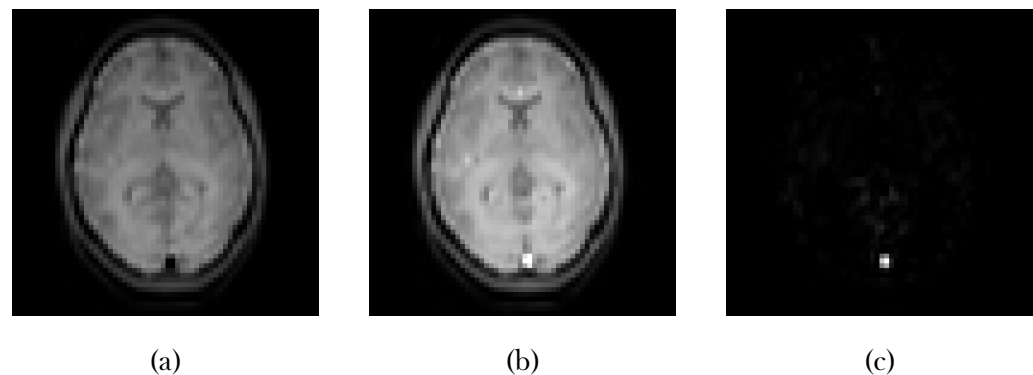


Figure 4.4: The TILT control image (a) was subtracted from the label image (b) to generate a difference image (c) of only the labelled venous blood in the sagittal sinus.

## 4.2. Methods

---

This process was then repeated for another pair of images, with additional 180° refocusing pulses in the  $T_2$  preparation block, this increases the Effective Echo Time (eTE) and therefore applied a  $T_2$  weighting to the image in addition to the constant weighting caused by the regular TE. Three label/control image pairs were acquired at each eTE of 1 ms, 40 ms, 80 ms and 160 ms.

The resulting signal in the superior sagittal sinus of the difference between the label and control image,  $\Delta S$ , is defined by Equation (4.5)

$$S_{\text{label}} = \left( 1 - 2 \cdot e^{-(T_I - eTE)/T_1} \right) \cdot e^{-eTE/T_2} \cdot e^{-TE/T_2^*} \quad (4.3)$$

$$S_{\text{control}} = e^{-eTE/T_2} \cdot e^{-TE/T_2^*} \quad (4.4)$$

$$\begin{aligned} \Delta S &= S_{\text{label}} - S_{\text{control}} \\ &= 2 \cdot e^{-(T_I - eTE)/T_1} \cdot e^{-eTE/T_2} \cdot e^{-TE/T_2^*} \\ &= 2 \cdot e^{-T_I/T_1 - TE/T_2^*} \cdot e^{eTE(1/T_1 - 1/T_2)} \\ &= S_0 \cdot e^{eTE(1/T_1 - 1/T_2)} \end{aligned} \quad (4.5)$$

where  $S_0 = 2 \cdot e^{-T_I/T_1 - TE/T_2^*}$  and;  $T_1$ ,  $T_2$  and  $T_2^*$  are the relaxation constants of blood [13]. If it is assumed that  $T_1$  of blood is approximately 1624 ms at 3T [25] then it is possible to fit the collected data to a mono-exponential function and estimate of  $T_2$  (and  $S_0$ ). It is deemed acceptable to use a mean value of  $T_1$  as it will always be much greater than the value of  $T_2$  and thus the possible small changes in blood  $T_1$  due to the oxygenation level and haematocrit become negligible when fitting the  $T_2$  curve.

The final step in this procedure is to convert the value of  $T_2$  into one of venous oxygenation,  $Y_v$ . The relationship between  $T_2$  and  $Y_v$  is well studied and a simple empirically derived calibration curve can be used for this conversion, Figure 4.5 [30, 31]. Measured  $T_2$  shows a dependence on  $\tau_{\text{CPMG}}$  [10], therefore both the calibration curve and TRUST sequence used a  $\tau_{\text{CPMG}}$  of 10 ms.

## 4.2. Methods

---

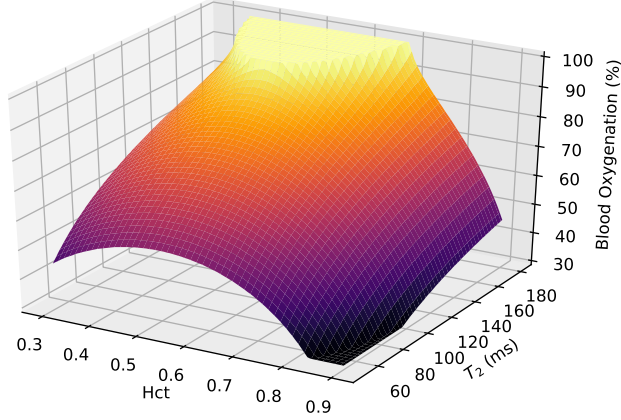


Figure 4.5: The calibration curve used to convert  $T_2$  values into venous blood oxygenation (%) for a given haematocrit (Hct) [32].

The parameters used in the brain TILT TRUST sequence were as follows: label slab thickness = 100 mm, imaging slice thickness = 5 mm, distance between centre of imaging slice and centre of labelling slice = 75 mm, FOV =  $220 \times 220 \times 5$  mm, matrix size =  $64 \times 64$ , voxel size =  $3.44 \times 3.44$  mm, Sensitivity Encoding (SENSE) = 3, EPI factor = 15,  $T_1 \text{ blood}$  = 1624 ms, PLD = 1022 ms, the choice of this value will be explored later for body imaging, TR = 3000 ms, TE = 2.9 ms, eTE = 1 ms, 40 ms, 80 ms and 160 ms with three pairs of images acquired at each. This led to a total scan duration of approximately 84 seconds.

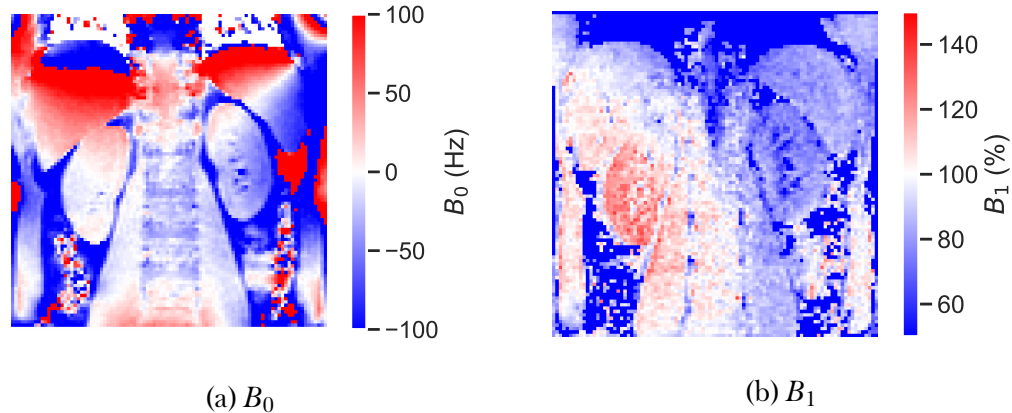


Figure 4.6: Example abdominal  $B_0$  (a) and  $B_1$  (b) field maps showing the inhomogeneity over the kidneys.

## 4.2. Methods

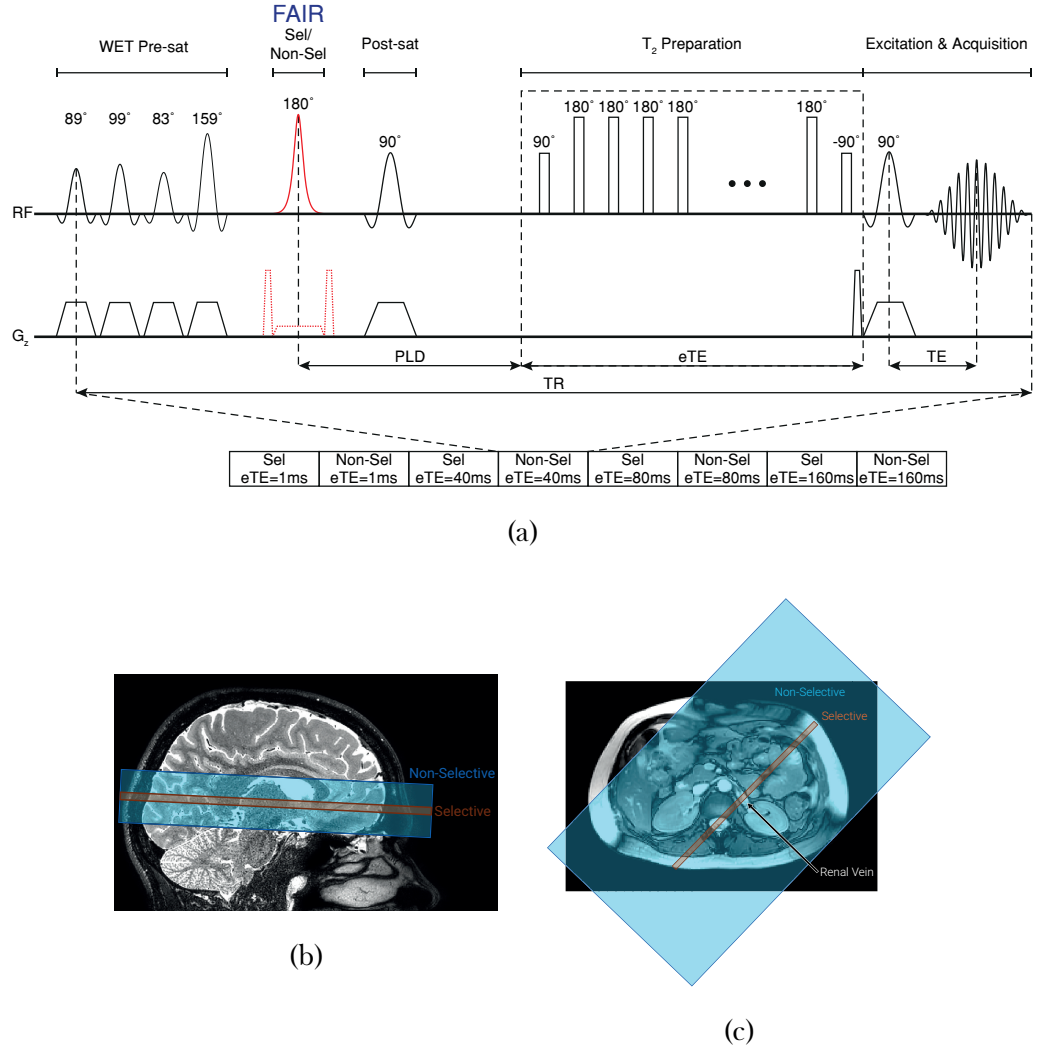


Figure 4.7: (a) The pulse sequence for TRUST MRI using the FAIR labelling scheme. (b) The selective and non-selective volumes used for labelling using the FAIR scheme applied in the brain. (c) The selective and non-selective volumes used for labelling via the FAIR scheme applied in the kidneys.

The main hurdle to be overcome when moving TRUST to the body was the inhomogeneity in the  $B_0$  and  $B_1$  magnetic fields caused by the far less homogeneous tissue susceptibilities within the body compared to the brain, Figure 4.6. These inhomogeneities limited the use of TILT as the labelling method, instead the Flow-sensitive Alternating Inversion Recovery (FAIR) labelling scheme was coded to be used [38]. This scheme uses an adiabatic inversion pulse (Section 2.2.1) which is insensitive to variations in  $B_1$ , a diagram of this pulse sequence is shown in Figure 4.7a. In the FAIR

## 4.2. Methods

---

labelling scheme a hyperbolic secant inversion pulse is applied with ‘control’ slice selective gradients followed by  $T_2$  preparation and acquisition to generate the first image in the pair, a non-selective inversion slab is then applied using a lower slice selective gradient followed by the same  $T_2$  preparation and then acquisition to generate the second ‘label’ image. A schematic of the planning of the selective and non-selective slabs in the brain to study the sagittal sinus and in the body to study the renal vein are shown in Figures 4.7b and 4.7c respectively. An example of the label and control images produced and the resulting signal in the renal vein are shown in Figure 4.8. The FAIR scheme also has the advantage of being far easier to plan in the body than TILT. In the brain having a separate labelling and imaging slice is relatively trivial, however the flow of blood in the body is far less ordered and as such, the use of a selective slab within a non-selective slab yields far more user independent results. Movement is a much greater problem in the body. Given the long acquisition time of TRUST it is impossible to carry out the scan in a single breath hold and repeated breath holds have the issue of between scan movement. Therefore the sequence was modified to allow its implementation with respiratory triggering via a respiratory belt applied around the subjects chest. The total scan time is therefore dependent upon respiratory rate. Depending on the subject, a delay can be applied between the respiratory trigger and the labelling pulse to acquire images at the point in the respiratory cycle when the subject has fully exhaled.

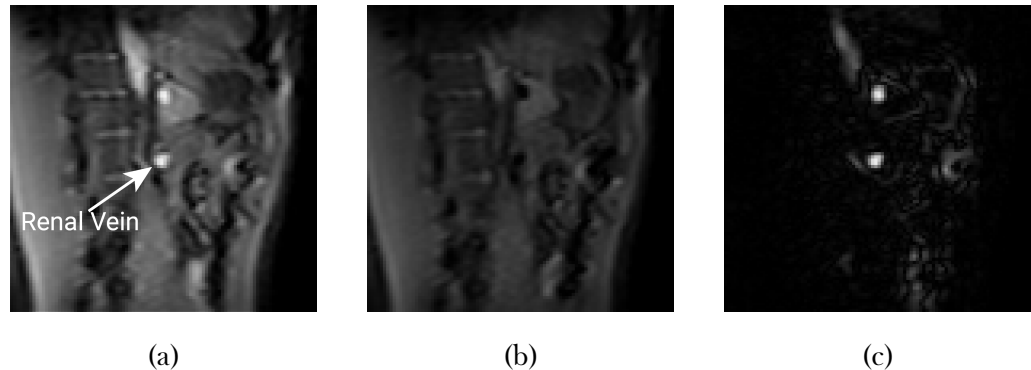


Figure 4.8: The raw images generated when using the FAIR labelling scheme on the kidneys. The non-selective image (a) from which the selective image is subtracted (b) to generate (c), an image of labelled blood in the renal vein. Note, the individual label and control FAIR images from the brain are omitted as they are very similar to those shown in Figure 4.4 for the TILT labelling scheme.

When using the FAIR labelling scheme on the brain the following parameters were used: selective slab thickness = 25 mm, non-selective slab thickness = 400 mm, FOV =  $220 \times 220 \times 5$  mm, matrix size =  $64 \times 64$ , voxel size =  $3.44 \times 3.44 \times 5$  mm, SENSE = 3, EPI factor = 15,  $T_1$  = 1624 ms, PLD = 800 ms, TR = 7276 ms, TE = 2.9 ms, eTE = 1 ms, 40 ms, 80 ms and 160 ms with three pairs of images acquired at each. When used on the body, the parameters were as follows: selective slab thickness = 25 mm, non-selective slab thickness = 400 mm, FOV =  $244 \times 244 \times 5$  mm, matrix size =  $96 \times 96$ , voxel size =  $3.44 \times 3.44 \times 5$  mm, SENSE = 3, EPI factor = 15,  $T_1$  = 1624 ms, PLD = 1000 ms, the choice of this value will be explored later, TR = 8076 ms, TE = 2.9 ms, eTE = 1 ms, 40 ms, 80 ms and 160 ms with three pairs of images acquired at each.

### Analysis

The analysis of the data collected using the above protocol was carried out using custom MATLAB (MathWorks, Natick, MA) software based upon code written by Liu *et al* (in collaboration with Professor Hanzhang Lu, John Hopkins University, USA) modified to work with data collected using the FAIR labelling method [34]. This software loads the data and performs a subtraction of each image pair then presents a difference image to the user so the vessel can be drawn around. At this point the voxels with the greatest intensity within the vessel, four voxels when calculating  $Y_v$  for the superior sagittal sinus and nine voxels when working on the renal vein, are averaged, as are the intensities of each repeat eTE. These mean signals are then fit to Equation (4.5) to compute a value of  $T_2$  with confidence bounds. The value of  $Y_v$  can then be found using the calibration curve, Figure 4.5. Once the software has completed, it saves all outputs and intermediary variables to a file on the computer for later analysis.

### 4.2.3 Inducing Changes in Oxygenation of Blood in the Renal Vein

In order to assess the ability of these methods to measure a change in renal oxygenation, a method of inducing such a change in the kidneys needed to be performed. To address this, literature suggests that changes in renal oxygenation can be induced by varying the subjects sodium intake, water intake or inspired oxygen level [35, 36].

The use of sodium intake was discounted due to the challenges associated with controlling subjects diet for two weeks as was performed in Prijm [37]. From pilot work we know that applying a large water load to subjects during the scanning session, as in Tumkur and Prasad [38, 39], can cause undesired effects on the resultant shim, as assessed by  $B_0$  maps, due to the large susceptibility change adding such a large quantity of water to the abdomen can

## 4.2. Methods

---

cause, as such, this method was discounted and so the study was performed by applying an oxygen challenge.

This method consisted of localisers and anatomical images collected followed by alternating BOLD  $T_2^*$  and TRUST scans while the subject was breathing room air to record a baseline. Pure oxygen was then delivered to the subject at 15  $\ell/\text{min}$  via a gas mask and, after a two minute wash in period, the BOLD  $T_2^*$  and TRUST scans were repeated. A visual representation of this protocol can be seen in Figure 4.9. The BOLD  $T_2^*$  scans had a slice thickness of 5 mm, 12 echoes with an initial TE of 5 ms and subsequent echo spacing of 3 ms, the flip angle was 30°. The total scan time was approximately 17 seconds with this being acquired during a single breath hold. The TRUST scans were conducted as described in Section 4.2.2.

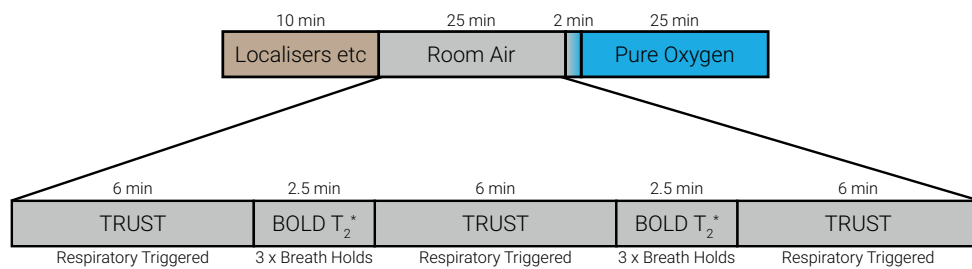


Figure 4.9: The gas challenge protocol used to induce changes in renal oxygenation.

## 4.3 Results and Discussion

### 4.3.1 Susceptibility-Based Oximetry

#### Susceptibility-Based Oximetry in the Brain

Data was collected using the SBO method outlined in 4.2.1 and Equation (4.2) used to estimate  $Y_v$  in the superior sagittal sinus with this found to yield a value of  $63 \pm 2.1\%$ . This is consistent with the value reported by Liu of  $61.1 \pm 1.4\%$  found in a multi centre TRUST trial with 250 participants over a wide range of ages and ethnicity distribution [16].

#### Susceptibility-Based Oximetry in the Renal Vein

Having calculated an acceptable result in the brain in agreement with literature, the pulse sequence was applied to assess oxygenation in the renal vein. Localisers were acquired in the coronal, sagittal and axial planes to enable accurate planning so the renal vein is normal to the phase maps. Three phase maps were acquired and a mean taken. If  $\Delta\phi$  is plotted against  $\theta$  for a typical  $Y_v$  of 85 %, Figure 4.10 is produced. It can be seen that, for an expected  $Y_v$ , the phase difference is greatest if the vessel runs parallel to the  $B_0$  field (as is the case for the sagittal sinus). No part of the renal vein is located parallel to the  $B_0$  field, typically the angle is in the region of  $75^\circ$  (there is a large degree of variability in vasculature geometry between subjects) and as such this delivers a very small phase difference. This coupled with the fact that the gradient of this function at these angles is large, means that a small uncertainty in angle corresponds to a larger uncertainty in  $Y_v$ , thus it is difficult to use SBO to accurately measure  $Y_v$  within the renal vein.

### 4.3. Results and Discussion

---

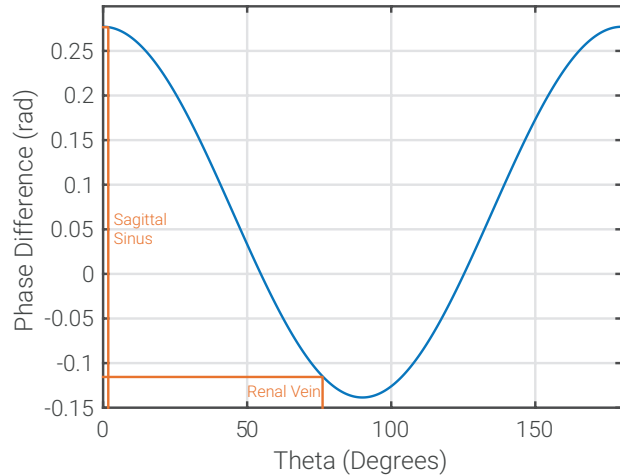


Figure 4.10: For a typical  $Y_v$  of 85 % the phase difference produced by a vessel at a range of angles to  $B_0$ . Note, in the brain the sagittal sinus typically runs at  $0^\circ$  to  $B_0$  whilst the renal vein is at approximately  $75^\circ$  to  $B_0$ .

The SBO technique would be better suited to use in the liver to assess oxygenation in the portal vein. This vessel runs at a much smaller angle to the  $B_0$  field and as such the model will still be valid with reasonable errors, Figure 4.11. This would potentially work much better than TRUST here as the sequence is much quicker allowing it to be collected in a breath hold, and therefore will be less susceptible to errors caused by movement.

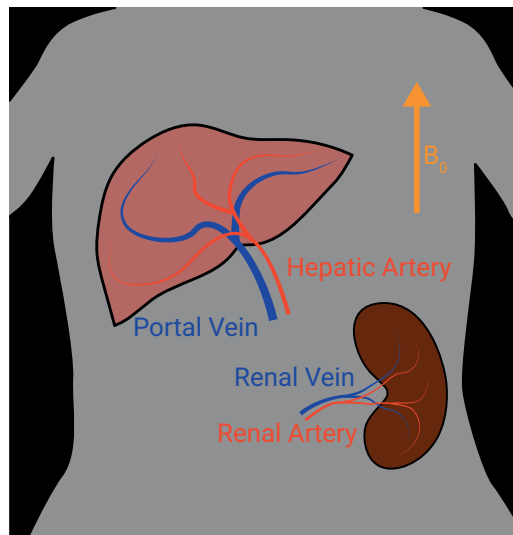


Figure 4.11: A schematic of the portal and renal veins entering the liver and left kidney respectively in relation to the  $B_0$  field.

### 4.3.2 $T_2$ Relaxation Under Spin Tagging

#### Applying TRUST in the Brain: Comparison of Labelling Schemes

To test if the FAIR labelling scheme delivered the same signal decay as the TILT sequence both labelling schemes were performed sequentially to assess the blood  $T_2$  of the superior sagittal sinus, here using a PLD of 800 ms as typically applied in the brain. The resulting normalised signals are shown in Figure 4.12.

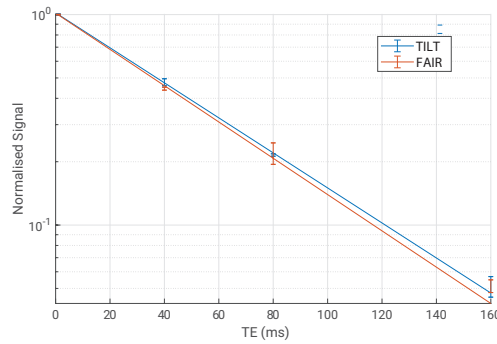


Figure 4.12: The signal decay within the superior sagittal sinus measured using TRUST for the TILT and FAIR labelling schemes scaled by their initial signal intensities at eTE = 1 ms. Error bars are the standard deviation within the ROI.

As can be seen these signals are in excellent agreement with the TILT sequence yielding a venous blood  $T_2$  of  $52 \pm 1$  ms corresponding to a  $Y_v$  of  $55 \pm 1\%$  and the FAIR sequence yielding a venous blood  $T_2$  of  $50 \pm 2$  ms corresponding to a  $Y_v$  of  $53 \pm 2\%$ , therefore in agreement within the bounds of error. Having evaluated the accuracy of the FAIR scheme to measure  $Y_v$  in the superior sagittal sinus it was then used for the renal TRUST measurements.

First, the dependence of the signal on PLD was measured with scans collected at a range of delays from 400 to 1400 ms for the FAIR labelling scheme. The signal from eTE=1 ms was then plotted against label delay. Figure 4.13 shows the signal from the sagittal sinus from the brain FAIR

### 4.3. Results and Discussion

---

difference images. The maximum signal is observed with a PLD of 800 ms. This value is reached due to the balance between  $T_1$  relaxation of the non-selective blood and inflow of unlabelled blood. This maximum in signal agrees with literature using the TILT labelling scheme for assessing the sagittal sinus [13]. By carrying out scans with this PLD the maximum Signal to Noise Ratio (SNR) will be achieved.

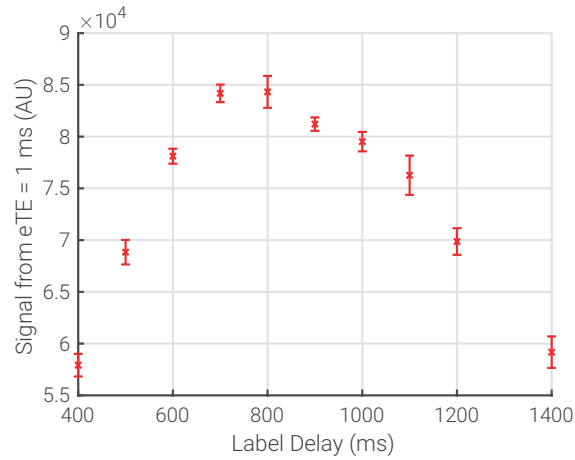


Figure 4.13: The mean signal from the first echo ( $eTE = 1$  ms) of each difference image over a range of PLD times.

$T_2$  should have no dependence upon PLD given the signal from the difference image will have the same decay time, it will just be of lower intensity for a non-optimal PLD thus leading to a larger confidence interval. To confirm this, the fit values of  $T_2$  in the sagittal sinus were plotted against PLD, Figure 4.14.

### 4.3. Results and Discussion

---

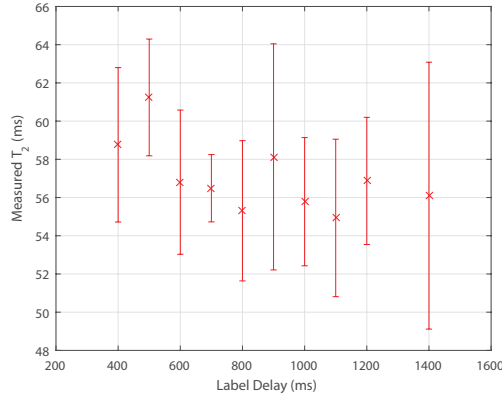


Figure 4.14: The dependence of  $T_2$  in the sagittal sinus on PLD. Error bars are calculated from the confidence in  $T_2$  fit.

It can be seen that, as predicted, there is no relationship between  $T_2$  and PLD. An increase in error with label delay was not observed, this effect may only show itself at larger values of PLD however here it is confirmed there is no large increase in error around the chosen PLD. This means that if there is a variation in the optimum PLD between subjects due to the larger range in RBF compared to Cerebral Blood Flow (CBF) then this will not have an affect upon the value of  $T_2$  and thus  $Y_v$ .

To further evaluate the brain TRUST data, an analysis was performed to assess the dependence of the measured  $T_2$  of blood in the sagittal sinus on number of voxels. Typically the four brightest voxels of the difference image are averaged before the fitting occurs, this number of voxels is chosen due to the average size of the superior sagittal sinus. The analysis was run multiple times with one to twelve voxels averaged before the calculation. Figure 4.15a shows how  $T_2$  changes as the number of voxels included in the calculation is increased.

### 4.3. Results and Discussion

---

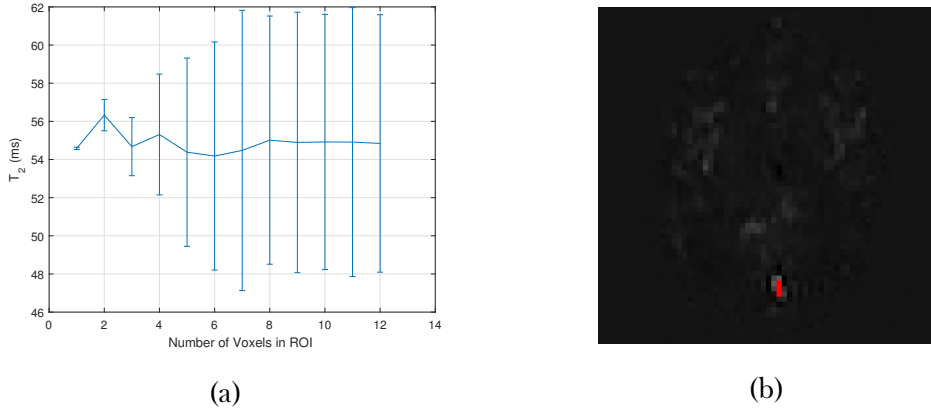


Figure 4.15: (a) The value of  $T_2$  computed for the superior sagittal sinus as a function of the number of voxels included in the calculation. Error bars are propagated errors based on the uncertainty in the  $T_2$  fit and variance between two repeated acquisitions. (b) The difference image of the superior sagittal sinus with a three voxel ROI shown. Note this size ROI contains most of the sagittal sinus, hence the noise level drawn into the fit as more voxels are included in the calculation, as seen in (a).

Although from Figure 4.15a including only the brightest voxel yields a very small confidence interval and a similar  $T_2$  as the results with far more voxels; this would not be a very robust method. It is fairly easy to conceive a greater than average level of noise being recorded on a single voxel in the relaxation and as such skewing the output of the calculation. The confidence interval is so large above six voxels because by this point the calculations are simply including the noise around the vessel rather than the signal from the blood within the sagittal sinus. Given these results, using four voxels in the calculation produces a reasonable balance between uncertainty and robustness. An alternative method to choose the number of voxels included in the ROI based on the standard deviation within the ROI could be developed, this would allow the number of voxels to be calculated on a subject by subject basis however should be validated on multiple subjects.

To assess the repeatability of this measure, the optimised scan was repeated ten times on a single subject during one scanning session. This

### 4.3. Results and Discussion

---

yielded a  $Y_v$  of  $69.5 \pm 0.6\%$ , a value consistent with literature [12, 16]. Given the success of the modified sequence on the superior sagittal sinus, the respiratory triggered version of the sequence was then applied to attempt to measure  $Y_v$  in the renal vein.

#### TRUST in the Body

Ideal vessels to initially test the TRUST sequence within the body are the portal vein and hepatic artery which feed the liver as these vessels are large and have very different oxygen saturations since the hepatic artery delivers oxygenated blood from the general circulation whilst the portal vein delivers deoxygenated blood from the small intestine. These vessels can easily be imaged at the same time in a single slice. Thus these vessels were evaluated using the modified TRUST sequence. The  $T_2$  and oxygen saturation of the portal vein was found to be  $109 \pm 5$  ms and  $79.9 \pm 0.8\%$  respectively; the  $T_2$  and oxygen saturation of the hepatic artery was found to be  $160 \pm 10$  ms and  $100 \pm 1\%$  respectively. This shows that, as expected, the oxygen saturation in the hepatic artery is greater than that of the portal vein and therefore the TRUST protocol is sensitive to the expected degrees of oxygenation in the body. Although normally the analysis would simply be based upon the mean of the brightest voxels in the difference image as outlined in Section 4.2.2, in Figure 4.16 a voxel-by-voxel analysis has been carried out for illustrative purposes. Note that far more voxels are available here than in the sagittal sinus.

To assess if the PLD that generates the greatest signal is the same in the renal vein as in the superior sagittal sinus, a series of TRUST scans were collected with PLD ranging from 400 ms to 1400 ms and the signal from  $eTE = 1$  ms plotted.

### 4.3. Results and Discussion

---

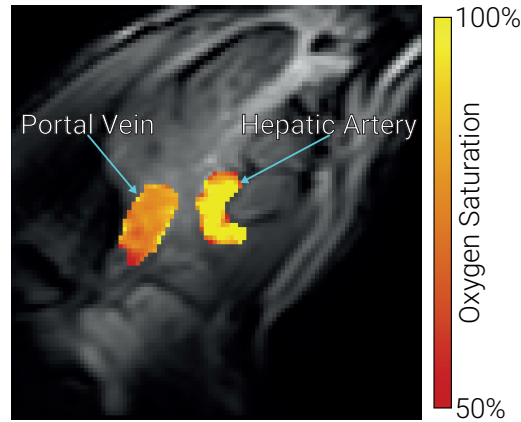


Figure 4.16: The oxygen saturation of the portal vein and hepatic artery measured using the TRUST sequence.

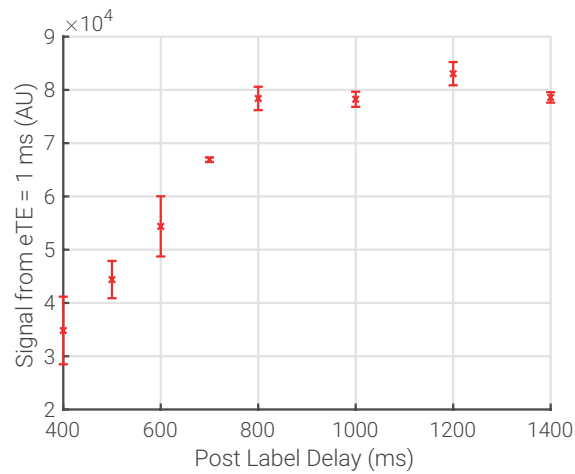


Figure 4.17: The mean signal from the first echo ( $eTE = 1$  ms) of each difference image of the renal vein over a range of PLDs.

As seen in Figure 4.17 the PLD producing the largest signal in the difference image of the renal vein is longer than that of the superior sagittal sinus. This is due to differences in labelling position and blood flow through each of these vessels,  $413 \pm 136$  ml/min in the renal vein [2] and  $285 \pm 19$  ml/min in the superior sagittal sinus [8]. Given the much larger uncertainty in blood flow in the renal vein, an additional subject was scanned. The maximum signal for the first subject was achieved at a PLD of 1200 ms whereas for the second subject the maximum is at a PLD of 800 ms. Given there was little dependence of  $T_2$  upon PLD at the peak, a PLD of 1000 ms

### 4.3. Results and Discussion

---

was chosen for optimum signal in most subjects.

Given the larger size of the renal vein compared to the superior sagittal sinus, it was assessed whether there would be an advantage in including more voxels in the calculations when fitting to compute of  $T_2$ . Three scans were acquired of the same subject, the value of  $T_2$  (and uncertainty in fit) was found using one to twelve voxels from each scan,  $T_2$  values of each scan were then averaged to generate Figure 4.18a.

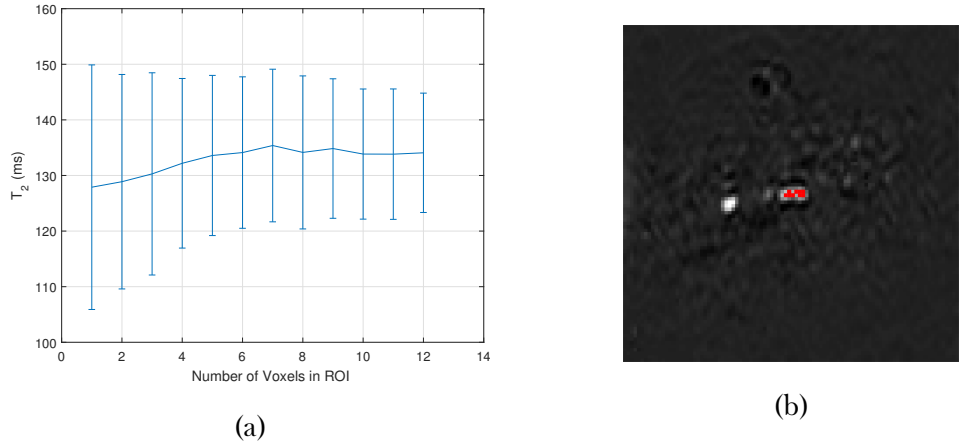


Figure 4.18: (a) The value of  $T_2$  calculated for the renal vein with different numbers of voxels included in the calculation. Error bars are propagated errors based on the uncertainty in the  $T_2$  fit and variance between four repeat acquisitions. (b) The difference image of the renal vein with a nine voxel ROI shown.

Unlike the results for when this process was carried out on the superior sagittal sinus, Figure 4.15a, here the error decreases as more voxels are added to the calculation. This uncertainty comes from the large variation in  $T_2$  for one voxel rather than a large error on the fit i.e. the error is coming from the differences between scans rather than the robustness of each individual result, this is the concern discussed above with using a single voxel in the context of superior sagittal sinus. As more voxels are added the error decreases until approximately six voxels are included, at this point the value of  $T_2$  plateaus to an approximate constant. Given the large variation in renal veins, this data suggests it would be advisable to include more voxels than used in the

### 4.3. Results and Discussion

---

sagittal sinus. Nine voxels was chosen as a suitable middle ground as to work effectively with both small and large vessels.

To assess the repeatability of the measurements within the kidney, the same scan was repeated ten times in a single session with the optimised renal parameters, Figure 4.19. This yielded a  $T_2$  of  $135 \pm 5$  ms corresponding to a  $Y_v$  of  $89 \pm 2$  %. The value of  $Y_v$  in the renal vein is much higher than in the sagittal sinus however is within the range found by Nielsen *et al* when drawing blood samples directly from the renal vein via insertion of a catheter and processing with an OSM<sub>2</sub> Radiometer to calculate  $Y_v$  [40, 41].

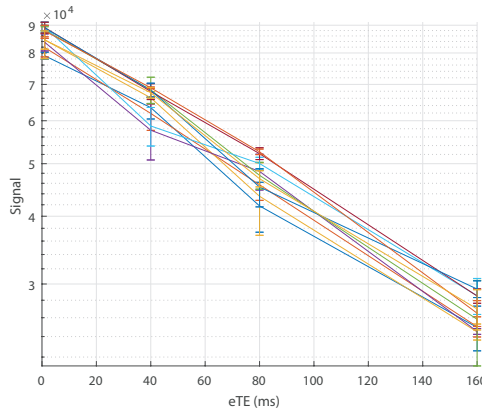


Figure 4.19: The  $T_2$  relaxation curves of ten scans repeated on a single subject.

Finally, to compare the ability of BOLD  $T_2^*$  maps and TRUST to measure changes in oxygenation in the kidneys, a hyperoxia challenge was conducted on a single subject as a proof of concept. In Figure 4.20a, no trend in change in  $T_2^*$  is observed. This indicates that any change in  $T_2^*$  caused by the introduction of pure oxygen is obscured by other confounding factors. This is confirmed when ROIs are defined for the renal cortex and renal medulla with the mean change in  $T_2^*$  found to be  $-2 \pm 8$  ms and  $-1 \pm 6$  ms respectively. When TRUST was used to measure the oxygen saturation in the renal vein an increase of  $16 \pm 3$  % was observed on hyperoxia, Figure 4.20b. This demonstrates that it is possible to measure changes in renal oxygenation using TRUST that would be undetectable using the current standard, BOLD  $T_2^*$  mapping.

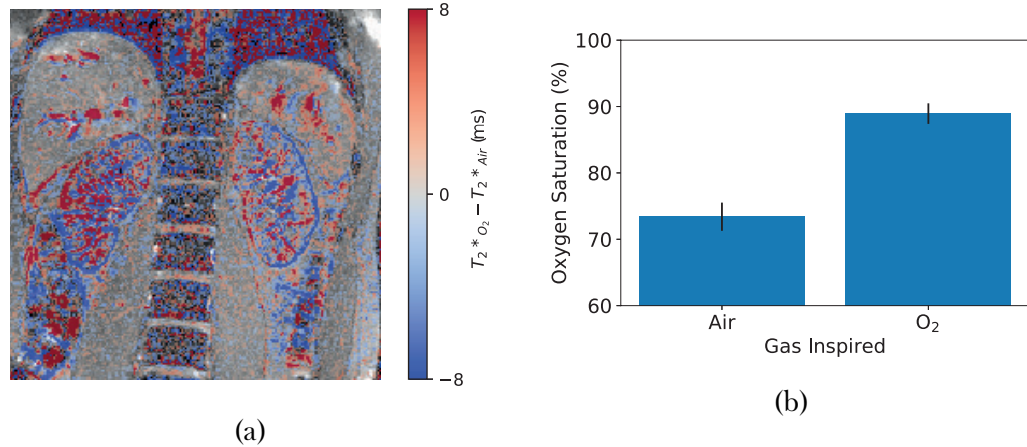


Figure 4.20: (a), The difference in  $T_2^*$  measured between baseline and the hyperoxia state. (b) The difference in  $Y_v$  measured using TRUST. Error bars are propagated from the certainty in the fit  $T_2$  over three scans while the subject was breathing air and three scans while the subject was breathing oxygen.

## 4.4 Conclusions and Future Work

This work has demonstrated the implementation of a modified TRUST sequence to measure oxygenation of blood within the body. The TRUST sequence was modified for use in the abdomen by coding it to be respiratory triggered and use the FAIR labelling scheme. Once these modifications had been carried out, parameters such as the PLD and the number of voxels used in the ROI were optimised. The sequence has been demonstrated initially on the portal vein and hepatic artery where the different degrees of deoxygenated and oxygenated blood can be mapped. The sequence is then developed for the assessment of renal vein oxygenation. The ability of TRUST to measure a change in renal oxygenation was successfully verified via a hyperoxia challenge which was able to measure an increase of  $16 \pm 3\%$  where the current standard measurement of renal oxygenation, BOLD  $T_2^*$  maps, recorded no significant change.

#### 4.4. Conclusions and Future Work

---

In future work this could be expanded by carrying out the hyperoxia challenge on more subjects. Although a small number of measurements were gathered on the hepatic vessels, further work could be undertaken to compare the use of SBO and TRUST to measure oxygenation in the portal vein in response to a hyperoxia challenge as conducted for the kidneys here. These methods could also be applied to the study of drugs on liver oxygenation. Due to limitations imposed by the COVID-19 pandemic, performing further studies of hyperoxia has not been feasible. In the current protocol, the haematocrit is assumed to be an average value of 0.41 unless a blood test has recently been undertaken. As stated above, there is a correlation between  $T_1$  of blood and its haematocrit, this means that an estimate of the subjects haematocrit could be taken while they are in the scanner, thus leading to a more accurate measurement of oxygenation with only a small increase in scan time. This would be especially important when using TRUST on patients rather than healthy volunteers as their haematocrit has a larger variance. By combining TRUST measurements with PC-MRI measures, it is possible to estimate the Renal Metabolic Rate of Oxygen ( $\text{RMRO}_2$ ).

During the course of this PhD, the effects of COVID-19 on the lungs has been well documented, however the effects of this disease on other organs, including the kidneys, is less well known. Initial reports show a high incidence of Acute Kidney Injury (AKI) in COVID-19 [42–44] with other retrospective studies showing that COVID-19 is an independent risk factor for AKI [45, 46]. It is hypothesised that COVID-19 induces a reduction in renal oxygenation leading to AKI. The modified TRUST sequence developed in this thesis, in addition to other quantitative renal MRI protocols, is currently being used to study COVID-19 subjects to better understand the link between AKI and the ongoing pandemic. In collaboration with Uppsala University, data is being collected in both the acute phase of COVID-19 whilst patients are on ventilators and at follow-up. Patients are scanned in Uppsala and data is analysed in Nottingham. It has been demonstrated that in healthy subjects the renal venous oxygenation is of the order of  $86 \pm 7\%$  whereas in COVID-19 oxygenation of blood in the renal vein is of the order of  $59 \pm 8\%$ . It may be

#### 4.5. Acknowledgements

---

that this hypoxia is the cause of inflammation in the kidney.

## **4.5 Acknowledgements**

I thank Professor Hanzhang Lu for sharing the TRUST methodology.

## 4.6 References

1. Daniel, A. J., Cox, E., Buchanan, C., Bradley, C. & Francis, S. *Applying T2 Relaxation Under Spin Tagging (TRUST) to Assess Renal Oxygenation in the Kidney* in *Proc. Intl. Soc. Mag. Reson. Med.* 26 International Society of Magnetic Resonance in Medicine Annual Meeting (Paris, 21st July 2018).
2. Cox, E. F., Buchanan, C. E., Bradley, C. R., Prestwich, B., Mahmoud, H., Taal, M., Selby, N. M. & Francis, S. T. Multiparametric Renal Magnetic Resonance Imaging: Validation, Interventions, and Alterations in Chronic Kidney Disease. *Frontiers in Physiology* **8**, 696 (2017).
3. Buchanan, C. E., Mahmoud, H., Cox, E. F., McCulloch, T., Prestwich, B. L., Taal, M. W., Selby, N. M. & Francis, S. T. Quantitative Assessment of Renal Structural and Functional Changes in Chronic Kidney Disease Using Multi-Parametric Magnetic Resonance Imaging. *Nephrology Dialysis Transplantation* **35**, 955–964 (29th June 2019).
4. Pruijm, M., Milani, B. & Burnier, M. Blood Oxygenation Level-Dependent MRI to Assess Renal Oxygenation in Renal Diseases: Progresses and Challenges. *Frontiers in Physiology* **7**. doi:10 . 3389 / fphys . 2016 . 00667. pmid: 28105019 (5th Jan. 2017).
5. Niendorf, T. *et al.* How Bold Is Blood Oxygenation Level-Dependent (BOLD) Magnetic Resonance Imaging of the Kidney? Opportunities, Challenges and Future Directions. *Acta Physiologica* **213**, 19–38 (10th Sept. 2014).
6. Milani, B. *et al.* Reduction of Cortical Oxygenation in Chronic Kidney Disease: Evidence Obtained with a New Analysis Method of Blood Oxygenation Level-Dependent Magnetic Resonance Imaging. *Nephrology Dialysis Transplantation* **32**, 2097–2105 (1st Dec. 2017).
7. Chong, S. P., Merkle, C. W., Leahy, C. & Srinivasan, V. J. Cerebral Metabolic Rate of Oxygen (CMRO<sub>2</sub>) Assessed by Combined Doppler and Spectroscopic OCT. *Biomedical Optics Express* **6**, 3941–3951 (11th Sept. 2015).

#### 4.6. References

---

8. Jordan, J. E., Pelc, N. J. & Enzmann, D. R. Velocity and Flow Quantitation in the Superior Sagittal Sinus with Ungated and Cine (Gated) Phase-Contrast MR Imaging. *Journal of Magnetic Resonance Imaging* **4**, 25–28 (1st Jan. 1994).
9. Miao, G., Qingsheng, Y., Zhiyuan, R., Hongxian, Z., Yanfang, Z. & Shuyan, Y. Reference Value of Presenile Human Hematocrit and Geographical Factors. *Journal of Clinical Laboratory Analysis* **16**, 26–29 (1st Jan. 2002).
10. Gardener, A. G., Francis, S. T., Prior, M., Peters, A. & Gowland, P. A. Dependence of Blood R2 Relaxivity on CPMG Echo-Spacing at 2.35 and 7 T. *Magnetic Resonance in Medicine* **64**, 967–974 (1st Oct. 2010).
11. Shimada, K., Nagasaka, T., Shidahara, M., Machida, Y. & Tamura, H. In Vivo Measurement of Longitudinal Relaxation Time of Human Blood by Inversion-Recovery Fast Gradient-Echo MR Imaging at 3T. *Magnetic resonance in medical sciences: MRMS: an official journal of Japan Society of Magnetic Resonance in Medicine* **11**, 265–271 (2012).
12. Nagdyman, N., Fleck, T., Schubert, S., Ewert, P., Peters, B., Lange, P. E. & Abdul-Khalil, H. Comparison between Cerebral Tissue Oxygenation Index Measured by Near-Infrared Spectroscopy and Venous Jugular Bulb Saturation in Children. *Intensive Care Medicine* **31**, 846–850 (1st June 2005).
13. Lu, H. & Ge, Y. Quantitative Evaluation of Oxygenation in Venous Vessels Using T2-Relaxation-Under-Spin-Tagging MRI. *Magnetic Resonance in Medicine* **60**, 357–363 (1st Aug. 2008).
14. Xu, F., Uh, J., Liu, P. & Lu, H. On Improving the Speed and Reliability of T2-Relaxation-Under-Spin-Tagging (TRUST) MRI. *Magnetic Resonance in Medicine* **68**, 198–204 (July 2012).
15. Liu, P., Xu, F. & Lu, H. Test–Retest Reproducibility of a Rapid Method to Measure Brain Oxygen Metabolism. *Magnetic Resonance in Medicine* **69**, 675–681 (1st Mar. 2013).

#### 4.6. References

---

16. Liu, P. *et al.* Multi-Site Evaluations of a T2-Relaxation-Under-Spin-Tagging (TRUST) MRI Technique to Measure Brain Oxygenation. *Magnetic resonance in medicine* **75**, 680–687 (Feb. 2016).
17. Jain, V., Langham, M. C. & Wehrli, F. W. MRI Estimation of Global Brain Oxygen Consumption Rate. *Journal of Cerebral Blood Flow & Metabolism* **30**, 1598–1607 (1st Sept. 2010).
18. Jain, V. *et al.* Cerebral Oxygen Metabolism in Neonates with Congenital Heart Disease Quantified by MRI and Optics. *Journal of Cerebral Blood Flow & Metabolism* **34**, 380–388 (1st Mar. 2014).
19. Driver, I. D., Wharton, S. J., Croal, P. L., Bowtell, R., Francis, S. T. & Gowland, P. A. Global Intravascular and Local Hyperoxia Contrast Phase-Based Blood Oxygenation Measurements. *NeuroImage* **101**, 458–465 (1st Nov. 2014).
20. Lee, H., Langham, M. C., Rodriguez-Soto, A. E. & Wehrli, F. W. Multiplexed MRI Methods for Rapid Estimation of Global Cerebral Metabolic Rate of Oxygen Consumption. *NeuroImage* **149**, 393–403 (1st Apr. 2017).
21. Wright, G. A., Hu, B. S. & Macovski, A. Estimating Oxygen Saturation of Blood in Vivo with MR Imaging at 1.5 T. *Journal of Magnetic Resonance Imaging* **1**, 275–283 (1st May 1991).
22. Haacke, E. M., Lai, S., Reichenbach, J. R., Kuppusamy, K., Hogenraad, F. G., Takeichi, H. & Lin, W. In Vivo Measurement of Blood Oxygen Saturation Using Magnetic Resonance Imaging: A Direct Validation of the Blood Oxygen Level-Dependent Concept in Functional Brain Imaging. *Human Brain Mapping* **5**, 341–346 (1st Jan. 1997).
23. Spees, W. M., Yablonskiy, D. A., Oswood, M. C. & Ackerman, J. J. Water Proton MR Properties of Human Blood at 1.5 Tesla: Magnetic Susceptibility, T1, T2, T\*2, and Non-Lorentzian Signal Behavior. *Magnetic Resonance in Medicine* **45**, 538–542 (1st Apr. 2001).
24. Jain, V., Abdulmalik, O., Propert, K. J. & Wehrli, F. W. Investigating the Magnetic Susceptibility Properties of Fresh Human Blood for

#### 4.6. References

---

- Noninvasive Oxygen Saturation Quantification. *Magnetic Resonance in Medicine* **68**, 863–867 (1st Sept. 2012).
- 25. Lu, H., Clingman, C., Golay, X. & van Zijl, P. C. Determining the Longitudinal Relaxation Time (T1) of Blood at 3.0 Tesla. *Magnetic Resonance in Medicine* **52**, 679–682 (1st Sept. 2004).
  - 26. Jenkinson, M. Fast, Automated, N-Dimensional Phase-Unwrapping Algorithm. *Magnetic Resonance in Medicine* **49**, 193–197 (1st Jan. 2003).
  - 27. Hendrikse, J., Lu, H., van der Grond, J., van Zijl, P. C. & Golay, X. Measurements of Cerebral Perfusion and Arterial Hemodynamics during Visual Stimulation Using TURBO-TILT. *Magnetic Resonance in Medicine* **50**, 429–433 (1st Aug. 2003).
  - 28. Golay, X., Petersen, E. T. & Hui, F. Pulsed Star Labeling of Arterial Regions (PULSAR): A Robust Regional Perfusion Technique for High Field Imaging. *Magnetic Resonance in Medicine* **53**, 15–21 (1st Jan. 2005).
  - 29. Golay, X., Stuber, M., Pruessmann, K. P., Meier, D. & Boesiger, P. Transfer Insensitive Labeling Technique (TILT): Application to Multislice Functional Perfusion Imaging. *Journal of Magnetic Resonance Imaging* **9**, 454–461 (1st Mar. 1999).
  - 30. Silvennoinen, M., Clingman, C., Golay, X., Kauppinen, R. & van Zijl, P. Comparison of the Dependence of Blood R2 and R2\* on Oxygen Saturation at 1.5 and 4.7 Tesla. *Magnetic Resonance in Medicine* **49**, 47–60 (1st Jan. 2003).
  - 31. Liu, P., Chalak, L. F., Krishnamurthy, L. C., Mir, I., Peng, S.-l., Huang, H. & Lu, H. T1 and T2 Values of Human Neonatal Blood at 3 Tesla: Dependence on Hematocrit, Oxygenation, and Temperature. *Magnetic Resonance in Medicine* **75**, 1730–1735 (Apr. 2016).
  - 32. Lu, H., Xu, F., Grgac, K., Liu, P., Qin, Q. & van Zijl, P. Calibration and Validation of TRUST MRI for the Estimation of Cerebral Blood Oxygenation. *Magnetic Resonance in Medicine* **67**, 42–49 (1st Jan. 2012).

#### 4.6. References

---

33. Martirosian, P., Klose, U., Mader, I. & Schick, F. FAIR True-FISP Perfusion Imaging of the Kidneys. *Magnetic Resonance in Medicine* **51**, 353–361 (1st Feb. 2004).
34. Liu, P., Cox, E. & Daniel, A. *Pro TRUST* version V2018.5. 23rd Aug. 2011.
35. O'Connor, J. P. *et al.* Comparison of Normal Tissue R1 and R\*2 Modulation by Oxygen and Carbogen. *Magnetic Resonance in Medicine* **61**, 75–83 (1st Jan. 2009).
36. Donati, O. F., Nanz, D., Serra, A. L. & Boss, A. Quantitative BOLD Response of the Renal Medulla to Hyperoxic Challenge at 1.5 T and 3.0 T. *NMR in Biomedicine* **25**, 1133–1138 (1st Oct. 2012).
37. Pruijm, M., Hofmann, L., Maillard, M., Tremblay, S., Glatz, N., Wuerzner, G., Burnier, M. & Vogt, B. Effect of Sodium Loading/Depletion on Renal Oxygenation in Young Normotensive and Hypertensive Men. *Hypertension* **55**, 1116–1122 (1st May 2010).
38. Tumkur, S. M., Vu, A. T., Li, L. P., Pierchala, L. & Prasad, P. V. Evaluation of Intra-Renal Oxygenation during Water Diuresis: A Time-Resolved Study Using BOLD MRI. *Kidney International* **70**, 139–143 (1st July 2006).
39. Prasad, P. V. & Epstein, F. H. Changes in Renal Medullary pO<sub>2</sub> during Water Diuresis as Evaluated by Blood Oxygenation Level-Dependent Magnetic Resonance Imaging: Effects of Aging and Cyclooxygenase Inhibition. *Kidney International* **55**, 294–298 (1st Jan. 1999).
40. Nielsen, K., Rehling, M. & Henriksen, J. H. Renal Vein Oxygen Saturation in Renal Artery Stenosis. *Clinical Physiology* **12**, 179–184 (1st Mar. 1992).
41. Saloojee, Y., Cole, P. V. & Adam, L. The Evaluation of a Photometer (the Radiometer OSM2) for the Determination of Haemoglobin Concentration and per Cent Oxyhaemoglobin and Carboxyhaemoglobin in Blood. *Journal of Medical Engineering & Technology* **5**, 298–300 (1st Jan. 1981).

#### 4.6. References

---

42. Selby, N. M., Forni, L. G., Laing, C. M., Horne, K. L., Evans, R. D., Lucas, B. J. & Fluck, R. J. Covid-19 and Acute Kidney Injury in Hospital: Summary of NICE Guidelines. *BMJ* **369**, m1963 (26th May 2020).
43. Fisher, M. *et al.* AKI in Hospitalized Patients with and without COVID-19: A Comparison Study. *Journal of the American Society of Nephrology* **31**, 2145–2157 (1st Sept. 2020).
44. Gabarre, P., Dumas, G., Dupont, T., Darmon, M., Azoulay, E. & Zafrani, L. Acute Kidney Injury in Critically Ill Patients with COVID-19. *Intensive Care Medicine* **46**, 1339–1348 (1st July 2020).
45. Kolhe, N. V., Fluck, R. J., Selby, N. M. & Taal, M. W. *Acute Kidney Injury Associated with COVID-19: A Retrospective Cohort Study* SSRN Scholarly Paper ID 3627261 (Social Science Research Network, Rochester, NY, 8th June 2020). doi:10.2139/ssrn.3627261.
46. Adapa, S. *et al.* COVID-19 Pandemic Causing Acute Kidney Injury and Impact on Patients With Chronic Kidney Disease and Renal Transplantation. *Journal of Clinical Medicine Research* **12**, 352–361 (June 2020).

## **Chapter 5**

# **Automated Segmentation of Kidneys using Machine Learning**

---

## Abstract

Total Kidney Volume (TKV) is an important measure in renal disease detection and monitoring. Here a fully automated method to segment the kidneys from  $T_2$ -weighted MR images to calculate TKV of Healthy Control (HC) and Chronic Kidney Disease (CKD) patients is developed.

This automated method uses machine learning, specifically a 2D Convolutional Neural Network (CNN), to accurately segment the left and right kidneys from  $T_2$ -weighted Half-Fourier Acquisition Single-shot Turbo spin Echo (HASTE) images. The dataset consisted of 30 HC subjects and 30 CKD patients. The model was trained on 50 manually defined HC and CKD kidney segmentations. It was subsequently evaluated on 50 test data sets, comprising data from five HCs and five CKD patients each scanned five times in a scan session to enable comparison of the precision of the CNN and manual segmentation of kidneys.

The unseen test data processed by the 2D CNN had a mean Dice score of  $0.93 \pm 0.01$ . The difference between manual and automatically computed TKV was  $1.2 \pm 16.2 \text{ mL}$  with a mean surface distance of  $0.65 \pm 0.21 \text{ mm}$ . The variance in TKV measurements from repeat acquisitions on the same subject was significantly lower using the automated method compared to manual segmentation of the kidneys.

The 2D CNN method provides fully automated segmentation of the left and right kidney and calculation of TKV in under ten seconds on a standard office computer, allowing high data throughput and is a freely available executable.

*This work was presented as an oral presentation at the International Society of Magnetic Resonance in Medicine (ISMRM) 28th Annual Meeting (2020) and received a Magna Cum Laude Merit Award [1] and has been published as “Automated renal segmentation in healthy and chronic kidney disease subjects using a convolutional neural network.” Magnetic Resonance in Medicine, 23 March 2021 doi: doi.org/10.1002/mrm.28768. [2].*

## 5.1 Introduction

Segmentation of the kidneys from Magnetic Resonance Imaging (MRI) is a time consuming aspect of many renal MRI studies [3–5]. Total Kidney Volume (TKV) gives insight into renal function and is therefore used as a measured parameter for a variety of renal pathologies. The use of TKV is an active area of ongoing research for Autosomal Dominant Polycystic Kidney Disease (ADPKD), which is characterised by an increase in TKV due to cyst formation. Disease progression can be monitored by recording TKV, with higher rates of TKV increase being associated with a more rapid decrease in renal function [6–8]. Measurements of TKV in Chronic Kidney Disease (CKD) subjects have shown a significant correlation with glomerular filtration rate [9], the primary measure of CKD severity [10], with more generally a decrease in TKV associated with a decrease in renal function [11]. When studying pathologies which commonly lead to a change in kidney function, global kidney perfusion is often measured, this metric relies on an accurate measurement of renal blood flow as defined from phase contrast MRI [12] and kidney volume of each kidney, and allows investigators to ascertain if the blood flow is preserved as the organ changes in size or if tissue perfusion is impaired. In addition to TKV measurements, renal segmentation is an important first step for many other processing pipelines, be that for automated cortical-medullary segmentations or to carry out multiparametric mapping within only the kidney to reduce computation time.

The gold standard of kidney segmentation is manual Region Of Interest (ROI) boundary tracing [13] or stereology [14] by experienced and skilled experts, with blood vessels in the kidney and the hilum excluded. These manual processes are highly time consuming (taking approximately 15 – 30 minutes per subject [15–17] and can be biased by investigator judgement due to the similar signal intensities between the kidneys and surrounding organs, anatomical differences between subjects, cysts and image artefacts. Consequently, the resulting kidney ROIs produced are subject to intra- and

### 5.1. Introduction

---

inter-expert variability as a result of the varying expertise levels; experts may segment a specific image differently when performed more than once, or different experts may segment the same image differently. These factors mean that the development of a faster and ideally fully automated method of renal segmentation is highly desirable. However the same factors that make manual segmentation difficult can also limit fully automated methods, for example the signal intensity of the kidneys closely matches that of other abdominal structures such as the spleen.

A number of automated methods to segment the kidneys have been proposed with varied success [15]. Some simply assume the kidney is an ellipse and calculate the volume from measurements of the pole-to-pole distance [18, 19] or include a correction factor to reduce overestimations [20]. Unfortunately these techniques produce a large confidence interval and still require human intervention to define the pole-to-pole length, a process that can produce inconsistencies between readers and takes a reasonable amount of time ( $\approx 5$  min) [21]. Other semi-automated methods use classical image processing techniques such as thresholding [22], water-shedding [23], level sets [17, 24], and spatial prior probability mapping [25]. These methods can either be inaccurate, over-segmenting the kidneys, or include a number of parameters that need to be manually adjusted and are computationally intensive. Further, the fact that each technique is highly optimised for a specific dataset means that it needs to be re-written to be applied to different pathology, another time consuming and highly skilled process.

Machine learning methods have the potential to automatically detect different patterns from data given to a model which has been trained. Deep learning is a class of machine learning algorithms that can model high-level information in an image using several processing layers of transformations. This uses an architecture of multi-level linear and non-linear operations, described by layers, to learn complex functions that can represent high-level detail to map the input data to the output segmentations directly. As more data becomes available the algorithm can become more accurate and

### 5.1. Introduction

---

generalised, without a need to rewrite the underlying methods, thus making it a good choice for long term development.

In recent years, deep learning-based methods have been applied to the segmentation of medical images, especially successful has been the U-Net [26]. This modified fully Convolutional Neural Network (CNN) architecture uses a number of convolution, pooling and up-sampling layers to detect features in the input data at multiple resolutions. The convolution layers convolve a learnable kernel with the input data to generate spatial feature maps that are passed to subsequent layers in the network. By adjusting the kernels, the resulting feature maps can be optimised to detect the location of the kidneys. Pooling layers are used to down-sample the data and allow some convolution kernels to become tuned to approximate features, this also reduces the tendency of the network to overfit the training data. When the data has been fully down-sampled, up-sampling layers are used to increase the resolution of the feature maps back to that of the original data while more convolution layers also learn the precise location of the kidneys. Parameters are adjusted by comparing the output from the network to a known ground truth. CNN methods have been applied to segmentation in other areas of medical imaging [27–30], for example prostate segmentation from MRI images [31], liver segmentation from x-ray Computed Tomography (CT) images [32] and segmentation of polycystic kidneys [33–35]. However, to date, these methods have not been successfully applied to CKD and healthy kidney segmentation from MR images.

Here a single 2D U-Net model CNN is used for the segmentation of the kidneys in both Healthy Control (HC) participants and CKD patients using  $T_2$ -weighted Half-Fourier Acquisition Single-shot Turbo spin Echo (HASTE) MR images. Automatically generated kidney masks are compared with manual masks defined by experts and assessed for similarity using multiple voxel and surface based metrics and total segmented volume. A subset of subjects were scanned multiple times to assess the repeatability of the segmentations.

## 5.2 Neural Networks for Image Segmentation

### 5.2.1 Artificial Neural Networks

Artificial Neural Networks (ANNs) aim to solve computational problems using a similar methodology to their biological namesake. Input data is passed through a series of connected nodes or neurons, each of which can have multiple input and output connections from and to other neurons mimicking synapses. At each neuron, a weighted sum of the input values is calculated before being passed on to the next hidden layer of neurons. The final layer of neurons is connected to the output layer which will give an estimation of the desired property, be that a number e.g. the probability that someone will like a television program, an image e.g. the probability that a pixel in an image is a road sign, or a sample in a time series e.g. audio in voice synthesis. More concisely, an ANN can be used to map a non-linear set of input data to an output dimension.

A very basic example could use the mass and colour of an animal to predict if it is a dog or a cat, Figure 5.1. The connections between neurons are initialised with random weights.

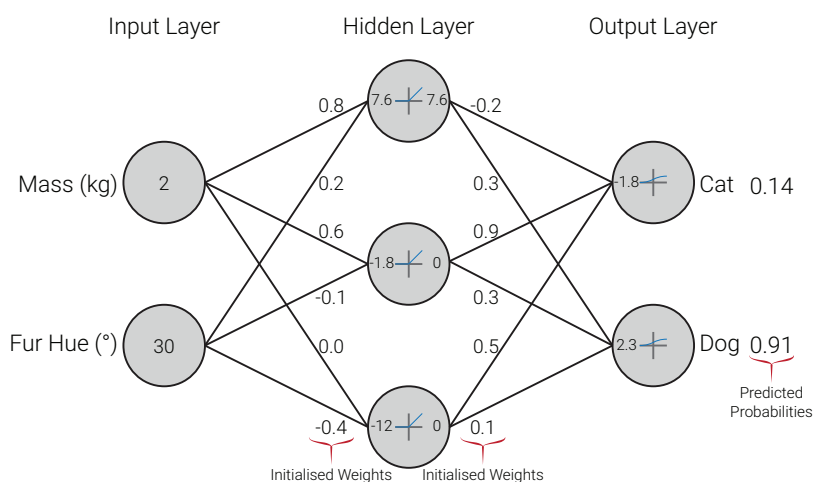


Figure 5.1: The ANN initialised with random numbers to predict the species of a small ginger cat.

At each neuron, a weighted sum of its inputs is taken, then an activation function applied, here a Rectified Linear Unit (ReLU), Figure 5.2a, for the hidden neurons and sigmoid, 5.2b, for the output neurons. These activation functions allow the network to act non-linearly, mimicking the action potential of biological neurons. The ReLU function represents a higher rate of firing for signals above zero; as it is impossible for a biological neuron to reduce its firing rate below zero, the ReLU outputs zero when the input signal is negative. The sigmoid function maps all values between zero and one, and therefore ensures the network outputs a probability at the output nodes.

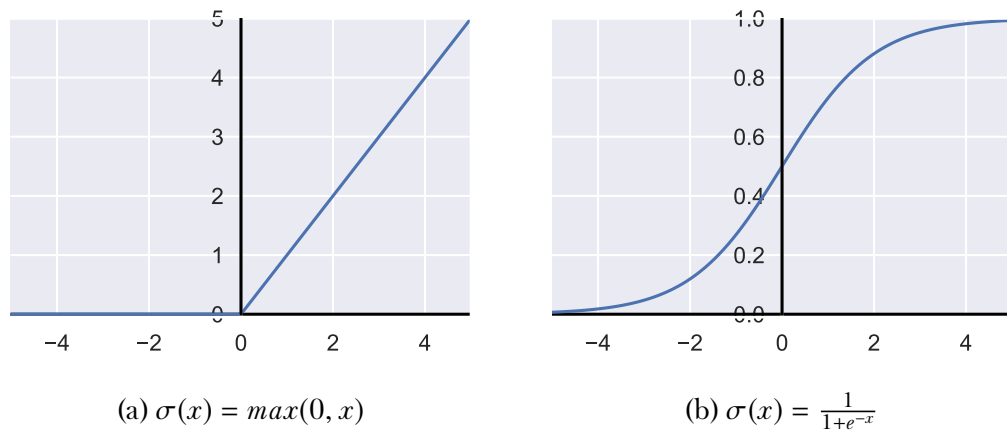


Figure 5.2: Activation functions.

As the weights were randomly initialised, the network has incorrectly predicted that the animal is a dog. By comparing the result output from the network to the known ground truth, the weights of the network can be adjusted in a process known as back propagation, Figure 5.3. Hyper-parameters such as learning rate and momentum control how much each weight is adjusted in response to the input data and the subsequent result.

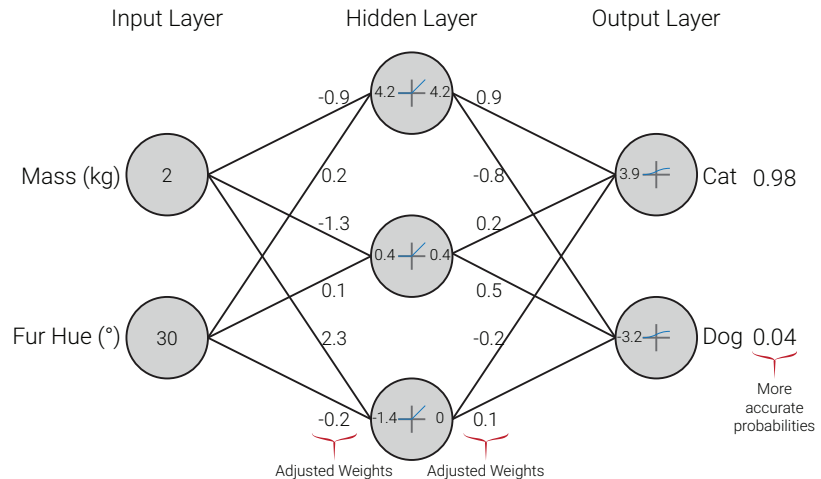


Figure 5.3: The weightings of each connection are adjusted so the output layer produces results closer to the ground truth.

When another animal is input to the network, here a smaller, darker coloured cat, the network now correctly predicts that it is a cat, Figure 5.4. By repeating this procedure many times, comparing the result to the ground truths and adjusting the weights, a process known as training, the network becomes more and more accurate. Once trained, the network can be used to infer the species of animals with no ground truth data.

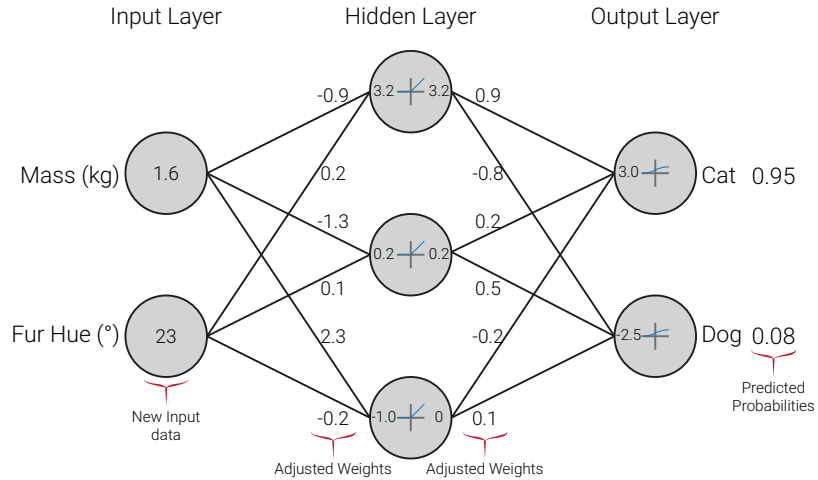


Figure 5.4: New data is presented to the network in the form of a smaller, darker coloured cat and the process of adjusting weights is repeated until more accurate results are produced.

The above example is highly simplified, real ANNs will have many more input nodes and hidden layers. In the case of imaging data, the input layer will simply be a node for each pixel in the image.

### 5.2.2 Convolutional Neural Networks

It was found that ANN segmentation performance was increased if additional features were input to the network. These features could be colour rather than greyscale data, different MRI contrasts e.g. fat/water images or artificially generated features. In Figure 5.5 a selection of artificially generated features are presented from a  $T_2$ -weighted HASTE image, some of these highlight the kidneys from the surrounding tissue e.g. the intensity range adjustment, Figure 5.5b, and edge detector, Figure 5.5f while others are better at providing contrast between the cyst in the right kidney and the renal tissue e.g. the intensity inversion, Figure 5.5c and sharpening filter, Figure 5.5e.

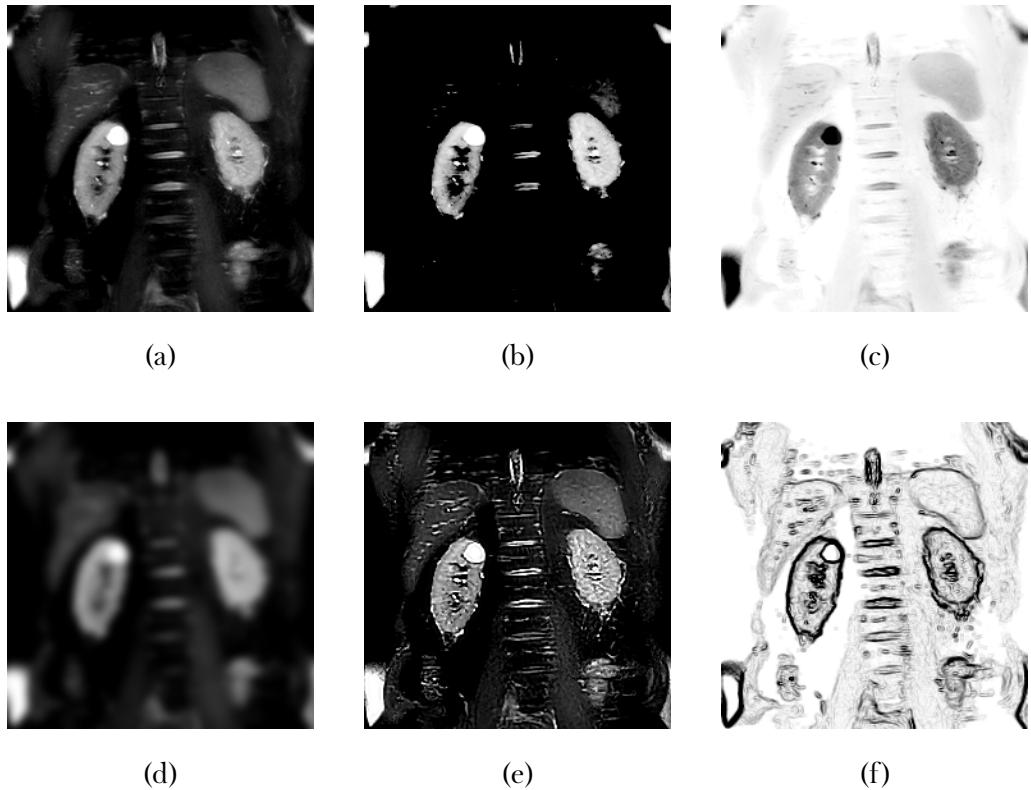


Figure 5.5: An example of the features that can be generated from a  $T_2$ -weighted HASTE image (a). Implemented here are intensity range adjustments (b), intensity inversion (c), Gaussian blur (d), sharpening (e) and edge detection (f).

Many of these artificially generated features can be implemented as convolutional operations, these involve convolving a numerical kernel with every pixel in the image. By adjusting the values of each cell in the kernel, different features or filters can be produced. The control of these kernels can be handed over to similar optimisation processes to those used to adjust the weights of the connections between neurons. Over the training period, this enables the network to learn what features are useful for the task at hand and which are less useful, rather than the network being given features that the programmer thinks will be helpful. Shallow layers of the network usually resemble features similar to those in Figure 5.5 while deeper layers represent more complex and specific objects such as, using the cat and dog example above, pointy noses to distinguish dogs and triangular ears to distinguish cats.

### 5.3. Methods

---

This architecture is known as a Convolutional Neural Network (CNN) [36, 37].

To aid with feature extraction, the raw image is often downsampled by max-pooling layers, this enables different kernels to act on different scales of the image which can help keep the network generalisable and avoid overfitting. The U-Net architecture [26] combines an arm with downsampling and feature extraction with an upsampling arm that returns the image to its initial dimensions making it especially useful for segmentation tasks.

## 5.3 Methods

The study was approved by the University of Nottingham Medical School Research Ethics Committee (H14082014 and E14032013), and East Midlands Research Ethics committee REC reference: 17/LO/2036 and 15/EM/0274.

### 5.3.1 MRI Data Acquisition

All kidney MRI scans were acquired on a 3T Philips Ingenia system (Philips Medical Systems, Best, The Netherlands) using a 2D  $T_2$ -weighted HASTE sequence optimised to achieve the maximum contrast between the kidneys and surrounding tissue, see Section 2.2.5 (Echo Time (TE) = 60 ms, Repetition Time (TR) = 1300 – 1800 ms, Sensitivity Encoding (SENSE) factor = 2.5, refocus angle = 120°, bandwidth = 792 Hz, Field Of View (FOV) =  $350 \times 350 \text{ mm}^2$ , voxel size =  $1.5 \times 1.5 \times 5 \text{ mm}^3$  and a slice gap of 0.5 mm with approximately 13 coronal slices, enough to image the entire kidney [38, 39], in a single 17 - 23 s breath hold.

### **5.3. Methods**

---

The dataset consisted of 60 subjects, 30 HC (10 female, 20 male) with a mean age of  $26 \pm 11$  (19–77) years and 30 CKD patients (6 female, 24 male) with a mean age of  $59 \pm 14$  (19–80) years and mean CKD Stage  $3.5 \pm 1.2$  (1–5). Ten of the subjects (5 HCs and 5 CKD patients) were scanned five times in the same scan session for use as test data. In each test data scan session, subjects were repositioned between each acquisition (removed from the scanner then asked to sit up and move on the bed), additionally the scanner operator attempted to vary the acquisition geometry between each scan while still acquiring full kidney coverage. These repeated test datasets allow the consistency of the networks ability to measure TKV to be assessed.

In total, 649 2D image slices from the 50 subjects in the training data and 650 2D image slices from the 10 subjects in the test data, were collected. A summary of the data collected is provided in Table 5.1 and Figure 5.9.

#### **5.3.2 Manual Segmentation**

The manual binary masks of the kidneys of each subject were generated by one of three observers (A, B and C who had been trained on kidney segmentation and had an average of 2 years of experience), with each observer segmenting data from both the training and testing datasets. Kidney boundaries were manually traced using freely available software (MRIcron [40]) and any area of non-renal parenchyma, such as the renal hilum and cysts, were excluded from the manual definition. Binary masks of the kidney were generated, and the volume of each kidney was computed from the product of the number of voxels in each kidney mask and the voxel volume. The separate kidney volume for the left and right kidneys was determined and summed to compute TKV. All measurements were performed by observers who were blinded to patient number and previous TKV measurements.

For the training phase, for each subject a manual mask was used from a single observer (randomised between observer A, B, or C). For the testing

### **5.3. Methods**

---

phase, all five scans from a given subject were segmented by a single observer with the ten subjects being segmented by a mix of the three observers i.e. the test data comprised of subjects segmented by all observers but the repeat scans of each subject were segmented by the same observer. For four HC subjects from the test dataset, manual masks were drawn by all three observers for all five repeat acquisitions to allow assessment of inter-observer variability in the manual masks. HCs were chosen for this analysis as healthy kidneys have a more consistent morphology and thus will give a best-case measure of observer variability and provide a comparison of the automated method to the highest standard of manual segmentation.

#### **5.3.3 Automated Segmentation Using a CNN Architecture**

Voxel intensities were normalised between 0 and 255, where 0 was set to the mean voxel intensity minus 0.5 times the standard deviation of that volume and 255 was set to the mean voxel intensity plus four times the standard deviation of the volume. This empirically derived windowing led to a clear contrast between the kidneys and surrounding tissue while negating the effects of bulk signal changes between volumes. Each dataset volume was then split into 2D coronal slices and resampled to a matrix size of  $256 \times 256$ . Twenty percent of slices were reserved for validation during the network optimisation process, this validation data was used to monitor over-fitting and direct the optimisation process between epochs. Once the data had been split into training and validation sets, the slice order was randomised within sets. Splitting the data before slice randomisation limited the possibility of slices from only one subject being split over both the training and validation datasets. During training, data augmentation was applied. At the start of each epoch, a batch of images and their corresponding masks was selected at random from the training data and a series of random shifts (up to 25 % of the image in both the horizontal and vertical direction), zooms (between 0.75 and 1.25 magnification), rotations (within a  $20^\circ$  range), and sheers (within a  $5^\circ$  range) were applied to the image/mask pair to produce different

### 5.3. Methods

---

yet anatomically reasonable images. The weights of the network were then adjusted based on this augmented data before selecting a new batch of images for the next epoch. Augmenting the data reduces the tendency of a model to over-fit the training data and thus increases accuracy when the model is applied to unseen images.

The U-Net consisted of two Fully Convolutional Neural Network-like structures that were cascaded in the form of an encoder-decoder (autoencoder) structure. The encoder was used for feature extraction and the decoder was used for feature mapping to the original input resolution. A summary of the network architecture is shown in Figure 5.6. The convolution layers use a set of small parameterised filters, referred to as kernels, to perform convolution operations to produce different feature maps of their input. Here each convolution and deconvolution layer uses a  $3 \times 3$  kernel. Activation layers use a ReLU. Following convolution at each resolution, max pooling with a stride 2 was used on the encoding half of the network.

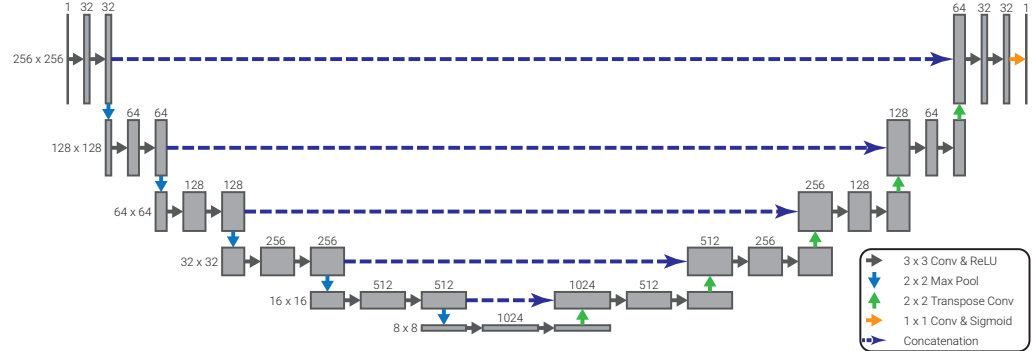


Figure 5.6: The architecture of the U-Net used.

The network was implemented using Keras (v2.2.4) [41] with a TensorFlow backend (v1.13.1) [42] in Python 3.6.9. All training was carried out on an NVIDIA Titan Xp Graphical Processing Unit (GPU) (3840 CUDA cores, 12 GB GDDR5X). The network uses a Dice score loss function, given by,

$$D(A, B) = \frac{2|A \cap B|}{|A| + |B|} = \frac{2TP}{2TP + FP + FN}, \quad (5.1)$$

where  $TP$  is true positive,  $FP$  is false positive and  $FN$  is false negative. A

### 5.3. Methods

---

value of 1 implies complete overlap between the automated mask and the manual mask while 0 implies no overlap. This function is ideal for renal segmentation as it does not weight true negatives which represent the majority of voxels input to the network and thus means that while the network is training, it does not become trapped in a local minimum outputting solely background voxels. Training was carried out over 150 epochs using stochastic gradient descent with an initial learning rate of 0.01 and learning rate decay of  $5 \times 10^{-7}$  and momentum of 0.8, these parameters help the optimiser converge quickly while also avoiding overshooting. As seen in Figure 5.7, after 150 epochs the validation Dice score plateaued while the training Dice score was still rising slightly, indicating that any further training would lead to overfitting. Training took approximately thirty minutes.

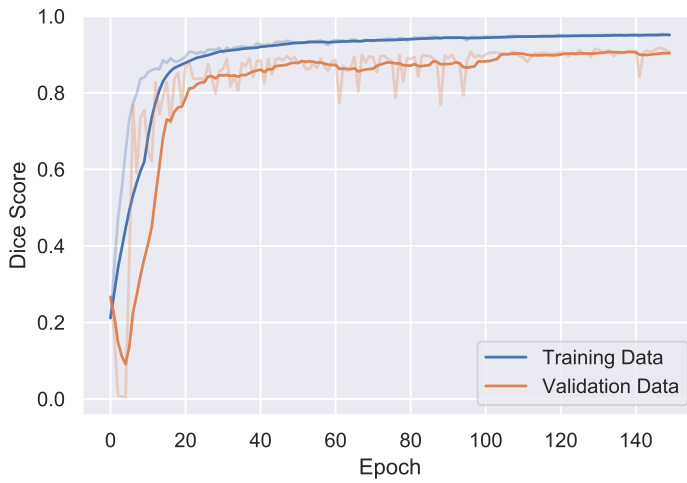


Figure 5.7: Dice score of the network for the training and validation data. Data is shown with a 10 epoch rolling average.

#### 5.3.4 Statistical Analysis

Baseline demographics are reported as mean  $\pm$  Standard Deviation (SD). Inter-observer variability in manual segmentation and TKV was calculated by comparing the TKV of the manual masks each observer generated for a given volume, and also assessing Bland-Altman and regression analysis. Intra-observer variability in manual segmentation was calculated by comparing

### 5.3. Methods

---

the TKV of the five masks generated by an observer for a given subject. For each, the mean Coefficient of Variation (CoV); defined as standard deviation/mean and Intraclass Correlation (ICC) were used as measures of repeatability of TKV. Voxel-based metrics (Dice score, Equation (5.1) and Jaccard index, Equation (5.2)) and surface based metrics such as the average distance between the surface of the two masks and Hausdorff Distance 95th percentile, the 95th percentile of the largest distance between the two surfaces, were also calculated between each observer.

$$J(A, B) = \frac{A \cap B}{A \cup B} = \frac{TP}{TP + FP + FN} \quad (5.2)$$

The performance of the automated segmentation was assessed using the voxel and surface based similarity metrics outlined above and, in addition, sensitivity, specificity, precision and accuracy, Equations (5.3) - (5.6). Performance was further assessed by determining the mean difference in TKV between the automatic and manual methods. Both actual and percentage (%) difference in TKV were evaluated. Bias (mean) obtained from the automatic and manual methods was assessed using a paired sample t-test. The mean CoV and ICC were also used as measures of repeatability of the automated TKV.

$$\text{Sensitivity} = \frac{TP}{TP + FN} \quad (5.3)$$

$$\text{Specificity} = \frac{TN}{TN + FP} \quad (5.4)$$

$$\text{Precision} = \frac{TP}{TP + FP} \quad (5.5)$$

$$\text{Accuracy} = \frac{TP + TN}{TP + TN + FP + FN} \quad (5.6)$$

## 5.4 Results

### 5.4.1 Characteristics of the Training Cohort

Data was collected using a  $T_2$ -weighted HASTE sequence with TE = 60 ms providing optimal contrast between the kidneys and surrounding tissue, examples shown in Figure 5.8. However there is limited contrast between the left kidney and spleen due to their similar  $T_2$ -weighting. Cysts of variable size are clearly visible in the kidneys of the CKD patient.

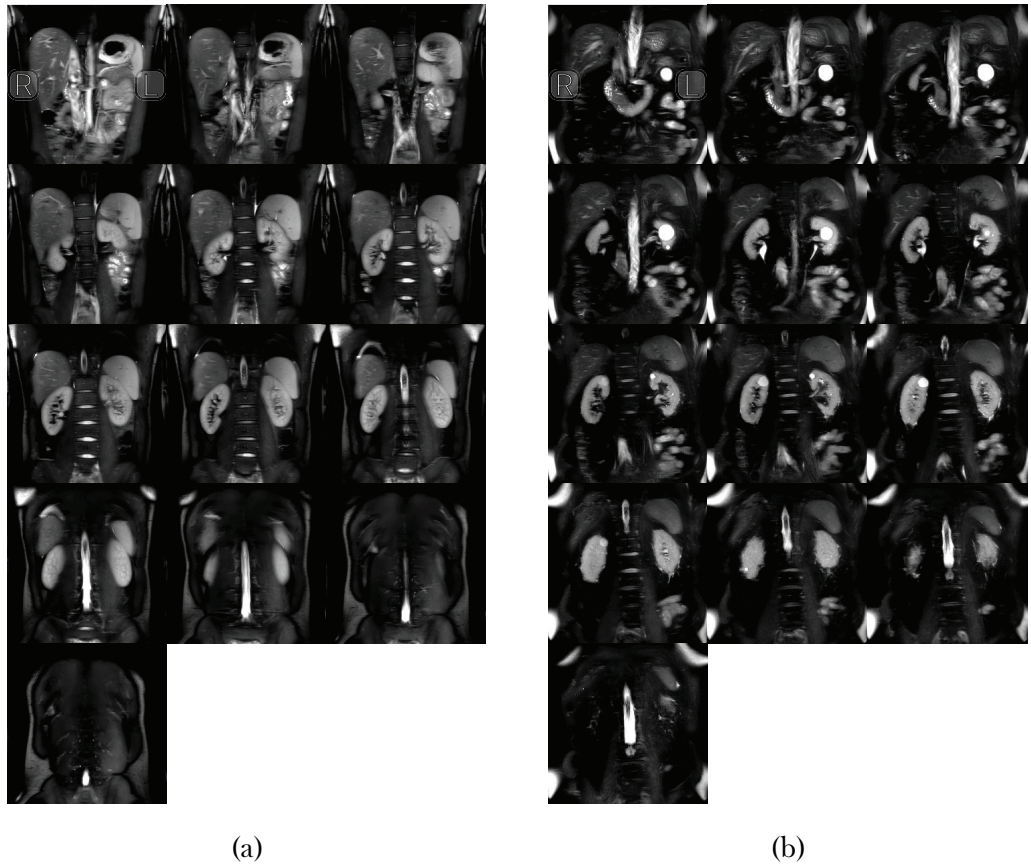


Figure 5.8: All slices of the  $T_2$ -weighted HASTE data from a representative subject of (a) the HC cohort and (b) the CKD cohort.

The training data comprised 25 HCs (9 female, 16 male) with a mean age of  $26 \pm 12$  (19–77) years and 25 CKD patients (6 female, 19 male) with a mean age of  $58 \pm 15$  (19–80) years and mean CKD stage  $3.3 \pm 1.1$  (1–5). The manual TKV was  $277 \pm 60$  mℓ, ranging between 145 and 422 mℓ.

## 5.4. Results

---

Including both HC subjects and CKD patients meant the kidneys had variable morphology (shape, size and heterogeneous cysts) within the training dataset. Table 5.1 provides the characteristics of the datasets used for training and testing of the CNN, whilst Figure 5.9 shows the distribution of TKV within the training and testing datasets.

	Number of Subjects	Number of Datasets	Number of 2D Slices	Sex (F/M)	Mean Age	TKV (mℓ)
Training HC	25	25	325	9/16	$26 \pm 12$	$296 \pm 38$
Training CKD	25	25	324	6/19	$58 \pm 15$	$258 \pm 72$
Testing HC	5	25	325	1/4	$25 \pm 3$	$330 \pm 35$
Testing CKD	5	25	325	0/5	$69 \pm 3$	$274 \pm 56$

Table 5.1: Characteristics of datasets used for training and testing of the 2D U-Net model CNN. Values are quoted as mean  $\pm$  standard deviation.

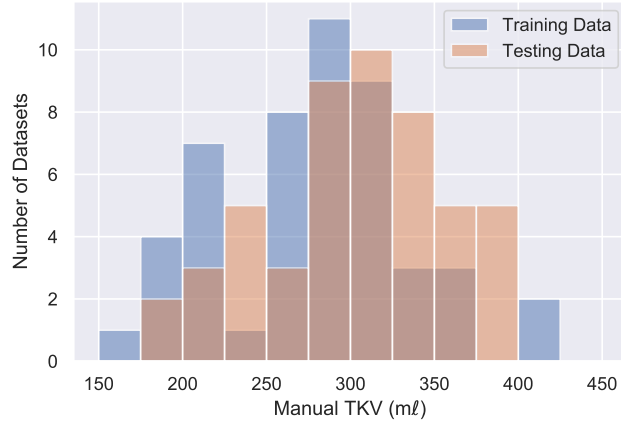


Figure 5.9: Distribution of TKV within the training and testing data.

### 5.4.2 Reducing Acquisition Time

Initial data was collected with a HASTE sequence with a TR of 1800 ms leading to an expiration breath hold of approximately 23 seconds. Some subjects struggled to hold their breath for this long on expiration, therefore the

## 5.4. Results

---

effects of reducing the TR of the sequence were investigated. As can be seen in Figure 5.10, there is no degradation in image quality from the image by reducing the TR from 1800 ms to a TR of 1300 ms, the differences between these images are due to the small movements between volumes, as can be seen in the difference data where the largest differences are seen around the periphery of the kidneys and in the gut. Moving forward, the a reduced TR of 1300 ms was used leading to a sequence with a breath hold of approximately 17 seconds.

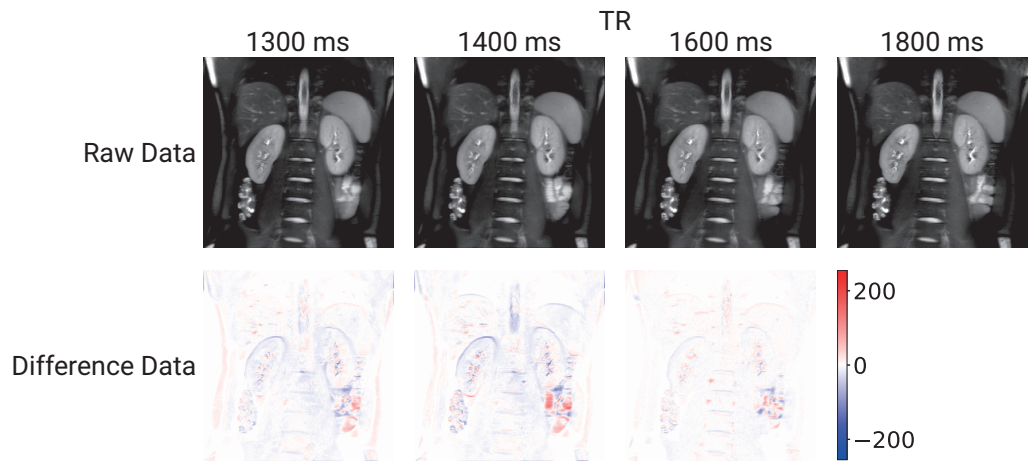


Figure 5.10: The effects of changing the TR of the HASTE sequence.

### 5.4.3 Repeatability of Manual Segmentation

Four of the healthy control test subjects were each scanned five times, with the left and right kidneys in these 20 datasets each masked by Observers A, B and C. The intra-observer and inter-observer variability for this manual segmentation was computed, as shown in Table 5.2. Performing this on healthy control subjects assessed the minimum error in manual segmentation, as healthy kidneys are much easier to segment than those of CKD patients.

## 5.4. Results

---

Observer	Kidneys	CoV (%)	ICC
Intra A	Total	$2.2 \pm 0.7$	0.939
	Left	$3.2 \pm 0.8$	0.783
	Right	$1.9 \pm 0.5$	0.957
Intra B	Total	$1.9 \pm 0.3$	0.895
	Left	$2.0 \pm 0.5$	0.807
	Right	$2.4 \pm 0.3$	0.892
Intra C	Total	$2.5 \pm 0.9$	0.908
	Left	$2.8 \pm 1.3$	0.769
	Right	$3.1 \pm 1.9$	0.940
Inter	Total	$3.0 \pm 1.0$	0.897
	Left	$4.0 \pm 1.4$	0.713
	Right	$2.9 \pm 1.0$	0.910

Table 5.2: Repeatability of the manual segmentation for left, right and TKV, with coefficient of variation and intraclass coefficient computed. CoV is quoted as mean  $\pm$  standard deviation across subjects.

Additionally, similarity metrics were used to assess the overlap between each observer’s manual masks, Table 5.3. Due to the large difference between in-plane ( $1.5 \text{ mm}^3$ ) and out-of-plane resolution ( $5.5 \text{ mm}^3$ ) the Hausdorff distance is very susceptible to inaccuracies in the anterior – posterior direction; this metric is highly sensitive to noise and as such the 95th percentile is used to generate a more representative value. Bland-Altman plots and regression analysis of inter-observer variance in measured TKV are provided in Figure 5.11.

## 5.4. Results

Observer	Kidney	Dice Score	Jaccard Index	Average Distance (mm)	Hausdorff Distance (mm) (95th Percentile)	Volume Difference (ml)
A - B	Both	0.93 ± 0.03	0.87 ± 0.05	0.81 ± 0.58	5.6 ± 2.8	20.8 ± 9.3
	Left	0.92 ± 0.07	0.85 ± 0.10	0.94 ± 1.12	5.5 ± 3.7	13.4 ± 5.8
	Right	0.94 ± 0.01	0.88 ± 0.02	0.65 ± 0.14	4.8 ± 1.2	7.5 ± 5.6
A - C	Both	0.93 ± 0.01	0.87 ± 0.02	0.79 ± 0.18	5.8 ± 1.9	16.0 ± 8.6
	Left	0.93 ± 0.01	0.87 ± 0.02	0.84 ± 0.27	6.8 ± 3.1	6.9 ± 5.8
	Right	0.93 ± 0.01	0.87 ± 0.02	0.72 ± 0.17	4.8 ± 1.3	9.1 ± 5.4
B - C	Both	0.94 ± 0.04	0.89 ± 0.06	0.68 ± 0.62	3.6 ± 2.7	-4.8 ± 9.9
	Left	0.93 ± 0.08	0.88 ± 0.11	0.78 ± 1.22	4.3 ± 3.6	-6.4 ± 6.2
	Right	0.95 ± 0.01	0.90 ± 0.02	0.48 ± 0.14	3.4 ± 1.1	1.6 ± 6.6

Table 5.3: Metrics comparing each combination of observers manual masks (A - B, A - C and B - C). All values are quoted as mean ± standard deviation.

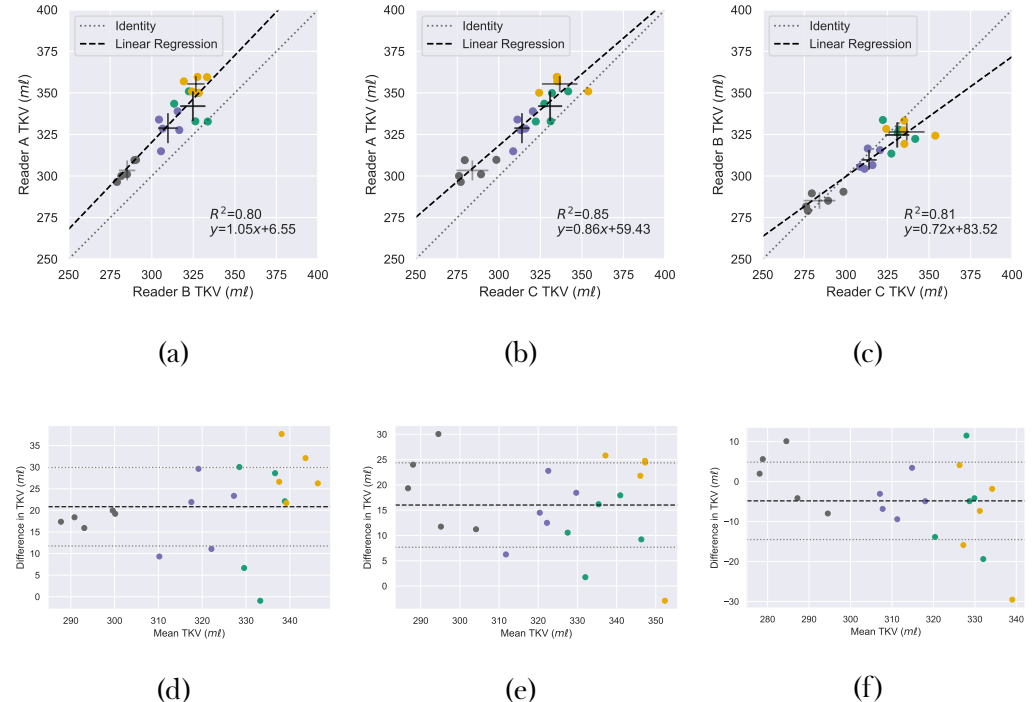


Figure 5.11: Bland-Altman and regression analysis of inter-reader variations in TKV.

#### 5.4.4 Network Testing

To verify that the trained network is behaving as expected saliency maps were produced, Figure 5.12, this is especially important given the black box nature of machine learning methods. This map shows the areas the network is using most in its classification [43]. It verifies that the network is using the peripheral areas of the kidney to make its prediction, with areas of a similar intensity outside the kidneys receiving some attention to distinguish them from the kidney. While this is precisely what is expected of the algorithm, it is important to confirm this as it is possible for such a method to have learnt a slightly different mechanism for the segmentation, one that is more prone to errors if new data is presented to it.

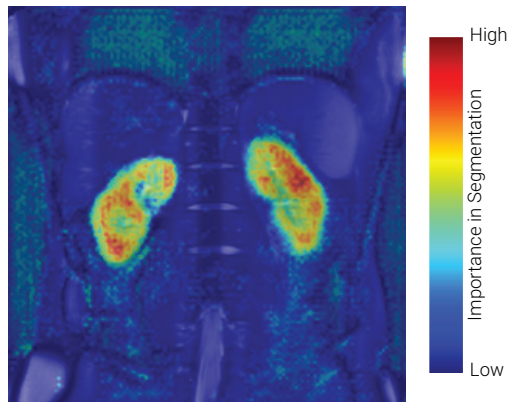


Figure 5.12: An example saliency map of the areas the network uses most for segmentation of the kidney.

The trained network was used to predict segmentations of the 2D kidney slices and compute TKV for each of the unseen test volumes. The mean Dice score over the 50 test volumes was  $0.93 \pm 0.01$  ( $0.94 \pm 0.02$  for HC and  $0.92 \pm 0.01$  for CKD patients). The TKV predicted by the network was, on average,  $1.2 \pm 16.2$  mℓ less than the manually segmented TKV and thus not significantly different ( $p = 0.615$ ) (Figure 5.13) This accuracy was comparable for the HC and CKD datasets, with automated CNN TKV measurements of  $4.7 \pm 17.7$  mℓ greater than manual and  $7.0 \pm 12.4$  mℓ less than manual respectively. A summary of the CNN accuracy when evaluated

## 5.4. Results

---

using similarity metrics and volume difference from manual measures is shown in Table 5.4. Note a slightly larger discrepancy for the left compared to the right kidney. Figure 5.13 shows plots of the difference in volume between the manual segmentation and automated segmentation of the test dataset.

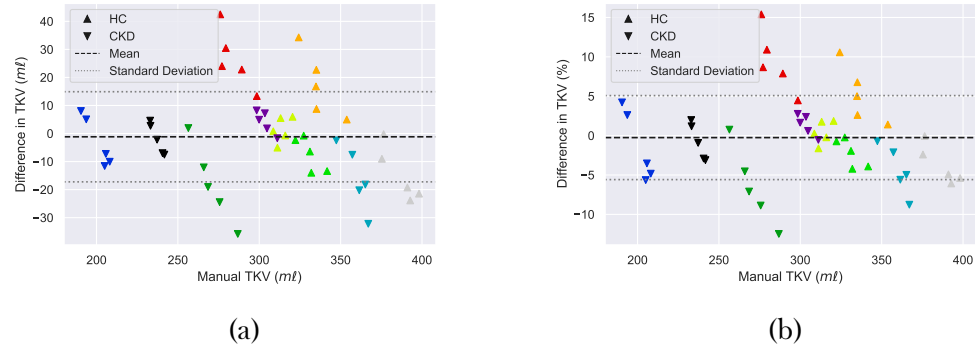


Figure 5.13: The difference between the TKV predicted by the CNN and the manually segmented true TKV. Mean and standard deviation TKV difference are shown as dashed and dotted lines respectively. Each subject is shown in a different colour, with (a) showing the absolute volume difference and (b) showing the percentage volume difference.

## 5.4. Results

Cohort	Kidney	Dice Score	Jaccard Index	Sensitivity	Specificity	Precision	Accuracy	Mean Surface Distance (mm)	Hausdorff Distance (mm) (95th Percentile)	Volume Difference (p)
All	Total	$0.93 \pm 0.01$	$0.87 \pm 0.03$	$0.93 \pm 0.03$	$0.997 \pm 0.001$	$0.93 \pm 0.02$	$0.995 \pm 0.001$	$0.65 \pm 0.21$	$4.3 \pm 1.6$	$-1.2 \pm 16.2$ (0.615)
	Left	$0.92 \pm 0.02$	$0.86 \pm 0.04$	$0.91 \pm 0.05$	$0.997 \pm 0.001$	$0.94 \pm 0.03$	$0.994 \pm 0.002$	$0.76 \pm 0.31$	$4.4 \pm 1.5$	$-4.0 \pm 12.4$ (0.029)
	Right	$0.94 \pm 0.02$	$0.89 \pm 0.03$	$0.95 \pm 0.03$	$0.997 \pm 0.001$	$0.93 \pm 0.03$	$0.996 \pm 0.001$	$0.54 \pm 0.21$	$3.7 \pm 1.8$	$2.8 \pm 6.8$ (0.006)
	Total	$0.94 \pm 0.02$	$0.88 \pm 0.03$	$0.95 \pm 0.05$	$0.997 \pm 0.001$	$0.93 \pm 0.03$	$0.995 \pm 0.001$	$0.68 \pm 0.27$	$4.5 \pm 2.0$	$4.7 \pm 17.7$ (0.201)
	Left	$0.93 \pm 0.02$	$0.87 \pm 0.04$	$0.94 \pm 0.05$	$0.997 \pm 0.001$	$0.93 \pm 0.03$	$0.994 \pm 0.002$	$0.79 \pm 0.37$	$4.5 \pm 1.8$	$1.9 \pm 12.9$ (0.467)
	Right	$0.95 \pm 0.02$	$0.90 \pm 0.03$	$0.96 \pm 0.03$	$0.997 \pm 0.001$	$0.94 \pm 0.02$	$0.996 \pm 0.001$	$0.56 \pm 0.26$	$3.8 \pm 2.1$	$2.8 \pm 7.7$ (0.087)
CKD	Total	$0.92 \pm 0.01$	$0.86 \pm 0.02$	$0.91 \pm 0.02$	$0.998 \pm 0.001$	$0.94 \pm 0.02$	$0.995 \pm 0.001$	$0.63 \pm 0.14$	$4.2 \pm 1.2$	$-7.0 \pm 12.4$ (0.009)
	Left	$0.92 \pm 0.02$	$0.85 \pm 0.03$	$0.89 \pm 0.04$	$0.998 \pm 0.001$	$0.95 \pm 0.02$	$0.994 \pm 0.002$	$0.78 \pm 0.24$	$4.4 \pm 1.2$	$-9.8 \pm 8.6$ (0.00001)
	Right	$0.93 \pm 0.01$	$0.88 \pm 0.02$	$0.94 \pm 0.02$	$0.997 \pm 0.001$	$0.92 \pm 0.03$	$0.996 \pm 0.001$	$0.51 \pm 0.13$	$3.5 \pm 1.3$	$2.8 \pm 6.0$ (0.027)

Table 5.4: The accuracy of the CNN compared to the manual segmentation using a variety of metrics stratifying the testing data by cohort and left vs right kidney. All values are given as mean  $\pm$  standard deviation.

## 5.4. Results

---

In Figure 5.14, the TKV predicted by the CNN is plot against the manual TKV, in 90 % of subjects the standard deviation of TKV measurements between each volume for a subject was smaller when the TKV was measured using the CNN as opposed to manual segmentation. The mean CoV and ICC were  $2.7 \pm 0.9$  % and 0.979 respectively across the 5 repeats of the manually segmented test data (using masks from observers A, B and C), compared to a value of  $1.5 \pm 0.5$  % and 0.993 respectively for the automatic CNN segmentations of the 5 repeats of test data. The CNN produced a significantly lower CoV than the manual segmentations ( $p = 0.008$ ).

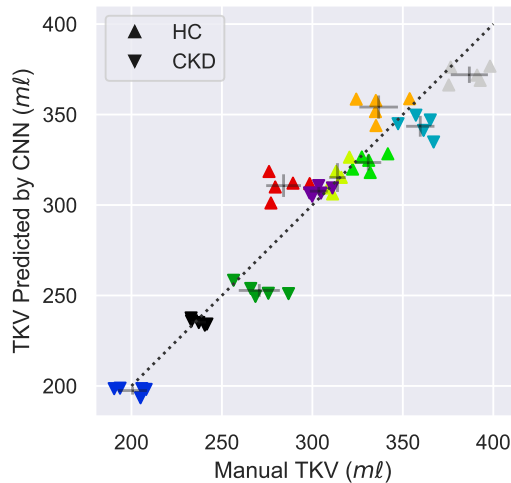
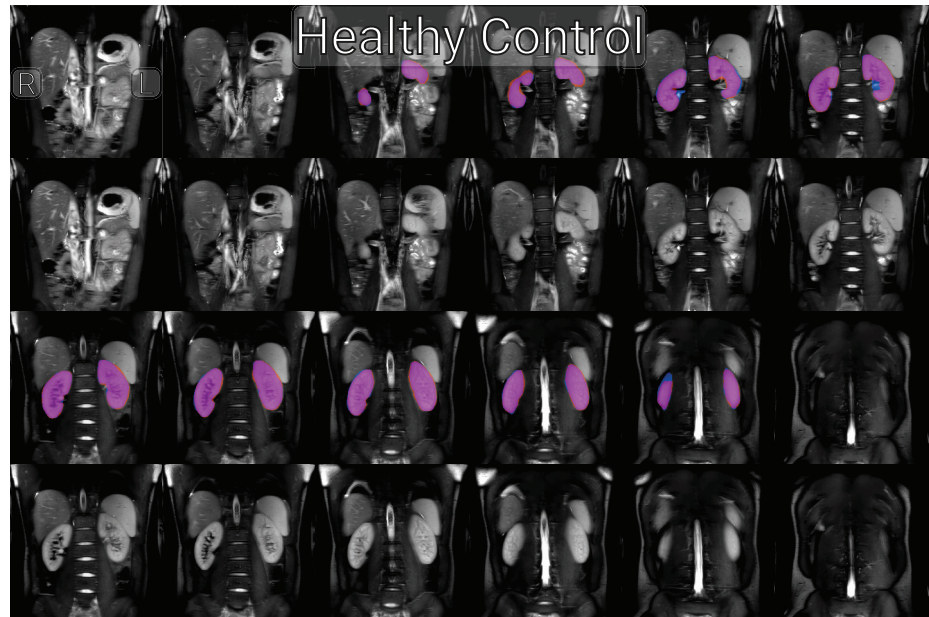


Figure 5.14: The TKV predicted by the CNN plot against the manually segmented true TKV with each subject plot in a different colour. The standard deviation measured using both methods is shown as error bars originating from the mean of each subject. The dotted line represents perfect correlation between the CNN and manual segmentation.

Representative examples of the output from the network for both HC and CKD data are shown in Figure 5.15. The automated CNN accurately segments the kidneys, and for CKD patients, omits the cysts from the masks.

### 5.4. Results

---



(a)



(b)

Figure 5.15: Representative raw test data and corresponding masks of a HC, (a) and CKD subject (b). Manually generated masks are shown in blue, automatically generated masks are shown in red and the overlap of the two is shown in magenta.

Since this is a 2D CNN, it is important to assess the accuracy across the anterior – posterior 2D slices of the kidney. This was achieved by comparing

## 5.4. Results

---

the Dice score of the CNN to the inter-reader Dice scores, Figure 5.16. A decrease in accuracy in the outer slices can be seen in both the CNN and manual masks.

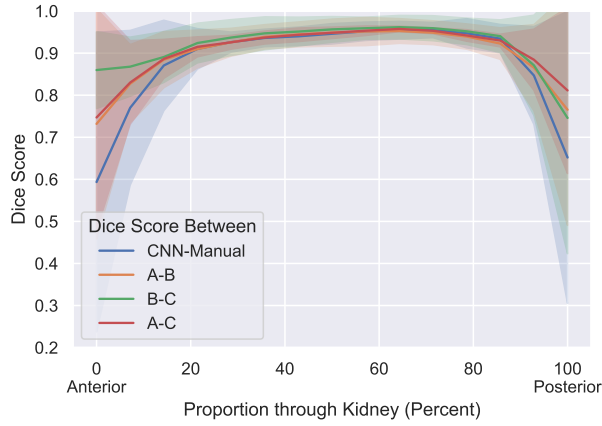


Figure 5.16: Mean Dice score for 2D slices from anterior to posterior. The shaded area represents one standard deviation from the mean Dice score.

This decrease in accuracy manifests itself on the outer slices of the volume, where the proportion of kidney per slice is smaller and as such the 2D network, with a lack of spatial context in the anterior – posterior direction, finds these outer slices more challenging. This decrease in accuracy can partly be explained by the fact that larger structures (in terms of number of voxels) will in general produce higher scores for comparable errors because the vast majority of errors are on the perimeter of the kidney in each slice, slices with fewer voxels of kidney have a smaller area to perimeter ratio, Figure 5.17.

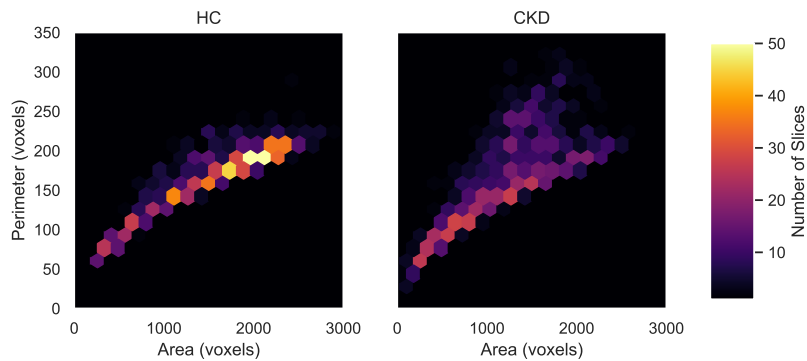


Figure 5.17: A 2D histogram of the perimeter and area of each slice for both the HC and CKD cohorts.

## 5.5 Discussion

In this chapter, a 2D CNN has been trained to generate automatic segmentations of healthy control and CKD patients. Segmentations of the left and right kidneys are computed from which total kidney volume is estimated. The CNN was trained on both healthy control and CKD kidneys with a range of TKV (145 – 422 ml) which included the presence of cysts. The automated segmentation by the CNN yielded a mean Dice score of  $0.93 \pm 0.01$  and took an average time of 9 s to measure TKV compared to 15 – 30 minutes [15] for each manual segmentation. The automated CNN has been made into a self-contained Graphical User Interface (GUI) with the data and programme freely available [44], Figure 5.18, thus avoiding the need for complicated software setup across the renal community. Note the software released at present can only be used to process coronal HASTE images of the type the network has been trained on. It will not be accurate with other geometries/contrasts, for this, training of the network with a different dataset would be required and thus necessitate the use of a GPU.

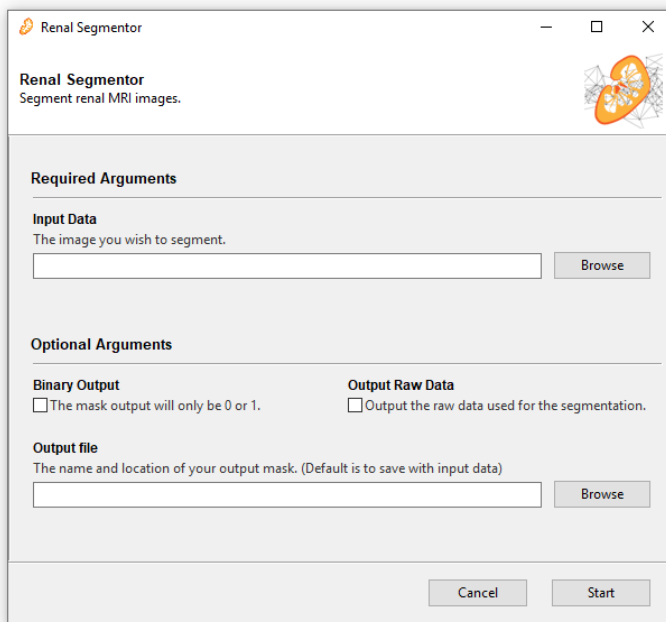


Figure 5.18: The Graphical User Interface (GUI) used to segment kidneys.

### 5.5.1 Evaluation of Methodology

The network performed with high precision on the test data with a  $1.2 \pm 16.2 \text{ ml}$ , statistically insignificant, discrepancy between manual and automated TKV measurements. Table 5.4 shows the agreement between the CNN and manual masks is higher for the right than left kidney, this is in part due to the proximity and lack of contrast between the left kidney and the spleen making distinguishing this boundary difficult for the CNN. This difficulty also leads to inconsistencies in manual masks, borne out by the increased CoV and decreased ICC and similarity metrics of the left kidney when compared to the right kidney in Table 5.2 and Table 5.4 assessing the variability in manual masks between observers. From Table 5.4 it can also be seen that the agreement between the CNN and manual masks is greater for the healthy control cohort than the CKD cohort, this is expected due to the increased variation in kidney morphology and the presence of cysts in the CKD cohort. Figure 5.13 shows that the difference between the manual TKV and CNN predicted TKV is not dependent on the true TKV, therefore the training data is balanced and well augmented as the network is able to accurately perform over the full range of kidney size in the test data.

Here, five datasets of  $T_2$ -weighted test data were collected for each subject by repositioning the subject in the scanner within an hour scan session, and therefore any variance in measured TKV is purely due to inaccuracies in the kidney ROI definition. On assessing the correlation between manual and CNN measured TKV in Figure 5.14, it can be seen that, in 90 % of subjects the intra-observer variance in manual TKV between the segmentation of the five volumes collected in each subject is larger than using the CNN to estimate TKV, as reflected by the lower CoV and increased ICC of the TKV measured using the CNN ( $\text{CoV } 1.5 \pm 0.5 \text{ \%}$ ,  $\text{ICC } 0.993$ ) compared to the manual measures ( $\text{CoV } 2.7 \pm 0.9 \text{ \%}$ ,  $\text{ICC } 0.979$ ). As the network is trained on the kidney segmentations from three observers (A, B and C), it has been optimised by inheriting the most accurate tendencies of each observer e.g. one observer may have been very accurate when excluding cysts but not as

## 5.5. Discussion

---

accurate at defining the kidney-spleen boundary. The network will have learnt to exclude cysts from this observer but to delineate between kidney and spleen from another observer. Thus the network can become more precise than each individual observers manual segmentations.

A disadvantage of using repeated scans on the same volunteer to evaluate the networks performance is that although the network is evaluated on 50 different volumes, these are only drawn from 10 subjects, as such the range of renal morphologies will be less than if 50 different subjects were scanned. While efforts were made to ensure the testing and training datasets were representative of each other, the ability of the network to accurately segment features such as cysts would be tested more thoroughly if a greater number of test subjects were scanned.

Figure 5.15 illustrates the masks produced by the manual segmentation and the CNN for both a HC and CKD patient. For the HC, the CNN includes more voxels around the edge of its mask than manual segmentation, and the network is more anatomically accurate e.g. where the interface between the kidney and spleen is very narrow, the CNN predicts the kidney is adjacent to the spleen whilst the observers manual segmentation leaves a gap. The CKD data shown in Figure 5.15b includes a cyst in each of the kidneys. The network was trained on a combination of healthy and CKD data, with 19 of the 25 CKD training datasets containing at least one cyst. The CNN can be seen to segment out the cysts, despite their highly variable morphology and prevalence in the overall training data.

The amount of augmentation applied to the training data was empirically derived (random shifts up to 25 % of the image in both the horizontal and vertical direction, zooms between 0.75 and 1.25 times magnification, rotations within a 20 degree range, and sheers within a 5 degree range) and led to the potential for large transforms being applied to the data and masks if the extremes of each transform were randomly selected. This large degree of augmentation was advantageous as it mirrors the large variation in acquisition

planning in abdominal imaging.

A 2D CNN was used to process each 2D slice of a full volume, rather than a 3D volume. This was advantageous for the relatively small training dataset the network was optimised on, as it avoids overfitting and allows the network to easily be used on volumes of variable slice number. However, this can come at the expense of accuracy as 2D CNNs do not leverage the information from adjacent slices in the segmentation as is done in a 3D CNN, but a 3D CNN comes with a computational cost as a result of the increased number of parameters used. 3D networks have successfully been implemented on neural data using patching methods where the image volume is divided up into smaller cubes [29] to reduce memory requirements and allow for differing input shapes. While this works well in the brain, there are a number of reasons why this method may not be as successful for body applications. The out-of-plane resolution is significantly less than the in-plane resolution; this results in far fewer slices in one direction than the other two. To avoid overfitting for a certain number of slices e.g. training on a 11 slice image with a 113 patch, and subsequently the network not performing well when the patch is applied to a 16 slice image, the patch would need to be much smaller than the number of slices, thus diminishing the benefits of the 3D methodology. Additionally, the extra memory requirements for a 3D network limit the ease of use of the software for inference on many standard office computers.

### 5.5.2 Future Directions

Future work will explore alternative network architectures. As the main source of inaccuracy with the current network is its lack of slice-to-slice context, there are multiple architectures that can address this. A relatively simple method would be exploiting the fact that the Keras framework is designed to work with colour images. By combining three slices into a single image where each slice represents either the red, green or blue channel, Figure 5.19, the network would be able to use contextual information about the

## 5.5. Discussion

---

adjacent slices to help inform its predictions. As each image processed by the CNN requires three slices to act as colour channels, processing peripheral slices becomes non-trivial. If, for example, the slice being masked is used as the green channel, with those either side becoming the red and blue channels to assist informing the ROI delineation, this method will not be able to mask the first and last slice of the volume as there will be no red or blue channel respectively. As such, if the kidneys occupy 13 slices, 15 slices of data would need to be acquired with the extra slices on each side of the FOV. Multiple network architectures such as Recursive Neural Network (RNN) [45], and Long Short-Term Memory (LSTM) [46] are designed to have a memory enabling them to retain contextual information from slice to slice, these could be explored. Alternatively, if more training data were available, a 3D CNN could be explored to ascertain if any improved accuracy is worth the increase in hardware requirements and reduced generalisability.



Figure 5.19: An example of using colour information to represent adjacent slices for processing by a CNN. Vessels in the liver can clearly be seen travelling through the three slices as they change from red to green to blue.

This image contrast was chosen as a result of recent publications comparing  $T_1$ - and  $T_2$ -weighted images for TKV assessment reporting that  $T_2$ -weighted images provide better quality to enable TKV measurements, leading to improved reproducibility with lower intra- and inter-reader variability

### 5.5. Discussion

---

[47]. Other contrasts e.g. a  $T_1$ -weighted scan, could also be collected, registered to the  $T_2$ -weighted images and used as another channel to inform segmentation. An example image is shown in Figure 5.20 where  $T_1$ -weighted data is shown in blue and  $T_2$ -weighted data is shown in red. A colour CNN could then be used to segment the kidneys with the network learning how much weighting to give each contrast.

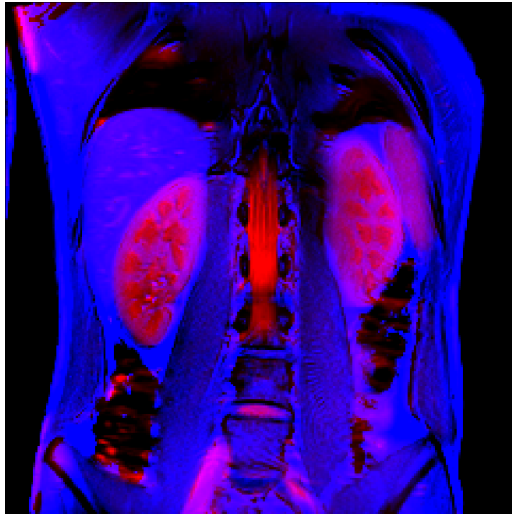


Figure 5.20: An example of using colour information to represent different image contrasts. Here the  $T_2$ -weighted image is shown in red and the  $T_1$ -weighted image is shown in blue.

This network was validated on healthy subjects and CKD patients, but has not been trained and validated on subjects with ADPKD. These subjects have many more cysts in their kidneys, while the CNN was able to segment cysts encountered in the CKD patients, it would be beneficial for future work on ADPKD to retrain the network with HC, CKD and ADPKD data, where TKV is a recognised biomarker of disease progression.

Another common segmentation task in renal imaging is generating an ROI for the renal cortex and medulla. There are some automated methods of achieving this once a total kidney mask has been produced [3, 48], however there has been no work on the application of deep learning to this task. In addition to the acquisition of the  $T_2$ -weighted HASTE dataset used here, a  $T_1$ -weighted dataset designed to optimise the contrast between cortex and

### **5.5. Discussion**

---

medulla was also collected on each subject [39], an example of which is shown in Figure 5.21. Using this data, it may be possible to develop this method further such that an automated mask for each tissue type is produced.



Figure 5.21: An example of the data collected to enable segmentation of the renal cortex and medulla.

## 5.6 Conclusion

A 2D CNN has been shown to successfully segment the kidneys of both HC and CKD subjects from  $T_2$ -weighted HASTE data delivering a mean Dice score of  $0.93 \pm 0.01$  leading to a mean volume of  $1.2 \pm 16.2 \text{ m}^3$  less than the manually segmented TKV and mean surface distance of  $0.65 \pm 0.21 \text{ mm}$ . The CNN produced higher than human precision, with a CoV and ICC of  $1.5 \pm 0.5 \%$  and  $0.993$  respectively. The accuracy of the network could be further increased via the acquisition of more training data, something that the renal group at Sir Peter Mansfield Imaging Centre (SPMIC) are actively pursuing.

The methods developed here can easily be deployed via the self contained, easy to use GUI, thus moving renal segmentation from a 15 to 30 minute skilled task, to a 10 second task for anyone, on any computer. Additionally, this executable can be called from a terminal, making it suitable for use in scripting applications and pipelines.

Future development will focus on exploring different network architectures, use of additional contrasts and expanding the tool to produce masks of both the cortex and medulla.

## 5.7 Acknowledgements

I gratefully acknowledge the support of NVIDIA Corporation with the donation of the Titan Xp GPU used for this research. I would also like to thank Thomas Allcock and Daniel Scerri for their assistance manually segmenting kidneys to generate training data.

## 5.8 References

1. Daniel, A. J., Buchanan, C., Allcock, T., Scerri, D., Cox, E., Prestwich, B. & Francis, S. *Automated Renal Segmentation in Healthy and Chronic Kidney Disease Subjects Using A Convolutional Neural Network* in *Proc. Intl. Soc. Mag. Reson. Med.* 28 International Society of Magnetic Resonance in Medicine Annual Meeting (Online, Aug. 2020).
2. Daniel, A. J., Buchanan, C. E., Allcock, T., Scerri, D., Cox, E. F., Prestwich, B. L. & Francis, S. T. Automated Renal Segmentation in Healthy and Chronic Kidney Disease Subjects Using a Convolutional Neural Network. *Magnetic Resonance in Medicine* **86**, 1125–1136 (2021).
3. Cox, E. F., Buchanan, C. E., Bradley, C. R., Prestwich, B., Mahmoud, H., Taal, M., Selby, N. M. & Francis, S. T. Multiparametric Renal Magnetic Resonance Imaging: Validation, Interventions, and Alterations in Chronic Kidney Disease. *Frontiers in Physiology* **8**, 696 (2017).
4. Cohen, E. I., Kelly, S. A., Edye, M., Mitty, H. A. & Bromberg, J. S. MRI Estimation of Total Renal Volume Demonstrates Significant Association with Healthy Donor Weight. *European Journal of Radiology. Rheumatoid Disease and Imaging* **71**, 283–287 (1st Aug. 2009).
5. Van den Dool, S. W., Wasser, M. N., de Fijter, J. W., Hoekstra, J. & van der Geest, R. J. Functional Renal Volume: Quantitative Analysis at Gadolinium-Enhanced MR Angiography—Feasibility Study in Healthy Potential Kidney Donors. *Radiology* **236**, 189–195 (1st July 2005).
6. Chapman, A. B. *et al.* Kidney Volume and Functional Outcomes in Autosomal Dominant Polycystic Kidney Disease. *Clinical Journal of the American Society of Nephrology* **7**, 479–486 (1st Mar. 2012).
7. Tangri, N., Hougen, I., Alam, A., Perrone, R., McFarlane, P. & Pei, Y. Total Kidney Volume as a Biomarker of Disease Progression in Autosomal Dominant Polycystic Kidney Disease. *Canadian Journal of Kidney Health and Disease* **4**, 2054358117693355 (1st Jan. 2017).
8. Grantham, J. J. *et al.* Volume Progression in Polycystic Kidney Disease. *New England Journal of Medicine* **354**, 2122–2130 (18th May 2006).

## 5.8. References

---

9. Buchanan, C. E., Mahmoud, H., Cox, E. F., McCulloch, T., Prestwich, B. L., Taal, M. W., Selby, N. M. & Francis, S. T. Quantitative Assessment of Renal Structural and Functional Changes in Chronic Kidney Disease Using Multi-Parametric Magnetic Resonance Imaging. *Nephrology Dialysis Transplantation* **35**, 955–964 (29th June 2019).
10. Stevens, L. A., Coresh, J., Greene, T. & Levey, A. S. Assessing Kidney Function — Measured and Estimated Glomerular Filtration Rate. *New England Journal of Medicine* **354**, 2473–2483 (8th June 2006).
11. Gong, I. H., Hwang, J., Choi, D. K., Lee, S. R., Hong, Y. K., Hong, J. Y., Park, D. S. & Jeon, H. G. Relationship Among Total Kidney Volume, Renal Function and Age. *The Journal of Urology* **187**, 344–349 (Jan. 2012).
12. Boer, A. de *et al.* Consensus-Based Technical Recommendations for Clinical Translation of Renal Phase Contrast MRI. *Journal of Magnetic Resonance Imaging* n/a. doi:10.1002/jmri.27419 (Oct. 2020).
13. Di Leo, G., Di Terlizzi, F., Flor, N., Morganti, A. & Sardanelli, F. Measurement of Renal Volume Using Respiratory-Gated MRI in Subjects without Known Kidney Disease: Intraobserver, Interobserver, and Interstudy Reproducibility. *European Journal of Radiology* **80**, e212–e216 (1st Dec. 2011).
14. Bae, K. T., Commean, P. K. & Lee, J. Volumetric Measurement of Renal Cysts and Parenchyma Using MRI: Phantoms and Patients with Polycystic Kidney Disease. *Journal of Computer Assisted Tomography* **24**, 614–619 (July–Aug. 2000).
15. Zöllner, F. G., Svarstad, E., Munthe-Kaas, A. Z., Schad, L. R., Lundervold, A. & Rørvik, J. Assessment of Kidney Volumes From MRI: Acquisition and Segmentation Techniques. *American Journal of Roentgenology* **199**, 1060–1069 (1st Nov. 2012).
16. Sharma, K., Caroli, A., Quach, L. V., Petzold, K., Bozzetto, M., Serra, A. L., Remuzzi, G. & Remuzzi, A. Kidney Volume Measurement Methods for Clinical Studies on Autosomal Dominant Polycystic Kidney Disease. *PLOS ONE* **12**, e0178488 (30th May 2017).

## 5.8. References

---

17. Simms, R. J. *et al.* A Rapid High-Performance Semi-Automated Tool to Measure Total Kidney Volume from MRI in Autosomal Dominant Polycystic Kidney Disease. *European Radiology* **29**, 4188–4197 (1st Aug. 2019).
18. Cheong, B., Muthupillai, R., Rubin, M. F. & Flamm, S. D. Normal Values for Renal Length and Volume as Measured by Magnetic Resonance Imaging. *Clinical Journal of the American Society of Nephrology* **2**, 38–45 (1st Jan. 2007).
19. Spithoven, E. M. *et al.* Estimation of Total Kidney Volume in Autosomal Dominant Polycystic Kidney Disease. *American Journal of Kidney Diseases* **66**, 792–801 (1st Nov. 2015).
20. Seuss, H. *et al.* Development and Evaluation of a Semi-Automated Segmentation Tool and a Modified Ellipsoid Formula for Volumetric Analysis of the Kidney in Non-Contrast T2-Weighted MR Images. *Journal of Digital Imaging* **30**, 244–254 (1st Apr. 2017).
21. Magistroni, R., Corsi, C., Martí, T. & Torra, R. A Review of the Imaging Techniques for Measuring Kidney and Cyst Volume in Establishing Autosomal Dominant Polycystic Kidney Disease Progression. *American Journal of Nephrology* **48**, 67–78 (2018).
22. Coulam, C. H., Bouley, D. M. & Sommer, F. G. Measurement of Renal Volumes with Contrast-Enhanced MRI. *Journal of Magnetic Resonance Imaging* **15**, 174–179 (2002).
23. Karstoft, K., Lødrup, A. B., Dissing, T. H., Sørensen, T. S., Nyengaard, J. R. & Pedersen, M. Different Strategies for MRI Measurements of Renal Cortical Volume. *Journal of Magnetic Resonance Imaging* **26**, 1564–1571 (2007).
24. Gloger, O., Tonnies, K. D., Liebscher, V., Kugelmann, B., Laqua, R. & Volzke, H. Prior Shape Level Set Segmentation on Multistep Generated Probability Maps of MR Datasets for Fully Automatic Kidney Parenchyma Volumetry. *IEEE Transactions on Medical Imaging* **31**, 312–325 (Feb. 2012).

## 5.8. References

---

25. Kim, Y. *et al.* Automated Segmentation of Kidneys from MR Images in Patients with Autosomal Dominant Polycystic Kidney Disease. *Clinical Journal of the American Society of Nephrology* **11**, 576–584 (7th Apr. 2016).
26. Ronneberger, O., Fischer, P. & Brox, T. *U-Net: Convolutional Networks for Biomedical Image Segmentation* in *Medical Image Computing and Computer-Assisted Intervention – MICCAI 2015* (eds Navab, N., Hornegger, J., Wells, W. M. & Frangi, A. F.) (Springer International Publishing, Cham, 2015), 234–241. doi:10.1007/978-3-319-24574-4\_28.
27. Lu, F., Wu, F., Hu, P., Peng, Z. & Kong, D. Automatic 3D Liver Location and Segmentation via Convolutional Neural Network and Graph Cut. *International Journal of Computer Assisted Radiology and Surgery* **12**, 171–182 (1st Feb. 2017).
28. Sharma, K., Rupprecht, C., Caroli, A., Aparicio, M. C., Remuzzi, A., Baust, M. & Navab, N. Automatic Segmentation of Kidneys Using Deep Learning for Total Kidney Volume Quantification in Autosomal Dominant Polycystic Kidney Disease. *Scientific Reports* **7**, 2049 (17th May 2017).
29. Wachinger, C., Reuter, M. & Klein, T. DeepNAT: Deep Convolutional Neural Network for Segmenting Neuroanatomy. *NeuroImage. Segmenting the Brain* **170**, 434–445 (15th Apr. 2018).
30. Fu, Y. *et al.* A Novel MRI Segmentation Method Using CNN-Based Correction Network for MRI-Guided Adaptive Radiotherapy. *Medical Physics* **45**, 5129–5137 (2018).
31. Hassanzadeh, T., Hamey, L. G. C. & Ho-Shon, K. Convolutional Neural Networks for Prostate Magnetic Resonance Image Segmentation. *IEEE Access* **7**, 36748–36760 (2019).
32. Li, X., Chen, H., Qi, X., Dou, Q., Fu, C.-W. & Heng, P.-A. H-DenseUNet: Hybrid Densely Connected UNet for Liver and Tumor Segmentation From CT Volumes. *IEEE Transactions on Medical Imaging* **37**, 2663–2674 (Dec. 2018).

## 5.8. References

---

33. Kline, T. L. *et al.* Performance of an Artificial Multi-Observer Deep Neural Network for Fully Automated Segmentation of Polycystic Kidneys. *Journal of Digital Imaging* **30**, 442–448 (1st Aug. 2017).
34. Van Gastel, M. D. A., Edwards, M. E., Torres, V. E., Erickson, B. J., Gansevoort, R. T. & Kline, T. L. Automatic Measurement of Kidney and Liver Volumes from MR Images of Patients Affected by Autosomal Dominant Polycystic Kidney Disease. *Journal of the American Society of Nephrology* **30**, 1514–1522 (1st Aug. 2019).
35. Shin, T. Y. *et al.* Expert-Level Segmentation Using Deep Learning for Volumetry of Polycystic Kidney and Liver. *Investigative and Clinical Urology* **61**, 555–564 (Nov. 2020).
36. Fukushima, K. Neocognitron: A Hierarchical Neural Network Capable of Visual Pattern Recognition. *Neural Networks* **1**, 119–130 (1st Jan. 1988).
37. Lecun, Y., Bottou, L., Bengio, Y. & Haffner, P. Gradient-Based Learning Applied to Document Recognition. *Proceedings of the IEEE* **86**, 2278–2324 (Nov. 1998).
38. Petzold, K. *et al.* Building a Network of ADPKD Reference Centres across Europe: The EuroCYST Initiative. *Nephrology Dialysis Transplantation* **29**, iv26–iv32 (suppl\_4 1st Sept. 2014).
39. Will, S., Martirosian, P., Würslin, C. & Schick, F. Automated Segmentation and Volumetric Analysis of Renal Cortex, Medulla, and Pelvis Based on Non-Contrast-Enhanced T1- and T2-Weighted MR Images. *Magnetic Resonance Materials in Physics, Biology and Medicine* **27**, 445–454 (1st Oct. 2014).
40. Rorden, C. *NeuroLabusc/MRIcron* 18th Jan. 2021.
41. Chollet, F. *Keras* version 2.2.4. Keras, 2015.
42. Abadi, M. *et al.* TensorFlow: Large-Scale Machine Learning on Heterogeneous Distributed Systems (9th Nov. 2015).
43. Mahapatra, D. & Buhmann, J. M. Visual Saliency-Based Active Learning for Prostate Magnetic Resonance Imaging Segmentation. *Journal of Medical Imaging* **3**, 014003 (Feb. 2016).

## 5.8. References

---

44. Daniel, A. J. *Alexdaniel654/Renal\_Segmentor: V1.0.0* version v1.0.0. Zenodo, 6th Oct. 2020. doi:10.5281/zenodo.4068851.
45. Chen, J., Yang, L., Zhang, Y., Alber, M. & Chen, D. Z. in *Advances in Neural Information Processing Systems 29* (eds Lee, D. D., Sugiyama, M., Luxburg, U. V., Guyon, I. & Garnett, R.) 3036–3044 (Curran Associates, Inc., 2016).
46. Stollenga, M. F., Byeon, W., Liwicki, M. & Schmidhuber, J. in *Advances in Neural Information Processing Systems 28* (eds Cortes, C., Lawrence, N. D., Lee, D. D., Sugiyama, M. & Garnett, R.) 2998–3006 (Curran Associates, Inc., 2015).
47. Van Gastel, M. D. A. *et al.* T1 vs. T2 Weighted Magnetic Resonance Imaging to Assess Total Kidney Volume in Patients with Autosomal Dominant Polycystic Kidney Disease. *Abdominal Radiology* **43**, 1215–1222 (1st May 2018).
48. Morris, D., Donnelly, M., Gifford, F., Dunne, P., Hayes, P., Simpson, K., Fallowfield, J. & Semple, S. *Segmentation of the Cortex and Medulla in Multiparametric Magnetic Resonance Images of the Kidney Using K-Means Clustering* in *Proc. Intl. Soc. Mag. Reson. Med.* 27 ISMRM. **27** (Montreal, 13th May 2019), 1915.

# **Chapter 6**

## **Ex-Vivo Renal MRI**

---

## Abstract

Despite recent developments in quantitative renal Magnetic Resonance Imaging (MRI) the current clinical standard for diagnosis of renal pathologies is limited to collection of a biopsy for histology, an invasive procedure that is not without risks and highly susceptible to sampling bias. To aid the clinical adoption of renal MRI the association between MRI contrasts and underlying histology must be better understood.

By scanning subjects who are due to undergo a nephrectomy as part of their standard clinical care, the same kidney can be imaged in-vivo using state of the art protocols prior to organ removal. Once the kidney has been removed, the explant can be imaged ex-vivo in exquisite detail to collect the highest quality of MRI data, this can then be correlated to histological analysis. These three complimentary streams of data will lead to a better understanding of the MRI parameters and validate quantitative MRI in the clinic. In future, such an ex-vivo MRI protocol could also be used to assess the viability of kidney grafts prior to transplant. Here a matched ex-vivo and in-vivo multiparametric renal MRI protocol and advance analysis methods are developed for future clinical studies.

*This work was presented at the International Society of Magnetic Resonance in Medicine (ISMRM) 27th Annual Meeting, 2019 [1] and United Kingdom Kidney Week (UKKW) 2019 [2]. The bespoke analysis pipelines and software developed here have been incorporated into the development of the United Kingdom Renal Imaging Network (UKRIN) Kidney Analysis Toolbox (UKAT) [3]. This work will be presented at the ISMRM 29th Annual Meeting, 2021, [4].*

## 6.1 Introduction

A recurring theme in renal Magnetic Resonance Imaging (MRI) studies are the limitations imposed by respiratory motion. Sequences must either be optimised and accelerated to fit within a breath-hold, hugely slowed down through the use of respiratory triggering or accepting that motion artefacts are inevitable during a free-breathing acquisition. Additionally the common trade-off in MRI between voxel size, Field Of View (FOV) and acquisition time becomes all the more limiting. While these issues are ever-present in day-to-day clinical practice, to validate methods for clinical adoption it is desirable to acquire data of higher quality (spatial resolution and multiple contrasts) in the research phase. This can provide a detailed understanding of the spatial variance of MRI contrasts across the whole kidney to inform lower resolution clinical scans.

In this chapter, techniques for ex-vivo renal MRI are developed. These allow research to be conducted without the limitations imposed by respiratory motion to study the kidney in great detail, develop new imaging protocols and understand multiparametric MRI contrast and its association with underlying histological features. In the future, this ex-vivo imaging protocol, could be used to compare in-vivo and ex-vivo measures in patients undergoing a nephrectomy or used in transplant centres to assess allograft viability prior to transplant.

### 6.1.1 Validation of Multiparametric MRI via a Nephrectomy Model

Blood and urine tests are commonly used to assess renal health and function however, these are indirect measures and given no indication as to the health of individual kidneys. Consequently, the gold standard in renal diagnostics is a biopsy followed by histological analysis. During a renal biopsy,

## 6.1. Introduction

---

an area on the patients back is injected with local anaesthetic then, using ultrasound as a guide, a biopsy needle is inserted into the kidney to remove a sample of the tissue. Acquiring the biopsy takes approximately half an hour. After the sample is removed the patient is then asked to lie in bed for several hours to minimise the risk of internal bleeding. In approximately 1 % of patients, the bleeding caused will require a blood transfusion and approximately 0.5 % of patients will require embolisation. While these risks are relatively small, the procedure is still an invasive, destructive and time consuming one for the patient thus making it poorly suited for longitudinal monitoring of renal health. Additionally, this method of biopsy is not viable for some patients such as those with coagulopathy or thrombocytopenia due to the increased risk if a hemorrhage occurs, or those that are unable to lie prone such as those patients who are intubated for respiratory assistance [5]. While techniques such as the transjugular renal biopsy have been developed (albeit accidentally after taking a wrong turn at the portal vein while trying to acquire a liver biopsy [6]) to serve these patients, this is a more technically complicated procedure. Finally, the samples acquired via biopsy are very small and thus are often not representative of the entirety of the kidney biopsied, let alone both kidneys.

These drawbacks of biopsy have provided a key incentive for the development of multiparametric renal MRI protocols which could prove to be advantageous for both clinical decision making and patient care and well-being. A key aspect in the widespread adoption of MRI into renal clinical practice, is a full understanding of the interplay between the current histological measures and MRI contrasts. While it is possible to correlate biopsy results with MRI findings and gain some information as to how different MRI measurements vary with tissue properties, this suffers from the small tissue sampling volumes outlined above [7]. An alternative paradigm is the nephrectomy model where it may be possible to scan the kidney in-vivo to collect multiparametric renal MRI data, and then scan the organ ex-vivo to acquire exquisite MRI data of a far higher spatial resolution or with many more contrasts than would be possible in-vivo and then perform whole organ

## 6.1. Introduction

---

histology on the tissue, Figure 6.1. These three streams of complimentary data, all acquired from the same organ, allow direct relationships to be formed while relating the data back to clinically feasible, lower spatial resolution measures.

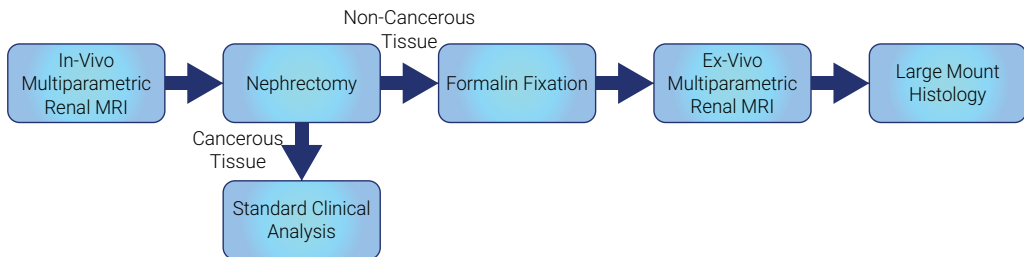


Figure 6.1: Flowchart showing an overview of the nephrectomy paradigm.

One of the first studies correlating in-vivo multiparametric MRI with renal histology was by Inoue *et al*, who found a statistically significant negative correlation between fibrosis area, as determined from a renal biopsy stained with Masson's trichrome, and Apparent Diffusion Coefficient (ADC) and  $T_2^*$  in 37 Chronic Kidney Disease (CKD) patients [8]. This was confirmed by Zhao *et al*, who also reported a strong negative correlation between ADC of both the renal cortex and medulla and histopathological fibrosis score in 25 CKD patients [9]; this study used a more comprehensive histopathology protocol. Feng *et al* also showed a negative correlation between glomerulosclerosis, fibrosis, Fractional Anisotropy (FA) and ADC in CKD subjects [10]. Friedli *et al* published a significant positive correlation between cortical-medullary differences in  $T_1$  and fibrosis and negative correlation between cortical-medullary differences in ADC and fibrosis, this was first published in rats, where MRI data was correlated with histology of whole organs rather than just biopsy samples [11]. The same group then validated this finding in 164 human subjects, correlating MRI measures with biopsy rather than whole organ measures [12].

Outside of the renal MRI community, studies have been done with registered whole-mount histology and both in-vivo and ex-vivo MRI. Jafari *et al* performed volume matched ex-vivo Quantitative Susceptibility Mapping

## 6.1. Introduction

---

(QSM) and  $T_2^*$  mapping with whole explant histopathology of the liver using the histopathology results to validate predictions of fibrosis using MRI [13]. The University of British Columbia group have carried out extensive work correlating histopathology of whole prostatectomy samples with in-vivo MRI [14, 15]. The same group have also made use of ex-vivo scanning techniques to correlate histopathology with 7T narrow-bore ex-vivo data and 3T in-vivo data [16]. The use of matched histology and MRI data is now becoming well established in the neuroimaging field [17] with studies correlating histopathology with diffusion measures [18–21], magnetisation transfer [22, 23], QSM [24, 25] and relaxometry measures [26, 27]. Additionally, post processing packages have been developed to enable accurate registration of whole mount histopathology and MRI data [28, 29].

Thus far, no work has been published comparing in-vivo and ex-vivo MRI measurements with whole organ renal histology. The ideal paradigm for this work is to scan patients who are undergoing a nephrectomy as part of their standard clinical care, typically for treatment of cancer. Briefly, this method would involve scanning a subject prior to surgery to acquire a multiparametric quantitative MRI dataset. The subject will then have part of their kidney removed, the cancerous tissue will be sent for standard lab tests whilst the non-cancerous tissue will be immersion fixed in formalin. Equivalent scans assessing the same quantitative parameters in-vivo can then be performed ex-vivo at a much higher spatial resolution. Finally, the ex-vivo tissue will be sliced for multi-stain histopathology. This pipeline enables the comparison of tried and tested histological staining with large sample sizes, with in-vivo quantitative MRI data; the ex-vivo high spatial resolution data acts as an intermediary which can be directly spatially correlated with histology and in-vivo MRI data. To address this goal the development of an ex-vivo MRI protocol to image renal tissue is first required.

### 6.1.2 Assessment of Allograft Viability

An alternative use of an ex-vivo MRI protocol is the assessment of allograft viability. Availability of transplant kidneys is a major limiting factor in the treatment of many patients with end-stage kidney disease. This results in long times on recipient waiting lists incurring additional risks to the patient from the adverse effects of dialysis upon the body and resulting in higher costs to health services.

Despite the shortage of donor kidneys, a significant proportion of those kidneys which are donated are currently discarded rather than transplanted. This is due to an understandably cautious approach to acceptance of organs from older donors or those with co-morbidities. However these discarded organs will inevitably span a range of organ qualities, some of which could have been viable grafts. One method of increasing the number of available organs for transplant is to reduce the proportion of discarded kidneys while also avoiding transplanting unviable grafts. To try and assess the viability of marginal organs two methods have been developed using data from the United Kingdom and United States transplant registries. These methods both produce a risk index designed to give 1 for a healthy 40 year old donor, with a risk index  $< 1$  indicating a lower risk donor and a risk index  $> 1$  indicating a higher risk donor. The United Kingdom Kidney Donor Risk Index (UKKDRI) is given by an empirically derived equation based on the risk factors of donor age, history of hypertension, donor weight, days in hospital and the use of adrenaline [30] while the United States Kidney Donor Risk Index (USKDRI) adds an additional ten risk factors to its model [31]. Receiver Operating Characteristic (ROC) analysis showed an Area Under Curve (AUC) of 0.62 and 0.63 for UKKDRI and USKDRI respectively, indicating both models have limited predictive ability. Model accuracy could likely be highly improved by including measures specific to the kidneys themselves rather than simply demographic and global clinical factors.

## 6.1. Introduction

---

Between 2009 and 2013, 65 % of kidney donations came from deceased donors rather than living donors [32]. As these donations are unplanned, there is a significant time period between kidney retrieval and surgery while a recipient is found, during this time tests could be run on the kidney allograft to assess its viability. One possible modality for such tests is a simple ex-vivo MRI of the organ whilst it is on cold storage prior to the transplant.

By developing a quantitative ex-vivo renal MRI protocol, the health of the kidney to be transplanted could be assessed while a recipient is being found. MRI is ideally suited due to its non-destructive, whole organ coverage, thus avoiding the sampling bias outlined as an issue with biopsy. The results from the MRI exam could be used to improve accuracy of the donor risk index and thus result in a lower rate of discarded organs and an increase in long term successful grafts.

In addition to scanning the allograft ex-vivo, an in-vivo post transplant protocol could be used to assess graft function. By proactively identifying the onset and progression of graft dysfunction, treatment could be modified to extend the life of the transplant. An overview of the potential pipeline is shown in Figure 6.2.

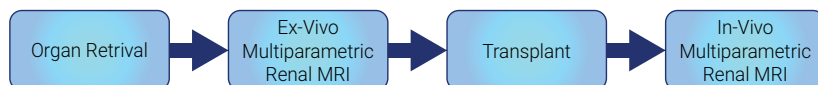


Figure 6.2: Flowchart showing the proposed pipeline for both pre-operative assessment of organ viability and post-operative assessment of graft success.

### 6.1.3 Ex-Vivo Protocol Aims

The first step to enable research into these topics is to develop a range of ex-vivo acquisition techniques with matched in-vivo counterparts. Keeping the long-term motivations outlined above in mind, the following aims and constraints were imposed on the ex-vivo protocol.

**Hardware:** Both the in-vivo and ex-vivo protocol should be able to run on readily available hospital hardware. Although some hospitals are linked to research institutions with access to pre-clinical MRI facilities, this is not the norm. Therefore the protocol should be able to be implemented on human whole body clinical scanners at 3T as these are available in most European/North American hospitals. Additionally, the use of bespoke Radio Frequency (RF) coils should be avoided, while these may deliver superior Signal to Noise Ratio (SNR) they are not readily available.

**Acquisition Time:** Without the limits on acquisition time imposed when scanning in-vivo, total protocol times can easily become very long. While it is commonplace in pre-clinical settings to scan samples for more than a day, this is not practical on a busy clinical scanner, especially in a hospital environment. As such, the ex-vivo protocol should be limited to about four hours and the in-vivo protocol limited to the standard of one hour.

## 6.2 MRI Protocol Development

Development work was performed on porcine kidney samples as these are an excellent analogue for human kidneys. Initially, samples were acquired from a local slaughterhouse however these samples were of variable quality. This was largely due to the legislation surrounding animals destined to enter the human food chain. If any part of the animal is to be consumed by humans,

## **6.2. MRI Protocol Development**

---

the carcase must be thoroughly inspected before any tissue can be released. This caused two problems. As part of the inspection, the kidneys need to be examined, this is done by making an incision in the organ, however the quality of this incision can vary massively with some samples having a neat 20 mm slice cut into them while others are roughly cut in half. The second issue is cause by the variable time between slaughter and the tissue being released after inspection. No preservation techniques, such as storing the kidneys on ice, are employed during the wait for tissue release and as such, the tissue can begin to degrade in this variable and unknown time period.

These issues meant later samples were procured from University of Nottingham Veterinary Science department in collaboration with Prof David Gardner. The animals slaughtered here are not destined for human consumption and as such the kidneys can be placed into Neutral Buffered Formalin (NBF) far quicker, additionally the kidneys do not need to be sliced open for inspection. The differing quality of samples acquired from the slaughterhouse and Veterinary Science can clearly be seen in Figure 6.3. The collaboration with Veterinary Science also enables the procurement of a more diverse range of samples such as kidneys from pigs of different ages and therefore different degrees of fibrosis or from animals with induced Acute Kidney Injury (AKI).

## 6.2. MRI Protocol Development

---

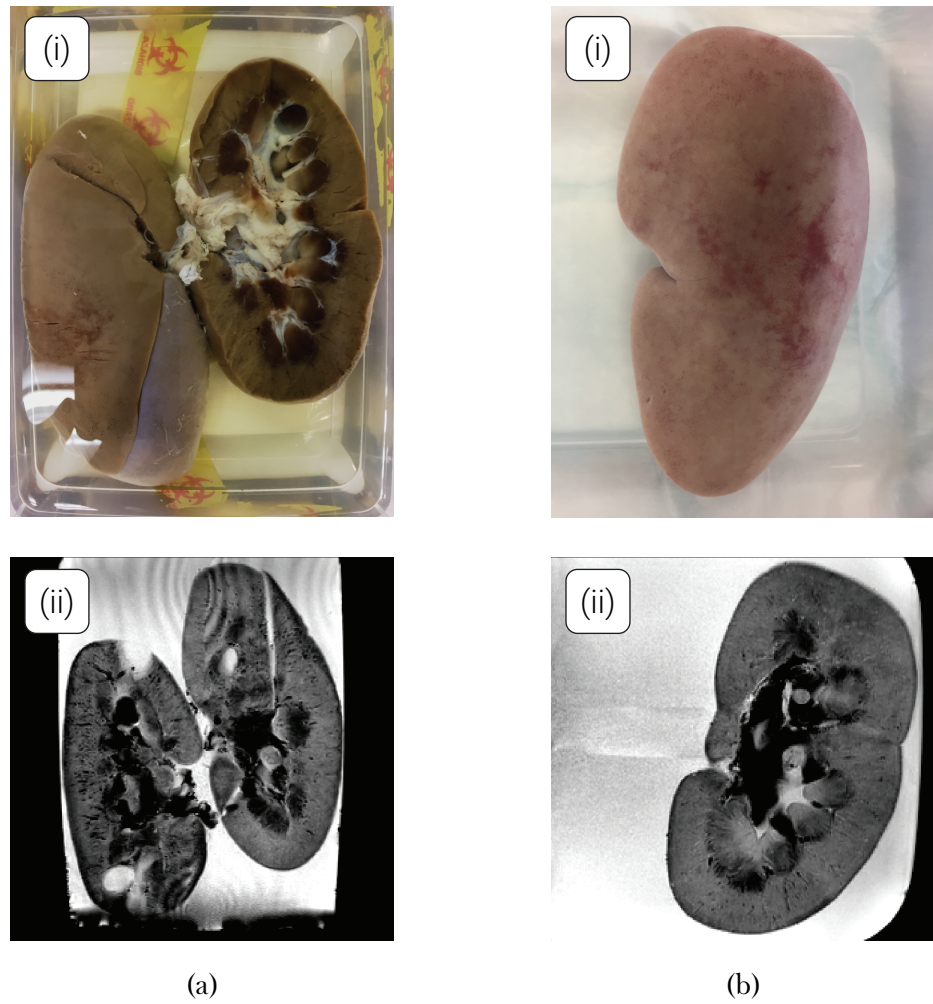


Figure 6.3: (i) Kidneys acquired from: (a) the slaughterhouse after fixation. The left hand kidney has been sliced in half; the right hand kidney has the incisions from the meat inspector clearly visible, (b) a sample procured from Veterinary Science after fixation. (ii) Associated T<sub>2</sub>-weighted Gradient Echo (GE) acquisition with TE = 40 ms.

Imaging was performed on a 3T Philips Ingenia system and some protocols were also developed for a 7T Philips Achieva system to assess the best case scenario ex-vivo images that could be acquired on human MRI scanners. Ex-vivo samples were scanned in 32-channel head coils, Figure 6.4, as these coils allowed for a whole organ to be imaged while also keeping array elements as close to the sample as possible. All in-vivo renal MRI was performed at 3T and utilised a 16-channel anterior coil array and 16-channel posterior coil array.

## 6.2. MRI Protocol Development

---

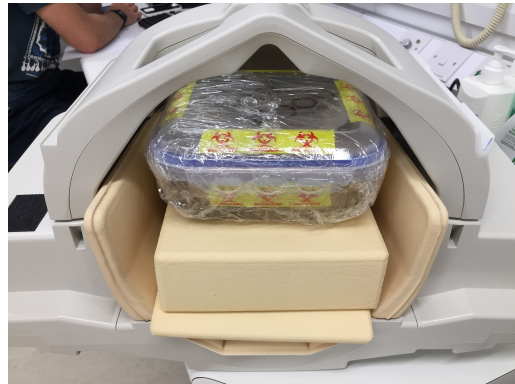


Figure 6.4: A sample sat within a sealed box in the 32 channel 8T head coil.

One of the aims of the ex-vivo protocol is to minimise time outside of the body as a confounding factor. This enables a greater degree of flexibility with regards to scan times and order of scans within the protocol. Tissue degradation occurs relatively quickly after removal from the body and as such, for this work to develop an ex-vivo protocol, the tissue was fixed to minimise this process. Samples were transported in Phosphate-buffered Saline (PBS) and then transferred into ten times the samples volume of 10 % Neutral Buffered Formalin (NBF) for twenty four hours. After fixation the samples were washed and rehydrated with PBS and remained in this solution while being scanned to minimise susceptibility artefacts arising if the sample were scanned either in air or the NBF [38]. All samples were scanned at room temperature ( $\sim 20^{\circ}\text{C}$ ).

The following sections outline the ex-vivo scan protocols set up.

### 6.2.1 Anatomical Scans

To evaluate the use of the layer based analysis techniques (outlined in Section 6.3) and calculate Total Kidney Volume (TKV) a high resolution, whole kidney coverage anatomical scan is required to segment the kidney from surrounding tissue/PBS. The ex-vivo protocol is outlined in Table 6.1; this scan was also used to plan subsequent ex-vivo scans. In-vivo,

## 6.2. MRI Protocol Development

---

the  $T_2$ -weighted Half-Fourier Acquisition Single-shot Turbo spin Echo (HASTE) structural scan from Chapter 5 is used.

Parameter	3T Ex-Vivo	3T In-Vivo
Voxel Size (mm)	$1 \times 1 \times 1$	$1.5 \times 1.5 \times 5$
FoV (mm)	$192 \times 192 \times 60$	$350 \times 350 \times 71.5$
Slices	60	13
Acquisition Mode	3D	M2D
TE (ms)	3.7	60
TR (ms)	8.1	1300
Flip Angle ( $^\circ$ )	15	90
Bandwidth (Hz)	191.5	792.3
NSA	1	1
Fold-over Suppression Oversampling (mm)	N/A	150
Sense	2 RL, 2AP	2.5
Halfscan	0.625	N/A
Fast Imaging Mode	TFE	TSE
TFE Factor	143	N/A
Shot Interval (ms)	4000	N/A
Acquisition Time	53 sec	17 sec (1 $\times$ Breath Hold)

Table 6.1: Acquisition parameters for anatomical scans.

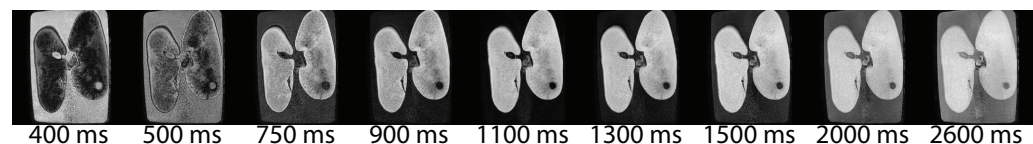
### 6.2.2 Longitudinal $T_1$ Mapping

$T_1$  mapping protocols were developed for both 3T and 7T systems using an ultrafast gradient echo inversion recovery scheme. The basics of this sequence and  $T_1$  mapping are outlined in Section 2.2.1. The sequence parameters for 3T and 7T are shown in Table 6.2. An example of the acquisitions at each Inversion Time (TI) is shown in Figure 6.5.

## 6.2. MRI Protocol Development

Parameter	3T Ex-Vivo	7T Ex-Vivo	3T In-Vivo
Voxel Size (mm)	$0.7 \times 0.7 \times 1.0$	$0.6 \times 0.6 \times 0.6$	$3 \times 3 \times 5$
FoV (mm)	$160 \times 160 \times 50$	$192 \times 170 \times 24$	$288 \times 288 \times 25$
Slices	50	40	5
Acquisition Mode	3D	3D	MS
TE (ms)	5.1	3.3	27
TR (ms)	11	7.2	5000
TI (ms)	400, 500, 750, 900, 1100, 1300, 1500, 2000, 2600	250, 500, 750, 900, 1100, 1300, 1500, 2000, 3000	0, 100, 200, 300, 400, 500, 600, 700, 800, 900, 1000, 1100, 1300
Flip Angle (°)	8	8	90
Bandwidth (Hz)	134	240	39 (Phase), 2048 (Freq)
NSA	1	2	1
Fold-over Suppression Oversampling (mm)	75	N/A	N/A
Sense	2.5 RL, 1 AP	2 RL, 1.5 AP	2.3
Halfscan	N/A	N/A	0.851
Fast Imaging Mode	TFE	TFE	EPI
TFE Factor	64	240	N/A
Shot Interval (ms)	3000	8000	N/A
Acquisition Time	1 hr 20 min 20 sec	48 min 55 sec	1 min 10 sec (Triggered)

Table 6.2:  $T_1$  mapping protocols for 3T and 7T.



(a) 3T



(b) 7T

Figure 6.5: Acquisitions at each TI.

## 6.2. MRI Protocol Development

---

After the  $180^\circ$  inversion pulse, the signal sampled at each inversion time is proportional to the modulus of the longitudinal magnetisation, as such, the true dynamic range of the inversion recovery is not sampled. There is also ambiguity as to the polarity of signals near the null point (zero crossing) which can lead to a decreased accuracy when fitting for  $T_1$  as any algorithm is essentially having to fit an extra parameter in the form of the null point. If the phase of the signal has been saved, the polarity of the magnitude can be corrected using the methods of Gowland *et al* [34, 35] thus increasing accuracy by increasing dynamic range and removing ambiguity as to the location of the null point for each voxel, Figure 6.6. Since phase data is only accurate if partial Fourier acquisition acceleration techniques (Section 2.3.2), known as halfscan, are not utilised, halfscan was not used for the ex-vivo work.

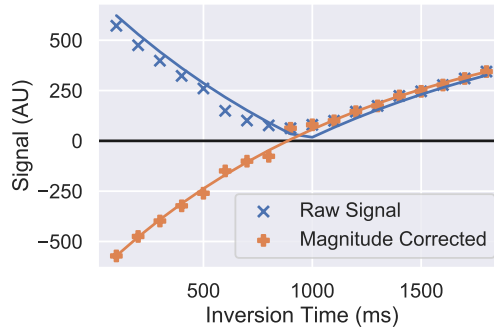


Figure 6.6: The raw signal recorded from a single voxel and the magnitude corrected signal with increased dynamic range.

Once the data has been polarity corrected, a voxel-by-voxel, least squares trust region reflective method was used to fit the data to Equation (6.1) to estimate the  $T_1$  and  $M_0$  of the tissue and an uncertainty in the fit as shown in Figure 6.7 [36]. For in-vivo acquisitions, halfscan was used and as such magnitude correction could not be employed, thus in-vivo data was fit to the modulus of Equation (6.1).

$$S(TI) = M_0 \left( 1 - 2 \cdot e^{-TI/T_1} \right) \quad (6.1)$$

## 6.2. MRI Protocol Development

---

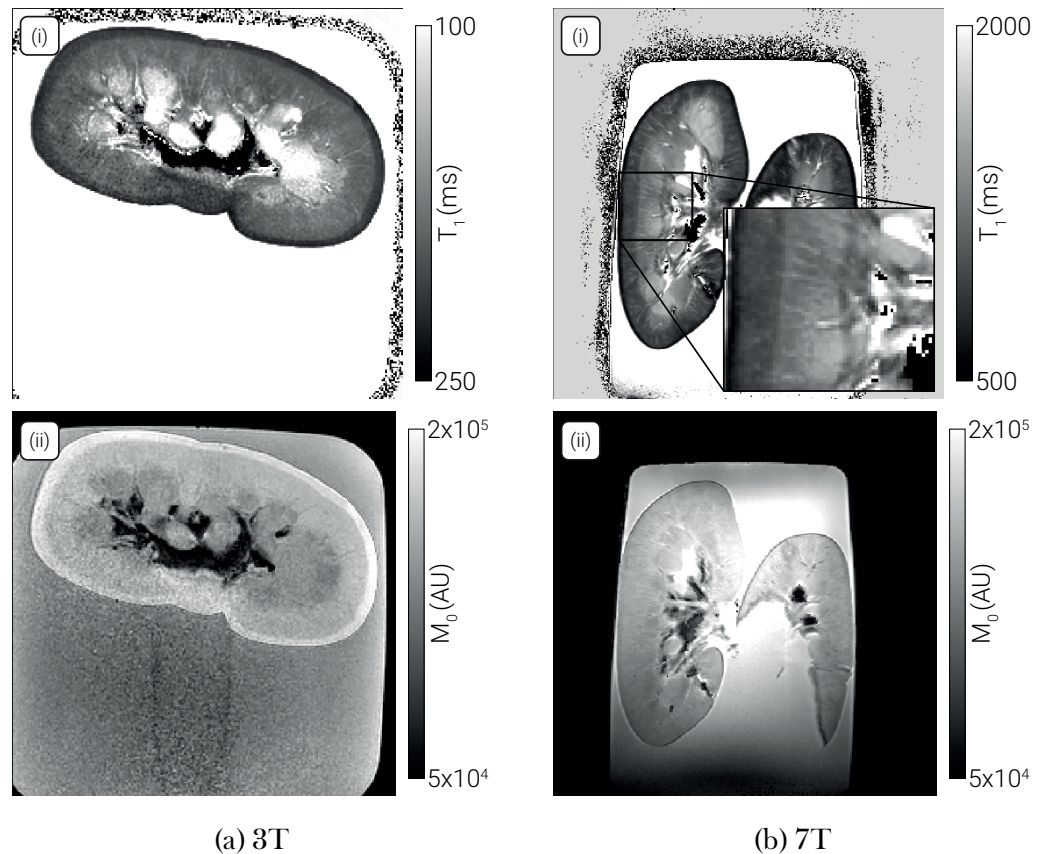


Figure 6.7: Example  $T_1$  (i) and  $M_0$  (ii) maps generated at both 3T (a) and 7T (b).

### 6.2.3 Transverse $T_2$ Mapping

The  $T_2$  mapping protocol is based on the Gradient Spin Echo (GraSE) sequence developed in Chapter 3. This sequence was only implemented at 3T and the sequence parameters are shown in Table 6.3, an example of the acquisitions at each Echo Time (TE) are shown in Figure 6.8.

## 6.2. MRI Protocol Development

Parameter	3T Ex-Vivo	3T In-Vivo
Voxel Size (mm)	$0.7 \times 0.7 \times 1.0$	$3 \times 3 \times 5$
FoV (mm)	$160 \times 160 \times 20$	$288 \times 288 \times 25$
Slices	20	5
Acquisition Mode	MS	MS
TE (ms) (Initial: Step: Final)	31:15.8:490	11:5.6:179
TR (ms)	3000	3000
Flip Angle ( $^\circ$ )	90	90
Bandwidth (Hz)	118.9 (Phase), 640 (Freq)	427.9 (Phase), 2454 (Freq)
NSA	2	1
Fold-over Suppression Oversampling (mm)	75	66
Sense	2.55	2.55
Halfscan	N/A	N/A
Fast Imaging Mode	GraSE	GraSE
TFE Factor	30	30
EPI Factor	3	3
Startup Echoes	1	1
Acquisition Time	30 min 30 sec	3 min 9 sec (Triggered)

Table 6.3:  $T_2$  mapping sequence parameters.

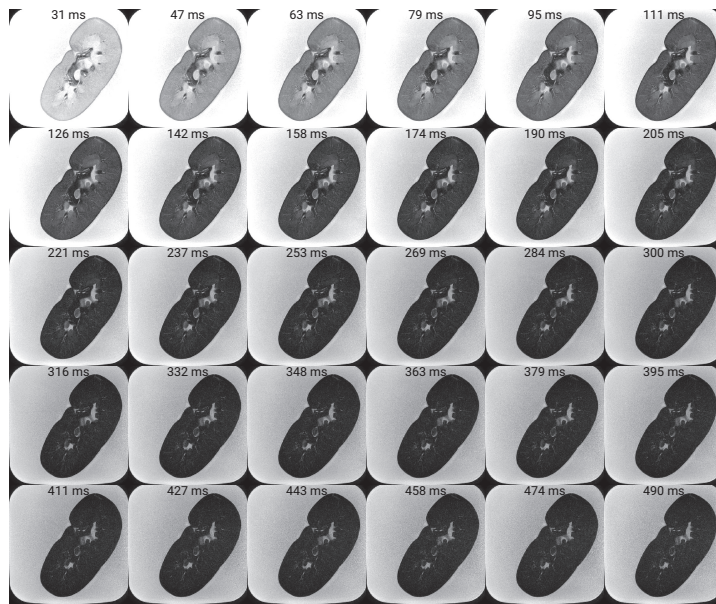


Figure 6.8: Acquisitions of an ex-vivo sample at each TE. The very wide range of TE sampled ex-vivo will enable future multi-exponential analysis of the data allowing for a more accurate quantification of the long  $T_2$  components of the tissue [14, 37].

## 6.2. MRI Protocol Development

---

$T_2$  maps were generated on a voxel-by-voxel basis using a least squares trust region reflective method to fit the data to Equation (6.2) and thus estimate  $T_2$  and  $M_0$ .

$$S(TE) = M_0 \cdot e^{-TE/T_2} \quad (6.2)$$

As outlined in Section 3.3.2 multiple methods of estimating  $T_2$  were compared with the basic two parameter fit delivering the most accurate results. Using this pipeline,  $T_2$  maps could be generated, an example of which is shown in Figure 6.9. While partial voluming has been minimised by keeping voxel sizes small, the use of multi-exponential fitting models should be explored in future. This would allow the long  $T_2$  components of the signal, such as the signal from PBS to be modelled separately to the renal tissue, thus increasing accuracy.

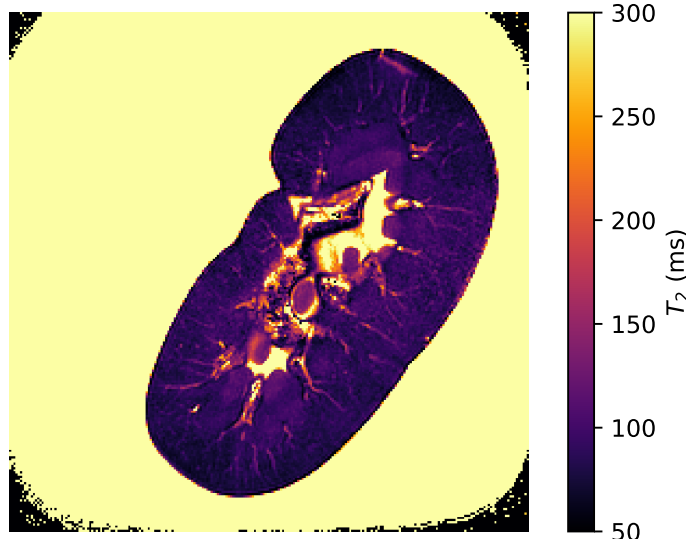


Figure 6.9: Example ex-vivo  $T_2$  map acquired using the GraSE scheme above. This sample had been formalin fixed and stored in PBS for multiple months, hence the lack of contrast between cortical and medullary tissue.

### 6.2.4 Transverse $T_2^*$ Mapping

Transverse  $T_2^*$  mapping was performed using a simple multi-slice gradient echo sequence as outlined in Section 2.2.2 with data collected at both 3T

## 6.2. MRI Protocol Development

---

and 7T. The acquisition parameters are shown in Table 6.4 and example acquisitions at each TE are shown in Figure 6.10. In addition to the magnitude data saved for  $T_2^*$  mapping, the phase data was also saved to allow a QSM pipeline to be developed in future.

Parameter	3T Ex-Vivo	7T Ex-Vivo	3T In-Vivo
Voxel Size (mm)	$0.7 \times 0.7 \times 1.0$	$0.5 \times 0.5 \times 1$	$1.5 \times 1.5 \times 5$
FoV (mm)	$160 \times 160 \times 25$	$145 \times 145 \times 10$	$288 \times 288 \times 25$
Slices	25	10	5
Acquisition Mode	MS	MS	MS
TE (ms) (Initial: Step: Final)	15:5:50	10, 13, 16, 19, 22, 25, 28, 30	5:3:38
TR (ms)	697	178 - 463	79
Flip Angle ( $^\circ$ )	38	38	25
Bandwidth (Hz)	35 - 56	35 - 88	1328.6
NSA	1	3	1
Fold-over Suppression Oversampling (mm)	75	N/A	144
Sense	2	2	2
Halfscan	N/A	N/A	N/A
Fast Imaging Mode	None	None	None
Acquisition Time	46 min 25 sec	20 min 8 sec	47 sec (3 $\times$ Breath Hold)

Table 6.4: Acquisition parameters for  $T_2^*$  mapping sequences at 3T and 7T.

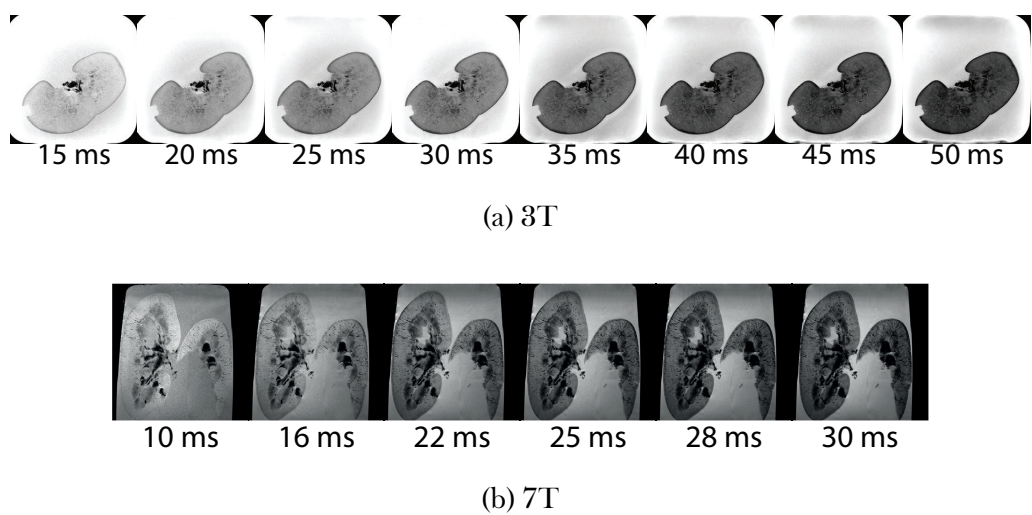


Figure 6.10: Acquisitions at each TE shown for (a) 3T and (b) 7T.

## 6.2. MRI Protocol Development

---

Estimation of  $T_2^*$  can be performed via two different methods, fitting to a two parameter exponential (Equation (6.3)) or performing a weighted linear fit to the natural logarithm of the signal. The latter of these methods is far less computationally intensive and as such, runs much quicker.

$$S(TE) = M_0 \cdot e^{-TE/T_2} \quad (6.3)$$

The acquisition parameters of the 3T ex-vivo protocol were simulated to compare the two fitting methods using Monte Carlo techniques. The linear fit produces a slightly greater Coefficient of Variation (CoV) than the exponential fit at lower  $T_2^*$ , Figure 6.11a. Additionally, the relative error, defined by Equation (6.4), has a greater magnitude below 20 ms when fitting with the linear fit than the exponential fit, Figure 6.11b. Since the  $T_2^*$  expected from the kidneys at 3T is greater than 20 ms, in the interests of computational efficiency, the linear fitting method was used.

$$\text{Relative Error} = \frac{t_2^* \text{ fit} - t_2^* \text{ simulated}}{t_2^* \text{ simulated}} \quad (6.4)$$

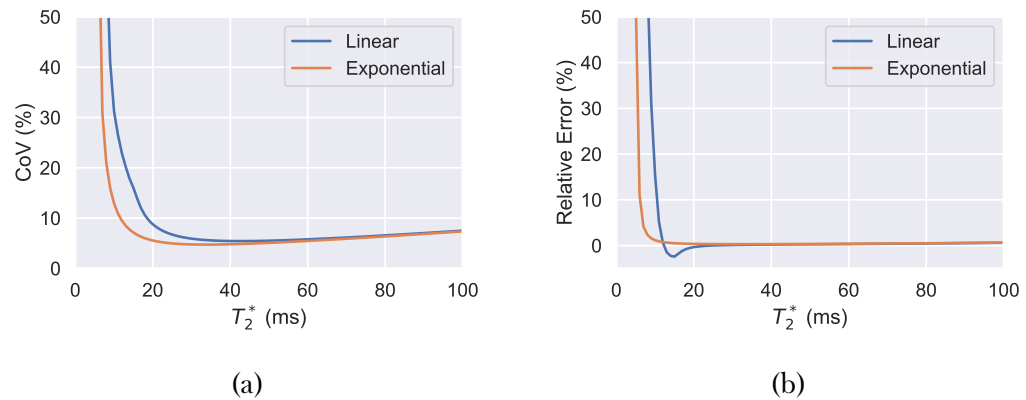


Figure 6.11: Simulations to ascertain the accuracy of each  $T_2^*$  fitting algorithm over a range of  $T_2^*$ .

## 6.2. MRI Protocol Development

---

Using the acquisition and post processing steps above,  $T_2^*$  maps were generated, examples of which are shown in Figure 6.12.

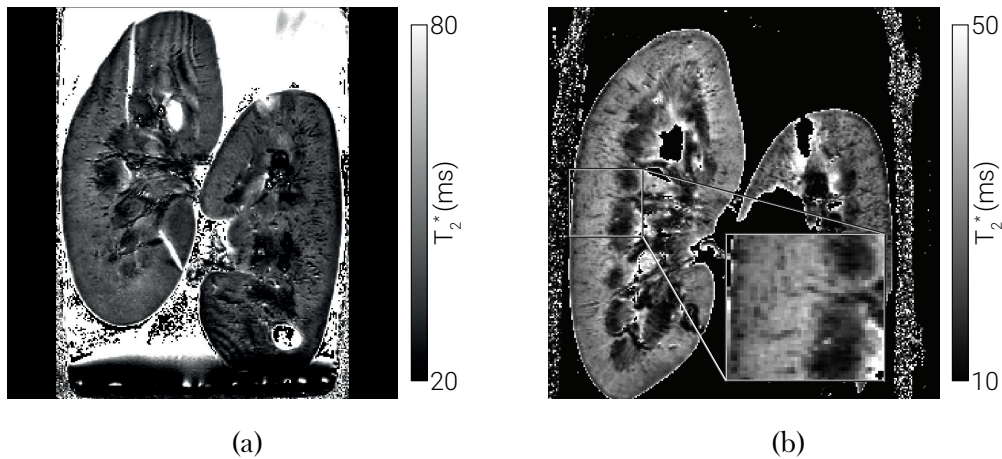


Figure 6.12: An example  $T_2^*$  map acquired at 3T (a) and 7T (b) fit using the weighted fit to the natural logarithm of the signal. Note the exquisite detail. This technique has shown potential to assess nephron number. The ripple artefact seen in the kidney at 3T is an artefact observed in the PBS which is then wrapping into the kidney. To negate this issue in later scans fold-over suppression oversampling was used.

### 6.2.5 Apparent Diffusion Coefficient Mapping

Here Diffusion Weighted Imaging (DWI) is performed using a single shot Spin Echo (SE)-Echo Planar Imaging (EPI) sequence over a range of b-values applied in three orthogonal directions. b-values are modulated by changing the gradient amplitude and keeping the duration of the gradients consistent across b-values. The underlying principles of diffusion imaging are outlined in Section 2.2.4. By acquiring diffusion gradients in three directions and calculating the mean, the effects of diffusion anisotropy can be minimised. The sequence was developed on the 3T scanner and sequence parameters are summarised in Table 6.5.

## 6.2. MRI Protocol Development

---

Parameter	3T Ex-Vivo	3T In-Vivo
Voxel Size (mm)	$1.5 \times 1.5 \times 1.5$	$1.5 \times 1.5 \times 5$
FoV (mm)	$160 \times 160 \times 51$	$288 \times 288 \times 25$
Slices	34	5
Acquisition Mode	MS	MS
TE (ms)	72	71
TR (ms)	1800	1800
b-values (s/mm <sup>2</sup> )	0, 5, 15, 30, 45, 60, 75, 90, 105, 120, 135, 150, 175, 200, 300, 400, 500, 600	0, 5, 15, 30, 45, 60, 75, 90, 105, 120, 135, 150, 175, 200, 300, 400, 500, 600
Flip Angle (°)	90	90
Bandwidth (Hz)	13.2 (Phase), 1332 (Freq)	13.7 (Phase), 1415 (Freq)
NSA	1	1
Fold-over Suppression Oversampling (mm)	75	N/A
Sense	2.3	2.3
Halfscan	0.676	0.676
Fast Imaging Mode	EPI	EPI
EPI Factor	91	83
Phase Encode Direction	L then R	L then R
Acquisition Time	9 min 44 sec	2 min 42 sec (Triggered)

Table 6.5: ADC mapping acquisition parameters.

The diffusion sensitising block of the pulse sequence is time consuming and as such necessitates the use of fast imaging techniques, EPI is the simplest to implement however is not without drawbacks. It suffers from geometric distortions in the phase encode direction, due to inhomogeneities in the  $B_0$  field caused by susceptibility differences. These geometric distortions can be problematic as the ability to correlate, on a voxel-by-voxel basis, parameters acquired with different sequences is at the core of multiparametric MRI. As the distortions are predominantly in the phase encode direction, by inverting the direction of the phase encode blips, the direction of the distortion can be reversed, Figure 6.13a. By acquiring images with both phase encode directions the underlying field map can be estimated and used to undistort the data [38]. This process can be carried out using fMRIB Software Library

## 6.2. MRI Protocol Development

---

(FSL) “topup” however, as this tool was designed for work in the brain, a custom configuration to perform more iterations of the field estimation algorithm with a greater degree of regularisation was required.

Although in some cases it is possible to acquire only the  $b = 0 \text{ s/mm}^2$  image in both phase encode directions to calculate the displacement field, then apply this field to other  $b$ -values, it was decided that the  $\sqrt{2}$  SNR increase of acquiring two volumes and averaging them is beneficial. Additionally if, in the case of in-vivo data, there are issues with motion in the  $b = 0 \text{ s/mm}^2$  volumes, then another diffusion weighting can be used to estimate the displacement, thus adding inherent redundancy to the pipeline. This process is shown in Figure 6.13 and resulting distortion corrected images in Figure 6.14.

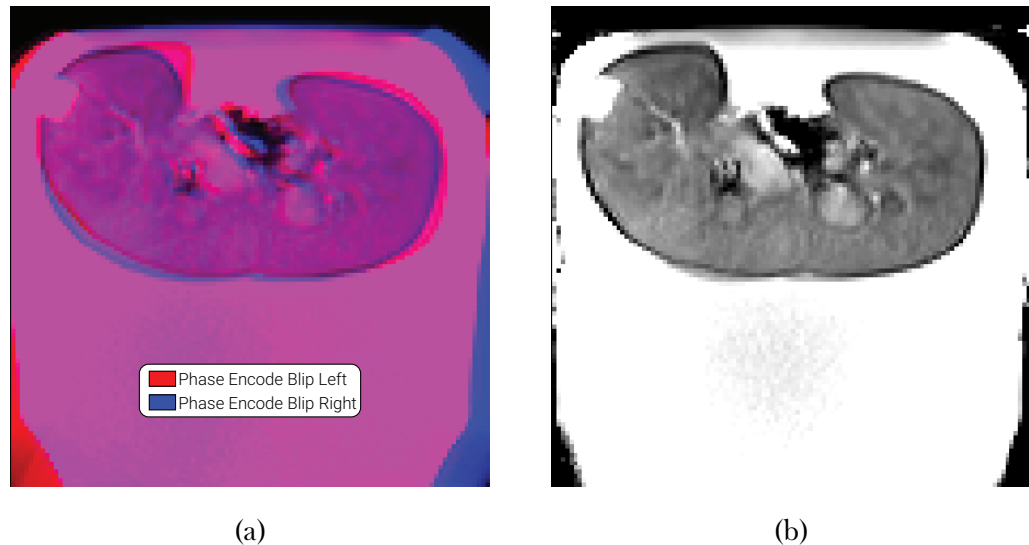


Figure 6.13: (a)  $b = 0 \text{ s/mm}^2$  images collected with opposing phase encode directions overlaid in red and blue. (b) A composite image with EPI distortions corrected using topup.

## 6.2. MRI Protocol Development

---

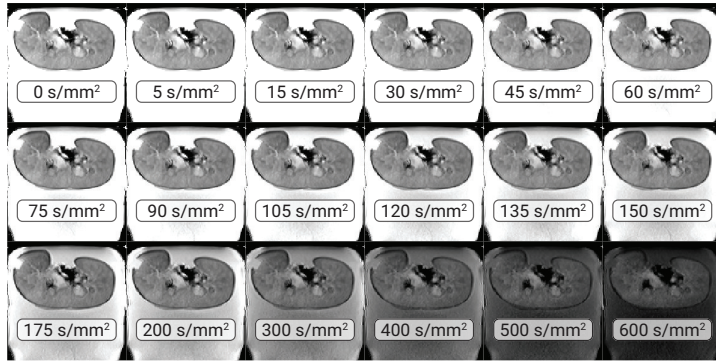


Figure 6.14: Distortion corrected images at each b-value.

The average of the three directions at each b-value and phase encode direction was calculated. EPI distortion correction was performed on both ex-vivo and in-vivo data using topup to enable accurate voxel-by-voxel comparison of ADC to other quantitative parameters. The natural logarithm of the distortion corrected signal from each voxel over each b-value was taken and a linear least squares fit performed. This enabled an estimation of ADC and an uncertainty in the fit.

Using these techniques, the ADC of both ex-vivo and in-vivo renal tissue can be calculated with no geometric distortions, Figure 6.15. Although not implemented here, the large number of low b-values sampled should make estimations of more advance diffusion parameters possible such as fitting the data to an Intravoxel Incoherent Motion (IVIM) model [39].

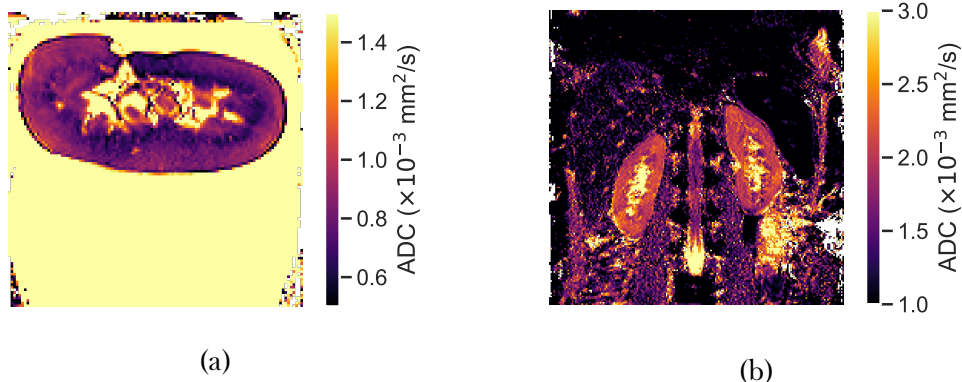


Figure 6.15: ADC maps acquired of both an ex-vivo sample (a) and in-vivo subject (b).

### 6.2.6 Diffusion Tensor Imaging

ADC maps provide an understanding as to how readily molecules can diffuse through a tissue, however they do not provide any information as to the directions molecules are travelling which can be directed by tissue structure. To measure this, Diffusion Tensor Imaging (DTI) is used. The renal group at Sir Peter Mansfield Imaging Centre (SPMIC) had no existing high resolution in-vivo (or ex-vivo) DTI protocol, as such this was specifically developed here.

The acquisition scheme uses a single shot SE-EPI scheme with monopolar diffusion gradients as in Section 6.2.5. The difference in DTI lies in the fact that, rather than acquiring a large range of b-values over three different directions, only a single  $b = 0 \text{ s/mm}^2$  and one other b-value are acquired over a minimum of six directions, although in practice many more. This is known as a single shell DTI scheme. As the diffusivity in, for example, the positive  $x$  direction is the same as the negative  $x$  direction most DTI schemes acquire a hemisphere of directions. However, to apply additional image deformation correction techniques outlined below, diffusion vectors were acquired over a full sphere, Figure 6.16.

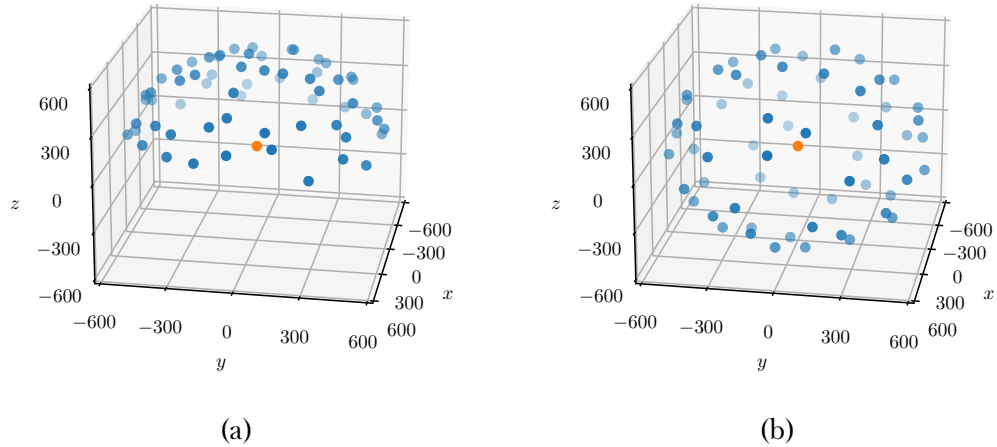


Figure 6.16: (a) 64 diffusion directions acquired over a hemisphere (b) 64 diffusion directions acquired over a full sphere as used in this chapter.  $b = 0 \text{ s/mm}^2$  is shown in orange with the high  $b$ -values shown in blue.

Mathematically, DTI estimates the tensor,  $\mathcal{D}$  in equation (6.5) where  $D_{xx}$ ,  $D_{yy}$  and  $D_{zz}$  represent diffusivity along the  $x$ ,  $y$  and  $z$  directions in the lab frame and are equivalent to the three directions sampled in Section 6.2.5.  $D_{yx}$ ,  $D_{zx}$  and  $D_{zy}$  represent diffusivity between the principle axis of the lab frame, as  $\mathcal{D}$  is symmetric,  $D_{yx} \equiv D_{xy}$ ,  $D_{zx} \equiv D_{xz}$  etc, hence DTI can be performed by only sampling a hemisphere of diffusion vectors.

$$\mathcal{D} = \begin{bmatrix} D_{xx} & D_{xy} & D_{xz} \\ D_{yx} & D_{yy} & D_{yz} \\ D_{zx} & D_{zy} & D_{zz} \end{bmatrix} \quad (6.5)$$

As for the ADC sequence, a full dataset was acquired with both opposing phase encode directions to assist with geometric distortion correction. A summary of the sequence parameters are shown in Table 6.6.

## 6.2. MRI Protocol Development

---

Parameter	3T Ex-Vivo	3T In-Vivo
Voxel Size (mm)	$2.3 \times 2.3 \times 2.3$	$3 \times 3 \times 3$
FoV (mm)	$160 \times 160 \times 51$	$288 \times 288 \times 60$
Slices	22	20
Acquisition Mode	MS	MS
TE (ms)	85	82
TR (ms)	5100	5100
b-values (s/mm <sup>2</sup> )	0, 600	0, 600
Directions	128	64
Flip Angle (°)	90	90
Bandwidth (Hz)	17.1 (Phase), 1947 (Freq)	30.5 (Phase), 2152 (Freq)
NSA	2	1
Fold-over Suppression Oversampling (mm)	100	N/A
Sense	2	2
Halfscan	0.609	0.609
Fast Imaging Mode	EPI	EPI
EPI Factor	79	47
Phase Encode Direction	L then R	L then R
Acquisition Time	52 min 42 sec	8 min 10 sec (Triggered)

Table 6.6: DTI acquisition parameters.

The large number of diffusion directions sampled makes additional geometric distortion correction possible. The rapidly switching fields of the diffusion sequence induce eddy currents in the sample, which in turn induce an opposing magnetic field. This leads to off-resonance distortions in the image which are different for each b-vector. To combat this FSLs “eddy” can be used [40]. This tool was developed for the brain data from the Human Connectome Project [41] however, here it is successfully used to reduce geometric distortions in ex-vivo and in-vivo DTI data and subject motion in the in-vivo data. The tools performance is optimal when b-vectors are distributed over a full sphere as this results in approximately opposing eddy current distortions and as such, makes estimation of the deformation more accurate.

## 6.2. MRI Protocol Development

---

Once the raw data has been processed with topup and eddy, quantitative maps can be generated. Eigenvalues ( $\lambda_1, \lambda_2, \lambda_3$ ) and eigenvectors ( $\epsilon_1, \epsilon_2, \epsilon_3$ ) are calculated for each diffusion tensor,  $\mathcal{D}$ . FA maps can be calculated from equation (6.6). Here it can be seen that if  $\lambda_1 = \lambda_2 = \lambda_3$ , as is the case for isotropic diffusion, FA tends to 0. An example renal FA map is shown in Figure 6.17a where bright voxels represent areas of higher FA and therefore more anisotropic diffusion.

$$FA = \sqrt{\frac{(\lambda_1 - \lambda_2)^2 + (\lambda_2 - \lambda_3)^2 + (\lambda_1 - \lambda_3)^2}{2(\lambda_1^2 + \lambda_2^2 + \lambda_3^2)}} \quad (6.6)$$

FA can also be used to create fibre direction maps as shown in Figure 6.17b. Here the colour is determined by the direction of the principal eigenvector,  $\epsilon_1$ , the primary direction of diffusion, and the brightness is modulated by FA. As the name suggests, these maps provide a visual indication as to the direction that diffusion is occurring in a tissue and how strongly it is constrained to that single direction.

The final voxel based map produced using the DTI data is an ADC map, often called Mean Diffusivity (MD) in DTI literature. This is calculated using equation (6.7) and an example is shown in Figure 6.17c. All three of these voxel based maps are generated using FSL.

$$MD = \frac{(\lambda_1 + \lambda_2 + \lambda_3)}{3} \quad (6.7)$$

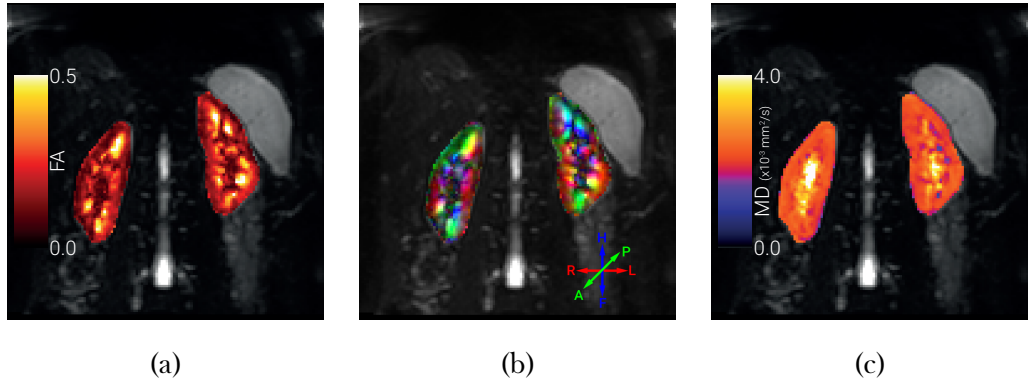


Figure 6.17: FA (a), fibre direction (b) and MD (c) maps generated from a single in-vivo DTI dataset with a single slice of 20 shown.

An extension of the fibre direction map is tractography, a technique that can remove the simplification that a voxel has a single direction of diffusion. Even at the highest resolutions achievable with MRI, the biological structures dictating diffusion are orders of magnitude smaller than the resolving power of MRI and as such multiple mechanisms can occur in a single voxel e.g. crossing of neurons or microstructure. In the brain this technique is used to visualise nerve tracts and connectivity within the brain; in the kidneys it can be used to visualise the coherent motion of renal processes and define medullary pyramids. Tractography calculations were performed using the open-source python package Dipy [42] and the resulting tracts are visualised using TrackVis [43].

To model multiple fibres entering and exiting a voxel, a more sophisticated model than simply the principle eigenvector is required. This takes the form of an Orientation Distribution Function (ODF) which can be thought of as the probability a fibre will enter or exit a voxel through a specific solid angle. ODFs can be visualised as isosurfaces where the surface represents all points of equal probability, example ODFs are shown in Figure 6.18. Techniques such as Q-ball imaging [44, 45] and diffusion spectrum imaging [44] can be used to estimate the ODF. However these methods tend to require high b-values and as such a lower SNR acquisition making them less suitable to abdominal imaging. Instead a constrained spherical deconvolution method

was used [46–48].

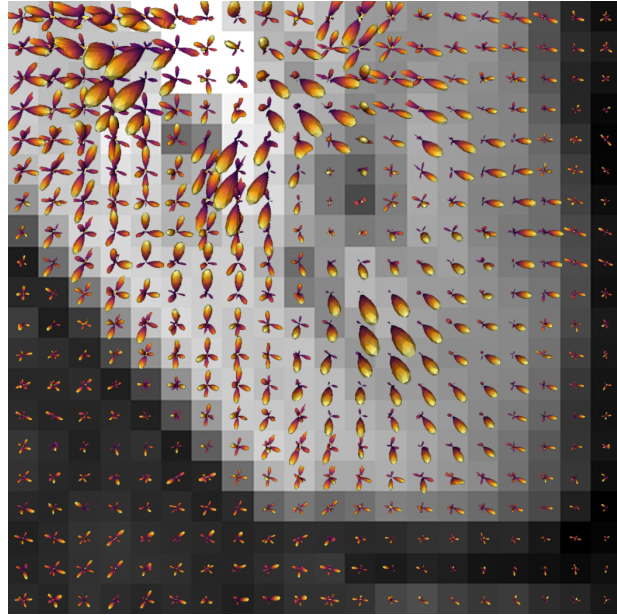


Figure 6.18: The ODFs for a small number of voxels of renal tissue overlayed on the corresponding  $b = 0 \text{ s/mm}^2$  image.

The peak values of ODFs are calculated and used to generate streamlines which represent the tracts of coherent diffusion. The calculation of streamline paths is performed using the Euler Delta Crossings (EuDX) method [49]. This tractography pipeline and its many hyper-parameters are best summarised in code form and as such are included in Appendix B. The results of this processing pipeline are tractograms as shown in Figure 6.19a. Renal in-vivo results were compared to those in literature and found to be in agreement [50–52]. Additionally, renal features with a known structure can be observed in the tractograms such as the radial structure of the medullary pyramids, Figure 6.19b.

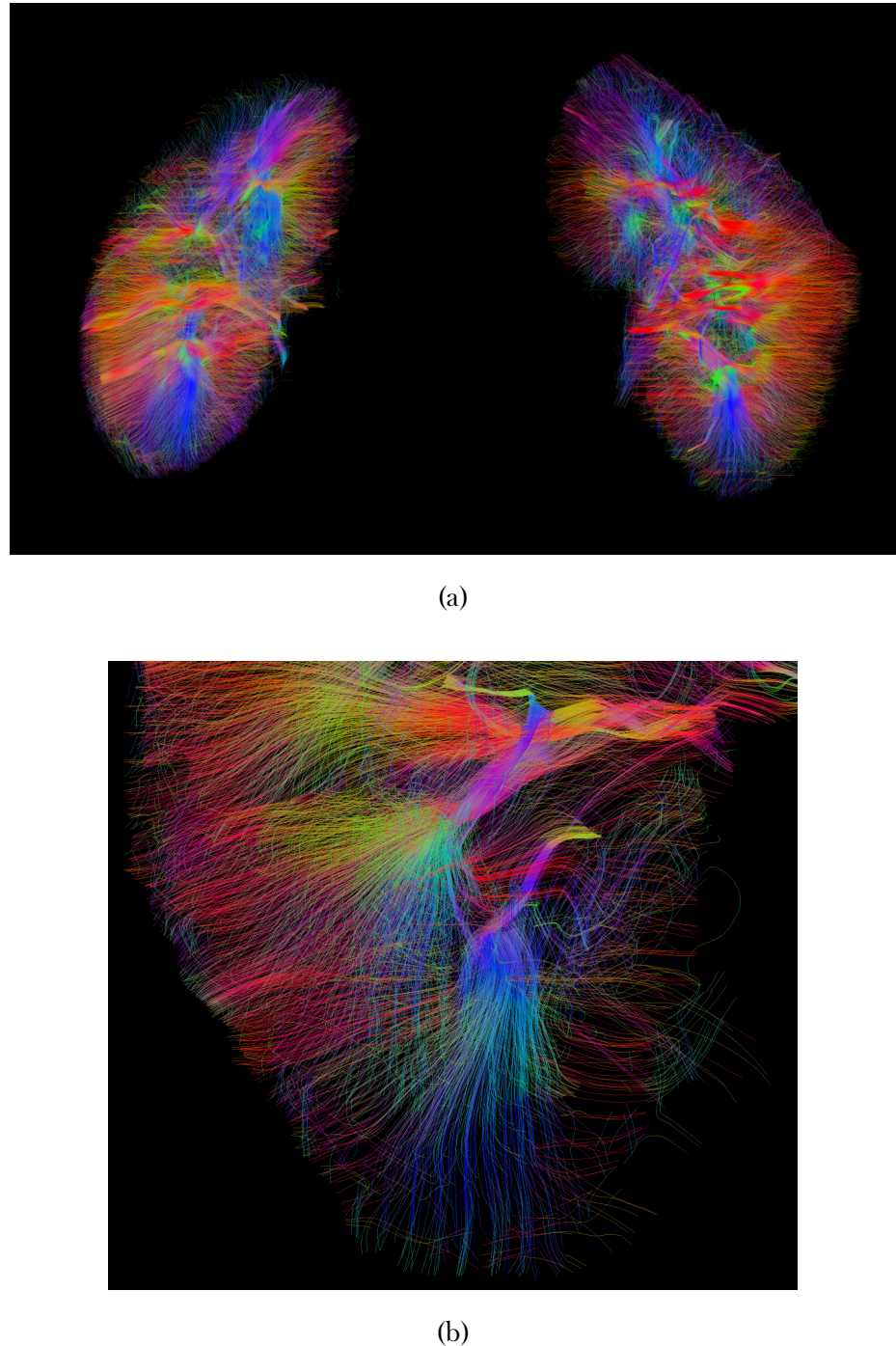


Figure 6.19: (a) Example in-vivo tractography generated using the above protocol. (b) The medullary pyramids observed in in-vivo tractography.

As this tractography protocol was developed from source for renal measures, both the acquisition and the post processing pipeline were verified in the brain. Tractography is a far more mature technique in neuroimaging and as such, verification that the pipeline produces reasonable results on a

### 6.3. Depth Based Analysis of Renal Data

---

more familiar anatomy lends confidence to the tractograms produced of the kidneys. The FOV of the acquisition was adjusted to cover the whole in-vivo brain whilst keeping all other parameters constant. The resulting tractogram of the brain produced using this pipeline is shown in Figure 6.20.



Figure 6.20: A tractogram of the brain produced to verify the DTI acquisition and post processing scheme developed for the kidneys produces expected results within a structure more commonly the subject of tractography.

## 6.3 Depth Based Analysis of Renal Data

### 6.3.1 Motivation

The vast majority of analysis of quantitative renal MRI data is based around defining Regions of Interest (ROI) within the kidneys to segment the renal cortex from the medulla and calculate the average of quantitative parameters within these ROI. While this method has provided excellent results, it is by no means perfect. The most common method to define these ROI is the manual drawing of voxels that represent each tissue type, this can lead to human bias, even if an anatomical scan is used for the segmentation

### 6.3. Depth Based Analysis of Renal Data

---

rather than the quantitative map. Automated methods have been proposed, however, as outlined in Chapter 5, these can be difficult to generalise.

There is a desire for a more objective and quantitative analysis methodology to complement the quantitative nature of the MRI data acquired. Here, inspiration has been taken from the analysis pipelines used by neuroimagers who stratify tissue by cortical layers [53–56]. Although in neuroimaging the layers are designed to mimic the underlying layer based architecture of neuroanatomy, the process of defining equidistant layers from a cortical surface can equally be applied to the kidneys where renal cortex is found at the surface of the kidney and medulla towards the centre, allowing the assessment of depth-base analysis.

The concept of applying layer based analysis to quantitative renal MRI was pioneered by Pruijm and Milani [57–60] in the context of analysis of Blood Oxygen Level Dependent (BOLD)  $R_2^*$  mapping, where  $R_2^* = 1/T_2^*$ . Their method, known as Twelve Layer Concentric Objects (TLCO), uses two user delineated boundaries, Figure 6.21a, to calculate twelve equidistant layers between the renal pelvis and cortex, Figure 6.21b. These layers can then be applied to an  $R_2^*$  map with the average of each layer calculated. The measurements of  $R_2^*$  in each layer can be used to estimate  $R_{2\text{ outer}}^*$ , analogous to cortical  $R_2^*$ ;  $R_{2\text{ inner}}^*$ , corresponding to medullary  $R_2^*$  and “slope”, comparable to cortico-medullary difference, Figure 6.21c. This technique works when it is applied to a single, coronal oblique, slice such that the cortex layer is in-plane.

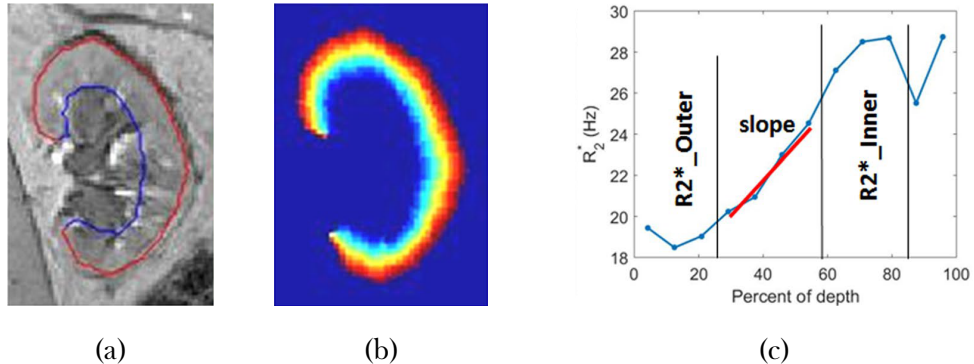


Figure 6.21: Manually defined paths of the inside (blue) and outside (red) of the kidney, (a), are used to generate layers using the TLCO technique (b). Average  $R_2^*$  is calculated within each layer and a gradient between outer and inner layers computed (c). Example images taken from Li *et al*, 2019 [60].

As part of a consensus survey, the question “The TLCO or onion peel is a preferred analysis method [for renal BOLD MRI]?” was recently put to an international panel of 24 leading experts in the field of renal BOLD MRI [61]. Only 53 % of respondents agreed with this question. One example reason for disagreement was a preference for true coronal acquisition rather than coronal oblique. This combined with the limitations of a single slice acquisition were the impetus for the development of the 3D depth based method which is presented here.

### 6.3.2 Method

This section develops a layer based analysis method using anatomical images (Section 6.2.1) to generate depth maps of the kidney. These depth maps can then be applied to any quantitative dataset collected in the same scanning session. This is conceptually similar to segmenting cortical and medullary tissue from a  $T_1$ -weighted scan, then applying those ROI to an ADC map, which itself would be difficult to segment tissues from, to calculate mean ADC for each tissue type.

#### Initial Masking

For this analysis method to be applied to quantitative data, a full kidney coverage scan must be acquired, Figure 6.22a, this scan can be any pulse sequence as long as there is sufficient contrast between the kidneys and surrounding tissue, for example in-vivo the  $T_2$ -weighted HASTE scan from Chapter 5 is ideal and for ex-vivo samples the anatomical scan in Section 6.2.1 was used. The kidneys are then segmented using this scan to generate a binary mask, Figure 6.22b. This segmentation can either be manual or automated methods can be used.

#### Generating Renal Surfaces

Using a bespoke FreeSurfer [62] pipeline, this mask can be converted from the binary voxel based representation into a smooth surface, Figures 6.22c and 6.22d. This surface is made of a very high resolution triangular mesh, Figure 6.22e, and as such allows layers to be calculated at a higher resolution than the original scan.

#### Depth Maps

The distance from the centre of each voxel to the closest point on the mesh is then calculated. The sign of this distance i.e. if the point is inside or outside the tissue, is calculated by taking the dot product of the vector from the voxel to the surface and the vector normal to the surface. If the magnitude of the dot product is positive the voxel is outside the surface, if it is negative, it is inside the surface. This results in a quantitative map of the depth of every voxel in the tissue, Figure 6.22f.

### 6.3. Depth Based Analysis of Renal Data

---

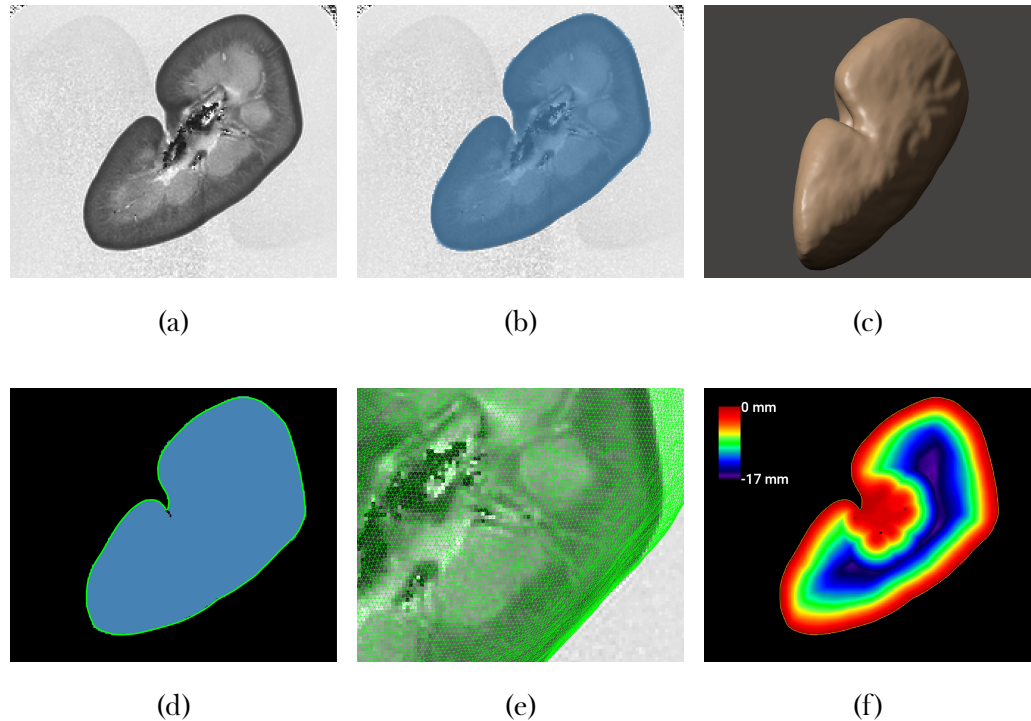


Figure 6.22: (a) The original MRI data with clear contrast between the ex-vivo kidney and surrounding tissue/PBS. (b) A binary mask generated from the image data. (c) The surface representation of the binary mask, note this does not appear blocky as it would if it were simply filled voxels. (d) The green line is the edge of the surface, the blue area is the binary mask, the surface edge is not limited to the voxel grid. (e) The mesh representation of the surface, coordinates of the vertexes of these polygons are used to calculate the distance from each voxel to the surface. (f) A depth map showing how far each voxel is from the surface of the kidney.

The depth map can be quantised to any desired precision e.g. the nearest 1 mm, resulting in layers of voxels equidistant from the surface of the kidney. Using the embedded affine transform of the quantised depth map, these layers can be transformed into the space of any other scan in the same session. This negates the need for quantitative scans to be modified either in FOV to acquire the full kidney, or geometry i.e. this addresses concern of the respondents from the renal BOLD MRI survey as they do not need to deviate from their preferred acquisition geometry. Once the quantised depth map is in the same space as a quantitative map, the average of all voxels in each layer can be

### 6.3. Depth Based Analysis of Renal Data

---

calculated. Note the layers generated using this method are quantitative by definition, rather than the percentage depth provided by the TLCO method.

#### Discussion

The 3D nature of this depth based methodology, shown in Figure 6.23 is a major advantage in quantitative renal MRI where it is common to acquire multiple slices of data; using this method all voxels in the kidney can be included in the layer calculations rather than just those of the central slice. By decoupling layer definition from quantitative map acquisition, a greater degree of robustness and flexibility is afforded. With TLCO a, off-coronal oblique  $R_2^*$  map will produce differing results to a coronal oblique acquisition, whereas this 3D method will apply the same layers to the map regardless of acquisition, thus increasing repeatability. This depth-specific renal analysis method is applied to analyse ex-vivo samples in Section 6.5.

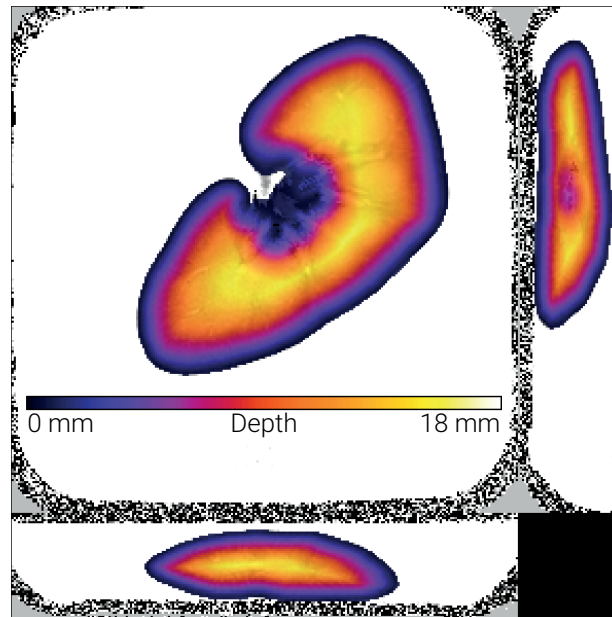


Figure 6.23: An example depth map showing the 3D nature of the layers produced using this technique.

The limitation of this method is the fact it can only be applied to whole kidneys. It relies on the surface of the sample also being the surface of the kidney; if this assumption does not hold then voxels that are at the surface of the sample will be incorrectly categorised as superficial renal tissue (generally cortex). Also the computational resources required to run the pipeline are not insignificant, both FreeSurfer and MATLAB are dependencies thus limiting the operating systems the pipeline can be run on and making setup more complicated. Additionally processing times are tens of minutes rather than seconds as is the case for TLCO.

In future a direct comparison of the depth based method outlined above and TLCO should be performed. While the methods are trying to achieve slightly different goals in their definition of layers, a comparison of which produces the most biologically relevant layers could be conducted. The depth based method is a equidistant layering technique, neuroimaging also makes use of equivolume layers [55]. These could also be relevant to renal imaging and should be explored in future.

## 6.4 Monitoring Changes in MR Parameters Post Fixation

In the study of nephrectomy samples, as outlined above, fixation is a necessity step to ensure a consistent protocol and minimise logistical hurdles in scanners availability at specific times when, by the nature of ex-vivo samples the acquisition process can be somewhat flexible in timings. The effects of fixation on brain tissue have already been reported [63–65], further it has been demonstrated that although relaxation time values shorten, they retain their sensitivity to fibrotic processes [13]; however no literature on the effects of fixation of renal tissue is available. Here we characterise the stability of  $T_1$  and  $T_2^*$  in renal tissue post fixation to ascertain the impact of the timings of the ex-vivo acquisition.

### 6.4.1 Method

The initial investigation assessed the long term stability of the kidneys by collecting  $T_1$  and  $T_2^*$  maps at both 3T and 7T over a ten week period post fixation, the kidneys were stored in PBS for the duration of the experiment. An unfixed kidney was also scanned at 3T at room temperature. Analysis was performed on the resulting maps by defining a ROI for the cortex and medulla, and calculating the mean and standard deviation of the voxels within each ROI. The changes in  $T_1$  and  $T_2^*$  can be seen in Figure 6.24.

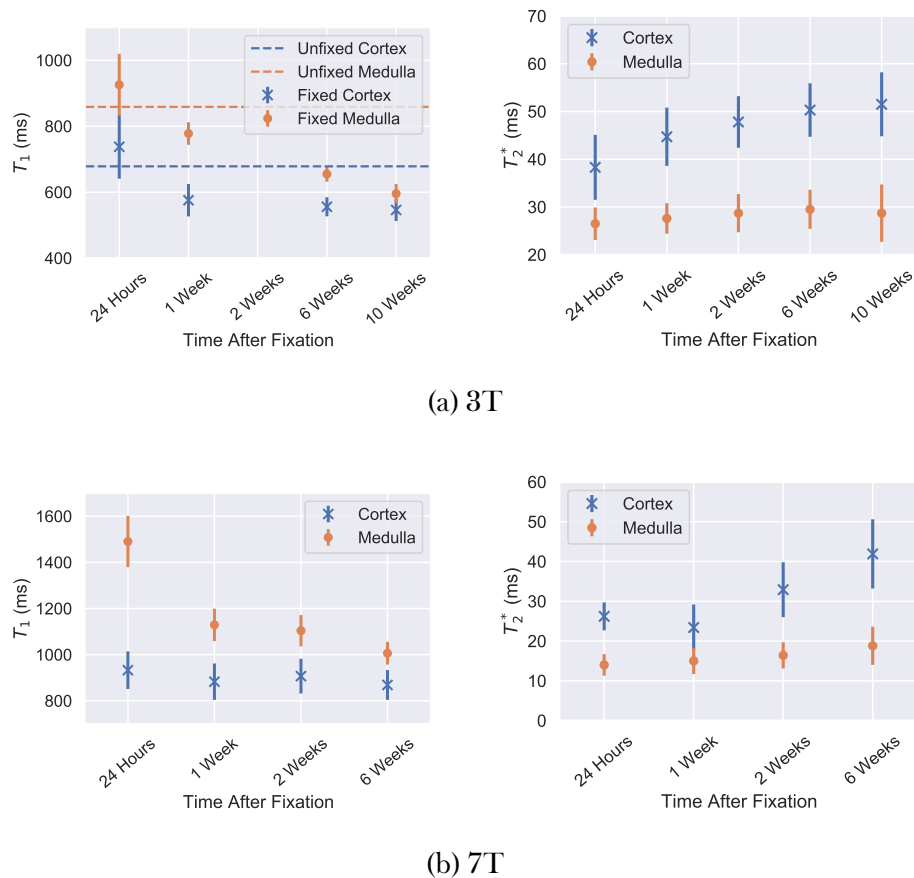


Figure 6.24: Variation in  $T_1$  and  $T_2^*$  at 3T (a) and 7T (b). Unfortunately due to technical scanner issues, it was not possible to scan the sample at 7T ten weeks post fixation and the quality of the 3T  $T_1$  data two weeks post fixation was significantly inferior due to mistakes during data acquisition; as such these data points have been omitted. Error bars show the standard deviation within each ROI.

Figure 6.24 shows the largest changes in quantitative parameters occurred between twenty four hours and one week after fixation. After this the general trend is that the  $T_1$  of the cortex and medulla converge. The  $T_2^*$  of the medulla remains relatively constant while the  $T_2^*$  of the cortex increases and begins to plateau by 10 weeks. One possible mechanism dictating the trend in  $T_2^*$  is the very slow washout of excess formalin. Formalin has a different magnetic susceptibility to PBS and renal tissue and as such, causes  $T_2^*$  to decrease. As the excess formalin washes out, the additional de-phasing caused by susceptibility differences decreases and thus  $T_2^*$  increases. The rebound in  $T_2^*$  after fixation and washing has been reported in other tissues [66, 67]. When comparing the  $T_2^*$  measured after fixation to in-vivo measurements at 3T [68] it can be seen that upon fixation the medulla shortens by a smaller proportion than the cortex and as such increases less during the washout phase. In the first week, when the samples have a  $T_1$  most similar to that of an unfixed kidney, the quantitative parameters measured will have a dependence on time and as such this necessitates a standardisation in the protocol, specifically the time at which the samples are scanned.

Since it is possible to scan most human samples within twenty four hours of fixation, it was desirable to ascertain how much  $T_1$ ,  $T_2^*$  and histology change over this period. For this, scanning was only performed at 3T as more frequent measurements were preferable to measurements at different field strengths. For this reason, the number of inversion/echo times collected was reduced to five/six inversion/echo times respectively to fit the protocol into one hour. The choice of TI and TE was arrived at empirically by calculating maps with every combination of five/six previously acquired TI/TE and comparing the resultant maps with those calculated using the full complement of inversion and echo times. The reduced protocol consisted of acquisitions with  $T_1$  mapping using TIs of 400 ms, 500 ms, 750 ms, 900 ms, 1100 ms and 2600 ms and  $T_2^*$  mapping using TEs of 15 ms, 20 ms, 25 ms, 40 ms and 50 ms. The reduction in time points sampled resulted in a mean increase in  $T_1$  of  $21 \pm 12$  ms and  $T_2^*$  of  $0.3 \pm 1.2$  ms compared to the fully sampled protocol.

#### 6.4. Monitoring Changes in MR Parameters Post Fixation

---

Scanning sessions commenced at 1.5 hours, 2.5 hours, 4 hours, 5.5 hours, 19 hours and 22 hours after the sample was removed from the NBF. Due to the potential for relatively rapid changes in properties, especially  $T_1$ , the order in which TI/TE were collected was randomised rather than ascending/descending order (however this order was kept consistent between scanning sessions). Thus any changes in  $T_1/T_2^*$  over the 30/20 minute acquisition period will manifest themselves as non-systematic noise and thus will simply increase the uncertainty in the fit rather than affecting the calculated value.

To correlate changes with histology at the same time period, the other kidney removed from the animal was biopsied at the start of each of the six scanning session. Mason's trichrome and Haematoxylin and Eosin (H and E) staining was performed on these samples.

Variation in  $T_1$  and  $T_2^*$  over the 24 hour period is shown in Figure 6.25. No significant change in either  $T_1$  and  $T_2^*$  was observed, the corresponding histology showed no change in the cortex however there was a noticeable inflammatory response in the medulla. This suggests that the ex-vivo protocol can be performed at any time in the first twenty four hours after fixation and as such makes future experimental logistics simpler.

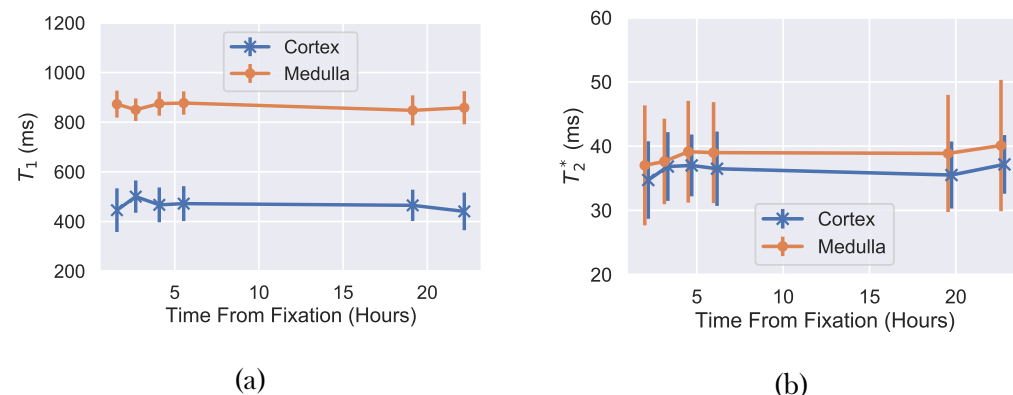


Figure 6.25: Changes in  $T_1$  (a) and  $T_2^*$  (b) in the first twenty four hours a sample is stored in PBS after being fixed in NBF. Error bars are the standard deviation within each ROI.

## 6.5 Correlating MRI Measures with Histology in Porcine Kidneys of Differing Ages

Kidneys were collected from a 0.5 year old and 2.5 year old pig. These different ages were chosen to assess whether differing levels of renal inflammation and fibrosis is detected.  $T_1$  and  $T_2^*$  maps were acquired from both samples and cortical biopsies were removed from the same animals for histological analysis.

Figure 6.26 shows example MRI data collected from these samples and Figure 6.27 shows the quantitative differences in  $T_1$  and  $T_2^*$  between the kidneys.

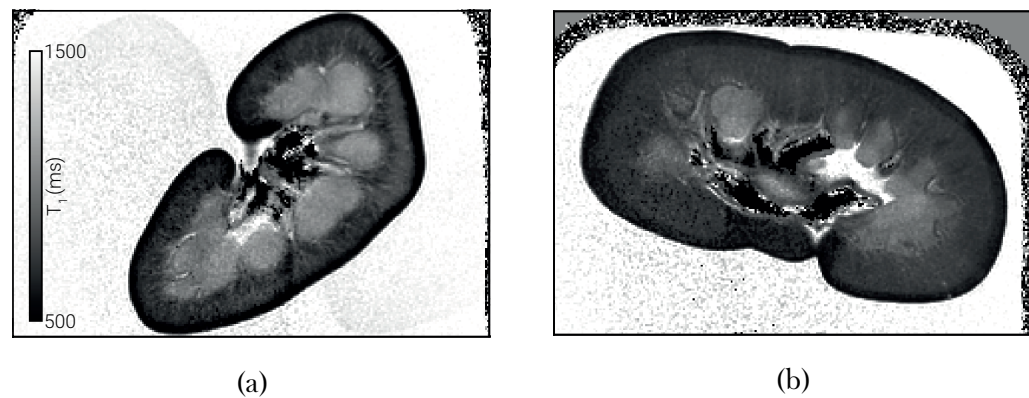


Figure 6.26: (a)  $T_1$  map of a 0.5 year old pig kidney. (b)  $T_1$  map of a 2.5 year old pig kidney.

## 6.5. Correlating MRI Measures with Histology in Porcine Kidneys of Differing Ages

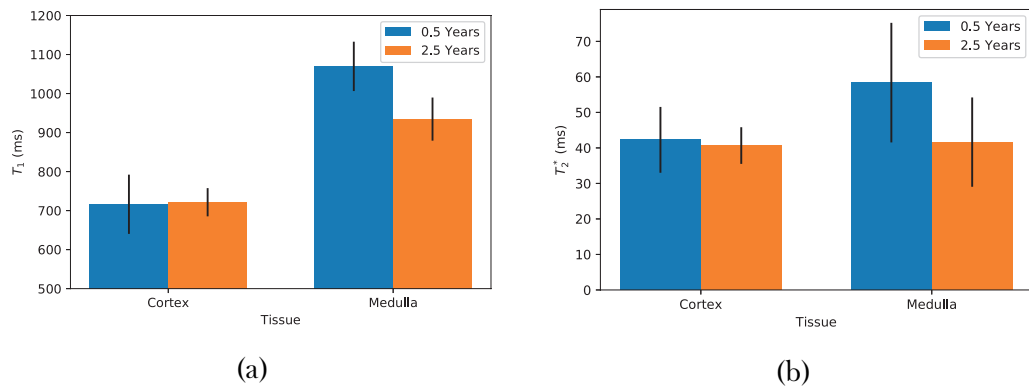


Figure 6.27: (a) The  $T_1$  of the renal cortex and medulla of the two samples. (b) The  $T_2^*$  of the renal cortex and medulla of the two samples. Error bars are the standard deviation within each ROI.

No significant change is observed in the  $T_1$  or  $T_2^*$  of the cortex; the medulla of the older kidney had lower  $T_1$ . No significant differences were observed in the biopsy samples taken from the renal cortex between the 0.5 year old and 2.5 year old samples, Figure 6.28. This suggests agreement between the MRI and histology measurements as neither showed any change in the cortex.

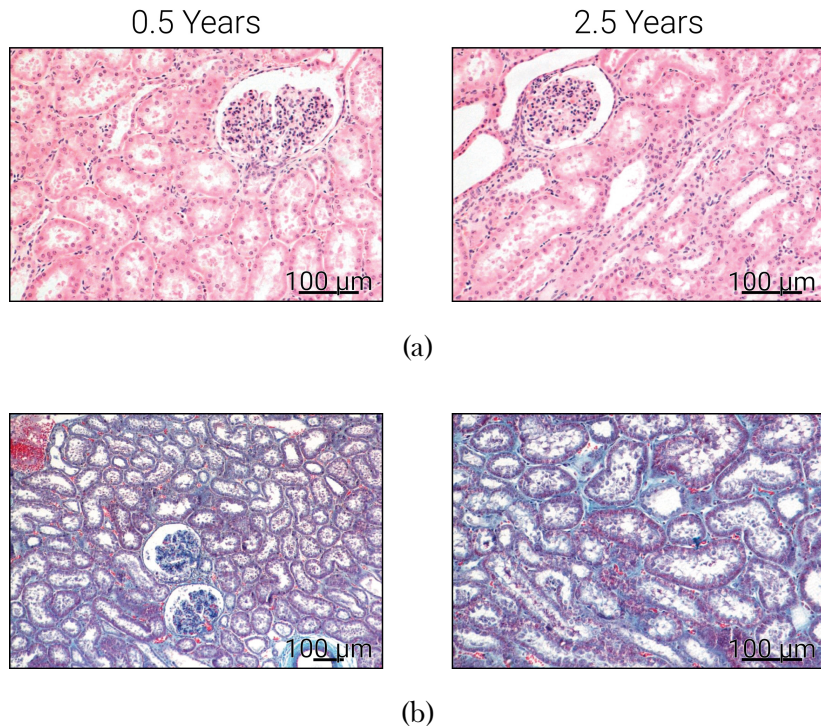


Figure 6.28: A sample of renal cortex of a 0.5 and 2.5 year old pig stained with (a) H and E and (b) Masson's trichrome.

## 6.5. Correlating MRI Measures with Histology in Porcine Kidneys of Differing Ages

---

To further investigate how  $T_1$  changes with age, kidneys of 1 day old and 4 week old pigs were scanned and compared to histology. Due to their much smaller size, manually segmenting the cortex and medulla of these samples was not possible, as such the depth based analysis outlined in Section 6.3 was employed with a layer thickness of 0.5 mm.

Initially an assessment of consistency between kidneys of the same age was performed.  $T_1$  maps of three kidneys from two different animals were generated i.e. both kidneys of one animal and the right kidney of another animal were scanned. In Figure 6.29 excellent agreement between all three kidneys can be seen, with an especially high correlation between kidneys from the same animal. This both gives confidence in the depth based analysis when applied to very small kidneys and indicates that there is a low degree of variance in kidneys of this age.

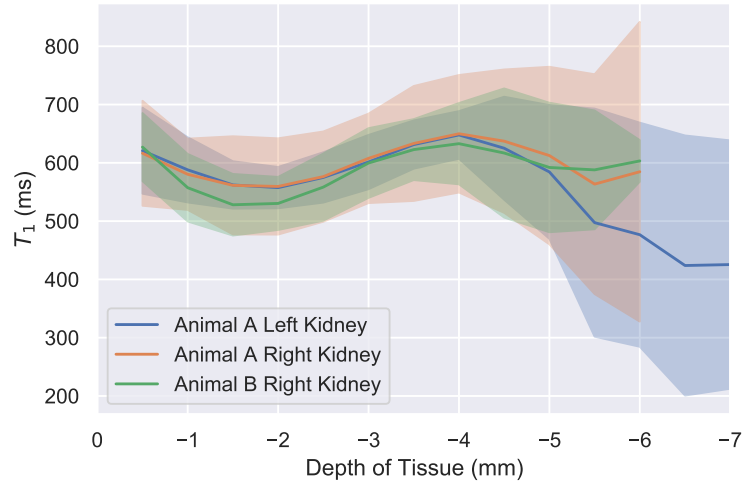


Figure 6.29: Changes in  $T_1$  with renal tissue depth in kidneys of one day old pigs. The shaded area is the standard deviation within each 0.5 mm thick layer of tissue.

The same depth based analysis was applied to a 4 week old kidney and the 0.5 year and 2.5 year old kidneys analysed above. The changes in  $T_1$  with depth are shown in Figure 6.30 both as absolute tissue depth in mm and relative tissue depth in percent, therefore normalising for kidney size. In

## 6.6. Conclusion and Future Work

---

in this figure it can be observed that the  $T_1$  of renal tissues differentiates with age. This is in part likely due to decreasing water content with age ( $\sim 85\%$  in neonatal kidneys, decreasing to  $\sim 65\text{-}70\%$  by adulthood) and in part due to the lower glomerular density in younger kidneys.

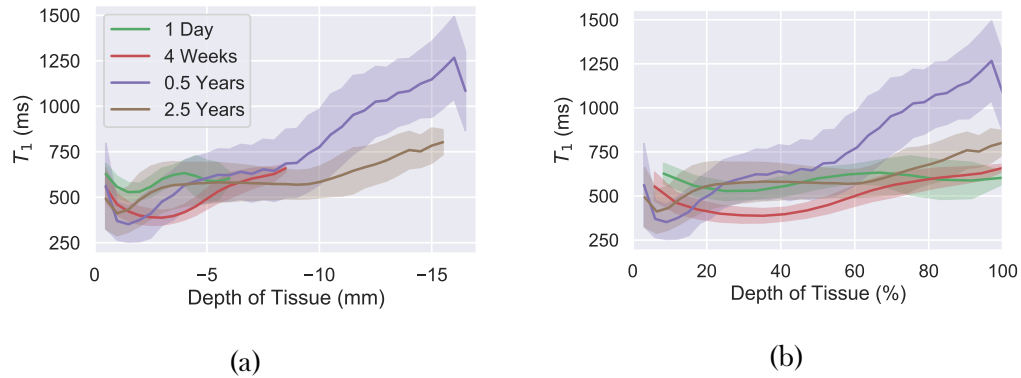


Figure 6.30: Changes in  $T_1$  with renal depth of pig kidneys of multiple ages. The shaded area is the standard deviation within each 0.5 mm thick layer of tissue. (a) shows the absolute depth, (b) shows the relative depth with 0 % being the surface of the kidney and 100 % being the deepest tissue.

In future, it would be advantageous to scan samples from older pigs as these will have a greater degree of fibrosis. However, it is not common for pigs to be kept to older ages and so this limits the possibility of highly fibrotic porcine kidneys. Biopsy samples should also include medullary tissue for histological analysis as both Figure 6.24 and Figure 6.27 indicate that medullary tissue is relatively variable in quantitative MRI and as such, being able to correlate this with histology would be insightful.

## 6.6 Conclusion and Future Work

Here an ex-vivo protocol has been developed to link with paired and in-vivo quantitative renal MRI. This has been developed to provide a pipeline for the assessment of  $T_1$ ,  $T_2$ ,  $T_2^*$ , ADC and FA and tractography in the same organ both inside and outside the body. The protocol has validated

## 6.6. Conclusion and Future Work

---

the effect of fixation time and its use in nephrectomy applications. This protocol can be combined with histological analysis of the samples to link cutting edge MRI measures with existing standards for assessment of renal health. Understanding this link will enable MRI to augment the current practice of renal biopsys. The highly localised sampling of a biopsy followed by histology can be combined with MRIs of whole organ coverage to give a better indication of the heterogeneity of renal health.

Further developments were planned in this area but unfortunately the covid-19 pandemic of 2020 limited the availability of samples, access to scanners and a human study of nephrectomy samples with coupled in-vivo and ex-vivo measurements. Firstly, the complete protocol has not been run on a single sample to collect and overlay all quantitative parameters. The correlation of histology and MRI data could also be improved. Currently, the histology and imaging data are not registered and as such voxel-by-voxel correlations with histology are not possible. Recently developed software packages focusing on the registration of histology and MRI data should assist with this aim [28].

The effects of temperature upon the quantitative measures of ex-vivo tissue has not been controlled or investigated here. All samples were scanned at room temperature of approximately 20°C however, in clinical settings kidneys are stored at approximately 0°C and in the body, the kidneys will be at approximately 37°C. Temperature has been shown to have a marked affect on quantitative MRI measurements [63, 69] and as such, given the large range of temperatures samples are likely to be scanned at, these effects should be investigated in the kidneys.

Another area of further development is the ex-vivo DTI protocol. There are promising early results, however ex-vivo diffusion imaging poses additional difficulties. During the fixation process, methyl bridges cross link with proteins within the tissue stiffening it and causing a small amount of shrinkage [70]. This combined with the lower temperatures of ex-vivo

## 6.6. Conclusion and Future Work

---

samples leads to a reduced degree of diffusion, seen in Figure 6.15. While this results in a higher SNR of diffusion sensitised volumes for a given b-value, the underlying diffusion signal being measured is much lower i.e. there is less of a difference between  $b = 0 \text{ s/mm}^2$  and  $b = 600 \text{ sec/mm}^2$  and thus the accuracy of the quantitative maps, Figure 6.31, and tractography, Figure 6.32, is reduced.

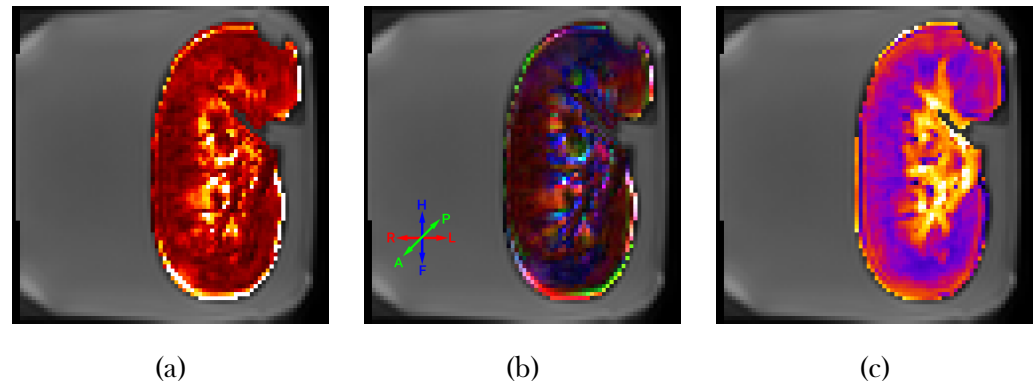


Figure 6.31: FA (a), fibre direction (b) and MD (c) maps of an ex-vivo sample.

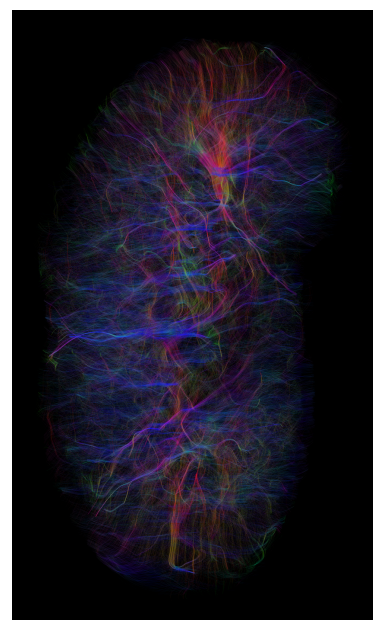


Figure 6.32: Tractography of an ex-vivo kidney sample.

The ex-vivo protocol presented here could also be used in future to assist stratification of donated organs prior to transplant by scanning organs on cold storage. Organ availability is the limiting factor in renal transplant rate, by

## 6.6. Conclusion and Future Work

---

increasing confidence in marginal quality organs the time a patient spends on the transplant waiting list could be reduced, reducing risks of complications for the patient due to extended time on dialysis and reduce cost to the health service. This would first require the validation of the effect of temperature on relaxometry measures and the linked histology on discarded organs prior to implementation. The in-vivo protocol could be used to proactively identify dysfunctional grafts and thus modify the course of treatment to extend the life of the transplant.

Further developments will explore the use of perfusion while storing kidneys waiting for a recipient to be matched. The current clinical standard in the UK is to store transplant organs in a preservation solution on ice however, reperfusing the kidneys while they are stored is an area of intense research [71–73]. Using the quantitative ex-vivo protocol developed here, the two storage methods could be compared. Additionally, the kidneys could undergo perfusion while in the scanner, this would enable the use of Arterial Spin Labelling (ASL) to assess ex-vivo renal perfusion.

Finally MRI techniques such as high resolution  $T_2^*$  weighted imaging for the an assessment of glomerular number and density would be an ideal comparison to certain histopathological metrics. While it is not possible to resolve individual glomeruli with the current protocol, other groups in Australia have recently had success applying deep learning and super resolution techniques to enable counting of the glomeruli in a sample at 3T from high resolution  $T_2^*$  weighted data.

## **6.7 Acknowledgements**

I am grateful for access to the University of Nottingham's Augusta high performance computing service. I would also like to thank Prof David Gardner of University of Nottingham Veterinary Science for his assistance with sample acquisition, histopathological processing of samples and general renal physiology expertise. Finally I wish to thank Dr Kevin Aquino for his work in developing 3D depth maps for layer analysis in the brain.

## 6.8 References

1. Daniel, A. J., Buchanan, C., Kazmi, I., Cox, E., Selby, N., Gardner, D. & Francis, S. *The Effects of Fixation and Age on Relaxometry Measurements of Ex-Vivo Kidneys* in *Proc. Intl. Soc. Mag. Reson. Med.* 27 International Society of Magnetic Resonance in Medicine Annual Meeting (Montreal, 13th May 2019).
2. Kazmi, I., Daniel, A. J., Buchanan, C., Francis, S., Taal, M. & Selby, N. *Determining Optimal Technique for Tissue Fixation for Ex-Vivo MRI Imaging of Porcine Kidneys* in. United Kingdom Kidney Week (Brighton, 6th May 2019).
3. Nery, F., Daniel, A. J., Sousa, J. & Buchanan, C. *UKRIN Kidney Analysis Toolbox* version v0.1.0. UK Renal Imaging Network, Dec. 2020.
4. Daniel, A. J. *et al.* *UKRIN Kidney Analysis Toolbox (UKAT): A Framework for Harmonized Quantitative Renal MRI Analysis* in *Proc. Intl. Soc. Mag. Reson. Med.* 29 International Society of Magnetic Resonance in Medicine Annual Meeting. **29** (Online, May 2021), 2379.
5. Rathod, K. R., Popat, B. A., Pandey, A., Jamale, T. E., Hase, N. K. & Deshmukh, H. L. Safety and Effectiveness of Transjugular Renal Biopsy: A Single Center Study. *Indian Journal of Nephrology* **27**, 118–123 (2017).
6. Mal, F., Meyrier, A., Callard, P., Altman, J. J., Kleinknecht, D., Beaugrand, M. & Ferrier, J. P. Transjugular Renal Biopsy. *Lancet (London, England)* **335**, 1512–1513 (23rd June 1990).
7. Leung, G., Kirpalani, A., Szeto, S. G., Deeb, M., Foltz, W., Simmons, C. A. & Yuen, D. A. Could MRI Be Used To Image Kidney Fibrosis? A Review of Recent Advances and Remaining Barriers. *Clinical Journal of the American Society of Nephrology* **12**, 1019–1028 (7th June 2017).
8. Inoue, T. *et al.* Noninvasive Evaluation of Kidney Hypoxia and Fibrosis Using Magnetic Resonance Imaging. *Journal of the American Society of Nephrology: JASN* **22**, 1429–1434 (Aug. 2011).
9. Zhao, J., Wang, Z. J., Liu, M., Zhu, J., Zhang, X., Zhang, T., Li, S. & Li, Y. Assessment of Renal Fibrosis in Chronic Kidney Disease

## 6.8. References

---

- Using Diffusion-Weighted MRI. *Clinical Radiology* **69**, 1117–1122 (Nov. 2014).
10. Feng, Q., Ma, Z., Wu, J. & Fang, W. DTI for the Assessment of Disease Stage in Patients with Glomerulonephritis - Correlation with Renal Histology. *European Radiology* **25**, 92–98 (1st Jan. 2015).
  11. Friedli, I. *et al.* New Magnetic Resonance Imaging Index for Renal Fibrosis Assessment: A Comparison between Diffusion-Weighted Imaging and T1 Mapping with Histological Validation. *Scientific Reports* **6**. doi:10.1038/srep30088. pmid: 27439482 (21st July 2016).
  12. Berchtold, L. *et al.* Validation of the Corticomedullary Difference in Magnetic Resonance Imaging-Derived Apparent Diffusion Coefficient for Kidney Fibrosis Detection: A Cross-Sectional Study. *Nephrology Dialysis Transplantation* **35**, 937–945 (1st June 2020).
  13. Jafari, R., Hectors, S. J., González, A. K. K. de, Spincemaille, P., Prince, M. R., Brittenham, G. M. & Wang, Y. Integrated Quantitative Susceptibility and R2\* Mapping for Evaluation of Liver Fibrosis: An Ex Vivo Feasibility Study. *NMR in Biomedicine* **34**, e4412 (2021).
  14. Sabouri, S., Fazli, L., Chang, S. D., Savdie, R., Jones, E. C., Goldenberg, S. L., Black, P. C. & Kozlowski, P. MR Measurement of Luminal Water in Prostate Gland: Quantitative Correlation between MRI and Histology. *Journal of Magnetic Resonance Imaging* **46**, 861–869 (2017).
  15. Dhatt, R. *et al.* MRI of the Prostate With and Without Endorectal Coil at 3 T: Correlation With Whole-Mount Histopathologic Gleason Score. *American Journal of Roentgenology* **215**, 133–141 (11th Mar. 2020).
  16. Uribe, C. F., Jones, E. C., Chang, S. D., Goldenberg, S. L., Reinsberg, S. A. & Kozlowski, P. In Vivo 3 T and Ex Vivo 7 T Diffusion Tensor Imaging of Prostate Cancer: Correlation with Histology. *Magnetic Resonance Imaging* **33**, 577–583 (1st June 2015).
  17. Lazari, A. & Lipp, I. Can MRI Measure Myelin? Systematic Review, Qualitative Assessment, and Meta-Analysis of Studies Validating Microstructural Imaging with Myelin Histology. *NeuroImage* **230**, 117744 (15th Apr. 2021).

## 6.8. References

---

18. Peters, J. M. *et al.* White Matter Mean Diffusivity Correlates with Myelination in Tuberous Sclerosis Complex. *Annals of Clinical and Translational Neurology* **6**, 1178–1190 (2019).
19. Moll, N. M. *et al.* Multiple Sclerosis Normal-Appearing White Matter: Pathology–Imaging Correlations. *Annals of Neurology* **70**, 764–773 (2011).
20. Howard, A. F., Mollink, J., Kleinnijenhuis, M., Pallebage-Gamarallage, M., Bastiani, M., Cottaar, M., Miller, K. L. & Jbabdi, S. Joint Modelling of Diffusion MRI and Microscopy. *NeuroImage* **201**, 116014 (1st Nov. 2019).
21. Mollink, J. *et al.* White Matter Changes in the Perforant Path Area in Patients with Amyotrophic Lateral Sclerosis. *Neuropathology and Applied Neurobiology* **45**, 570–585 (2019).
22. Mottershead, J. P. *et al.* High Field MRI Correlates of Myelincontent and Axonal Density in Multiple Sclerosis. *Journal of Neurology* **250**, 1293–1301 (1st Nov. 2003).
23. Seewann, A. *et al.* Diffusely Abnormal White Matter in Chronic Multiple Sclerosis: Imaging and Histopathologic Analysis. *Archives of Neurology* **66**, 601–609 (1st May 2009).
24. Hametner, S. *et al.* The Influence of Brain Iron and Myelin on Magnetic Susceptibility and Effective Transverse Relaxation - A Biochemical and Histological Validation Study. *NeuroImage* **179**, 117–133 (1st Oct. 2018).
25. Stüber, C. *et al.* Myelin and Iron Concentration in the Human Brain: A Quantitative Study of MRI Contrast. *NeuroImage* **93**, 95–106 (1st June 2014).
26. Bagnato, F. *et al.* Untangling the R2\* Contrast in Multiple Sclerosis: A Combined MRI-Histology Study at 7.0 Tesla. *PLOS ONE* **13**, e0193839 (21st Mar. 2018).
27. Reeves, C. *et al.* Combined Ex Vivo 9.4T MRI and Quantitative Histopathological Study in Normal and Pathological Neocortical Resections in Focal Epilepsy. *Brain Pathology* **26**, 319–333 (2016).

## 6.8. References

---

28. Huszar, I. N. *et al.* Tensor Image Registration Library: Automated Non-Linear Registration of Sparsely Sampled Histological Specimens to Post-Mortem MRI of the Whole Human Brain. *bioRxiv*, 849570 (26th Nov. 2019).
29. Huszar, I. N. *et al.* *Automated Slice-to-Volume Registration between Histology and Whole-Brain Post-Mortem MRI* in *Proc. Intl. Soc. Mag. Reson. Med.* 27 International Society of Magnetic Resonance in Medicine Annual Meeting (Montreal, 16th May 2019).
30. Watson, C. J. E., Johnson, R. J., Birch, R., Collett, D. & Bradley, J. A. A Simplified Donor Risk Index for Predicting Outcome After Deceased Donor Kidney Transplantation. *Transplantation* **93**, 314–318 (15th Feb. 2012).
31. Rao, P. S., Schaubel, D. E., Guidinger, M. K., Andreoni, K. A., Wolfe, R. A., Merion, R. M., Port, F. K. & Sung, R. S. A Comprehensive Risk Quantification Score for Deceased Donor Kidneys: The Kidney Donor Risk Index. *Transplantation* **88**, 231–236 (27th July 2009).
32. Burton, H., Iyamu Perisanidou, L., Steenkamp, R., Evans, R., Mumford, L., Evans, K. M., Caskey, F. J. & Hilton, R. Causes of Renal Allograft Failure in the UK: Trends in UK Renal Registry and National Health Service Blood and Transplant Data from 2000 to 2013. *Nephrology Dialysis Transplantation* **34**, 355–364 (1st Feb. 2019).
33. Sengupta, S., Fritz, F. J., Harms, R. L., Hildebrand, S., Tse, D. H. Y., Poser, B. A., Goebel, R. & Roebroeck, A. High Resolution Anatomical and Quantitative MRI of the Entire Human Occipital Lobe Ex Vivo at 9.4T. *NeuroImage*. doi:10 . 1016 / j . neuroimage . 2017 . 03 . 039 (20th Mar. 2017).
34. Gowland, P. A. & Leach, M. O. A Simple Method for the Restoration of Signal Polarity in Multi-Image Inversion Recovery Sequences for Measuring T1. *Magnetic Resonance in Medicine* **18**, 224–231 (1991).
35. Szumowski, J., Durkan, M. G., Foss, E. W., Brown, D. S., Schwarz, E. & Crawford, D. C. Signal Polarity Restoration in a 3D Inversion Recovery Sequence Used with Delayed Gadolinium-Enhanced Magnetic Reson-

## 6.8. References

---

- ance Imaging of Cartilage (dGEMRIC). *Journal of Magnetic Resonance Imaging* **36**, 1248–1255 (1st Nov. 2012).
36. Branch, M., Coleman, T. & Li, Y. A Subspace, Interior, and Conjugate Gradient Method for Large-Scale Bound-Constrained Minimization Problems. *SIAM Journal on Scientific Computing* **21**, 1–23 (1st Jan. 1999).
  37. Bjarnason, T. A. & Mitchell, J. R. AnalyzeNNLS: Magnetic Resonance Multiexponential Decay Image Analysis. *Journal of Magnetic Resonance* **206**, 200–204 (1st Oct. 2010).
  38. Andersson, J. L. R., Skare, S. & Ashburner, J. How to Correct Susceptibility Distortions in Spin-Echo Echo-Planar Images: Application to Diffusion Tensor Imaging. *NeuroImage* **20**, 870–888 (1st Oct. 2003).
  39. Le Bihan, D., Breton, E., Lallemand, D., Aubin, M. L., Vignaud, J. & Laval-Jeantet, M. Separation of Diffusion and Perfusion in Intravoxel Incoherent Motion MR Imaging. *Radiology* **168**, 497–505 (1st Aug. 1988).
  40. Andersson, J. L. R. & Sotiroopoulos, S. N. An Integrated Approach to Correction for Off-Resonance Effects and Subject Movement in Diffusion MR Imaging. *NeuroImage* **125**, 1063–1078 (15th Jan. 2016).
  41. Andersson, J. L. R. & Sotiroopoulos, S. N. Non-Parametric Representation and Prediction of Single- and Multi-Shell Diffusion-Weighted MRI Data Using Gaussian Processes. *NeuroImage* **122**, 166–176 (15th Nov. 2015).
  42. Garyfallidis, E., Brett, M., Amirbekian, B., Rokem, A., Van Der Walt, S., Descoteaux, M. & Nimmo-Smith, I. Dipy, a Library for the Analysis of Diffusion MRI Data. *Frontiers in Neuroinformatics* **8**. doi:10 . 3389 / fninf . 2014 . 00008 (2014).
  43. Wang, R., Benner, T., Sorensen, A. G. & Wedeen, V. J. *Diffusion Toolkit: A Software Package for Diffusion Imaging Data Processing and Tractography* in *Proc. Intl. Soc. Mag. Reson. Med.* 15 International Society of Magnetic Resonance in Medicine Annual Meeting (Aug. 2007), 3720.

## 6.8. References

---

44. Descoteaux, M., Angelino, E., Fitzgibbons, S. & Deriche, R. Regularized, Fast, and Robust Analytical Q-Ball Imaging. *Magnetic Resonance in Medicine* **58**, 497–510 (2007).
45. Hess, C. P., Mukherjee, P., Han, E. T., Xu, D. & Vigneron, D. B. Q-Ball Reconstruction of Multimodal Fiber Orientations Using the Spherical Harmonic Basis. *Magnetic Resonance in Medicine* **56**, 104–117 (2006).
46. Tournier, J. .-.-D., Calamante, F., Gadian, D. G. & Connelly, A. Direct Estimation of the Fiber Orientation Density Function from Diffusion-Weighted MRI Data Using Spherical Deconvolution. *NeuroImage* **23**, 1176–1185 (1st Nov. 2004).
47. Tournier, J.-D., Calamante, F. & Connelly, A. Robust Determination of the Fibre Orientation Distribution in Diffusion MRI: Non-Negativity Constrained Super-Resolved Spherical Deconvolution. *NeuroImage* **35**, 1459–1472 (1st May 2007).
48. Tax, C. M. W., Jeurissen, B., Vos, S. B., Viergever, M. A. & Leemans, A. Recursive Calibration of the Fiber Response Function for Spherical Deconvolution of Diffusion MRI Data. *NeuroImage* **86**, 67–80 (1st Feb. 2014).
49. Garyfallidis, E. *Towards an Accurate Brain Tractography* Ph.D. (University of Cambridge, 2013).
50. Gürses, B., Kılıçkesmez, O., Taşdelen, N., Firat, Z. & Gürmen, N. Diffusion Tensor Imaging of the Kidney at 3 Tesla MRI: Normative Values and Repeatability of Measurements in Healthy Volunteers. *Diagnostic and Interventional Radiology (Ankara, Turkey)* **17**, 317–322 (Dec. 2011).
51. Jaimes, C., Darge, K., Khrichenko, D., Carson, R. H. & Berman, J. I. Diffusion Tensor Imaging and Tractography of the Kidney in Children: Feasibility and Preliminary Experience. *Pediatric Radiology* **44**, 30–41 (1st Jan. 2014).
52. Notohamiprodjo, M., Dietrich, O., Horger, W., Horng, A., Helck, A. D., Herrmann, K. A., Reiser, M. F. & Glaser, C. Diffusion Tensor Imaging (DTI) of the Kidney at 3 Tesla—Feasibility, Protocol Evaluation

## 6.8. References

---

- and Comparison to 1.5 Tesla. *Investigative Radiology* **45**, 245 (May 2010).
53. Self, M. W., van Kerkoerle, T., Goebel, R. & Roelfsema, P. R. Benchmarking Laminar fMRI: Neuronal Spiking and Synaptic Activity during Top-down and Bottom-up Processing in the Different Layers of Cortex. *NeuroImage* **197**, 806–817 (15th Aug. 2019).
  54. Muckli, L., De Martino, F., Vizioli, L., Petro, L. S., Smith, F. W., Ugurbil, K., Goebel, R. & Yacoub, E. Contextual Feedback to Superficial Layers of V1. *Current Biology* **25**, 2690–2695 (19th Oct. 2015).
  55. Waehnert, M. D., Dinse, J., Weiss, M., Streicher, M. N., Waehnert, P., Geyer, S., Turner, R. & Bazin, P. .-.L. Anatomically Motivated Modeling of Cortical Laminae. *NeuroImage. In-Vivo Brodmann Mapping of the Human Brain* **93**, 210–220 (1st June 2014).
  56. Taso, M., Munsch, F., Zhao, L. & Alsop, D. C. Regional and Depth-Dependence of Cortical Blood-Flow Assessed with High-Resolution Arterial Spin Labeling (ASL). *Journal of Cerebral Blood Flow & Metabolism*, 0271678X20982382 (14th Jan. 2021).
  57. Piskunowicz, M. *et al.* A New Technique with High Reproducibility to Estimate Renal Oxygenation Using BOLD-MRI in Chronic Kidney Disease. *Magnetic Resonance Imaging* **33**, 253–261 (1st Apr. 2015).
  58. Milani, B. *et al.* Reduction of Cortical Oxygenation in Chronic Kidney Disease: Evidence Obtained with a New Analysis Method of Blood Oxygenation Level-Dependent Magnetic Resonance Imaging. *Nephrology Dialysis Transplantation* **32**, 2097–2105 (1st Dec. 2017).
  59. Pruijm, M., Milani, B. & Burnier, M. Blood Oxygenation Level-Dependent MRI to Assess Renal Oxygenation in Renal Diseases: Progresses and Challenges. *Frontiers in Physiology* **7**. doi:10 . 3389 / fphys.2016.00667. pmid: 28105019 (5th Jan. 2017).
  60. Li, L.-P., Milani, B., Pruijm, M., Kohn, O., Sprague, S., Hack, B. & Prasad, P. Renal BOLD MRI in Patients with Chronic Kidney Disease: Comparison of the Semi-Automated Twelve Layer Concentric Objects (TLCO) and Manual ROI Methods. *Magnetic Resonance Materials in*

## 6.8. References

---

- Physics, Biology and Medicine.* doi:10 . 1007 / s10334 - 019 - 00808 - 5 (10th Dec. 2019).
61. Bane, O. *et al.* Consensus-Based Technical Recommendations for Clinical Translation of Renal BOLD MRI. *Magnetic Resonance Materials in Physics, Biology and Medicine* **33**, 199–215 (1st Feb. 2020).
  62. Dale, A. M., Fischl, B. & Sereno, M. I. Cortical Surface-Based Analysis: I. Segmentation and Surface Reconstruction. *NeuroImage* **9**, 179–194 (1st Feb. 1999).
  63. Birkl, C., Langkammer, C., Golob-Schwarzl, N., Leoni, M., Haybaeck, J., Goessler, W., Fazekas, F. & Ropele, S. Effects of Formalin Fixation and Temperature on MR Relaxation Times in the Human Brain. *NMR in Biomedicine* **29**, 458–465 (1st Apr. 2016).
  64. Schmierer, K. *et al.* Quantitative Magnetic Resonance of Postmortem Multiple Sclerosis Brain before and after Fixation. *Magnetic Resonance in Medicine* **59**, 268–277 (1st Feb. 2008).
  65. Shatil, A. S., Uddin, M. N., Matsuda, K. M. & Figley, C. R. Quantitative Ex Vivo MRI Changes Due to Progressive Formalin Fixation in Whole Human Brain Specimens: Longitudinal Characterization of Diffusion, Relaxometry, and Myelin Water Fraction Measurements at 3T. *Frontiers in Medicine* **5**. doi:10.3389/fmed.2018.00031 (2018).
  66. Shepherd, T. M., Thelwall, P. E., Stanisz, G. J. & Blackband, S. J. Aldehyde Fixative Solutions Alter the Water Relaxation and Diffusion Properties of Nervous Tissue. *Magnetic Resonance in Medicine* **62**, 26–34 (2009).
  67. Thelwall, P. E., Shepherd, T. M., Stanisz, G. J. & Blackband, S. J. Effects of Temperature and Aldehyde Fixation on Tissue Water Diffusion Properties, Studied in an Erythrocyte Ghost Tissue Model. *Magnetic Resonance in Medicine* **56**, 282–289 (2006).
  68. Cox, E. F., Buchanan, C. E., Bradley, C. R., Prestwich, B., Mahmoud, H., Taal, M., Selby, N. M. & Francis, S. T. Multiparametric Renal Magnetic Resonance Imaging: Validation, Interventions, and Alterations in Chronic Kidney Disease. *Frontiers in Physiology* **8**, 696 (2017).

## 6.8. References

---

69. Keenan, K. E. *et al.* Multi-Site, Multi-Vendor Comparison of T1 Measurement Using ISMRM/NIST System Phantom in Proc. Intl. Soc. Mag. Reson. Med. 24 International Society of Magnetic Resonance in Medicine Annual Meeting. **24** (Singapore, 10th May 2016), 3290.
70. Thavarajah, R., Mudimbaimannar, V. K., Elizabeth, J., Rao, U. K. & Ranganathan, K. Chemical and Physical Basics of Routine Formaldehyde Fixation. *Journal of Oral and Maxillofacial Pathology : JOMFP* **16**, 400–405 (2012).
71. Bellini, M. I., Charalampidis, S., Herbert, P. E., Bonatsos, V., Crane, J., Muthusamy, A., Dor, F. J. M. F. & Papalois, V. Cold Pulsatile Machine Perfusion versus Static Cold Storage in Kidney Transplantation: A Single Centre Experience. *BioMed Research International* **2019**, e7435248 (16th Jan. 2019).
72. Moers, C. *et al.* The Value of Machine Perfusion Perfusate Biomarkers for Predicting Kidney Transplant Outcome. *Transplantation* **90**, 966–973 (15th Nov. 2010).
73. Wight, J. P., Chilcott, J. B., Holmes, M. W. & Brewer, N. Pulsatile Machine Perfusion vs. Cold Storage of Kidneys for Transplantation: A Rapid and Systematic Review. *Clinical Transplantation* **17**, 293–307 (2003).

# **Chapter 7**

## **Conclusion**

The work presented in this thesis has developed techniques for quantitative renal Magnetic Resonance Imaging (MRI). These techniques will complement existing multiparametric renal protocols, Figure 7.1.

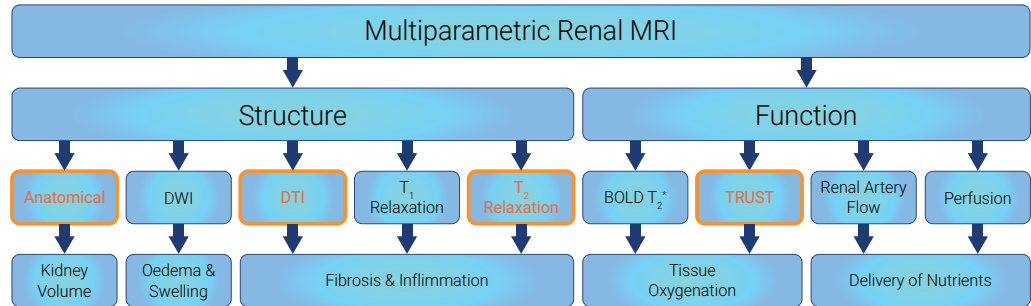


Figure 7.1: An overview of the multiparametric renal MRI protocol. This shows how the areas focused on in this thesis (highlighted in orange) fit into the full protocol designed to provide a complete evaluation of renal health using MRI.

In Chapter 3, the four commonly used renal  $T_2$  mapping sequences of Spin Echo (SE)-Echo Planar Imaging (EPI), Multi-Echo Turbo Spin Echo (ME-TSE), Gradient Spin Echo (GrASE) and Carr-Purcell-Meiboom-Gill (CPMG)  $T_2$  preparation, were methodically evaluated. In addition to the  $T_2$  mapping acquisition schemes, methods of calculating  $T_2$  maps from resulting multi-echo data were compared. This comparison was first performed using multiple calibrated phantoms to assess accuracy, including sensitivity to flow, and spatial blurring. Each method was then used to collect  $T_2$  maps of five healthy volunteers to evaluate their performance in-vivo.

The SE-EPI sequence was the most accurate over the range of  $T_2$  found in the kidneys (40 - 200 ms) with a Mean Percentage Error (MPE) of  $8 \pm 5\%$  in the static phantom however this sequence was also highly sensitive to flow. This is sub-optimal for renal  $T_2$  mapping given the kidneys are highly perfused and the effects of flow of water-like filtrates through renal tubules can clearly be seen in-vivo. The ME-TSE sequence was the least accurate of the sequences evaluated in the static phantom (MPE of  $23 \pm 13\%$ ) however its sensitivity to flow and degree of spatial blurring were an improvement on

---

those of the SE-EPI. The GraSE sequence produced a MPE of  $15 \pm 4\%$  in the static phantom and was the least sensitive to flow of the sequences compared. In-vivo it showed the greatest contrast between cortex and medulla. The CPMG  $T_2$  prep sequence yielded a MPE of  $11 \pm 1\%$  and was relatively insensitive to flow however suffered from a large degree of spatial blurring thus limiting its in-vivo utility. It was concluded that the GraSE sequence is the optimum protocol for renal  $T_2$  mapping on the Philips platform due to its combination of quantitative accuracy, insensitivity to flow and superior image quality. For the kidneys, a basic two parameter fitting model produces the most accurate  $T_2$  map of the fitting method compared. In future these techniques should be applied to study renal disease patients to assess inflammation of tissues. Here the GraSE sequence was optimised for the Philips platform; for multicentre studies the availability of sequences across vendors must be considered. The ME-TSE sequence is more commonly implemented across vendors and as such may be preferable for multicentre studies.

Chapter 4 focused on the translation of methods for measuring blood oxygen saturation from the superior sagittal sinus in the brain to the renal vein. Currently renal oxygenation is typically assessed using Blood Oxygen Level Dependent (BOLD)  $T_2^*$  maps, however, these maps are influenced by factors other than tissue oxygenation such as susceptibility effects, shimming and baseline blood flow. As such, it is desirable to have an alternative method to measuring renal oxygenation. Susceptibility Based Oximetry (SBO) was performed and  $T_2$  Relaxation Under Spin Tagging (TRUST) optimised for use in the abdomen. The TRUST optimisation involved replacing the Transfer Insensitive Labelling Technique (TILT) labelling scheme with a Flow-sensitive Alternating Inversion Recovery (FAIR) labelling scheme, applying respiratory triggering and optimising the Post Label Delay (PLD) for the renal vessels. SBO was found to be unsuitable for use in the kidneys due to the geometry of the angle of the renal vein to the  $B_0$  field. TRUST was successfully used to measure the oxygen saturation of the portal vein and hepatic artery and measured an increase in oxygen saturation in the renal vein

---

of  $16 \pm 3\%$  during an oxygen challenge.

The TRUST scheme is currently being applied in the study of COVID-19 in which 35 % of patients experience acute kidney injury for which hypoxia and altered blood flow are thought to be key determinants. Data is demonstrating a reduction in venous oxygenation from  $86 \pm 7\%$  to  $59 \pm 8\%$  in acute Intensive Care Unit (ICU) ventilated COVID-19 patients. This work is being performed in collaboration with Uppsala University. The use of TRUST to study oxygenation in the liver circulation within patient populations is also being explored in collaboration with Dr Bryan Haddock of Rigshospitalet, Copenhagen University Hospital.

Machine learning methods were used in Chapter 5 to segment the kidneys from  $T_2$ -weighted Half-Fourier Acquisition Single-shot Turbo spin Echo (HASTE) images to calculate Total Kidney Volume (TKV). A Convolutional Neural Network (CNN) was trained on images from both healthy volunteers and Chronic Kidney Disease (CKD) patients and used to predict the TKV of ten unseen subjects, each scanned five times. This resulted in a mean Dice score of  $0.93 \pm 0.01$  and a mean volume difference from manual segmentations of  $1.2 \pm 16.2\text{ m}\ell$ . The CNN also produced a significantly lower Coefficient of Variation (CoV) than the human observers ( $1.5 \pm 0.5\%$  and  $2.7 \pm 0.9\%$  respectively,  $p = 0.008$ ). A self contained executable has been produced to enable use of the CNN by inexperienced users to reduce segmentation times from 15 - 30 minutes per subject to approximately 10 seconds. In future work the performance of the network will be evaluated across multiple vendors (GE, Philips and Siemens,) and additional architectures will be explored, initially by including adjacent slices as colour channels and later expanding to a full 3D CNN.

In Chapter 6 a multiparametric ex-vivo protocol is developed to enable the assessment of explanted renal samples. This protocol involved the acquisition of relaxation maps and diffusion based measures ex-vivo, for each an in-vivo counterpart is also demonstrated. The aim for the future is to apply these ex-

---

vivo protocols and in-vivo measures in a nephrectomy model where the ex-vivo measures can be used with existing histopathological processing pipelines to better understand the interplay between quantitative MRI parameters and underlying histological processes. Additionally the ex-vivo paradigm is an excellent foundation for future developments of MRI based nephron number measurements utilising super resolution techniques to upsample data beyond the acquisition resolution.

Further, the high spatial resolution, statistical nature of ex-vivo data has been used to validate a method of assessing the change in quantitative MRI measures with depth of renal tissue. This method was implemented using a bespoke Freesurfer and MATLAB pipeline to generate quantitative maps of tissue depth. This pipeline can be applied to any quantitative data in the multiparametric protocol provided a full organ coverage anatomical scan is acquired in the same session. It avoids the need to adjust quantitative acquisition protocols and allows an additional analysis method for renal MRI data to augment the long-established practice of cortical and medullary segmentation.

Moving forward, the techniques developed in this thesis can be incorporated into multiparametric renal MRI studies undertaken at the Sir Peter Mansfield Imaging Centre (SPMIC) and more widely across the United Kingdom Renal Imaging Network (UKRIN) and Parenchima European Cooperation in Science and Technology (COST) initiatives. Current areas of active research in patient populations at the SPMIC focus on Chronic Kidney Disease, Acute Kidney Injury (AKI), the effects of dialysis and COVID-19. Additionally, the ex-vivo protocol could be used for the assessment of renal transplants, increasing confidence in organ quality prior to transplant and thus enabling an increased use of kidneys currently deemed marginal in quality. In the long term, this could be used as a rapid scan of allografts in transplant centres to increase transplant rates and therefore reduce waiting list times.

## Appendix A

### $T_2$ Fitting Methods

## A.1 NIST Standard $T_2$ Mapping Protocol

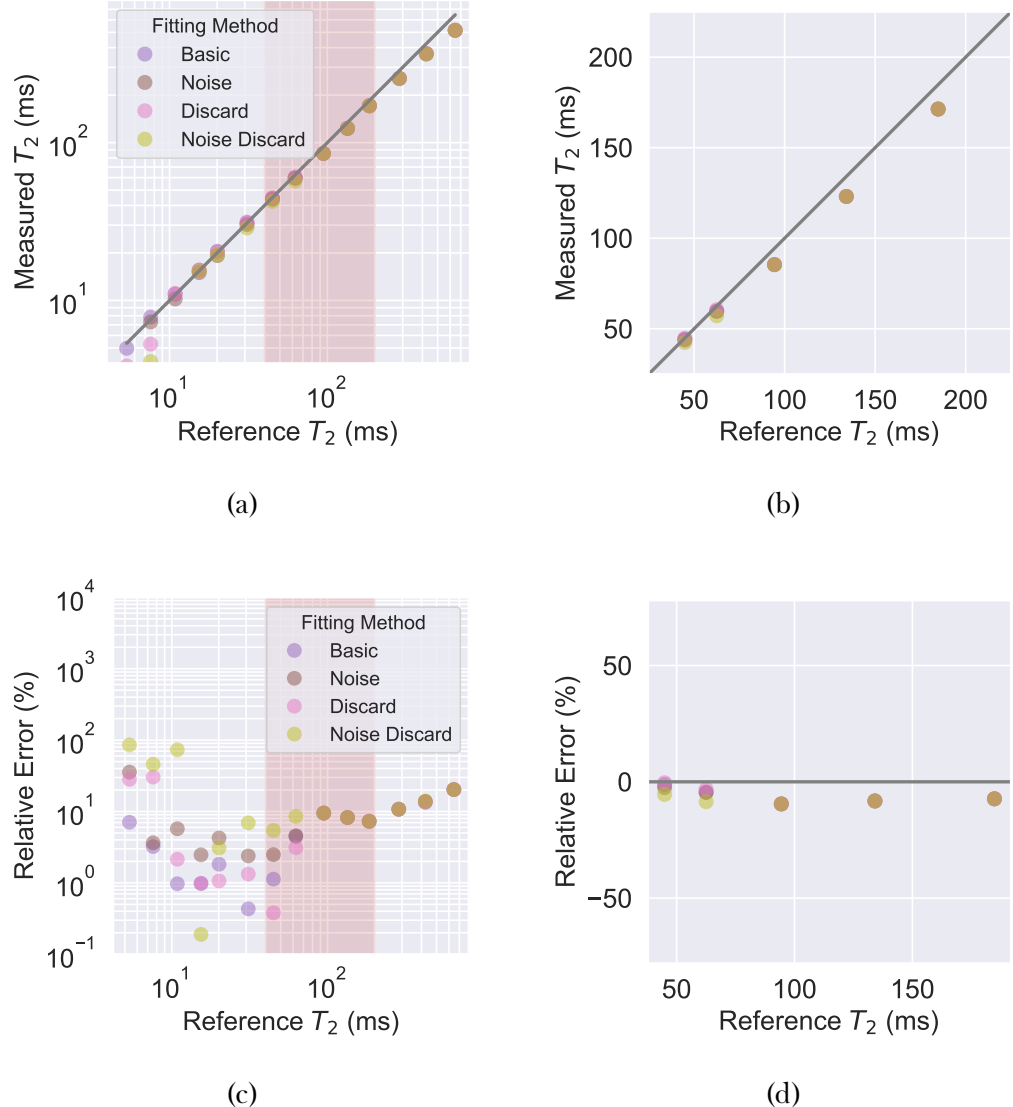


Figure A.1:  $T_2$  measured using the National Institute of Standards and Technology (NIST) recommended Multi Echo-Spin Echo (ME-SE) protocol, fit using each of the four fitting methods compared. (a) The full range of  $T_2$  spheres is shown on logarithmic axis with the range of  $T_2$  reported in the kidneys shaded in red (b) The spheres with  $T_2$  in the range of the kidneys are shown on linear axis. (c) and (d) show the relative error of each sphere for the full and renal range of spheres respectively.

### A.1. NIST Standard $T_2$ Mapping Protocol

---

$T_2$ Range	MPE (5 ms – 650 ms) (%)				MPE (40 ms – 200 ms) (%)			
Fitting Method	Basic	Noise	Discard	Discard and Noise	Basic	Noise	Discard	Discard and Noise
ME-SE	5 ± 7	9 ± 9	9 ± 10	21 ± 26	6 ± 3	6 ± 3	6 ± 3	8 ± 1

Table A.1: Mean Percentage Error (MPE) when measuring  $T_2$  of the QalibreMD phantom over different ranges using the NIST recommended ME-SE protocol and each fitting method. 5 ms – 650 ms is the full range of  $T_2$  available in the phantom and 40 ms – 200 ms is the range of  $T_2$  reported in the kidneys.

## A.2 Renal $T_2$ Mapping Protocols

### A.2.1 Basic Fit

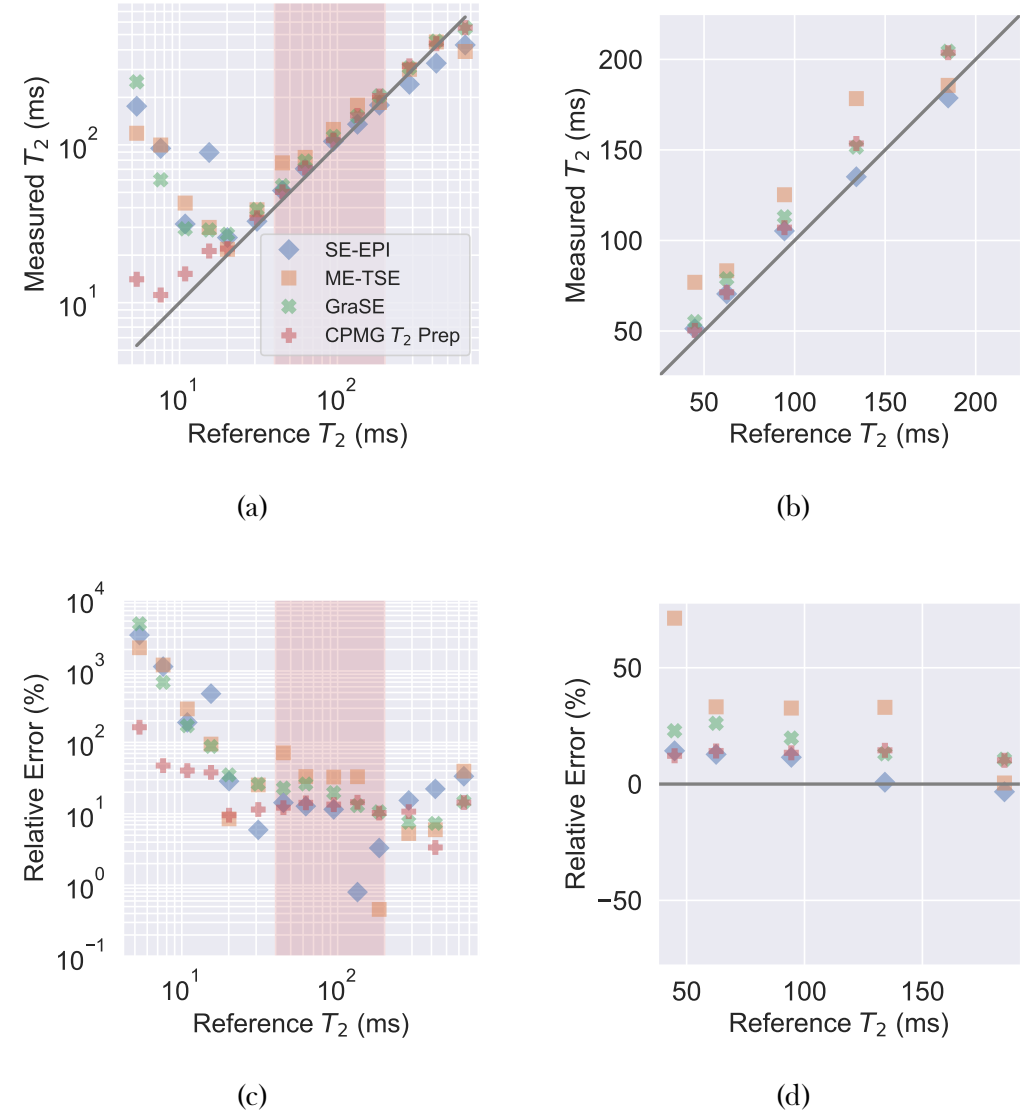


Figure A.2:  $T_2$  measured using each acquisition method and basic fitting compared to the reference  $T_2$  from literature. (a) The full range of  $T_2$  spheres is shown on logarithmic axis with the range of  $T_2$  reported in the kidneys shaded in red (b) The spheres with  $T_2$  in the range of the kidneys are shown on linear axis. (c) and (d) show the relative error of each sphere for the full and renal range of spheres respectively.

### A.2.2 Noise Fit

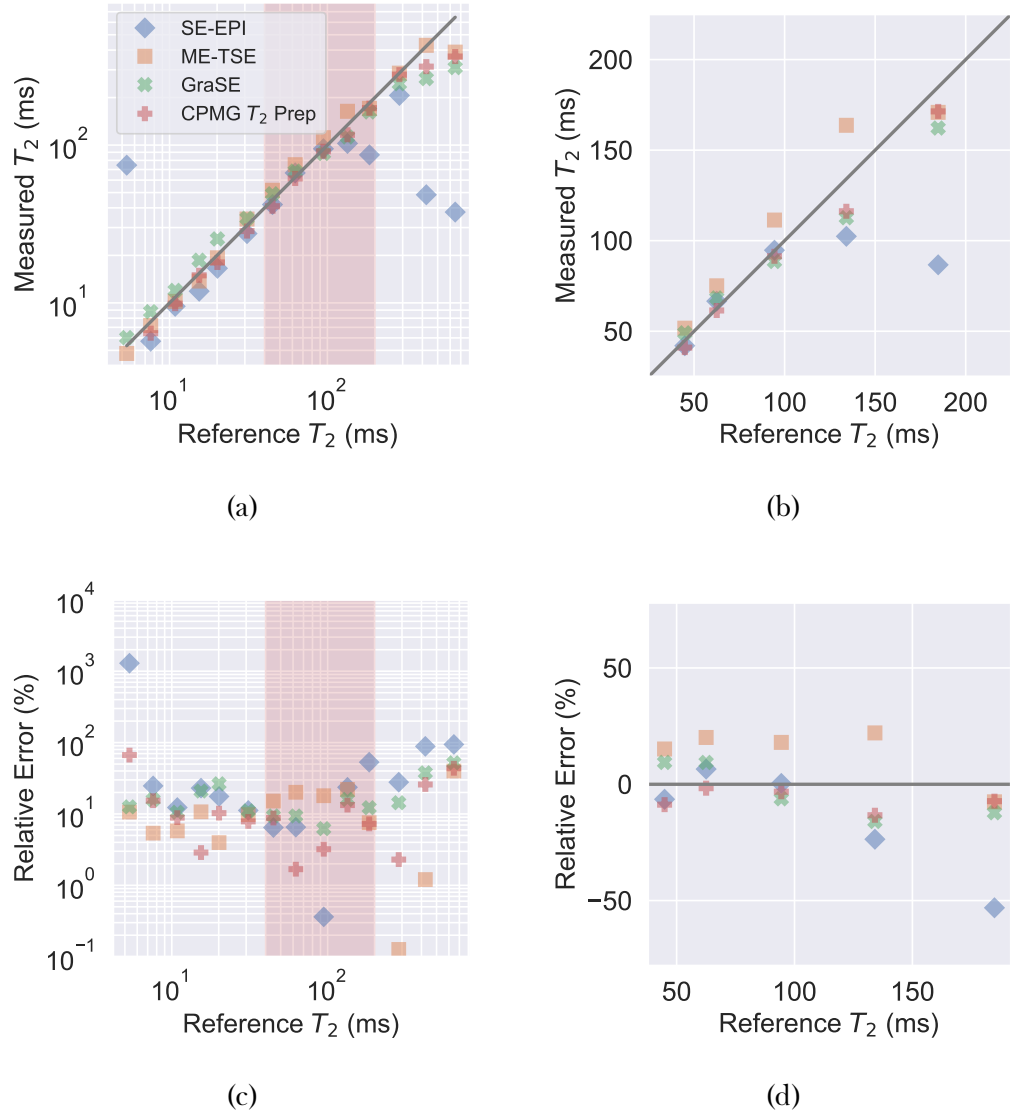


Figure A.3:  $T_2$  measured using each acquisition method and noise fitting compared to the reference  $T_2$  from literature. (a) The full range of  $T_2$  spheres is shown on logarithmic axis with the range of  $T_2$  reported in the kidneys shaded in red (b) The spheres with  $T_2$  in the range of the kidneys are shown on linear axis. (c) and (d) show the relative error of each sphere for the full and renal range of spheres respectively.

### A.2.3 Discard Fit

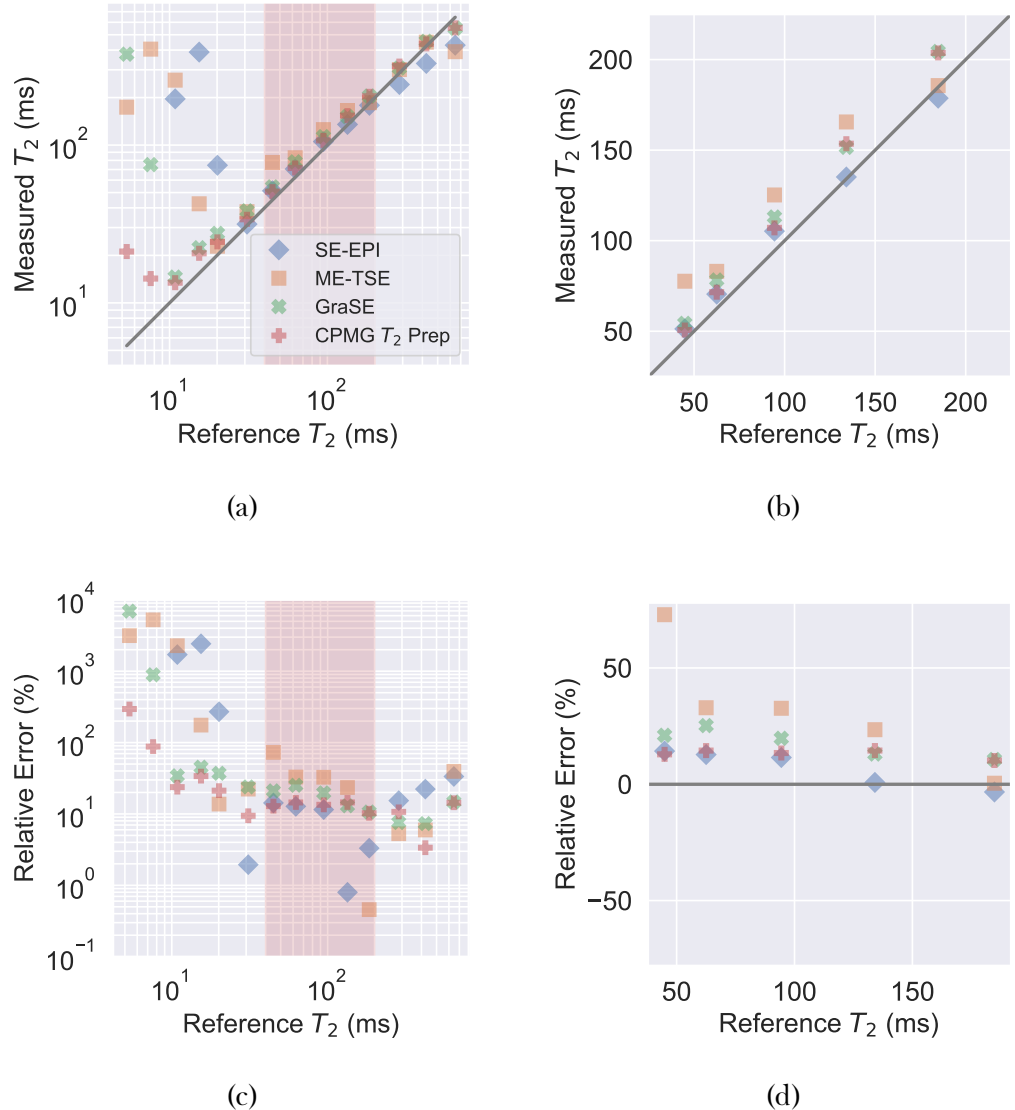


Figure A.4:  $T_2$  measured using each acquisition method and discard fitting compared to the reference  $T_2$  from literature. (a) The full range of  $T_2$  spheres is shown on logarithmic axis with the range of  $T_2$  reported in the kidneys shaded in red (b) The spheres with  $T_2$  in the range of the kidneys are shown on linear axis. (c) and (d) show the relative error of each sphere for the full and renal range of spheres respectively.

### A.2.4 Noise and Discard Fit

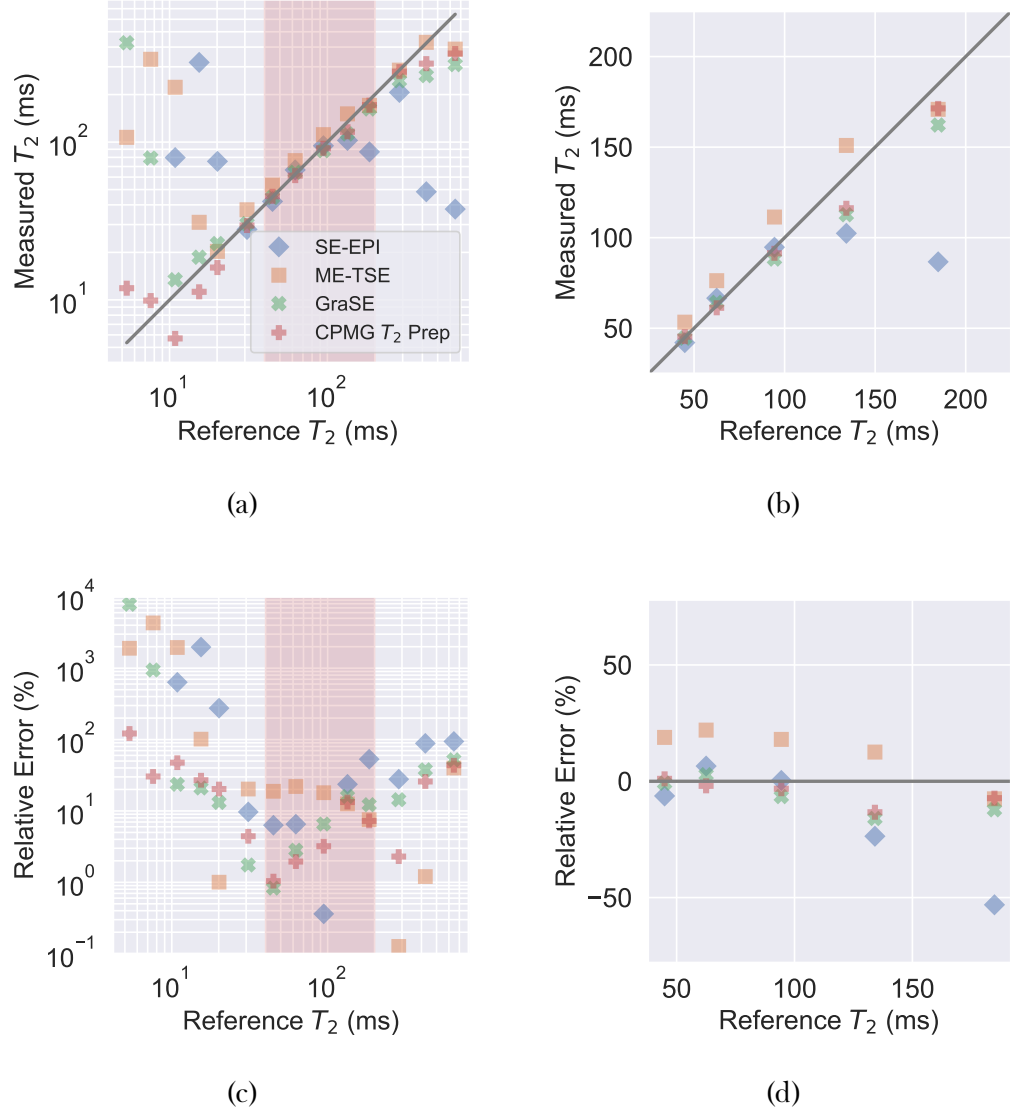


Figure A.5:  $T_2$  measured using each acquisition method and noise and discard fitting compared to the reference  $T_2$  from literature. (a) The full range of  $T_2$  spheres is shown on logarithmic axis with the range of  $T_2$  reported in the kidneys shaded in red (b) The spheres with  $T_2$  in the range of the kidneys are shown on linear axis. (c) and (d) show the relative error of each sphere for the full and renal range of spheres respectively.

# Appendix B

## Tractography Pipeline

```
1 import numpy as np
2 import nibabel as nib
3 from dipy.tracking.eudx import EuDX
4 from dipy.tracking import utils
5 from dipy.tracking.streamline import Streamlines
6 from dipy.reconst import peaks
7 from dipy.reconst.csdeconv import \
8     ConstrainedSphericalDeconvModel, recursive_response
9 from dipy.core.gradients import gradient_table_from_bvals_bvecs
10 from dipy.io.streamline import save_trk
11
12 if __name__ == '__main__':
13     print('Ingesting Data')
14     img = nib.load('data.nii.gz')
15     mask = nib.load('mask.nii.gz')
16     bvals = np.loadtxt('bvals')
17     bvecs = np.loadtxt('bvecs')
18     data = img.get_fdata()
19
20     mask_data = mask.get_fdata()
21     mask_data = (mask_data>0)
22
23     gtab = gradient_table_from_bvals_bvecs(bvals.T, bvecs.T)
24
25     print('Estimating Fibre Response Function')
```

---

```
26     response = recursive_response(gtab, data,
27                                     mask=mask_data, sh_order=8,
28                                     peak_thr=0.01, init_fa=0.08,
29                                     init_trace=0.0021, iter=8,
30                                     convergence=0.001, parallel=False)
31
32     print('Generating CSD Model')
33     csd_model = ConstrainedSphericalDeconvModel(gtab, response,
34                                                   sh_order=6)
35
36     print('Getting Peaks From Model')
37     csd_peaks = peaks.peaks_from_model(model=csd_model,
38                                         data=data,
39                                         sphere=peaks.default_sphere,
40                                         relative_peak_threshold=.8,
41                                         min_separation_angle=45,
42                                         mask=mask_data)
43
44     print('Generating Seeds')
45     seeds = utils.seeds_from_mask(mask_data, density=1)
46
47     print('Propogating From Seeds')
48     streamline_gen = EuDX(csd_peaks.peak_values,
49                            csd_peaks.peak_indices,
50                            odf_vertices=peaks.default_sphere.vertices,
51                            a_low=.05, step_sz=.5, seeds=seeds)
52
53     print('Generating Streamlines')
54     streamlines = Streamlines(streamline_gen, buffer_size=512)
55
56     print('Saving Output For Your Perusal')
57     save_trk('tracts.trk', streamlines,
58               shape=mask.shape, vox_size=data.header.get_zooms(),
59               affine=data.affine)
```